MODIFYING FERRITIC STAINLESS STEELS FOR SOLID OXIDE FUEL CELL APPLICATIONS

by

Scot Jason Laney

BS, University of Pittsburgh, 2001

MS, University of Pittsburgh, 2004

Submitted to the Graduate Faculty of

School of Engineering in partial fulfillment

of the requirements for the degree of

Doctor of Philosophy

University of Pittsburgh

2007

UNIVERSITY OF PITTSBURGH

SCHOOL OF ENGINEERING

This dissertation was presented

by

Scot Laney

It was defended on

March 2, 2007

and approved by

Dr. J. Leonard, Professor, Department of Mechanical Engineering and Materials Science

Dr. J. Barnard, Professor, Department of Mechanical Engineering and Materials Science

Dr. C. Johnson, Research Chemist, National Energy Technology Laboratory, WV

Dissertation Co-Director: Dr. G.H. Meier, Professor, Department of Mechanical Engineering and Materials Science

Dissertation Co-Director: Dr. F.S. Pettit, Professor, Department of Mechanical Engineering and Materials Science

MODIFYING FERRITIC STAINLESS STEELS FOR SOLID OXIDE FUEL CELL APPLICATIONS

Scot Laney, PhD

University of Pittsburgh, 2007

One of the most important problem areas associated with the solid oxide fuel cells is selection of a cost effective material for use as the interconnect component of the cell. Metals are now being considered as materials for this component, with ferritic stainless steels being the leading candidate. This work evaluates methods to combat the problem areas, namely rapid growth rate and vaporization of the oxide scale, that hinder the use of these materials. Oxidation experiments have been performed in dry and wet single atmosphere exposures as well as a dual environment exposure to simulate the conditions in a working SOFC. Measurements of the electrical properties of the oxides that formed were also performed. Commercial alloys, E-Brite and Crofer 22APU, were tested to form a baseline and resultant oxidation and electrical behaviors match those found in the literature. Isothermal oxidation tests for short exposure times have also led to a possible mechanism for the formation of the $MnCr_2O_4$ layer on Crofer. All of these tests were then replicated on a series of experimental Fe-22Cr-XTi (X=0-4) alloys. These alloys are shown to form a rutile layer analogous to the $MnCr_2O_4$ layer on Crofer. While this layer does prevent some chromia vaporization, the consequences due to the presence of Ti in the chromia include increased growth rate, decreased resistivity, extensive internal oxidation and nitridation of Ti, and a change of the growth direction of the chromia. The alloys containing ~2 – 3 wt%Ti appear to offer the best combination of oxidation, electrical, and mechanical properties. Coatings of lanthanum chromites and ferrites were also tested and shown to be very

sensitive to exposure condition, resulting in the formation of pores, and to coating thickness, where thicker coatings are subject to cracking. Finally, reactive element oxide doping was attempted to slow the oxide growth rate for E-Brite (CeO_2 doping) and for the Fe-Cr-Ti alloys (CeO_2 and La_2O_3 doping). A significant effect was observed for E-Brite, while both dopants produced little change in the amount of oxide formed on the Ti bearing alloys.

TABLE OF CONTENTS

LIST OF TABLES

LIST OF FIGURES

1.0 INTRODUCTION

In the quest for efficient, environmentally friendly energy sources, fuel cells have begun to come into their own as a viable method to produce electricity. They are simple and conceptually utilize a practically ideal chemical reaction, very efficient and with the different electrolytes available, are flexible enough for several types of applications. Most importantly, the existence of programs such as SECA (Solid State Energy Conversion Alliance)[1] shows that there is a commitment to developing the field.

Fuel cells are also not without problems. The work described here is related to solid oxide fuel cells (SOFC). Most of the problems with SOFCs can be traced to the high temperatures required to operate the cell. Without going into specifics, fully ceramic designs require expensive materials and very high temperatures, while lower temperature cells with cheaper metallic components lack long term durability. This work concentrates on improving the durability of ferritic stainless steels for use as interconnect materials in the cell in order to improve the lifetime of the low temperature SOFCs.

The challenge of selecting materials for use as interconnects lies in the somewhat contradictory requirements. A material must be inexpensive and easy to form, yet exhibit long term durability (~40,000 hrs). The aim is to use metallic alloys, but the thermal expansion characteristics must match those of the ceramic electrolyte, anode, and cathode (α = ~10-11x10^{-6}/^{o}C). The alloy must resist oxidation, but must also be electrically conductive. The material should not adversely affect other components, but most of the alloys that fit the previous

requirements are chromia formers, which form volatile gas species that poison the cathode in the cell. Ferritic stainless steels are promising candidate materials, and this work addresses some of the shortcomings, namely the oxidation/conductivity and vaporization issues. It is also of vital importance that once effective methods for achieving these goals are developed, that these systems must be tested to show acceptable electrical conductivity and good behavior in a simulated fuel cell environment.

2.0 BACKGROUND

To gain the fullest appreciation for the work proposed here, it is important to first understand more about the SOFC. Background information will be presented in the form of an overview of fuel cell history, a description of the SOFC components and mechanisms, and finally specific information on the ferritic stainless steels that are being studied here as materials for the interconnect component of the cell.

2.1 FUEL CELL HISTORY

With the seemingly sudden interest in fuel cells, it is hard to believe that they comprise a quite old technology. The following points are from a review on the past 100 years of fuel cell history with an emphasis on the relation to the Electrochemical Society by Perry and Fuller[2]. The development of the fuel cell is credited to Sir William Grove in 1839. Mond and Langer attempted to scale up the fuel cell to be a useful power generating device, and their work introduced some improvements such as powdered catalysts to increase the surface area. In 1896, Jacques built large carbon/air batteries that had a 1.5kW output. Around this time, the "Nernst Glower" demonstrated the use of a solid ionic conductor, which is the basis for the solid oxide fuel cell. Sir Francis Bacon began working on a hydrogen/oxygen cell in 1933 that used an alkaline electrolyte. Pratt and Whitney eventually licensed this technology and it was eventually used in the Apollo space program. Strangely, unlike other technologies used in the space

program, fuel cells have not caught on commercially. This is also despite the consistent yearly increase in the number of papers published on the topic.

More currently, fuel cells are being considered for several new applications including "distributed" power plants and for electric or hybrid cars. Distributed power is the concept of utilizing several small power plants, as opposed to fewer large plants, which reduce transmission losses and prevent large scale black outs. Ford has built the Focus FCV, which is a fuel cell powered version of the popular Focus[3]. Other car manufacturers are developing similar vehicles. Honda recently supplied a fuel cell powered vehicle to a California family for real world testing[4]. SOFCs are the leading candidates for use in fuel cell power plants and are being considered for use in automobiles.

2.2 COMPONENTS

A fuel cell is a deceptively simple device. It is most easily thought of as a battery that utilizes gases instead of liquid or solid fuels. A cell consists of an electrolyte, a cathode, an anode, and current carrier (interconnect), which is the same as the Duracells or Energizers that everyone knows. Figure 2-1 shows the two common arrangements of the components into a working SOFC. The planar style shown in Figure 2-1a is the one that is the subject of this work and is the configuration that most current research is working towards perfecting. This is due to the use of what are essentially sheets of material, and are frequently made by tape casting the layers. This makes the cell easy to manufacture and stack.

Fuel cells typically generate about 0.7 V of output, and therefore the ability to stack the cells easily allows them to be used in series. This makes the fuel cell scaleable for several applications. As an example, cars utilize 12 V batteries. That battery could theoretically be

replaced by a fuel cell stack consisting of a stack of 17 (12 V/0.7 V = 17) individual fuel cells. Figure 2-2 shows a picture of a used fuel cell without the interconnect, while Figure 2-3 shows a fuel cell stack. Each component will be discussed in more detail.

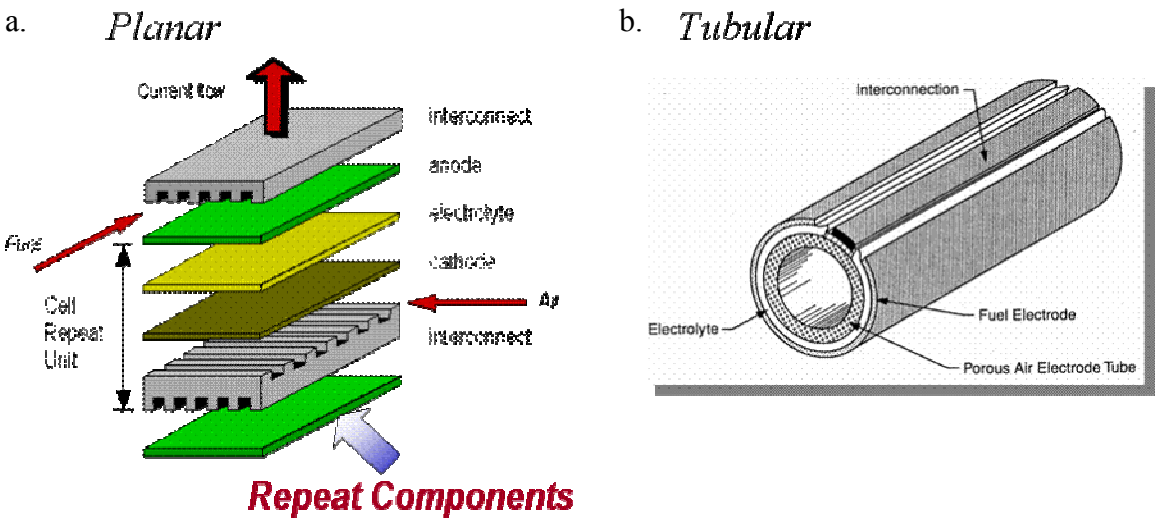

Figure 2–1 Diagrams showing the planar (a.) and tubular (b.) fuel cell configurations

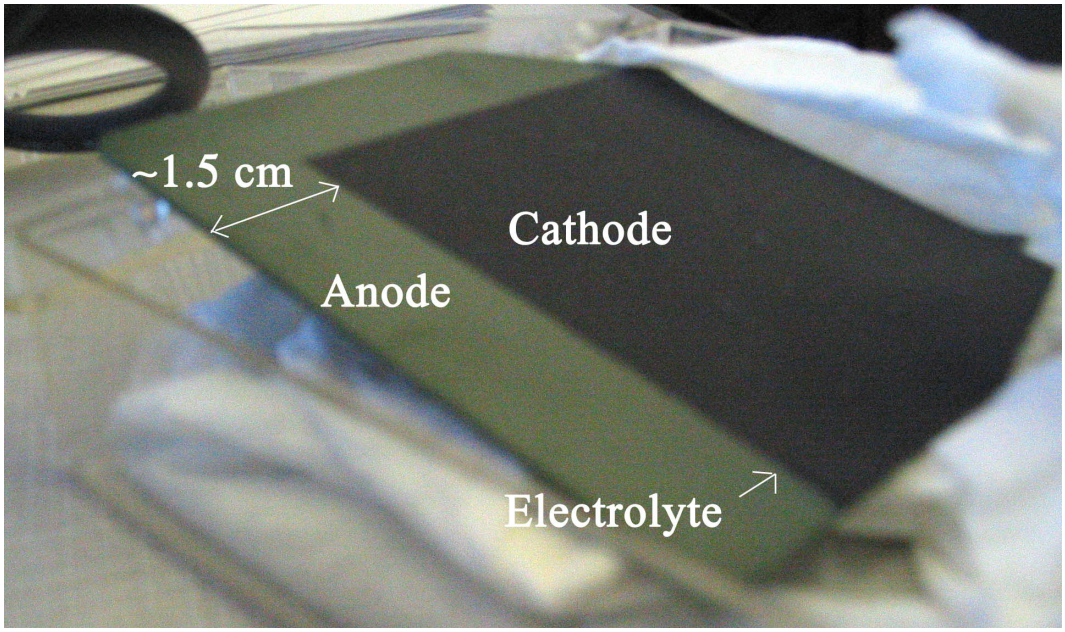

Figure 2–2 Photograph of a used (broken) single stack fuel cell without an interconnect

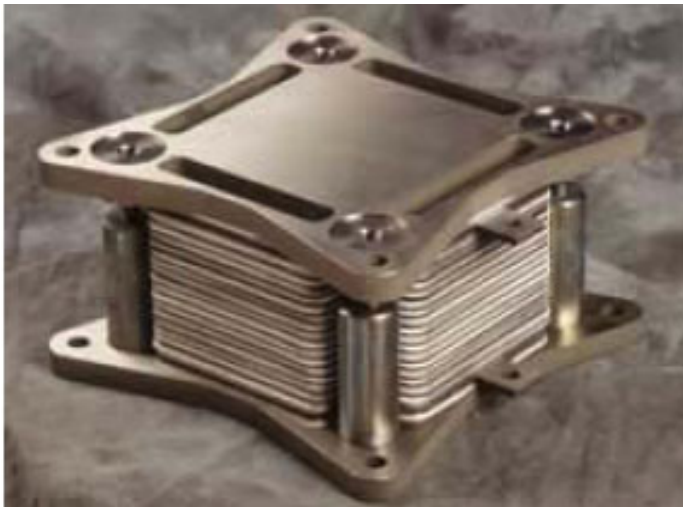

Figure 2-3 Photograph of a fuel cell stack[5]

Table 2-1 Types of fuel cells[6]

Comparisons of Fuel Cell Technologies

Fuel Cell Type	Electrolyte	Operating Temp	Applications	Advantages	Disadvantages
Polymer Electrolyte Membrane (PEM)	Solid organic polymer polysulfonic acid	60-100C	-electric utility -portable power -transportation	-Solid electrolyte reduces corrosion & management problems -Low temperature -Quick start up time	-Low temperature requires expensive catalysts -High sensitivity to fuel impurities
Alkaline (AFC)	Aqueous solution of KOH soaked in a matrix	90-100C	-military -space	-Cathode reaction faster in alkaline electrolyte => high performance	-Expensive removal of CO2 from fuel and air streams required
Phosphoric Acid (PAFC)	Liquid phosphoric acid soaked in a matrix	175-200C	-electric utility -transportation	'-Up to 85% efficiency in cogeneration of electricity and heat -Can use impure H2 as fuel	-Requires platinum catalyst -Low current and power -Large size/weight
Molten Carbonate (MCFC)	Liquid solution of Li, Na, and/or K carbonates soaked in a matrix	600-1000C	-electric utility	-High efficiency -Fuel flexibility -Can use a variety of catalysts	-High temperature enhances corrosion and breakdown of cell components
Solid Oxide (SOFC)	Solid zirconium oxide with small yttria additions	600-1000C	-electric utility	-High Efficiency -Fuel Flexibility -Can use a variety of catalysts -Solid electrolyte reduces corrosion & management problems	-High temperature enhances corrosion and breakdown of cell components

2.2.1 Electrolyte

The most important part of a fuel cell is the electrolyte. Indeed, the various fuel cells types are designated by the electrolyte used, which will be described below in more detail. The material chosen must be able to quickly transport ions from one side of the cell to the other, with fast diffusion of oxygen or hydrogen ions being preferred. It is also preferred that the rapid ionic transport occur at the lowest possible temperature.

2.2.1.1 Types of Fuels Cells: The Department of Energy recognizes six different types of fuel cells, which, as mentioned above, are named for the electrolyte used. Table 2-1 below shows the aspects of five of these, including the electrolyte material, operating temperature range, advantages, and disadvantages.

2.2.1.2 Aspects of the SOFC Due to the Electrolyte: The electrolyte material currently used in SOFCs is yttrium stabilized zirconia (YSZ), which is very well known for its ionic transport of oxygen. SOFCs with YSZ electrolytes are quoted as being able to reach fuel efficiencies of around 40%[5]. The temperature range in which YSZ performs acceptably is 600 – 1000^{o}C. Relatively recent advances in processing have produced thinner YSZ layers, thereby decreasing the operating temperatures to the mid – lower end of this range. This temperature is still rather high and can lead to degradation of some components, namely any metallic ones, in the system. There are also some important advantages in the higher temperatures that make its development attractive. These include the ability to use a variety of less pure fuels, internal fuel reforming, and can be combined with gas turbine systems to further increase the fuel efficiency to 70%[5]. The latter statement makes the hybrid solid oxide fuel cell/gas turbine systems the most efficient

method for generation of electricity currently available. There are several other materials being investigated as possible electrolyte materials, including: Sc_2O_3 doped ZrO_2, Gd doped CeO_2, and Sr and Mg doped Lanthanum Gallate.[5]

2.2.2 Cathode

The cathode is the positive electrode in the fuel cell. Oxidizing gas is flowed into the system on this side of the cell and the cathode material must be such that it catalyzes the following reaction:

$$\frac{1}{2}O_2+2e^-=O^{2-} \quad (1)$$

Electrodes in general must have good electrical conductance in order to transport ions to or from the three phase (cathode, electrolyte, gas) interface. They are porous in order to increase the surface area for reaction and to shorten the conduction distance. They must also act as a physical barrier between the bulk gas and the electrolyte. The most common cathode material used in SOFCs is the perovskite, strontium doped $LaMnO_3$ (LSM). Strontium doped $La(Fe,Co)O_3$ (LSCF) is another candidate material.

2.2.3 Anode

The anode is the negative electrode in the cell. Reducing or fuel gases are flowed into this side of the system. These include H_2, CO, CH_4, combinations of these, and other, more exotic reducing gases. The anode must catalyze a reaction similar to the following:

$$O^{2-}+H_2=H_2O+2e^- \quad (2)$$

The anode must also conform to the requirements discussed above for electrodes. A Ni/YSZ cermet is commonly used as the anode. The anode is usually produced as NiO/YSZ, in which case the NiO is reduced in the presence of the fuel gas to Ni metal. Co/YSZ has also been

utilized. With the movement for lower operating temperatures and thereby thinner electrolytes, most SOFCs are designed to be anode supported. This makes the anode by far the thickest layer in the planar cell in order to provide support for the ceramic electrolyte and cathode. This is illustrated in Figure 2-4.

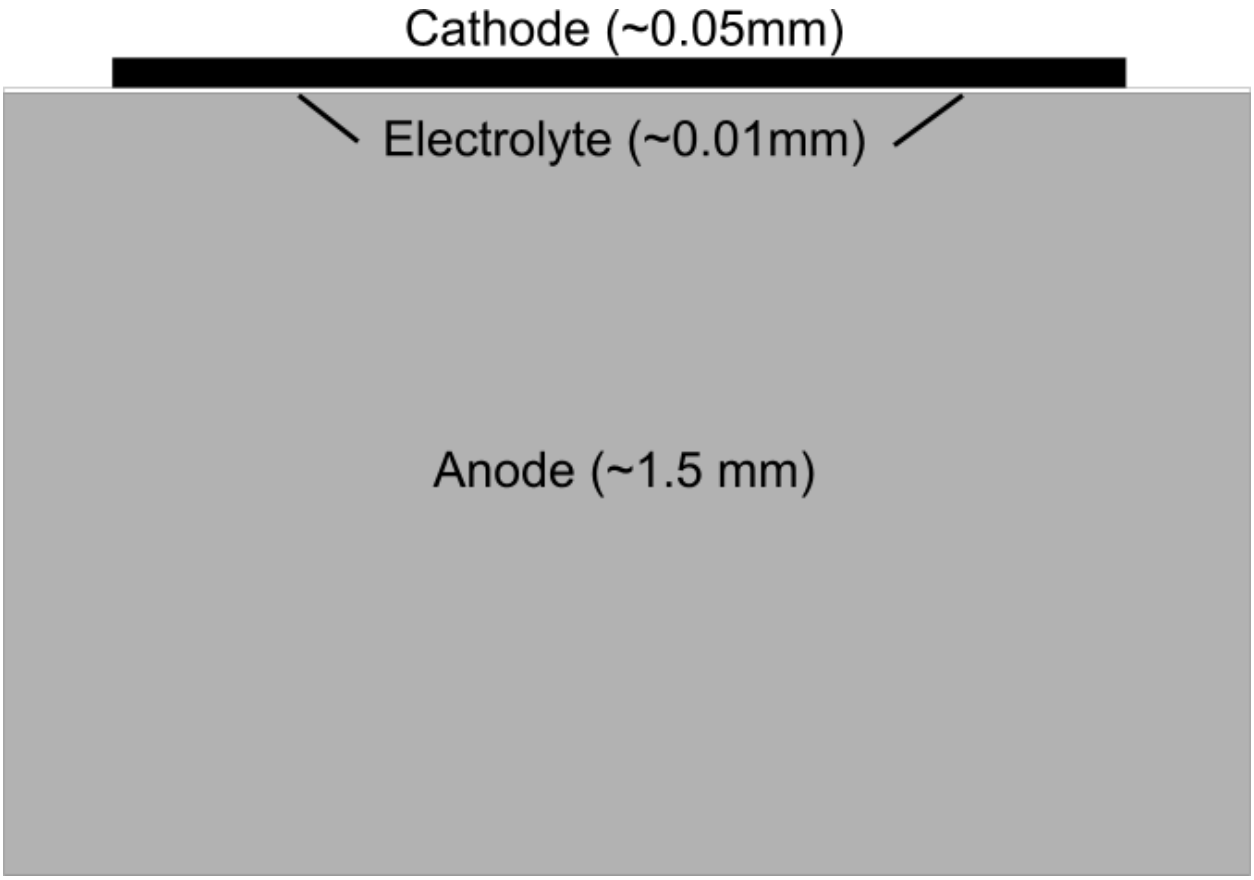

Figure 2-4 Schematic of a planar, anode supported SOFC

2.2.4 Interconnect

The interconnect, as the name implies, connects the anode and cathode sides of the cell together. In the case of the SOFC, the electrons that are freed on the anode side due to the reaction in Equation 2 are transported through the interconnect to the cathode side where they are required for the ionization of the oxygen prior to transport through the electrolyte. The interconnect is also the component which is contacted with other cells to form stacks and to the external leads to conduct the electricity out of the cell. A final purpose of the interconnect is as a bipolar gas separator. This means it is the barrier between the gas environments on the cathode and anode sides when the cells are stacked.

2.2.5 Description of How a Fuel Cell Works

Mentioned above, YSZ is a good ionic conductor, particularlly for oxygen ions. Figure 2-5 shows the mechanisms at work in the cell to exploit this fact. Oxygen present in the oxidant gas on the cathode side penetrates the porous cathode until it reaches the cathode/electrolyte interface. At this point the oxygen reacts with the cathode to form O^{2-} ions according to the cathodic reaction shown in Figure 2-5. Due to the difference in chemical potential and the good ionic conductivity of YSZ, these ions diffuse through the electrolyte. On the anode side, hydrogen, CO, or hydrocarbon (ex. CH_4) fuel gases penetrate the porous anode to the anode/electrolyte interface. The O^{2-} ions arriving from the cathode side react with the fuel gas to form H_2O and/or CO_2 according to the anodic reactions shown in Figure 2-5. These reactions result in two free electrons. A current is created when the electrons are conducted by the interconnect to the cathode side to supply the electrons needed for the ionization of oxygen, thereby completing the cycle.

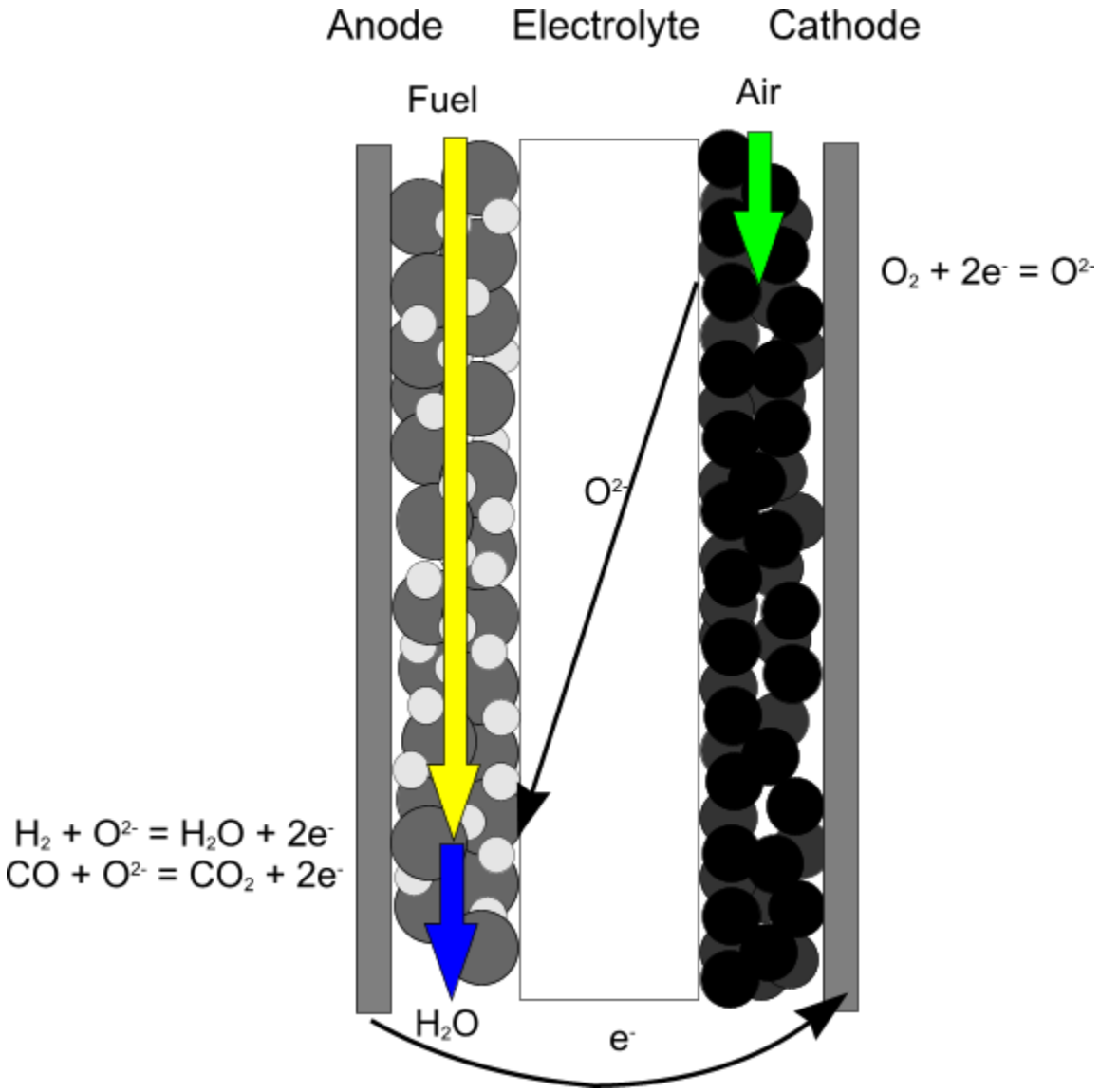

Figure 2-5 Schematic showing the relevant mechanisms at work in a SOFC

2.3 INTERCONNECTS

The basic functions performed by the interconnect in a planar SOFC have been described above. Unfortunately, a unanimous choice for the interconnect material has not been determined. In fact, it has been said that the development of interconnect materials is the number one problem in SOFC research. Below some of the requirements will be discussed with the pros and cons of some types of materials that have come into consideration.

2.3.1 Requirements

There are several vital physical, chemical, and electrical property requirements for an effective interconnect material. Table 2-2 has been constructed from requirements for the optimal interconnect listed in recent reviews by Zhu et al[7] and Yang, et al[8]. It also offers an explanation for the requirement. The final two columns show whether the requirement is met by a typical metal and/or ceramic.

2.3.2 Materials

As illustrated by the last two columns in the table, neither metals nor ceramics adequately fulfill all of these requirements. Ceramic materials are generally thought of as electrically insulating, while metals conduct very well. It is important to note that at the SOFC operating temperatures, most metals will oxidize, forming an insulating layer that will increase the cell resistance. Oxidation resistant alloys are designed to form slowly growing protective oxides of alumina, chromia, or silica by selective oxidation. Chromia is the only of these that is acceptable in terms of electrical conductivity, with a value of approximately 100 Ωcm^2 (compared to 10^8 Ωcm^2 for Al_2O_3). As both metals and ceramics are crystalline solids, they are impermeable to gases. When contacted with other cell components, ceramics are in general very stable. Metals can also

be stable (particularly if they are oxidized), but that is not always the case. Table 2-3 shows the thermal expansion coefficients for several candidate metallic materials. The goal is to be as closely match the expansion coefficient of YSZ for an electrolyte supported cell or the anode material for an anode supported cell. Chromium or high Cr stainless steels are the closest in terms of metals to both types of cells. Ceramic materials are usually rather similar in expansion properties. The final four requirements are dominated by metals. Metals are much more thermally conductive than ceramics, which are usually thought of as thermal insulators. This will help reduce the chance of stress concentrations resulting from temperature gradients that arise due to uneven heating. The mechanical properties of metals are in general much better for durable components than those of brittle ceramics. Because of the good mechanical properties, metals are also easy to fabricate and mass produce. The existing technology and infrastructure for stainless steel make it particularly attractive. For the most part, metals are also inexpensive when compared to ceramics. As an example, ferritic stainless steels are typically in the area of \$5/kg, whereas, $LaCrO_3$, the interconnect material in a tubular cell is in the range of \$25-\$35/kg[9]. Once again, the mass production of stainless steel makes it very attractive.

Table 2-2 Requirements for SOFC interconnect materials

Requirement	Purpose	Metals	Ceramics
Low electrical resistivity	Maximizes cell efficiency	*	
Impermeability to anode and cathode gases	Bipolar Gas Separator	X	X
Stability in both anode and cathode gases under thermal cycling conditions	Dimensional stability to maintain electrical contacts		X
Chemical compatibility with other cell components	Minimizes contamination to maintain cell efficiency		X
Close match in coefficient of thermal expansion with other components	Maintain contact and reduce breakage of ceramic components		X
Good mechanical properties	Adds ductility to make system more durable	X	
High thermal conductivity	Reduce thermal gradients	X	
Ease of fabrication.	Reduces Manufacturing Cost	X	
Low cost	Increase acceptance as a viable power source	X	

Table 2-3. Coefficient of thermal expansion values for YSZ and selected metallic materials

Material	CTE
YSZ	10-11 x $10^{-6}/^{o}C$
Cr-Based	11-12 x $10^{-6}/^{o}C$
400 series stainless steel alloys (Fe-Cr)	12-13 x $10^{-6}/^{o}C$
X10 Cr alloys (Fe-Cr-1Al)	13-14 x $10^{-6}/^{o}C$
Ni Based alloys (Ni>60%)	13-16 x $10^{-6}/^{o}C$
Ni Based alloys (Ni<60%)	16-19 x $10^{-6}/^{o}C$
Other Stainless Steel alloys (Fe-Cr-5Al)	15-18 x $10^{-6}/^{o}C$

2.4 FERRITIC STAINLESS STEELS

Stainless steels, the high Cr ferritic varieties in particular, are candidate materials that fit several of the requirements previously discussed. These alloys easily fulfill those requirements above that were advantages of metals. Add to that the fact they are chromia forming alloys, which makes them acceptably conductive, and that the thermal expansion coefficient is also in the desired range. In fact, Figure 2-6 shows the good CTE match in the SOFC temperatures range between a typical anode supported SOFC and a Fe – 18Cr – 1.5Al alloy. All of this makes ferritic stainless steels extremely attractive for SOFC applications.

Ferritic stainless steels can be thought of as essentially Fe – Cr alloys. The Fe – Cr phase diagram is shown in Figure 2-7. From the diagram, it is seen that these alloys will be mostly, if not totally, α – Fe with Cr substitutions on Fe sites. This gives the material the bcc structure. Some stainless steel grades, such as T304 (typically Fe-18Cr-8Ni) do contain alloying elements such as nickel that are austenite (fcc phase, γ - Fe) stabilizers. Due to the fact that chromium is a ferrite stabilizer, austenitic alloys that contain similar amounts of chromium as the ferritic alloys, which is required for long term oxidation resistance, must also have increased amounts of austenite stabilizers (at increased price). Austenitic alloys are, therefore, less attractive for this application and will not be explored in this work. The final common phase that can be present is σ – FeCr, which is tetragonal. The ramifications of the σ – phase will be discussed in more detail below. For Fe – Cr alloys to be considered "stainless", it must contain at least 12-14% Cr for aqueous corrosion. Even more Cr is required if the alloy is to be able to selectively oxidize the Cr to form a continuous, protective layer of Cr_2O_3.

At the lowest temperature used in this work (700°C), Cr contents above ~25% will also contain σ phase (see red lines in Figure 2-7). The σ – phase is very brittle, and from the author's personal experience, seen to be very problematic in the steel making process if formed. Hammer[10] and Birch[11] have shown the presence of σ- phase in the higher Cr alloys studied here. In the case of Hammer, there was cracking within the σ- phase region during thermal cycling. The formation of the sigma phase is sluggish even at the elevated temperatures. The presence of steam appeared to increase its formation rate. Birch showed massive amounts of σ – phase formation in SeaCure (Fe – 28%Cr – Mo) in both dry and dual atmospheres (Figure 2-8).

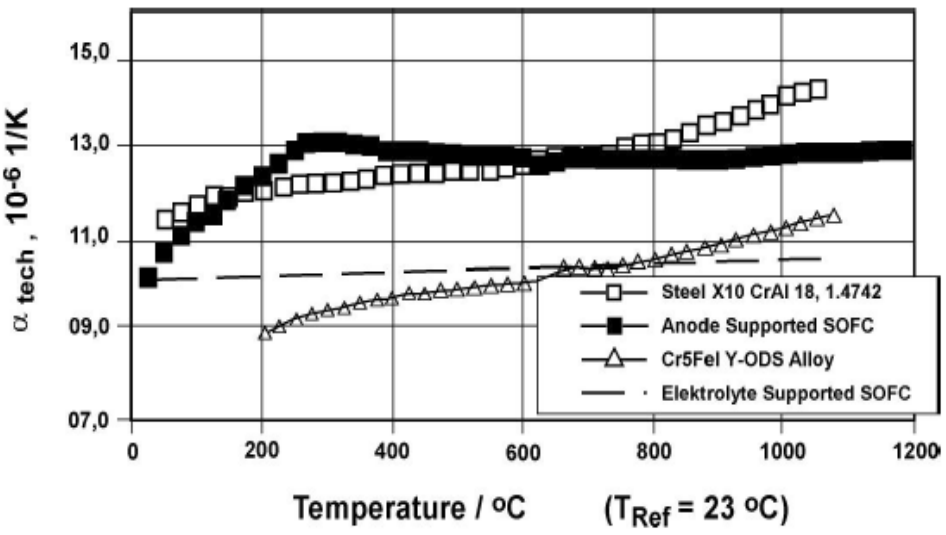

Figure 2-6 Plot of thermal expansion coefficient vs. temperature for selected materials[5]

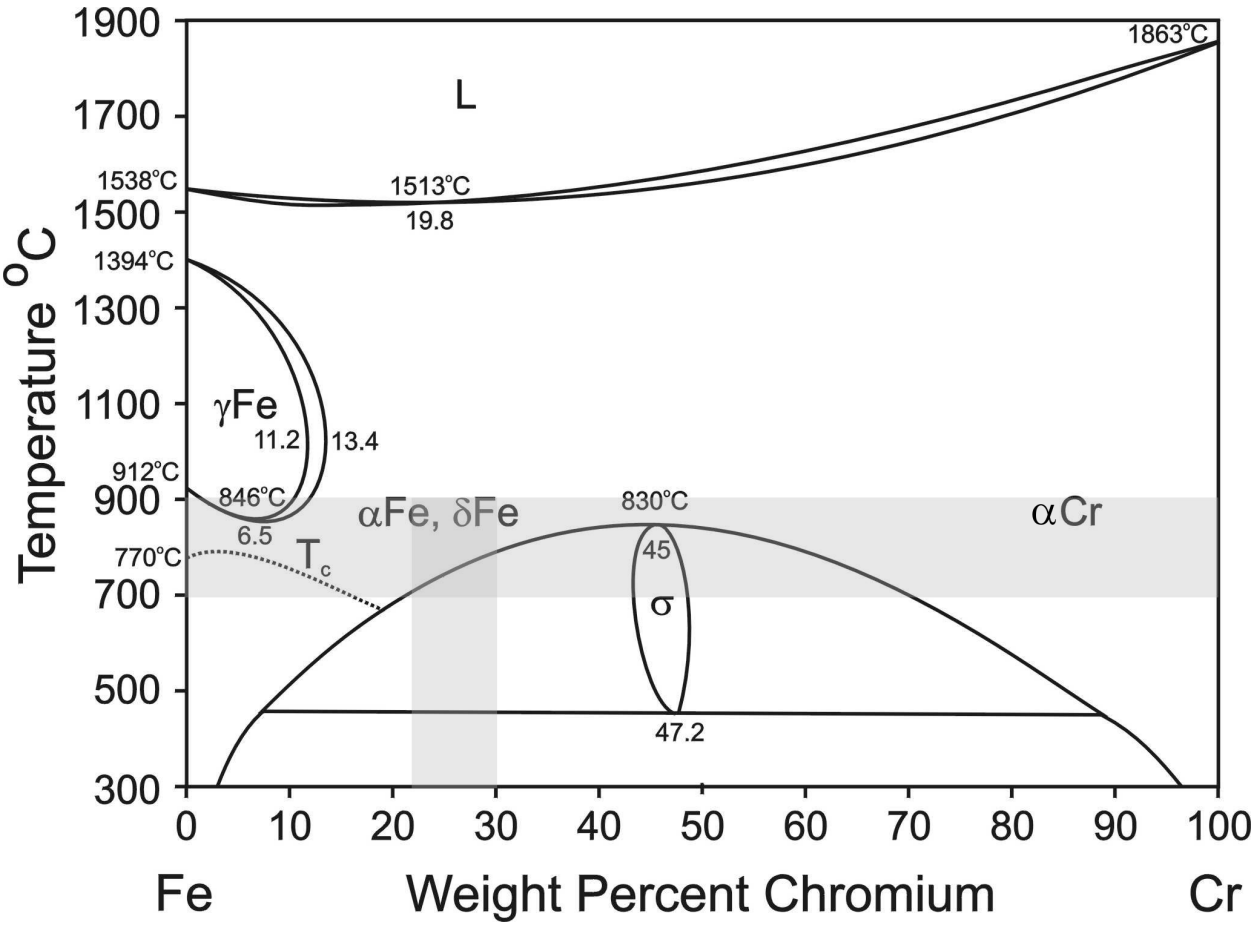

Figure 2-7 Fe – Cr phase diagram

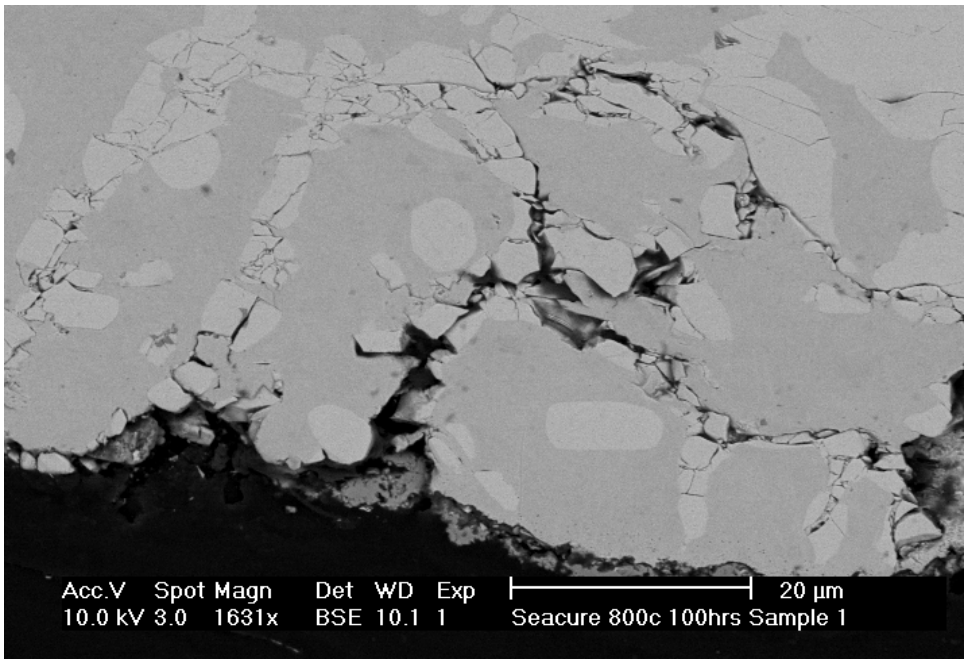

Figure 2-8 Cross-sectional micrograph of Seacure oxidized for 100hrs at 800^{o}C showing large scale formation and cracking of σ phase[11]

2.4.1 Oxidation

One of the biggest downfalls of using a metal as an interconnect is that they do react with oxygen in the environment, forming an oxide, which is more insulating than most metals. Ferritic stainless steels are no different. What makes the material attractive is that it selectively oxidizes the chromium in the alloy to form a slowly growing chromia oxide. The significance of selective oxidation and the conditions that must be met for it to occur will be described below. It is important at this point to quickly review some of the basic thermodynamics and kinetics of the oxidation reaction.

Most people familiar with chemistry or materials science know that oxygen is one of the most reactive elements. Using thermodynamics, it is possible to quantify the stability or strength of a reaction such as the following:

$$xM + \frac{y}{2}O_2(g) = M_xO_y \tag{3}$$

where

$$K = \frac{a_{M_xO_y}}{a_M^x P_{O_2}^{\frac{y}{2}}} = e^{\frac{-\Delta G^o}{RT}} \tag{4}$$

After some rearranging,

$$-\Delta G^o = RT \ln\left(\frac{a_{M_xO_y}}{a_M^x P_{O_2}^{\frac{y}{2}}}\right) \tag{5}$$

where ΔG^o is the standard Gibbs Free Energy change for Eq. 3, where reactants and products are in their standard state, R is the gas constant, T is temperature, a is activity, and P is pressure. The value of ΔG^o is negative for most metals, and the more negative the number, the more reactive with oxygen a given element is. The Ellingham – Richardson diagram (Figure 2-9) plots

ΔG^o vs temperature (assuming unit activity) for several elements and can be used to graphically rank elements. Near the bottom of the diagram are the elements mentioned previously that are typically used for high temperature oxidation, namely Al, Si, and Cr. The more reactive elements form what are considered most stable oxides, meaning the reaction to form the oxide is very highly favored (reaction proceeds strongly in the forward direction) and is more favored than reactions with other elements without large amounts of additional energy. Other elements such as Mg and Ca are not used due to poor oxidation kinetics.

As always, thermodynamics can only give information about what can occur, while kinetics are needed to determine how fast it can occur. Initially, oxidation occurs by a series of reactions involving the adsorbtion and dissociation of the oxygen molecules in the gas leading to the incorporation into the metal lattice. Oxide nuclei then form, when the oxygen concentration is sufficient, and grow laterally. The nuclei can be oxides of any alloying element present on the surface. Eventually, the conglomerate of various oxides becomes continuous and becomes a physical barrier between the metal and the gas[12]. It is important to note that this period of multiple oxides forming is a temporary state, called the transient oxidation stage, and it remains in effect until the most stable oxide is able to form a continuous layer underneath. At this point, the stable oxide cuts off the access to the alloy after which, the transient oxides are no longer able to form, The transient oxides remain on the surface. Until the alloy is depleted of the metal element that is forming the stable oxide, that stable oxide is all that will form.

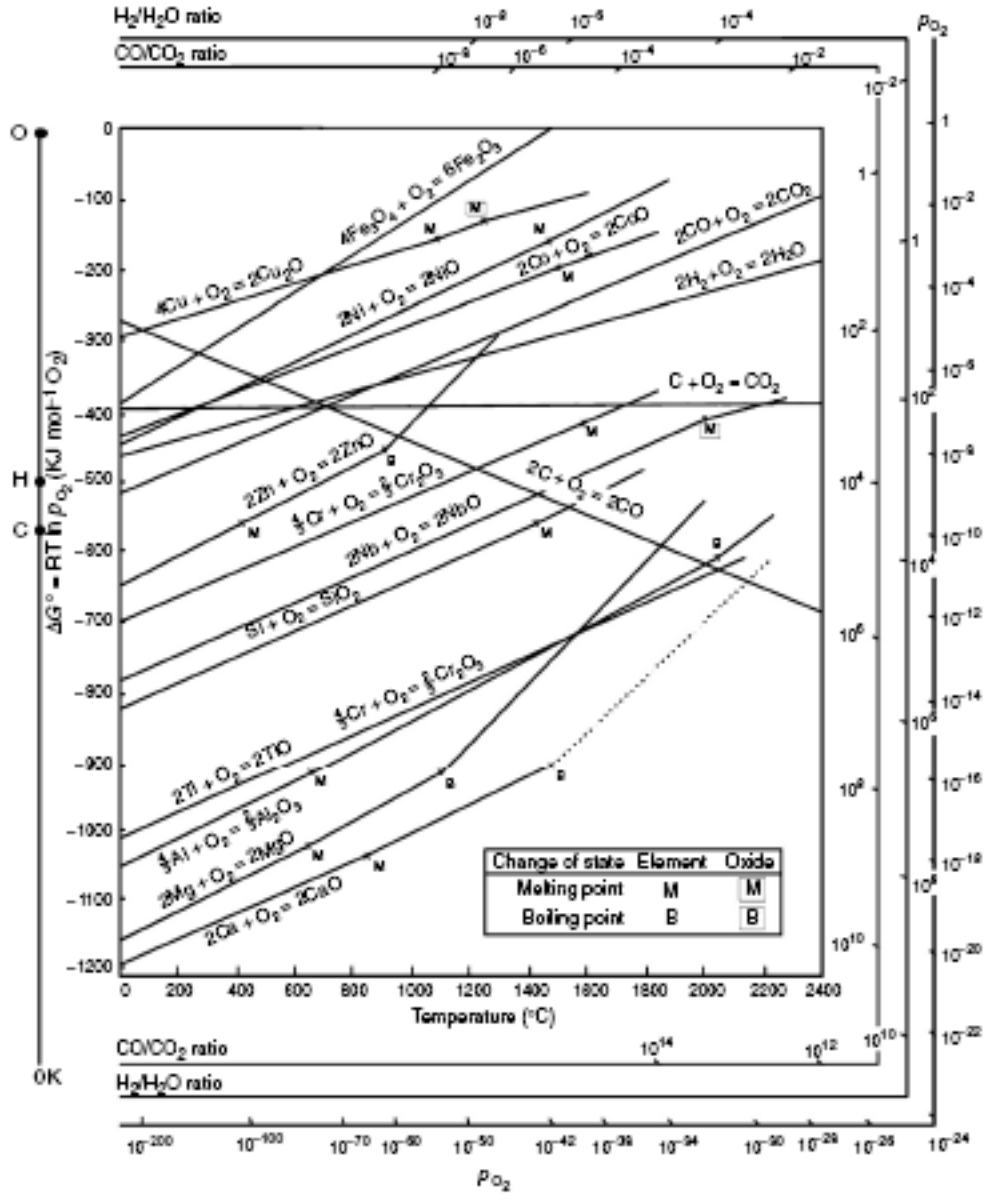

Figure 2-9 Ellingham diagram for common oxides[13].

When a continuous oxide layer is formed, oxidation becomes a solid state diffusion process and is controlled by how fast oxygen can diffuse to the metal/oxide interface or metal can diffuse to the oxide gas interface. This transport of oxygen anions or metal cations (most metal oxides are ionic in nature) is driven by a chemical potential gradient that is created across the scale, as shown in Figure 2-10. The activities and partial pressures at both interfaces are fixed by thermodynamic equilibrium. At the metal/oxide interface, the activity of metal in the oxide is equal to the activity in the alloy and the dissociation pressure of the oxide is equivalent to the oxygen partial pressure, while at the oxide/gas interface, the oxygen pressure in the ambient atmosphere is used to calculate the activity of the metal in the oxide. The cations, anions, and vacancies move according to the diagram in Figure 2-10. Electronic defects must also be considered due to the requirement to maintain electroneutrality and are also included in the diagram.

As the oxide grows, the diffusion distances constantly increase, leading to an ever decreasing growth rate. Wagner[14] discovered that the growth of the oxide could be characterized by a parabolic equation resulting in his model of oxidation:

$$x^2 = 2k_p t \tag{6}$$

where x is the oxide thickness, k_p is the parabolic rate constant, and t is time. As the thickness of the oxide layer is not an easily monitored value, the equation can be expressed in terms of mass change (or oxygen uptake) where the conversion terms are absorbed by a new rate constant, giving:

$$\left(\frac{\Delta m}{A}\right)^2 = k'' t \tag{7}$$

where A is the surface area and is included as a normalization term. All parabolic rate constants reported in this work are values of k" and not k_p, although k" is frequently reported as k_p in the literature. Figure 2-11 is a plot of k" values vs. reciprical temperature for typical oxides used for high temperature oxidation and is used to rank the oxides in terms of rate of growth. Chromia is near the bottom of the diagram indicating slower growth.

When developing high temperature alloys, designers typically utilize a phenomenon called selective oxidation, which occurs when one or more of the alloying elements form more thermodynamically stable oxides than the base metal. As can be seen in Figures 2-10 and 2-11, chromia is much more stable and slower growing than the Fe oxides and therefore will selectively oxidize. It is also important to note the locations of SiO_2 and Al_2O_3, as they are more stable than Cr_2O_3. Due to difficulty in removing these elements by typical processing routes, they are commonly present in stainless steels.

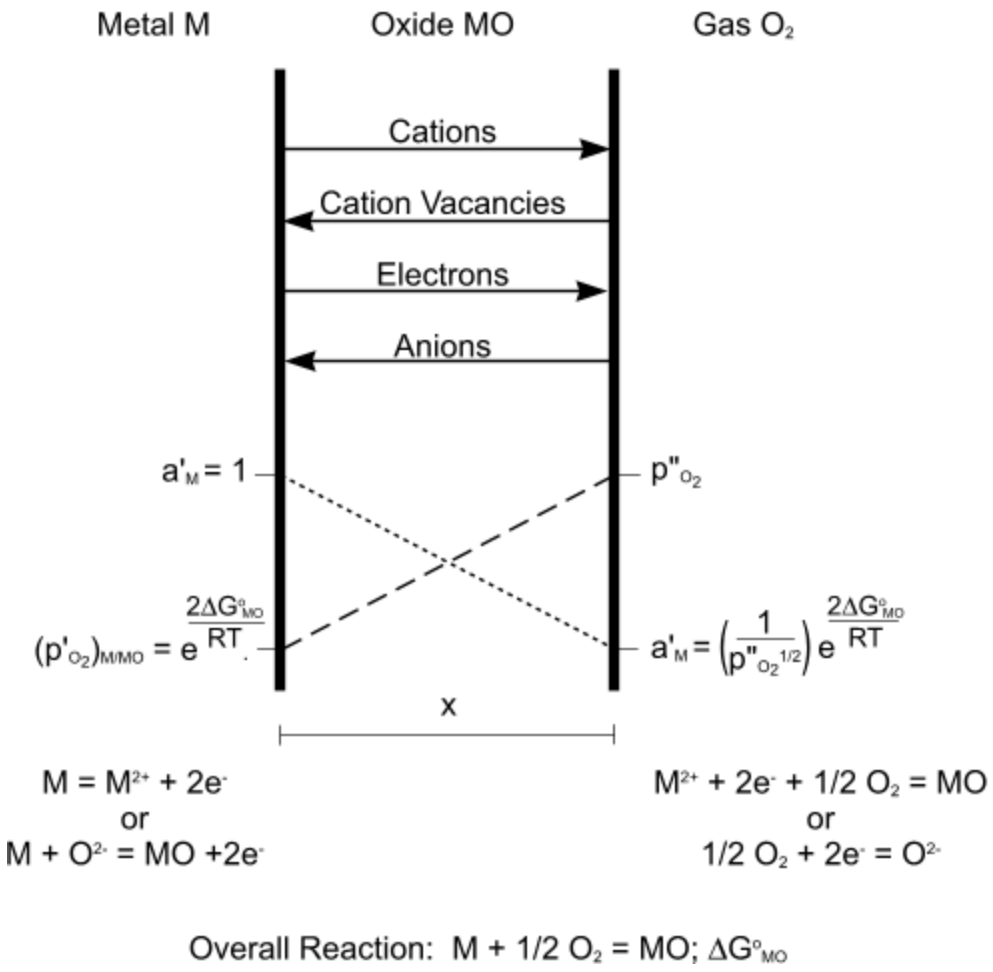

Figure 2-10 Schematic diagram of the mechanism of oxidation[13]

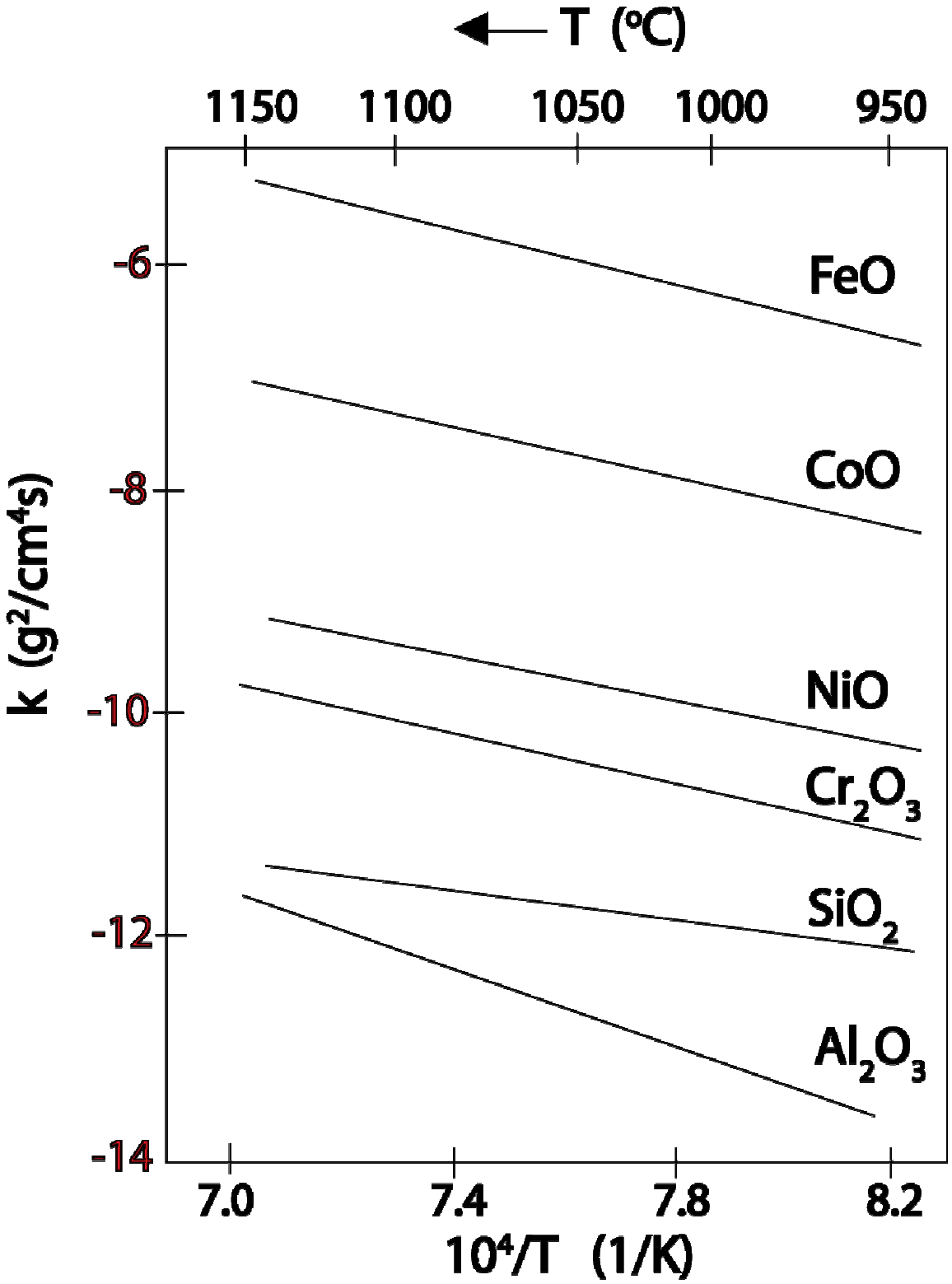

Figure 2-11 Plot of parabolic rate constant k" vs. 1/T for various oxides[13]

The presence of a less noble alloying element does not guarantee that a continuous protective layer will form. If the concentration of the minor element is too low, that element will form islands of oxide in the alloy. This is called internal oxidation. The following equation is used to determine the amount of the minor alloying element that is needed to form an external oxide in an A-B system:

$$N_B^o > \left[N_O^s \left(\frac{\pi g}{2\nu} \right) \left(\frac{D_O V_m}{D_B V_{ox}} \right) \right]^{\frac{1}{2}} \tag{8}$$

where N_B^o is the initial, bulk concentration of B, N_O^s is the surface concentration of oxygen, D_O and D_B are diffusivities of O and B, V_m and V_{ox} are the molar volumes of the bulk and oxide, g is the the critical volume fraction (g = f(V_{ox} / V_m) required for lateral growth of the oxide, and ν is the stoichiometric amount of oxygen in the chemical formula of the oxide.

A second condition for protection of the alloy by selective oxidation is the ability to maintain the oxide scale. The formation of the oxide scale causes depletion of B in the alloy near the metal/oxide interface. For the scale to be maintained, there must first be enough B in the bulk to continue forming the oxide and the B must be able to diffuse readily from the bulk alloy to the interface. The following equation estimates the amount of B needed to maintain the scale:

$$N_B = \left(\frac{V}{Z_B M_O} \right) \left(\frac{\pi k_p}{D_B^{alloy}} \right)^{\frac{1}{2}} \tag{9}$$

where N_B is the bulk concentration of B, V is the molar volume of the alloy, Z_B is the valence of B atoms, M_O is the molecular weight of oxygen, k_p is the parabolic rate constant, and D_B^{alloy} is the diffusivity of B in the alloy.

The oxidation product that forms varies, depending on the conditions. If the amount of B is too low to form a continuous oxide (neither condition met), internal oxidation of B will occur, with an outer oxide containing A will form. If there is enough B to form the layer, but not enough to maintain it (first condition met), B will form until the local concentration drops below the critical value. At that point, A will begin to oxidize If there is enough B to satisfy both conditions, only the B oxide will form.

2.4.1.1 Defect Chemistry and Electrical Properties of Oxides : It is rare to find a perfect crystal of any material. There is always an equilibrium concentration of defects. These defects can cause several effects in the materials, but only two are of major interest with this work. First, is that the defects can be in the form of point defects, most frequently as vacant lattice sites. Since diffusion usually occurs by a vacancy mechanism, the concentration of vacancies is related to the growth rate of the oxide. Larger numbers of vacancies lead to faster growth rates. The second effect is a secondary effect related to the defects themselves and the individual system being observed. For a point defect to form, then mass, lattice sites, charge, etc. must but be conserved. The reaction of the system to vacancies, interstitials, and impurities can result in compensation by ionic (vacancies and interstitials) or electronic (electrons and electron holes) means. Obviously, the addition of electronic compensation will alter the electrical properties of the material, as the conductivity is a function of the mobility of electrons and holes and the concentration of each defect.

The following is a simplistic view of what occurs in pure metals to give them their excellent electrical properties[15]. The electrical behavior of a material is related to the arrangement of the electrons in the atoms that make up the material. When two metal atoms are brought together, the outer most orbitals interact. The Pauli exclusion principle does not allow

these orbitals to have the same energy and, therefore, they split into higher and lower energies, with the electrons filling in the lower energy states first. As more atoms are added, the number of energy levels must increase to compensate, eventually leading to a continuum of states as the higher, unfilled energy levels begin to overlap the occupied energy levels. Therefore, the arrangement of electrons in a metal are such that there is a continuum of states that allow the electrons to easily move to higher states as a response to an applied field. The promotion to a higher state allows the electrons to participate in conduction.

Semiconducting pure elements like Si show a hybridization of an occupied and a higher energy empty state to an intermediate energy level that leaves a small gap in the continuum that requires some additional energy for an electron to bridge for conduction to occur. In this case, the lower energy level is called the valence band, the higher energy level is the conduction band, and the space between is the band gap. When the temperature is increased, some electrons are able to jump the gap to the conduction band. The number of negative charges is designated n. A positive charge, called an electron hole, is left in the valence band (the number of which is designated p). The number of electrons and holes is equal. The following equation describes the reaction:

$$null = e' + h^{\bullet} \tag{10}$$

where null is the perfect crystal, e represents electrons and h the holes. Treating this as a chemical reaction allows various thermodynamic values to be calculated.

In a compound such as an oxide, the two elements can be thought of as being similar to the energy states of a metal. The difference is that an element such as oxygen has a much higher electron affinity (one of a few correlations between some property of the element and location of its energy states) will have all its energy states at a level much lower than an element that has a

low electron affinity, such as chromium. Upon allowing to equilibrate, the electrons from the higher energy chromium states will drop to fill the oxygen states, creating a gap similar to that seen for Si. The band gaps for chromium oxide and titanium oxide are in the vicinity of 3eV and semiconducting, while something like aluminum oxide is ~8eV and insulating.

In a stoichiometric oxide, two types of defect structures can occur. These are Schottky defects and Frenkel defects. Schottky defects are those in which a metal vacancy is compensated by an oxygen vacancy according to the following equation:

$$null = V_O^{\bullet\bullet} + V_M'' \tag{11}$$

with equilibrium given by

$$K_S = [V_O^{\bullet\bullet}][V_M''] \tag{12}$$

When Schottky defects are the dominant defect in a stoichiometric oxide, the concentration of defects is independent of oxygen partial pressure. A Frenkel defect occurs when a vacancy is compensated by an interstitial on the same sub lattice. The corresponding equations for the cation lattice are

$$M_M = M_i^{\bullet\bullet} + V_M'' \tag{13}$$

$$K_F = [M_i^{\bullet\bullet}][V_M''] \tag{14}$$

Similar equations can be written for the anion lattice as well. A stoichiometric oxide with Frekel defects dominating will maintain a defect concentration that is independent of oxygen partial pressure.

All of the discussion above depends on the material in question being stoichiometric. This is rarely the case, as there is almost always an equilibrium content of defects in a crystal. For example, Cr_2O_3 is most stable when it is in fact $Cr_{2-x}O_3$ where $x = 9*10^{-5}$ in air at 1100^oC[12].

As conditions, such as the oxygen partial pressure, change, the value of x will change. With that change, the defects that are dominant will change. As a consequence, there will be regions of increased effect of the various vacancies and interstitials, as well as a deviation from the situation where the Equation 10 holds true. The number of electrons and holes are not necessarily equal when the oxide deviates from stoichiometry, meaning it can be a n type (higher in electrons) and/or p type (higher in holes) semiconductor depending on the conditions. To further emphasize the consequences of nonstoichiometry, the diagram in Figure 2-10 also shows that, for Wagner's theory[14] to work properly, there must be electrons or holes present for the ionic transport required for the oxide to grow.

There are several situations which can arise in terms of the defect structure of these stoichiometric oxides. The oxide can be metal deficient or oxygen rich relative to stoichiometry (i.e. $M_{1-x}O$), or the reverse case of MO_{1-y} where the oxide is either metal rich or oxygen deficient. It is important to note that that metal deficient and oxygen rich can be imagined to be the same thing, the reactions that occur are in fact different. The same is true for the opposite case of metal rich and oxygen deficient. The reason for the grouping is that the metal rich/oxygen deficient oxides are n type conductors, while the metal deficient/oxygen rich oxides are p type conductors. For each of these four cases, the defect equilibrium can be determined similar to any chemical reaction. An electroneutrality condition must also be given. Using these two equations, it is possible to determine the dependence of defect concentration on the oxygen partial pressure. There are also instances of the defect interactions that result in the defect in question to be ionized to a different state, which will change the oxygen pressure dependence. Table 2-4 shows the reactions that can occur for the general case of an oxide with the formula MO. In the temperature range of interest, chromia has been shown to be a p type conductor and

to have an oxygen partial pressure dependence on the electrical conductivity of 1/20, which is difficult to explain in terms of the equations similar those in the Table[16]. Impurities and hydrogen in the environment were also shown to have large effects on the properties of Cr_2O_3

Even considering the nonstoichiometry of the oxide does not completely account for the electrical properties. It is very rare to not have some form of impurities present in a material that will have a doping effect, thereby altering properties. Materials that have altered properties due to doping are called extrinsic semiconductors. There are two types of doping, namely, acceptor doping and donor doping.

Acceptor doping infers that the dopant element has a lower valence state than the host cation. From this, only certain defect reactions can typically occur and are listed below for incorporation into a chromia scale:

$$2MO \overset{(Cr_2O_3)}{=} 2M'_{Cr} + 2O_O + V_O^{\cdot\cdot} \tag{15}$$

$$Cr_{Cr}^{x} + 3MO \overset{(Cr_2O_3)}{=} 3M'_{Cr} + Cr_i^{\cdot\cdot\cdot} + 3O_O \tag{16}$$

$$2MO + \frac{1}{2}O_2 \overset{(Cr_2O_3)}{=} 2M'_{Cr} + 3O_O + 2h^{\cdot} \tag{17}$$

Holt and Kofstad[17] have done work on Mg doping of Cr_2O_3 and have shown that the oxide is a p type conductor at all oxygen pressures. In near atmospheric conditions, the conductivity of the oxide shows little dependence on oxygen pressures, but gains a dependence of about ¼ in low oxygen pressures. This is shown in Figure 2-12. Similar results would be expected from doping with Mn, which, despite having a large number of allowable states, is most stable in the +2 state. Mn doping comes into play with respect to this work, as it is known to be present in the oxide grown on Crofer 22APU.

Donor doping occurs, as the name implies, when the dopant has a higher valence state than he host cation. Once again, only certain reactions are feasible with donor doping, with compensation by cation vacancies, anion interstitials, and/or electrons. These are listed below for the case of MO_2 in a Cr_2O_3 scale.

$$3MO_2 \overset{(2Cr_2O_3)}{=} 3M_{Cr}^{\bullet} + 6O_O + V_{Cr}^{3'} \tag{18}$$

$$2MO_2 \overset{(Cr_2O_3)}{=} 2M_{Cr}^{\bullet} + 3O_O + O_I^{''} \tag{19}$$

$$2MO_2 \overset{(Cr_2O_3)}{=} 2M_{Cr}^{\bullet} + 3O_O + \frac{1}{2}O_2 + 2e' \tag{20}$$

These equations describe what can occur in the case of doping the chromia with TiO_2. Holt and Kofstad[18] have also worked with Ti doping of Cr_2O_3. They state that the defects of importance are cation vacancies and electrons, resulting in oxygen partial pressure dependencies of conductivity of 3/8 and -1/8 respectively in low oxygen conditions. This makes the oxide an n type conductor in these conditions. At near atmospheric conditions, cation vacancies are independent of p_{O2} and electrons show a -1/4 dependency. If it is assumed that the intrinsic relation n=p holds, then it is shown that the hole concentration shows a ¼ dependency. The oxide is a p type conductor in these conditions. The electrical conductivity will therefore decrease with increasing oxygen pressure to a minimum and then begin to increase again as the oxide switches from n type to p type behavior. This is shown in Figure 2-12.

Table 2-4 General defect equations and dependencies on the electrical conductivities for various situations

Case	Oxide	Ionization	Reaction	Equilibrium Eqn.	Electroneutrality Eqn	P_{O2} dependence
Nonmetal Deficient	$M_{1+\delta}O$	Double	$O_O = V_O^{**} + 2e' + \frac{1}{2}O_2(g)$	$K = [V_O^{**}] n^2 p_{O_2}^{\frac{1}{2}}$	$2[V_O^{**}] = n$	$-\frac{1}{6}$
		Single	$O_O = V_O^{*} + e' + \frac{1}{2}O_2(g)$	$K = [V_O^{*}] n\, p_{O_2}^{\frac{1}{2}}$	$[V_O^{*}] = n$	$-\frac{1}{4}$
		Neutral	$K = [V_O] p_{O_2}^{\frac{1}{2}}$	$K = [V_O] p_{O_2}^{\frac{1}{2}}$	X	independent
Metal Excess	$MO_{1+\delta}$	Double	$MO = M_i^{**} + 2e' + \frac{1}{2}O_2(g)$	$K = [M_i^{**}] n^2 p_{O_2}^{\frac{1}{2}}$	$2[M_i^{**}] = n$	$-\frac{1}{6}$
		Single	$MO = M_i^{*} + e' + \frac{1}{2}O_2(g)$	$K = [M_i^{*}] n\, p_{O_2}^{\frac{1}{2}}$	$[M_i^{*}] = n$	$-\frac{1}{4}$
		Neutral	$MO = M_i + \frac{1}{2}O_2(g)$	$K = [M_i] p_{O_2}^{\frac{1}{2}}$	X	independent
Metal Deficient	$M_{1-\delta}O$	Double	$\frac{1}{2}O_2(g) = O_O + V_M'' + 2h^{*}$	$K = [V_M''] p^2 p_{O_2}^{-\frac{1}{2}}$	$2[V_M''] = p$	$\frac{1}{6}$
		Single	$\frac{1}{2}O_2(g) = O_O + V_M' + h^{*}$	$K = [V_M'] p\, p_{O_2}^{-\frac{1}{2}}$	$[V_M'] = p$	$\frac{1}{4}$
		Neutral	$\frac{1}{2}O_2(g) = O_O + V_M$	$K = [V_M] p_{O_2}^{-\frac{1}{2}}$	X	independent
Nonmetal Excess	$MO_{1+\delta}$	Double	$\frac{1}{2}O_2(g) = O_i'' + 2h^{*}$	$K = [O_i''] p^2 p_{O_2}^{-\frac{1}{2}}$	$2[V_M''] = p$	$\frac{1}{6}$
		Single	$\frac{1}{2}O_2(g) = O_i' + h^{*}$	$K = [O_i'] p\, p_{O_2}^{-\frac{1}{2}}$	$[V_M''] = p$	$\frac{1}{4}$
		Neutral	$\frac{1}{2}O_2(g) = O_i$	$K = [O_i] p_{O_2}^{-\frac{1}{2}}$	X	independent

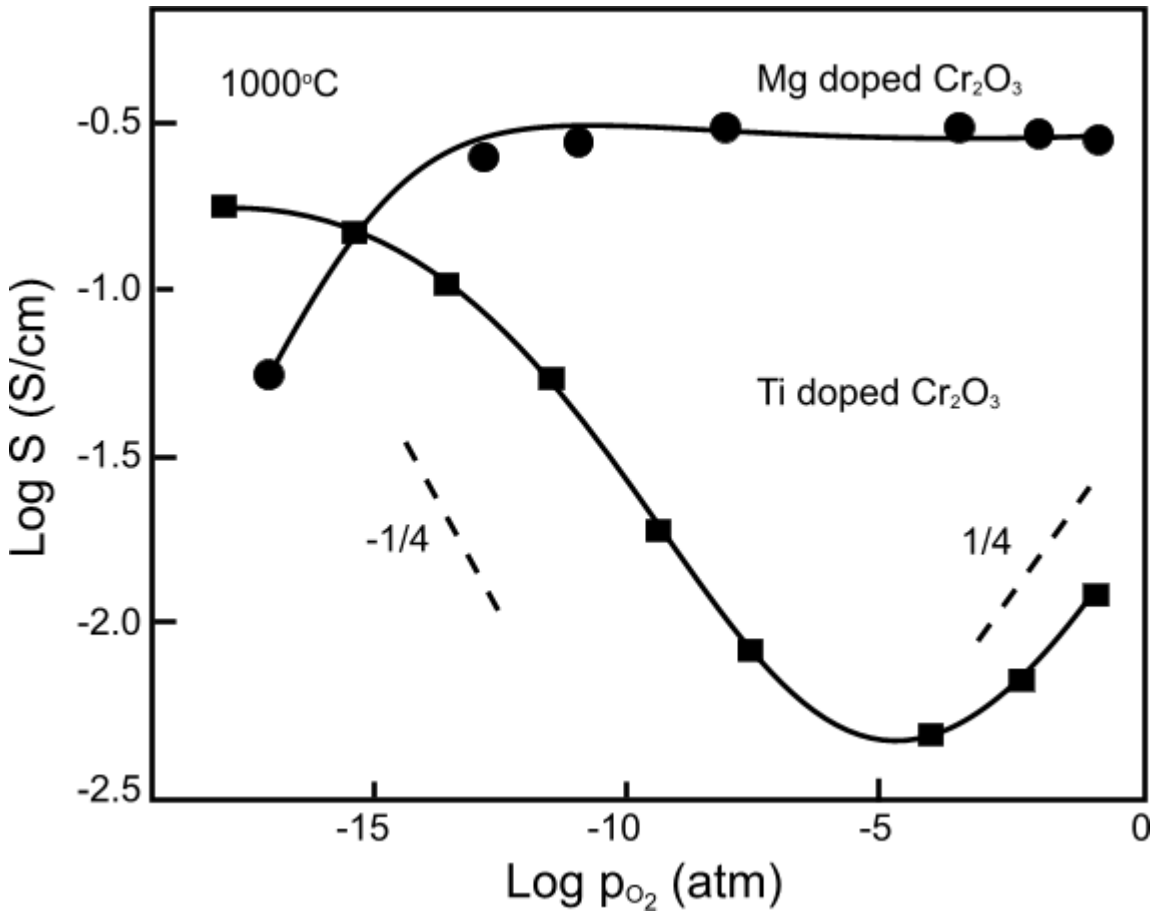

Figure 2-12 Plot of electrical conductivity as a function of p_{O2} for Mg and Ti doped (2 atm%) Cr_2O_3 at 1000°C[18]

2.4.1.2 Chromia Volatility: It has been long known that chromia forms volatile oxide species[19]. Figure 2-13 shows the vapor species diagram for the Cr – O system at ~1000°C. It shows that the partial pressures of both CrO_2 and CrO_3 increase as the oxygen partial pressure increases, with CrO_3 being the most prevalent. The vaporization becomes more dramatic in moist environments (>~0.1% steam), as the hydrated forms of chromia vapor, $CrO_2(OH)_2$ in particular, display an even higher partial pressure[20]. This results in accelerated vaporization rates in wet environments.

Volatilization does have an effect on the oxidation kinetics. The oxide is thinned by the removal of material by vaporization, allowing for rapid diffusive transport through the scale. Tedmon analyzed the effect of volatility on the oxidation kinetics. The thickness of the chromia scale depends on two competing processes, i.e. normal parabolic, diffusive growth and linear thinning by vaporization, yielding the following equation:

$$\frac{dx}{dt} = \frac{k'_d}{x} - k'_s \tag{21}$$

where k'_d is the parabolic rate constant and k'_s is the rate of vaporization. After some mathematical manipulation (rearranging, integration, and evaluating the constant at initial conditions), the equation becomes:

$$t = \frac{k'_d}{k'^2_s}\left[-\frac{k'_s}{k'_d}x - \ln\left(1 - \frac{k'_s}{k'_d}x\right)\right] \tag{22}$$

When the oxide is thin, diffusion is rapid through the scale and the oxide grows faster than it vaporizes. With the thickening of the scale, diffusion slows and, therefore, the growth slows and the vaporization has a larger effect. Eventually the situation is reached where the rates are equal and dx/dt = 0. Substituting this condition into the initial equation yields:

$$x_0 = \frac{k_d'}{k_s'} \tag{23}$$

where x_o is a limiting thickness. If there are no changes in the system, the oxide will remain at this thickness indefinitely.

Chromia vaporization in a SOFC does have some additional consequences. The first one, which may or may not be of vital importance is the thinning of the interconnect by material loss. Depending on the configuration of the cell, this could lead to a loss of electrical contact, and therefore reducing or stopping the cell operation. The second consequence, which is considered more severe, is cathode poisoning. Here, the chromia vapor reacts with the cathode material with detrimental results. The mechanisms of poisoning will be described below in more detail. The process of poisoning appears to occur very rapidly, but does not continue after the intial stages. Due to this, manufacturers are currently designing the cells using a burn in period to poison the cell prior to use, then optimizing the cell from that point.

According to the literature[21,22,23], the way poisoning occurs in a cell is dependent on the cathode material, either LSM or LSCF. In the perfect case, oxygen penetrates the porous cathode material, electrons from the interconnect move through the interior of the cathode, and then the ionization reaction occurs, as shown in Figure 2-14a, at the triple phase boundary (gas/cathode/electrolyte). The reaction can occur away from the electrolyte, but diffusion of the oxygen ion in the cathode can be slow.

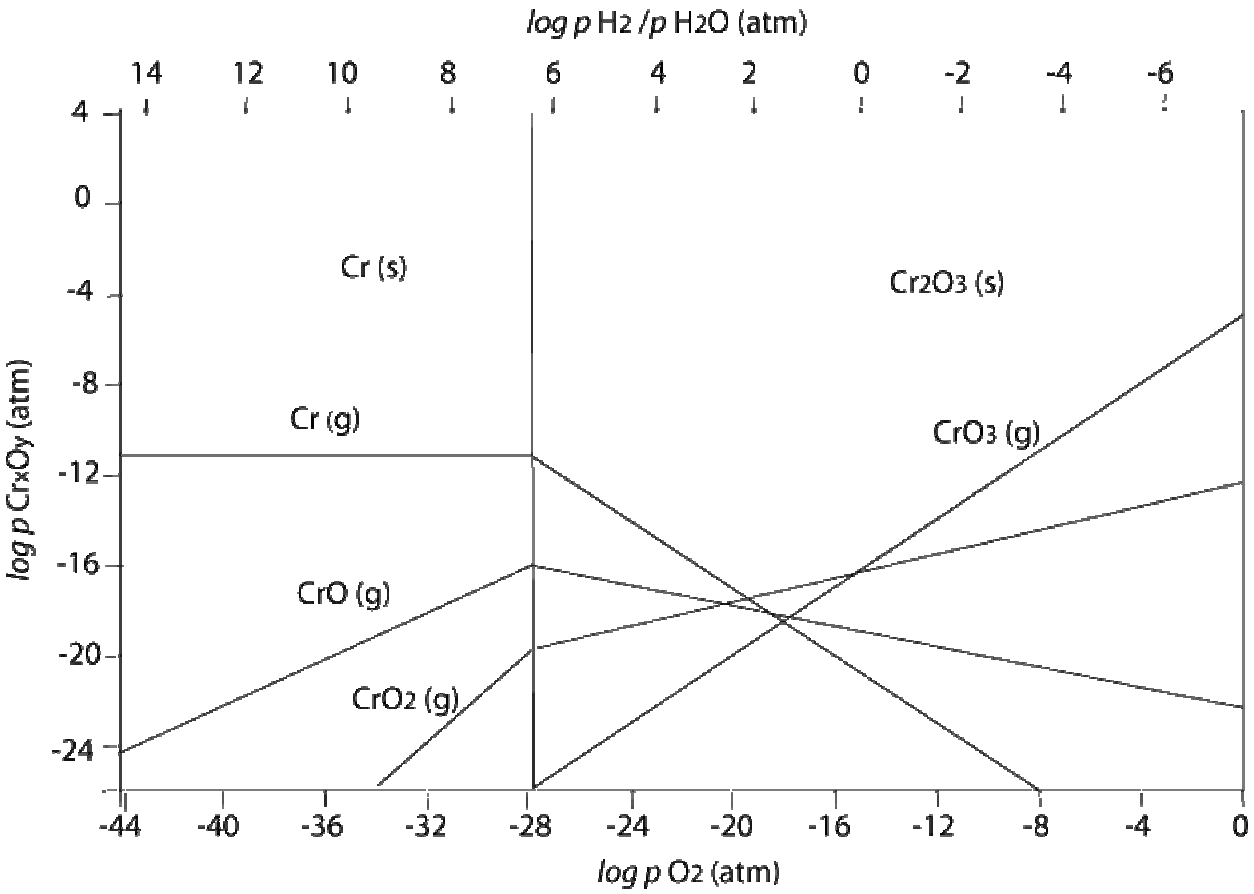

Figure 2-13 Vapor species diagram for the Cr-O system at 1250 K .

When LSM is used as the cathode material and a chromia forming interconnect is also used, the CrO_3 vapor is reduced at the electrochemically active sites according to the simplified reaction:

$$2CrO_3(g)=Cr_2O_3+\frac{3}{2}O_2(g) \tag{24}$$

This reaction deposits solid chromia on the LSM sites that are intended for the oxygen ionization reaction, therefore decreasing the occurrence of oxygen ions. To further aggravate the system, the chromia reacts with the manganese in the cathode to form manganese chromate at the cathode/electrolyte interface. The manganese chromate eventually will form a continuous layer. With this layer in place, all of the oxygen ionization must occur at the cathode/chromate/oxygen boundary, with the chromate and manganese depleted LSM having reduced catalytic properties. The ions that now form must then diffuse through the $MnCr_2O_4$ layer before entering the electrolyte, further slowing the process. This is shown in Figure 2-14b.

The situation is better when LSCF is used as the cathode material. In this case, most of the chromia deposition occurs near the interconnect/cathode interface by the same reaction as above. The chromia can remain as chromia, or it can react with the Sr in the LSCF to form Sr-Cr oxides. The poisoning effect is simply the reduction of sites for the ionization reaction. Because there is less likely to be a continuous blocking layer formed and the poisoning occurs far from the electrolyte, the LSCF is much more tolerant to chromia vapor.

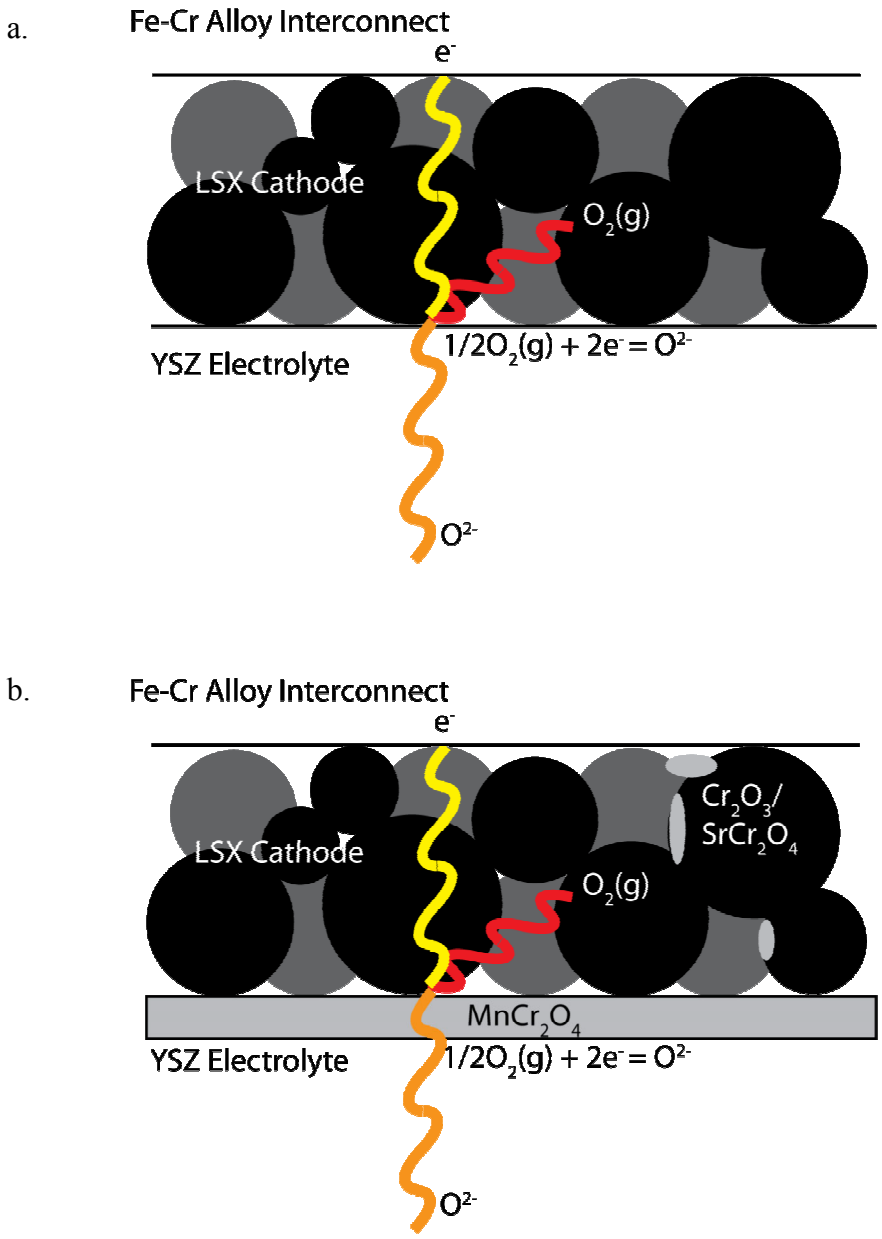

Figure 2-14 Schematic diagram of the ionization reaction on the cathode side (a.) and the change after poisoning has occurred (b.)

2.4.2 Studies of Chromia Forming Alloys in the Literature

The mass production and widespread use of stainless steels have resulted in numerous studies. The results from some of the oxidation studies on ferritic alloys, as well as some other chromia formers, will be discussed below as they relate to the SOFC gas environments. The parabolic growth rate constant, k_p, will be the most frequently reported value as it easily relates to the thickness of the oxide formed. In turn, the oxide thickness can relate to the resistance on the interconnect and the useful lifetime of the material.

2.4.2.1 Cathode Gas: In a SOFC, the cathode is responsible for the formation of the ions that will be transported through the electrolyte, namely O^{2-}. To supply the oxygen required and to keep costs down, air is used. Most of the literature studies discussed in this section were performed in an air environment.

Ni based alloys are very commonly used for high temperature applications. England and Virkar[24] performed isothermal experiments on four such alloys (Inconel 625, Inconel 718, Hastelloy X, and Haynes 230) in air at temperatures between 800^{o}C and 1100^{o}C. As designed, the scales were mostly chromia. The reported rate constants varied between 1 x 10^{-15} and 2.8 x 10^{-14} g^2/cm^4 at 800^{o}C. Hance[25] performed isothermal and cyclic tests on various chromia formers (Inconel 738, Co based X40 and model alloys) in wet and dry air environments at temperatures between 700^{o}C and 1000^{o}C. Cyclic tests on the commercial alloys show good performance at 700^{o}C, in cases better than alumina formers. The degree of attack was increased in moist environments. The situation worsened significantly at 900^{o}C as the alloys rapidly degraded, with the moist environments being more severe. Results on the binary alloy Ni – 30 Cr show that in both environments continuous chromia scales form, but the moist air sample had a thinner oxide scale. This is most likely due to increased vaporization due to formation of

hydrated chromia vapor species. Proof of this is illustrated in the data from tests on Inconel 738, where the alloy behaved similarly in both wet and dry air. This was attributed to the formation of a TiO_2 overlayer that reduced the vaporization rate in both cases. While the Ni and Co based alloys behave well, they are also much more expensive than the ferritic alloys and do not exhibit the good CTE match that is required.

Some literature results from experiments on ferritic stainless steels will now be discussed. Sabioni et al[26] performed TGA tests on T439 (ferritic) and T304 (austenititic) stainless steels in O_2 at 850°C, 900°C, and 950°C for 50 hours. They report the k_p's (in $g^2cm^{-4}s^{-1}$) of $3.2X10^{-13}$ and $1.3x10^{-13}$ for these two alloys, respectively at 850°C to $2.5x10^{-12}$ for the ferritic alloy at 950°C. T304 showed two distinct stages where the k_p was $1.1x10^{-12}$ for about a quarter of the test time then changed to $1.2x10^{-9}$ for the remainder of the test. Brylewski et al[27] performed tests on Fe – 16Cr and reported the k_p (in $g^2cm^{-4}s^{-1}$) to be 8.5×10^{-14}. The oxide was described as fine grained, uniform in thickness, and well adhered to the substrate. Brylewski et al[28] also performed experiments on a Fe – 25 Cr alloy. TGA experiments were done at temperatures ranging from 750°C to 900°C. The resultant k_p values ranged from $1.35x10^{-14}$ at 750°C to $2.17x10^{-12}$ at 900°C, with a value of $4.94x10^{-14}$ for the first 310hr and $8.00x10^{-14}$ up to 480 hrs at 800°C. The scale consisted of a chromia base layer with a thin manganese chromate on top. Huang et al[29] looked at a Fe – 26Cr alloy and its oxidation kinetics at different temperatures. At 800°C they calculate the k_p (in $g^2cm^{-4}s^{-1}$)to be $8.8x10^{-14}$ and at 900°C the value is $9.8x10^{-13}$.

All of the ferritic stainless steel literature discussed thus far has involved isothermal tests in dry air or oxygen. Peraldi and Pint[30] have done cyclic tests on Fe – Cr and Fe – Ni – Cr alloys with varying Cr and Ni contents in wet environments at 650°C and 800°C. While all alloys showed accelerated attack, none of the ferritic alloys (Cr contents 14% - 20%) showed signs of

spallation. All of the ferritic alloys showed accelerated attack at 650°C. At 800°C the low Cr alloys showed accelerated attack, while those above 16% formed a protective Cr_2O_3 oxide scale. Hammer, et al.[10] performed cyclic tests on three ferritic stainless steels (Fe – 26Cr, Crofer 22APU, and AL453) at 700°C and 900°C in dry and wet air. The samples showed positive weight gains in dry air at 700°C and 900°C after 2000 cycles, with larger changes at 900°C. In wet air, Crofer 22APU and AL453 both exhibited positive weight gains at both temperatures. At 700°C, the Fe – 26Cr alloy started losing weight after ~400 cycles and showed negative weight change after 800 cycles. This is mostly due to spallation. At 900°C, the alloy reached a steady state rather quickly, where the oxide is growing at the same rate as it is vaporizing. AL453 was most likely showing similar behavior, but that fact is hidden by the formation of a thick and nearly continuous alumina layer. Crofer also showed some internal oxidation, but also forms a $MnCr_2O_4$ layer that hinders vaporization.

2.4.2.2 Anode Gas: The anode gas or fuel gas can consist of H_2 and/or hydrocarbons as well as reaction products such as H_2O, CO and CO_2. This environment has an extremely low PO_2 . In the following results, all of the exposures were done in H_2 or non C bearing simulated anode gases. The presence of carbon adds additional complications such as sensitization, where Cr carbides form (frequently at grain boundaries) and reduce the amount of Cr available to maintain the oxide scale, and metal dusting, where carbon from a gas with greater than unit carbon activity diffuses into the alloy to form metastable carbides that decompose into small metal and graphite particles[31]. Both of these effects can drastically reduce the performance of the alloy, with metal dusting being particularly severe. No testing was performed in these types of environments and, therefore, will not be discussed further.

The fuel gas is a somewhat specialized environment, and therefore there are fewer studies that are related to this problem. England and Virkar[32] performed tests in H_2 saturated with water at 40^{o}C that compliment the results on commercial Ni based alloys discussed above. They report higher growth rates as well as higher electrical resistance of the scales relative to their results in air. Sabioni et al[26] also performed identical TGA tests described above in an Ar-H_2 environment. The k_p's calculated for T439 varied only slightly from those mentioned above. The results for T304 were similar at 850^{o}C and did not vary much with increased temperature as the pure oxygen results did. T304 performed better than T439 in the low P_{O2} environment. Quadakkers et al[33] performed tests on ferritic alloys in a simulated anode gas at 800^{o}C. The resultant scales were thinner than those formed in air. Brylewski[27] also performed isothermal tests in $94H_2/6H_2O$ and $97H_2/3H_2O$ on Fe – 16Cr. The k_ps reported were $8.8x10^{-14}$ and $7.1x10^{-14}$ respectively. In terms of cyclic testing, Hammer, et al.[10] have performed cyclic tests at 700^{o}C and 900^{o}C in an Ar – 4%H_2 + H_20 environment. After 2000 one hour cycles at 700^{o}C, all of the

alloys (AL453, Crofer22APU, and Fe – 26Cr) had positive weight gains with the higher Cr containing Fe – 26 Cr alloy showing the lowest gains. In all cases, the weight gains were greater than those in air. This is explained as a reduction of the chromia vaporization rate due to the low P_{O2}.

2.4.2.3 Dual Environments: While the studies discussed above are useful, they cannot provide the complete picture of how a metal will behave in the actual SOFC environment. The interconnect is exposed to the same oxygen partial pressure gradient as the electrolyte, and not a simple single environment. Some interesting, and in some cases, disturbing behaviors have been reported. PNNL has performed a series of experiments using dual atmospheres containing air to represent the cathode side and H_2+3%H_2O representing the anode gas. An early test was performed on silver, which was used due to its relative nobility[34]. The sample failed catastrophically, as the hydrogen and oxygen dissolved in the sample and reacted to form H_2O bubbles inside the sample. Low purity Ni and various stainless steels have been subsequently tested and have not demonstrated the same behavior. The stainless steel alloys were reported to demonstrate a dual atmosphere effect[35]. The first effect is an increased chromia growth rate on the cathode side. The second effect is the formation of Fe oxide nodules on top of the chromia on the cathode side. The behavior was seen in the cases of T430 ferritic stainless steel and Crofer 22APU (Fe-22Cr-1Mn) after 300 hours of isothermal exposure as well as after three 100 hour cycles, both exposure types at 800^{o}C. The nodules were not seen on air/air and fuel/fuel samples oxidized at the same time. E – Brite (Fe-26Cr) does not appear to form the nodules after 300 hrs of testing in the same manner, leading to the belief that nodule formation is characteristic of marginally good (lower Cr content) chromia forming alloys. Jackson[36] has produced results of the silver experiments in agreement with PNNL as well as the relatively insignificant effect on

the NiO growth rate on Ni in a dual atmosphere seen by Yang. Birch[11] reported similar results for the same Fe based alloys. Both of these later experiments were performed in an air/Ar – 4% H_2 + 0.1atm H_2O dual atmosphere. Kurokowa et al[37] have done dual atmosphere results on T430 (Fe – 16Cr – 0.21Mn) at 800°C and show crystals of Mn and Fe chromates on top of the chromia scale after 24 hrs.

Yang, et al.[35] propose a mechanism for the dual atmosphere effect. Figure 2-15 was drawn to illustrate the steps that occur. First, hydrogen gas is dissolved into the metal via the reaction:

$$H_2(g) = 2H \tag{25}$$

on the anode side. This dissolved hydrogen diffuses through the sample rapidly, while further hydrogen is incorporated into the metal. At the metal/oxide interface on the cathode side, the hydrogen reacts with oxygen and electron holes to form a hydroxyl group according to the reaction:

$$H + O_O^x + h^{\cdot} = (OH)_O \tag{26}$$

For electroneutrality, the following condition must apply:

$$[h^{\cdot}] + [(OH)_O^{\cdot}] = 3[V_M^{''''}] \tag{27}$$

With the increase in the number of metal vacancies at the interface, elements such as Fe and Mn are more easily assimilated into the Cr_2O_3 scale. These elements have higher diffusivities than the self diffusion constant of Cr in the oxide, and therefore can rapidly diffuse to the oxide/gas interface. The result is a local area that consists of mixed oxides (with a Fe_2O_3 outermost layer)

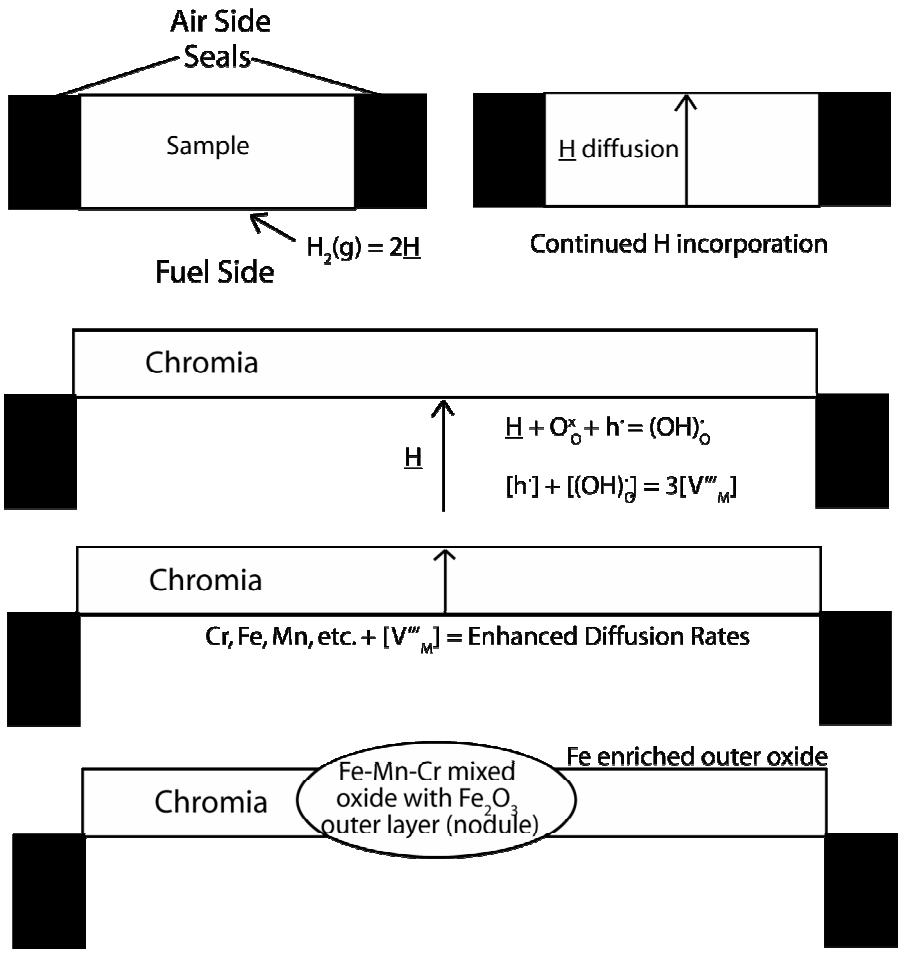

Figure 2.15 Schematic diagram of the dual atmosphere mechanism proposed by Yang, et al.[35]

of increased thickness relative to the bulk of the oxide scale. Although is it not explicitly stated, the local nature of the phenomenon can be attributed to locations were the hydrogen would emerge at the metal/oxide after diffusing on short circuit paths through the metal.

2.4.2.4 Measurements of Electrical Properties: Unfortunately for SOFC applications, the metal/oxide systems that are more conductive (ex. Ni, Co, and Cu) grow too fast at the required temperatures and systems that grow slower than the chromia forming alloys (i.e. alumina and silica formers) are much too insulating. Noble metals do not oxidize, but would add substantial cost to the system. Until a new breakthrough occurs, the SOFC industry must look to chromia forming alloys as interconnect materials, as chromia offers the best compromise between growth rate and electrical properties.

The most common method for evaluating the electrical properties with respect to SOFC applications is to measure the area specific resistance (ASR) of the oxide scale. This is done using a four point probe technique, show schematically in Figure 2-16. The four point probe technique is more commonly used for measuring the resistance of wafers. The contributions to the measurement from system away from the sample are reduced or eliminated by the four probe technique. For the measurement for SOFC applications, there are four probes (as the name implies) or leads. Two are current leads and two are voltage leads and one of each is attached to an electrode on either side of the sample. A current of known value is applied via a current source and the voltage drop across the sample is measured via a voltmeter (Both the current source and voltmeter can be found in some multimeters). Then using Ohm's law:

$$V = I\,R \tag{28}$$

the resistance of the total oxide thickness can be calculated. Finally, multiplying the resistance and the electrode area (similar to a normalization factor for different electrode sizes) will give the ASR value i.e.,

$$RA = ASR \tag{29}$$

Furthermore, due to the fact that

$$ASR = \rho x = \frac{x}{\sigma} \tag{30}$$

the ASR value can also be related to the oxide thickness (and therefore the parabolic rate constant) by the following equation:

$$ASR = \rho x = \rho \sqrt{2 k_p t} = \frac{\sqrt{2 k_p t}}{\sigma} \tag{31}$$

where x is the total oxide thickness, ρ is the resistivity, k_p is the parabolic rate constant, t is time, and σ is the electrical conductivity. Due to this fact, plotting ASR values measured at different exposure times versus. the square root of time should give a straight line, and allow calculations of k_p and predictions of the ASR at longer times (assuming there is no spallation or change in growth mechanism). A second and probably more popular method for representing the data is to plot the log of ASR measurements for the same thickness of oxide, but at different temperatures versus reciprical temperature. Due to an Arrhenius relationship, this plot is a straight line and the slope is proportional to the apparent activation energy, which involves a number of processes.

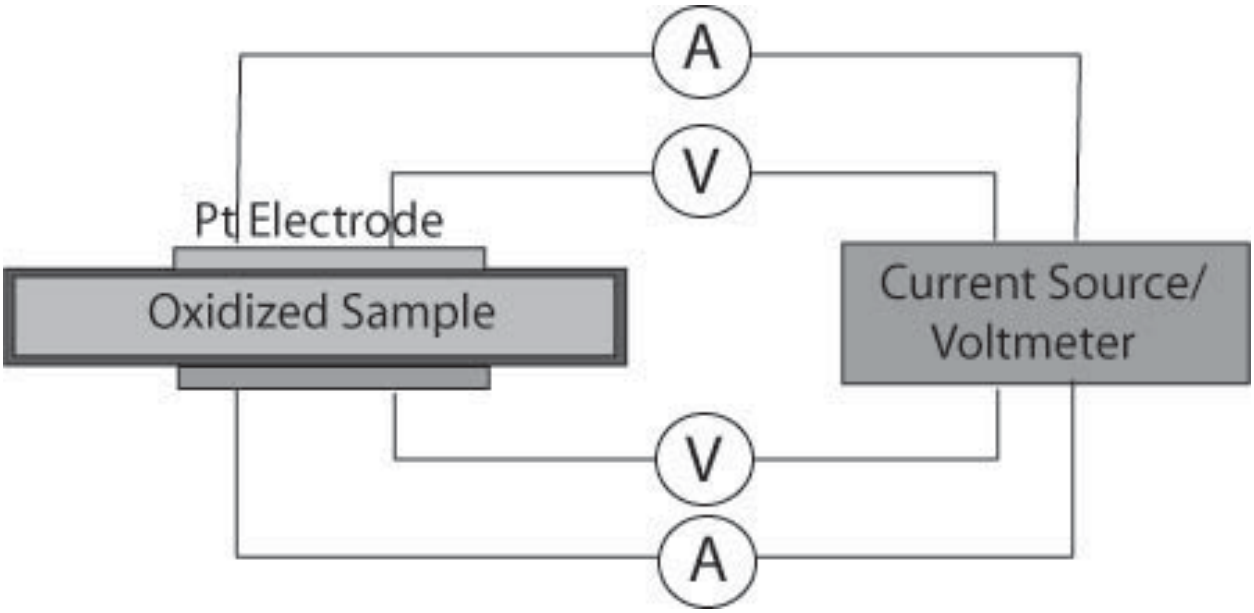

Figure 2.16 Schematic diagram of a four point probe experiment modified for oxidized coupon samples

Despite the difficulty in comparing the ASR values, some results are available in the literature. Huang, et al[29]. oxidized iron based alloys for 24 hours at 900°C, prior to performing the ASR measurement. The setup in this test used Ag electrodes and yielded ASR values on the order of 0.02 Ωcm^2. Some of the reported testing utilized in situ techniques to measure the ASR as the oxide grows. Quadakkers, et al[33]. performed tests of this type on a modified ferritic alloy. After 100 hours the ASR was reported to be 0.01 Ωcm^2. The ASR increased to 0.1Ωcm^2 after 8000 hours. Yang, et al.[38] also performed in situ type tests on Crofer 22APU and E-Brite. In this test, the ASR for both alloys dropped from the initial value to some minimum value before increasing steadily as the oxide grew. For E-Brite, the minimum value reached was about 0.012 Ωcm^2 in about 50 hours. Crofer 22APU dropped more slowly to about 0.0075 Ωcm^2 in 200 hours and also increased much more slowly from that point than E-Brite for the duration of the 500 hour test. Yang also states that the goal value is an ASR of less than 0.05 Ωcm^2 over tens of thousands of hours of operation.

2.4.3 Methods for improvement

The majority of the work discussed above was performed on either commercially available alloys or model alloys. In most cases these alloys are not optimized for use as an interconnect material. There are three areas in which improvements could be realized. One of the most common and detrimental aspects of these alloys is the lack of a check on the aluminum and silicon content. If the concentration of these elements is too high, they can either form internal oxides or in some cases continuous or near continuous layers. The electrical properties of the interconnect will be adversely affected. Hammer[10] has demonstrated improved performance with comparisons of E-Brite vs. similar, yet higher Si content, Fe-26Cr alloy and the second

commercial heat of Crofer (low Al) vs. the first heat. AL453 also shows a very large ASR value due to continuous or nearly continuous alumina layers forming below the chromia. This type of improvement falls to the alloy manufacturers to amend by improving processing. The second area of improvement is to reduce the vaporization rate of the chromia. The final area is to utilize doping to slow the growth rate of the chromia. The latter two will be discussed further below.

2.4.3.1 Thermally Grown Overlayers: As shown in the vapor species diagram in Figure 2-13 above, the partial pressure, and therefore the rate of chromia vaporization increases with increasing oxygen partial pressure. The only way to reduce the vaporization is to change the conditions at the surface of the oxide. One way to do that is to apply a coating. In a simplistic view, the coating would act as a physical barrier between the gas interface and the oxide and thereby reduces the amount of oxygen able to react with the chromia (reduces the chromia growth rate as well). In a more complicated view, the equilibrium reaction at the outer surface of the chromia goes from

$$Cr_2O_3+\frac{3}{2}O_2=2CrO_3 \tag{32}$$

where,

$$K=\frac{P_{CrO_3}^2}{P_{O_2}^{3/2}a_{Cr_2O_3}} \tag{33}$$

to some equation involving a reaction between Cr_2O_3 and the coating material. Due to the fact that the Cr_2O_3 is no longer the outermost layer, its activity is determined by the thermodyanmic equilibrium between the two and is required to be less than unity. The oxygen partial pressure will also be reduced due to the presence of the overlayer. If K is to remain constant, as it must,

then the CrO_3 vapor pressure must be reduced. Figure 2-17 was constructed using thermodynamic data from the vaporization above, giving the following equation:

$$MnCr_2O_4+\frac{3}{2}O_2(g)=MnO+2CrO_3(g) \tag{34}$$

and data on a similar reaction with $LaCrO_3$ from Hilpert[20]. Assuming MnO saturation, the chromia activity is reduced. The effect of this reduction on the CrO_3 partial pressure is shown on the plot in Figure 2-17 for the cases of $LaCrO_3$ and $MnCr_2O_4$ overlayers. $LaCrO_3$ overlayers are applied overlayers and will be discussed in the next section.

A thermally grown oxide overlayer is probably the most economical method for reducing the vaporization rate, as the effect is due to careful alloying. Unfortunately this process and the requirements for overlayer formation to occur are not well understood. For the overlayer to form in a useful amount of time, one or more elements in the alloy must be able to diffuse rapidly through the stable, protective scale. In the case of chromia scales, several elements show faster diffusion in the oxide than Cr itself. Cox, et al.[39] propose that the diffusion rate of various transition metals is related to the crystal field preference energy, which in turn is related to the energy of placing an atom in an interstitial site and the strain energy to move between tetrahedral and octahedral sites. They predict that cation mobility, in order from fastest to slowest, for the transition metals in chromia would be Fe^{3+}, Mn^{2+}, Fe^{2+}, Ti^{3+}, Co^{2+}, V^{3+}, Cu^{2+}, Ni^{2+}, Mn^{3+}, and Cr^{3+}. Given this, it makes sense that elements such as Mn dissolve into the oxide and then diffuse to the oxide/gas interface, where they form their oxides. In the case of MnO, the oxide mixes with the Cr_2O_3 to form a spinel $MnCr_2O_4$. Lobnig, et al.[40] performed experiments where transition metals were deposited on preoxidized surfaces of Fe-25Cr and Fe-25Cr-12Ni. The samples were then annealed at 1173K for 10 minutes to 4 hours. Diffusion profiles were

determined by sputtered neutral mass spectroscopy. From the profiles, Fe, Cr, and Ni were determined to be dominated by lattice diffusion near the outer regions and much slower grain boundary diffusion in the inner regions. Mn on the other hand was shown to have extremely fast lattice diffusion throughout.

Quadakkers et al[33,41] have used this concept to design alloys specifically for SOFC applications. The design philosophy included doping (La) for improving the growth rate and adherence, reducing the Al and Si contents for improved electrical conductivity, and the additions of Ti and Mn to form chromates to reduce the vaporization. The laboratory alloys in this case form the basis for the Thyssen – Krupp commercial alloy known as Crofer 22APU. This alloy has been experimented upon in some of the literature described above.

The most interesting fact of note is that MnO is more stable than chromia, yet it forms its oxide in the higher oxygen partial pressure. It is expected that the Mn would form an oxide beneath the chromia scale where the oxygen partial pressure is still sufficient for the more stable oxide to form. A possible reason for this is that the following reaction:

$$Mn+\frac{1}{2}O_2-MnO \tag{35}$$

where

$$\Delta G^o=-RT\ln\frac{a_{MnO}}{a_{Mn}\,p_{O_2}^{\frac{1}{2}}} \tag{36}$$

is not able to proceed. The oxygen partial pressure will be very low, as it can be estimated by the equilibrium dissociation pressure of the chromia scale. If the activity of Mn is estimated by the mole fraction of Mn, then the Mn activity will be very low and not sufficient for the reaction to occur until more favorable conditions are achieved when Mn enters the chromia scale.

The effectiveness of Ti additions to Inconel 738 from the work of Hance[25] has been discussed above and this work largely deals with characterizing a series of experimental Fe-22Cr-XTi ferritic stainless steels (Table X). The Ti makes its way through the scale and forms an outer layer of TiO_2 in this case, possibly similar to what occurs with Mn. This may be a more effective method for preventing vaporization than a chromium bearing compound, as shown in the superimposed vapor species diagrams Figure 2-18 for chromia and titania. The TiO_2 is much more stable than Cr_2O_3 (as seen by the locations of the vertical lines for each in the diagram) and MnO, and therefore if a dense continuous layer is formed on top of the chromia, the oxygen and CrO_3 partial pressures underneath it will be very low. The possible downside to using TiO_2 is that its greater stability may actually prevent Ti from diffusing through the chromia scale, but rather form internal oxides beneath it. While TiO_2 and other Ti oxides are very good conductors at low oxygen partial pressures and, therefore, not extremely detrimental, tying up all the Ti in internal oxides defeats the purpose of its addition to the alloy. A final concern with the difference in stability is that TiO_2 is a relatively rapidly growing oxide and therefore may form transient oxides until the alloy is depleted of Ti near the surface, chromia then gains continuity, and the TiO_2 oxidizes internally when the concentration is sufficient. In this case, the transient outer oxide will never grow to a continuous layer and will most likely be more detrimental than beneficial.

Further effects of adding Ti to an alloy are changes in the defect chemistry and mechanical properties. Figures 2-19 is a plot of the value of the thermal expansion coefficients versus temperature for the Fe-Cr-Ti alloys used in this work. It is clear that increased levels of Ti increases the CTE. Comparing to the plot in Figure 2-6, these values are in the correct range for use in an anode supported SOFC. Figure 2-20 is a plot of the yield strength (YS), ultimate

tensile strength (UTS), and elongation versus Ti concentration for the same alloys. As is often a problem with adding Al to alloys, Ti increases the YS and UTS, and decreases the elongation, making the alloys hard and brittle. The effect is so strong in the alloy containing four percent Ti that the elongation is practically zero. This may force a compromise in the amount of Ti added to get the vaporization reduction, yet be able to easily machine the alloy to the ribbed structure seen in the diagram in Figure 2-1. The equations for the changes in the defect chemistry have been discussed above, as Ti doping of Cr_2O_3 was purposely mentioned as the example for donor doping. The effects that are observed because of the doping are twofold. First, there will be an increase in the number of chromia vacancies, and that will increase the growth rate of the chromia scale. The second effect is to increase the electrical conductivity of the scale by making it a n type conductor. Once again, a balance will most likely need to be reached between increasing the overall conductivity of the scale while maintaining a reasonable growth rate, as the enhanced conductivity can be overwhelmed by the growth rate and increased thickness also leads to increased stored strain energy, leading to spallation. As this is a newly designed alloy system, some of these issues may not be addressable in this work, but will be left as future work as the system is optimized.

There is some work in the literature related to these alloys. Issartel, et.al.[42] have performed 100 hour TGA experiments in air at 950^{o}C on ferritic alloys with ~16-18 wt% Cr, ~0.5 wt% Mn, and 0-0.44 wt% Ti to determine the effects of Ti on the oxidation. There findings show that the k_p values ($g^2cm^{-4}s^{-1}$) range from 4.61 x 10^{-13} for the Ti free control sample to 3.31 x 10^{-12} for the highest Ti content alloy. The roughly parabolic data shows increasing mass gains with increasing Ti content. They also performed in situ XRD experiments, which show the alloys initially forming Cr_2O_3 and $Mn_{1.5}Cr_{1.5}O_4$, with TiO_2 peaks appearing after a few hours

exposure and increasing with time and Ti content. The highest Ti content alloy behaved slightly differently, in that in addition to the chromia and manganese chromate, Cr_2TiO_5 was observed, which rapidly separates to TiO_2 and Cr_2O_3. Ti was detected near the outer surfaces of the oxide in analysis of cross-sections as well as in unidentified dark areas in the substrate. Sigler[43] experimented on Fe-20Cr with 0.15 and 0.46 Ti added for catalytic converter applications. The alloy with lower Ti was shown to form protrusions on the oxide surface that contained Cr and significant amounts on Mn as well as voids below the oxide. The k_p values were reported to be 7.2×10^{-13} ($g^2cm^{-4}s^{-1}$) at 900°C and 4.2×10^{-14} at 800°C.

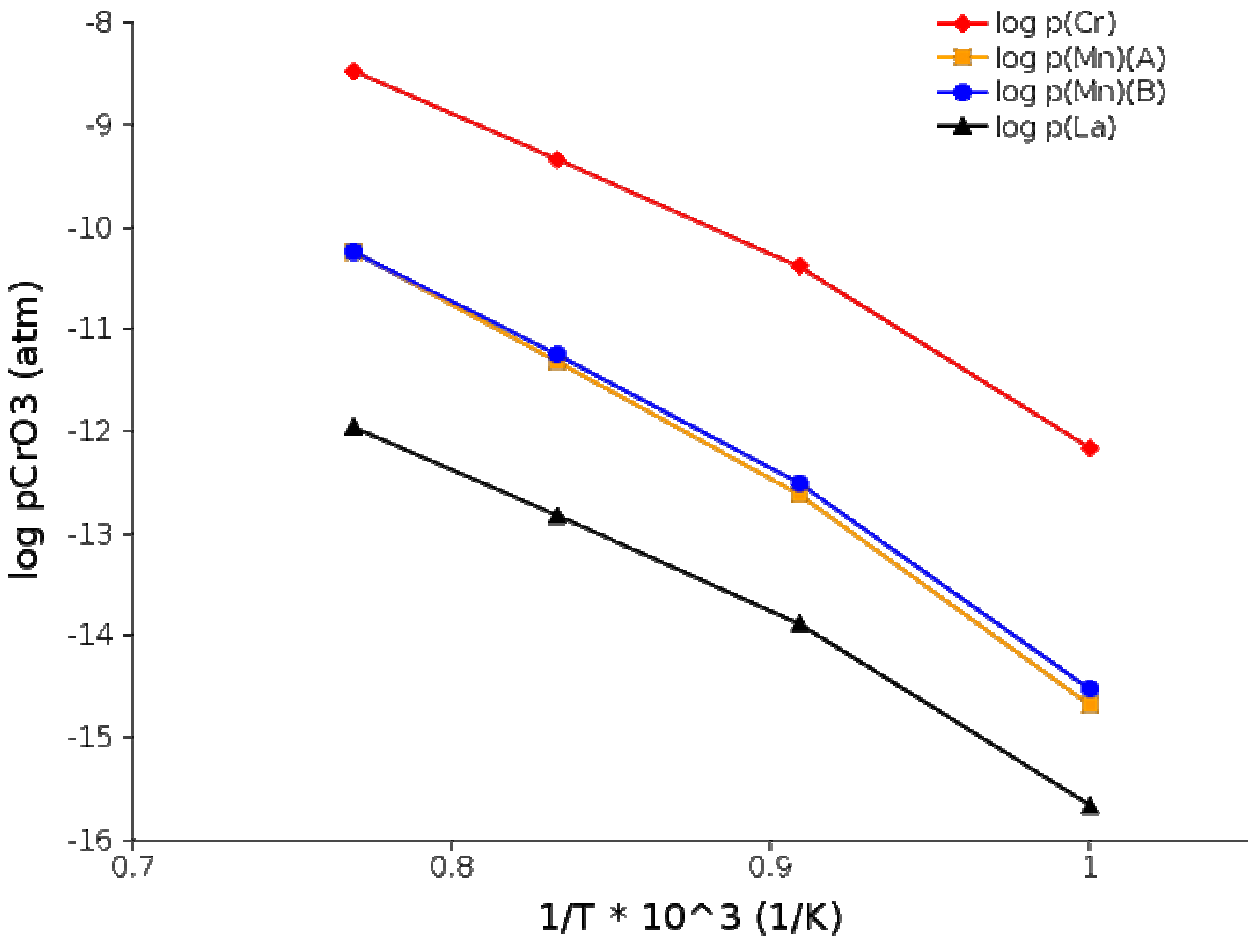

Figure 2-17 Plot of Log(P_{CrO3}) vs 1/T for pure chromia, $MnCr_2O_4$, and $LaCrO_3$

Table 2-5 Composition of the Fe-22Cr-XTi alloys (X=0,1,2,3, or 4)

	Heat Identification Code				
Element	**0**	**1**	**2**	**3**	**4**
Cr	21.8	21.8	22.1	22.2	22.2
Ti	0.004	0.84	1.65	2.72	3.98
Mn	0.033	0.030	0.031	0.024	0.023
C	0.010	0.013	0.010	0.016	0.017
N	0.018	0.018	0.011	0.008	0.008
Ce	0.004	0.027	0.031	0.027	0.027
La	0.001	0.009	0.012	0.012	0.010
Al	0.005	0.005	0.008	0.030	0.049
Si	0.043	0.042	0.036	0.020	0.020

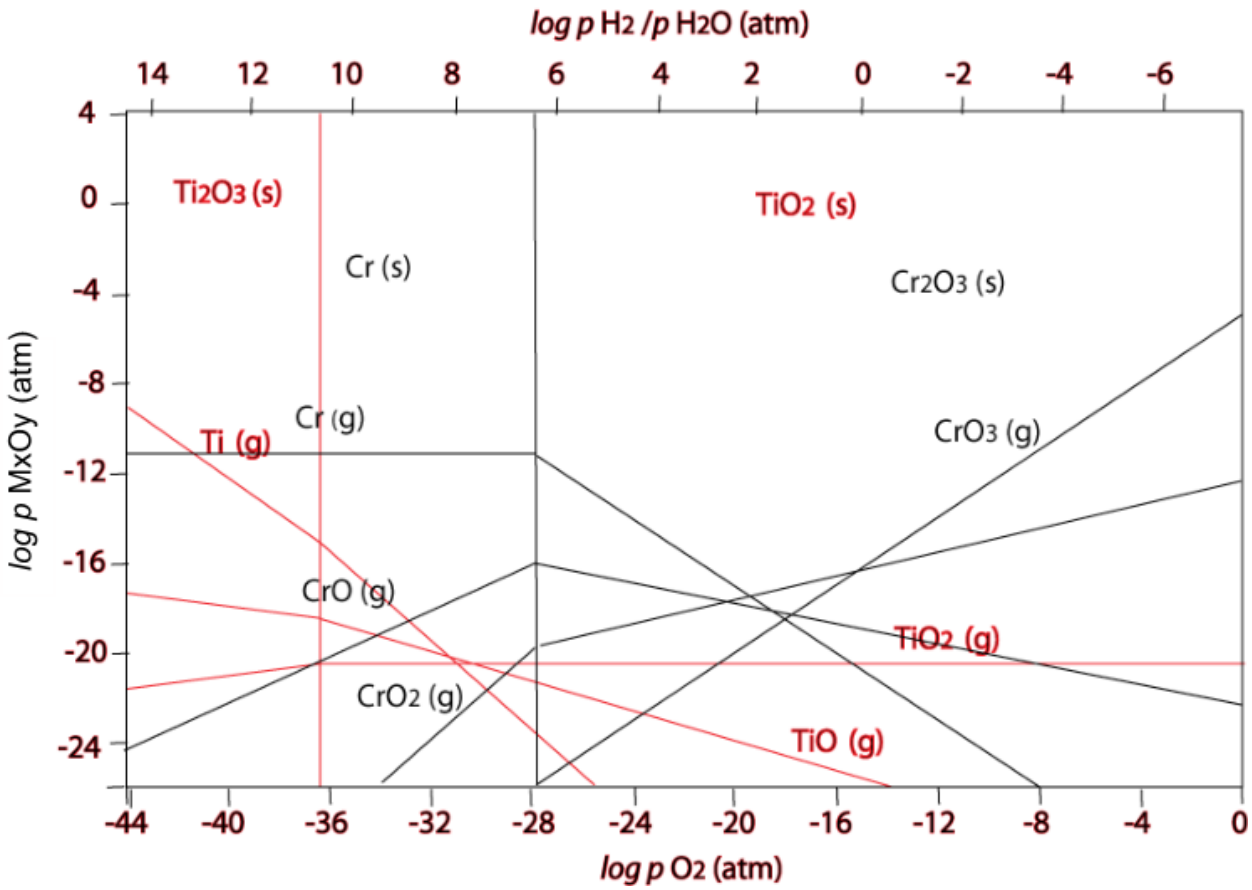

Figure 2-18 Superimposed vapor species diagrams for Cr (black) and Ti (red).

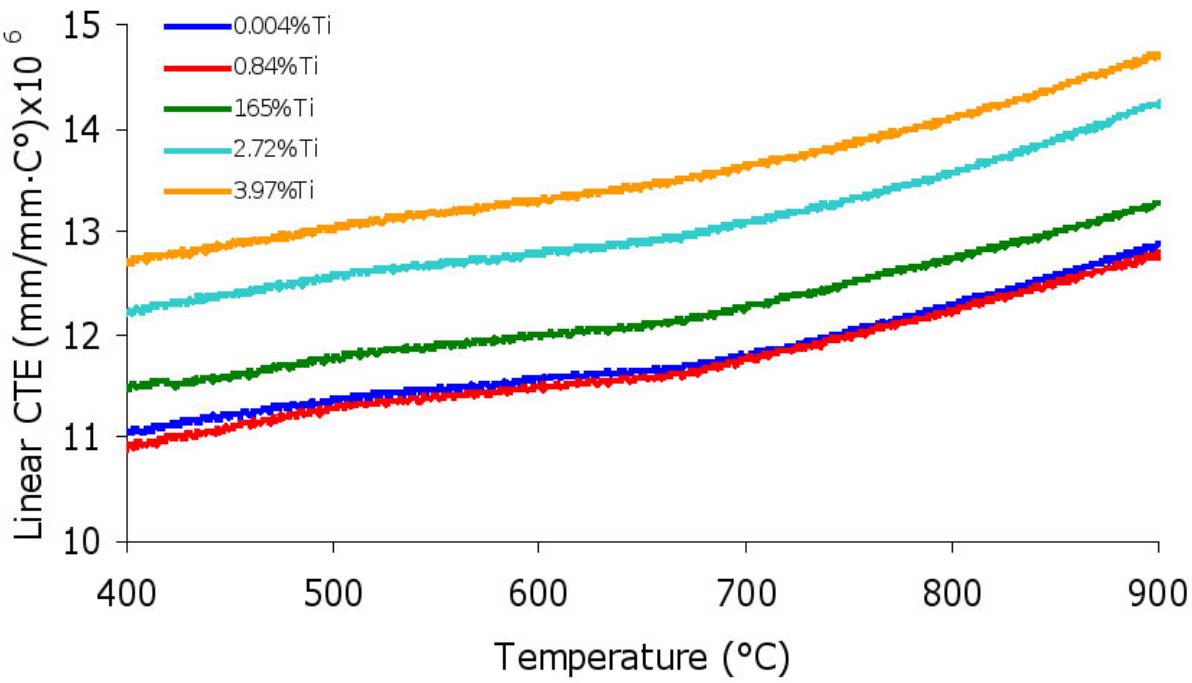

Figure 2-19 Plot of linear coefficient of thermal expansion (CTE) vs temperature for Fe-22Cr-XTi alloys where X = 0-4.(courtesy of J. Rakowski)

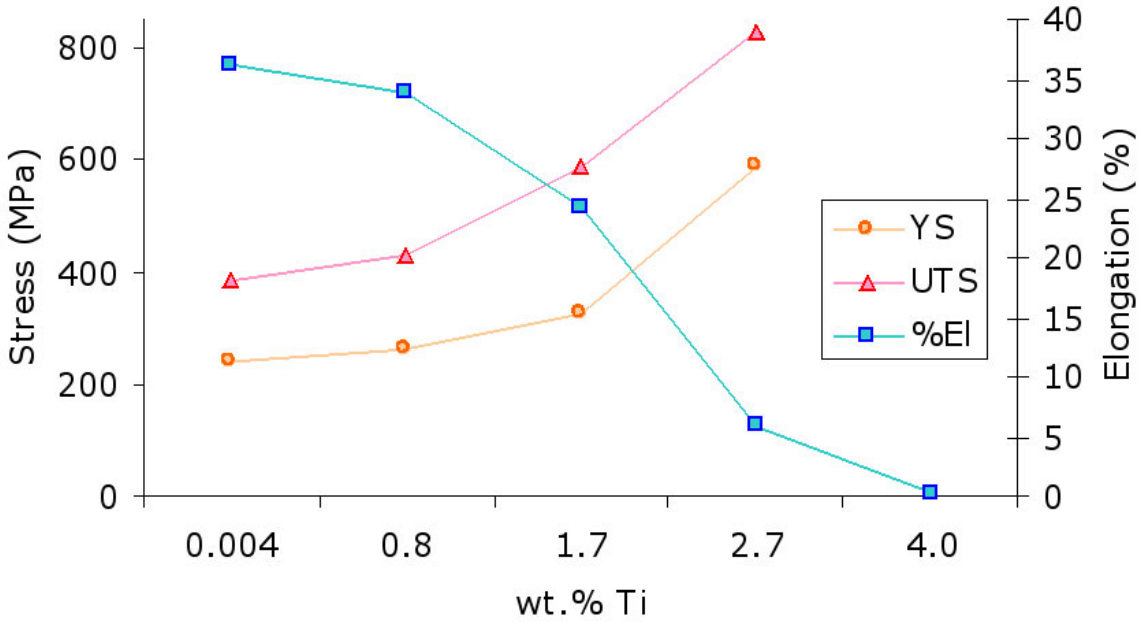

Figure 2-20 Plot showing the change in yield strength, ultimate tensile strength, and elongation with various amounts of Ti additions to Fe-22Cr stainless steel.(courtesy of J. Rakowski)

The higher Ti content alloy showed a ridge structure, where the ridges were nearly 50% Ti and the flat areas between showed Cr, Mn, Fe, and Ti present. The kp values were 1.2×10^{-12} at 900°C and 1.28×10^{-13} ($g^2cm^{-4}s^{-1}$) at 800°C.

2.4.3.2 Coatings: Externally applied coatings are possibly more effective at reducing the chromia activity (ex. compare $MnCr_2O_4$ to $LaCrO_3$ in Figure 2-17), but are much more expensive. There are several types of coatings which can be used to accomplish the goal of reducing the chromia activity, but the coating must also be adherent and electrically conductive. Lanthanum chromite is one of the most common candidate materials. This is the interconnect material of choice for the high temperature tubular cells, so its electrical conductivity properties are well known and Figure 2-17 shows that it does indeed lower the chromia activity. The $LaCrO_3$ is often doped to increase the electrical, sintering, or other properties. Johnson[44] is currently working with undoped and Ca doped $LaCrO_3$. Yang et al[34] have performed work on Sr doped $LaCrO_3$ and $LaFeO_3$. Currently this group is utilizing a manganese cobaltite type coating that has been claimed to perform extremely well[45]. This is of importance because the presence of the coating is not a guarantee against chromia vaporization if the coating itself contains Cr. On the more exotic side, a group at Montana State University is exploring the use of thin, alternating layers of Cr and Al nitrides[46].

The coatings can be applied in several ways. The coatings discussed above were applied by sputtering processes. Several experimenters are developing alternative methods including dip coatings, EBPVD (electron beam physical vapor deposition), a self combustive glycine nitrate process[47]. These methods will be vital if an applied coating is widely accepted due to the fact that sputtering is not an ideally suited mass production process.

2.4.3.3 Reactive Element Doping: The final method of improvement, namely doping, is solely intended to reduce the oxide growth rate. Doping is essentially the presence of a minute amount of a foreign element in a material. The presence of a doping element can alter the properties of a material in numerous ways, ranging from improving the electrical conductivity, as described above, to changing the color, as seen in gemstones. The particular effect that is of use in slowing the oxide growth rate of a high temperature system is the reactive element effect. Here large cations that form extremely stable oxides are used, such as La, Zr, Y, and Ce. They segregate to and/or react with the internal boundaries of the oxide scale and by various mechanisms to hinder the rapid diffusion paths through the oxide. This forces the oxide growth to be more dependent on slower, bulk diffusion. The effect can be so strong, that in some cases as to change the growth direction of the oxide.

Several authors have done work with doping of chromia scales. Ecer et al. investigated the effect of Ce as an alloying element in Ni-50Cr alloys[48], as well as superficially applied CeO_2, Cr_2O_3, and Co_3O_4 on Ni-50Cr and CeO_2 and MgO on Fe-25Cr[49]. The results show that CeO_2 was the most effective at reducing the chromia growth rate on both alloys, with the reduction being very large for the case of the Fe – 25Cr alloy. The oxide grain size was reduced by a factor of five from the undoped alloy and the formation of Fe oxides after long exposure times did not occur during the lifetime of the test. The ceria particles mostly remained on at the gas metal interface, indicating that the chromia growth was mostly inward. Qi and Lees[50] have shown large reductions of the mass gain on Fe – 25%Cr when surface applied Y_2O_3 and Cr_2O_3 – Y_2O_3 coatings when exposed at 1000^{o}C. Bennett et al[51]. implanted Ce into pure chromia and exposed at 750^{o}C, 850^{o}C, and 950^{o}C in pure oxygen. The results of testing show that the mass gain of the implanted sample at 950^{o}C is below that of the unimplanted sample at 750^{o}C.

Ramanathan[52] showed that externally applied Y_2O_3 and CeO_2 as well as Y and Ce alloy additions improved the oxidation resistance of Fe – 20Ni alloys. Patil et al[53]. have showed a large improvement in the oxidation resistance with agglomerated CeO_2 nanoparticles applied and even more resistance when the nanoparticles are nonagglomerated. Shen et al.[54] exposed Fe – 20Cr with and without surface applied CeO_2 in wet oxygen at 1000^{o}C. The doped sample showed steady oxide growth while the undoped samples showed extremely rapid mass gains after 5 – 10 hours.

3.0 RESEARCH OBJECTIVES

The ability to use ferritic stainless steels as an interconnect material would allow drastic reductions in materials and fabrication costs of the SOFC. Considering the theoretical cost reduction and increased public awareness, popular acceptance of SOFC technology may be on the horizon. This obviously makes research involved with improving the performance of these alloys vital. Several types of experiments are described below to address the two main issues relevant to ferritic alloys, i.e. controlling the oxide growth and vaporization rates.

3.1 EVALUATION OF COMMERCIAL MATERIALS

The logical first step to improving the ferritic stainless steels is to test the materials that are currently available in an unaltered state. This will form a baseline that will allow the performance of the improved material to be evaluated. Several types of tests were done to fully capture the effectiveness of a material as a SOFC interconnect, and the results from each must be carefully considered in any sort of ranking.

3.1.1 Alloys

Two commercial ferritic alloys were evaluated. E-Brite is an Allegheny Ludlum alloy, typically used as the baseline alloy for testing in fuel cell applications. This alloy is essentially a Fe-26Cr alloy. Crofer 22APU is generally considered the leading candidate alloy, and is made by Thyssen - Krupp. Crofer is a Fe-22Cr-1Mn alloy that forms a $MnCr_2O_4$ layer on top of the chromia scale.

3.1.2 Normal Oxidation Resistance

As with most other high temperature applications, the behavior of a material in simple oxidizing environments is important. This usually means isothermal and cyclic exposures at the desired test temperature. Weight change measurements that are continuous (isothermal – TGA) and discontinuous (cyclic) provide insight into the some of the properties of the protective oxide. This also provides a quick way to rank materials. The isothermal/TGA test allows for the calculation of the parabolic rate constant, which is related to the oxide growth rate. The cyclic test is a more severe test and will give insight into the effects of thermal expansion mismatches and the strength of the metal/oxide interface. A large amount of the work on these materials using cyclic testing has been done in the previously discussed work of Hammer, et al.[10]

3.1.3 Oxidation in a Dual Atmosphere

SOFC interconnects are subject to a very complicated exposure environment. The work of Yang discussed above show that it is not plainly obvious from knowledge of the normal oxidation properties and behaviors how the material will behave in a dual atmosphere in an actual SOFC. An apparatus has been built to allow for high temperature exposure in a dual environment. For safety purposes, the dual environments consist of dry air and an Ar-4%H_2 + H_2O mixture. By repeating testing in the literature and comparing results, it is possible to determine if this latter

gas mixture satisfactorily simulates the anode side environment. These tests will be run on most materials and composite systems involved in this work. The overall aim is to determine which materials show a dual atmosphere effect, as well as the kinetics and mechanism.

3.1.4 Electrical Properties of the Material at Temperature

Thus far, the testing discussed has not considered the most important aspect of the interconnect, i.e. its current collecting function. Oxides are typically insulating and add significant resistance to the fuel cell stack. For a true comparison of candidates for an interconnect material must include both the oxidation behavior and the resulting addition to the electrical resistance. An apparatus has been designed and built to test this property. Currently results of this type of testing are only comparable to other in house results due to the vast differences in experimental setup.

3.2 REDUCTION OF CHROMIA VAPORIZATION RATE

Chromia forms volatile species, and these gaseous products have been shown to reduce the output capability of the cell by poisoning the cathode material. For this reason it is important to develop schemes for reducing the rate at which the scale vaporizes. Two methods for achieving this were utilized, both of which ultimately end up with a layer of material above the chromia scale that reduces the activity of chromia at the gas interface and thereby reduces the vaporization rate. The two methods, specifically forming a thermally grown layered oxide and applying an overlay coating, are discussed separately below. They may also be analyzed in conjunction in order to observe possible synergistic effects.

3.2.1 Thermally Grown Oxide Overlayers

The first of the two methods mentioned above involves the formation of a thermally grown, layered oxide scale. This is achieved by adding alloying elements that are known to have high diffusivities and relatively low solubilities in chromia, as well as the ability to form a new, stable oxide at the gas/oxide surface with acceptable properties (CTE match, conductivity, etc.). While alloying in ferritic stainless steels is fairly easy and relatively inexpensive, it is very complicated to understand and may involve some trade offs (ex. doping the Cr_2O_3 in a manner that increases the growth rate) if used alone. Currently, two alloying element additions, manganese and titanium, have been examined.

3.2.1.1 Short Time Testing: The work in this area was done mostly on Crofer 22APU, which, as mentioned above, contains Mn additions which allow the formation of a $MnCr_2O_4$ layer on top of the chromia scale. This is well documented to occur in long time exposure, but the mechanism and kinetics of the overlayer formation in short times has not been. Short time exposures were done to show the evolution of the overlayer.

3.2.1.2 Fe-Cr-Ti Alloys: Combining the concept utilized in Crofer 22APU and that the Ni based superalloy IN738 forms a TiO_2 surface layer that also reduces chromia vaporization, a series of Fe-22Cr-xTi (x=~1 - 4) alloys have been melted at Allegheny Ludlum Technical Center. Testing was done to first show that the TiO_2 layer does form in a ferritic alloy. Once this was established, the testing paralleled the work on Crofer 22APU to determine the mechanism at work. As these are new materials, longer term and cyclic oxidation testing to fully characterize the oxidation behavior were also done. The fuel cell specific tests were done to determine if there are benefits of using these alloys in the SOFC.

3.2.2 Overlay Coatings

Experiments with alloying elements that enable the formation of the outer oxide layer above can be expensive and time consuming. There is also the issue of the kinetics of the layer formation and how much vaporization takes place before it is continuous. Placing a thin coating on the substrate prior to exposure ensures that chromia vaporization from the substrate is drastically reduced. Due to the fact that substrates with $LaCrO_3$ and $LaFeO_3$ based coatings have been generously supplied by Dr. P. Singh (PNNL) and Dr. C. Johnson (NETL), those are the systems which were examined. As will be described in more detail in the results section, there have been some problems with porosity and cracking of the coating. This is most likely the result of the deposition conditions. As a result of this, it was attempted to fill the cracks in some manner to prevent vaporization from those locations.

3.3 REDUCTION OF CHROMIA GROWTH RATE

While most of the proposed work above involves reducing the chromia vaporization rate, reducing the growth rate is also equally important. The electrical resistance of the oxide is directly related to its thickness, where obviously the thinner the better for SOFC applications. Thin layers (nano scale thickness) of CeO_2 were applied to alloy surfaces by pulsed laser deposition as a dopant. The ceria layer will act as a reactive element, segregating to oxide grain boundaries and impeding diffusion. This in turn should slow down the growth of the protective oxide. After doping, the materials will be put through a series of tests as the substrates to allow comparisons to the unaltered alloy.

4.0 EXPERIMENTAL DETAILS

Below are detailed descriptions of the types of tests that were run in order to fully evaluate the candidate materials described above. Where possible, schematic diagrams of the equipment are provided. Unless otherwise noted, all morphological analysis was done using scanning electron microscopy (SEM) and all samples were prepared with a 600 grit finish. The first types of experiments to be described are the more typical, single atmosphere oxidation tests. This will be followed by descriptions of more fuel cell specific testing, i.e. dual atmosphere and electrical conductivity. Finally more light will be shed on the techniques for applying the overlay coatings and dopant layers.

4.1 SIMPLE OXIDATION EXPERIMENTS

The vast majority of the work done on oxidation of materials consists of two types of testing, isothermal and cyclic oxidation. These tests are intended to simulate the conditions the sample would see in use as accurately as possible. In the case of the SOFC interconnect, this testing is questionable in its relevance, since single atmospheres are used. It is valuable since it allows for ranking of performance in each atmosphere and eliminates complications that may arise due to a dual atmosphere effect.

4.1.1 Isothermal Exposures

Isothermal exposures, as can be understood from the name, are those that take place at the same temperature throughout the testing period. Discussed below are simple isothermal exposure and thermo gravimetric analysis (TGA).

4.1.1.1 Simple Isothermal Testing: This type of testing is done in a horizontal furnace, schematically shown in Figure 4-1. The sample is prepared with a hole in it, and is suspended from a slide rod using fine wire. The rod/sample is slid into the preheated furnace using a magnet, and slid out after the prescribed exposure time has elapsed. The gas atmosphere consists of dry air which is constantly flowing through the system during testing. Other gas atmospheres were also be used.

Isothermal testing is the used test most in this work. It is used to track the oxide morphology of Crofer 22APU and the high Ti ferritic alloys. The coated materials have been tested isothermally for coating durability and morphology. All ASR tests were done on samples that have oxides that were grown isothermally.

4.1.1.2 Thermo Gravimetric Analysis: Thermo gravimetric analysis (TGA) is essentially measuring the weight change of the sample continuously during the isothermal exposure. The results from this are curves of the normalized mass gain vs. time and the square of the normalized mass gain vs. time. The combination of these allows for determination of the oxide growth rate and gives some insight into some mechanisms that may be in effect (i.e. vaporization, spallation, internal oxidation). This in turn can be used to rank materials.

The TGA apparatus is shown schematically in Figure 4-2. The sample (less than 1 g) is suspended from a platinum wire, which runs into a microbalance. The reaction tube is put around the sample and sealed to the glassware on the balance. Weights are added to the other side of the balance to counterbalance the sample mass. Once balance is achieved, the desired gas is allowed to flow into the system. The vertically arranged furnace is then raised to surround the sample. The computer attached to the microbalance records the change in mass every 10 seconds for 168 hours or one week (limits of the computer). The resulting data are manipulated to give the plots described above.

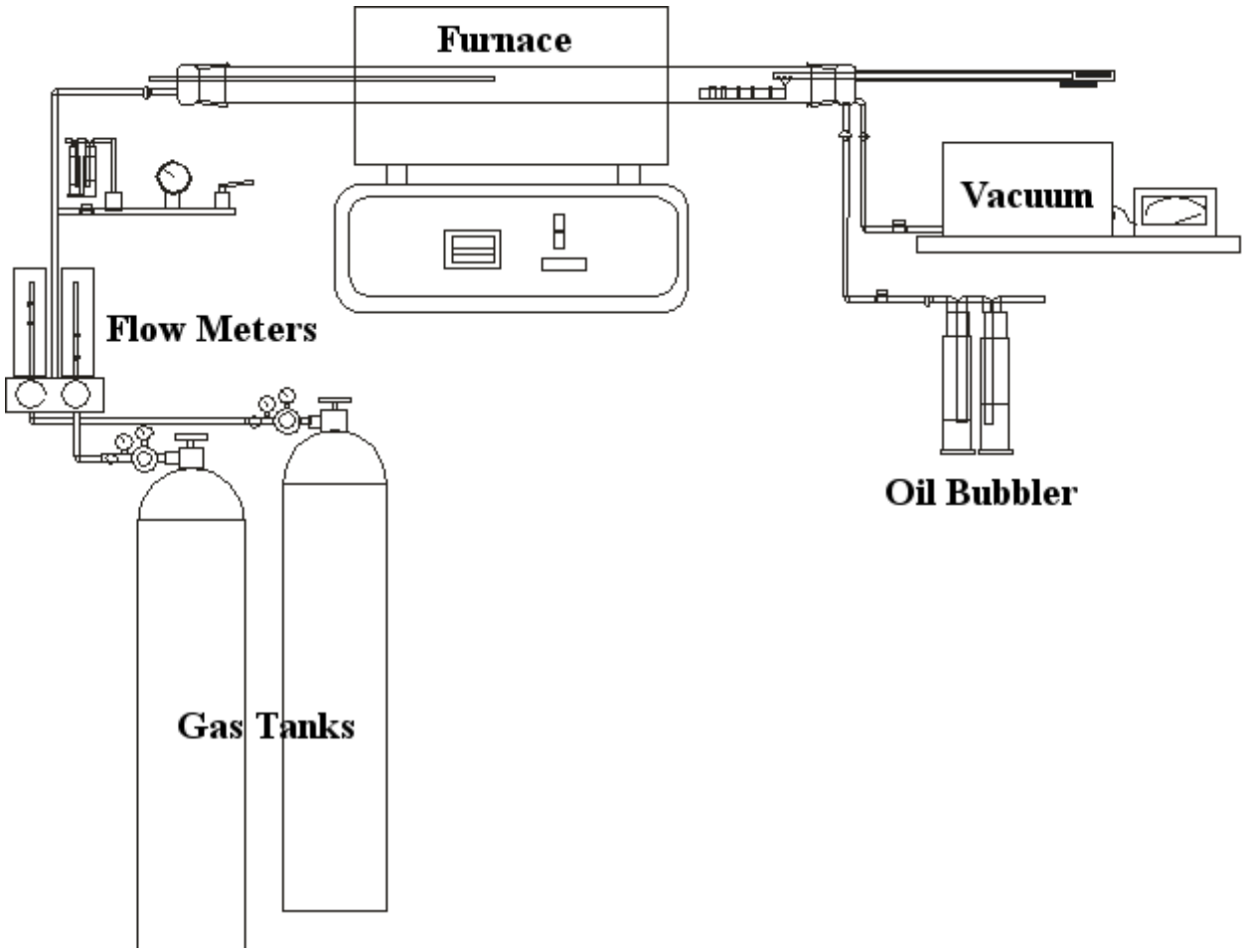

Figure 4-1 Schematic diagram of the a horizontal furnace set up used for isothermal exposures

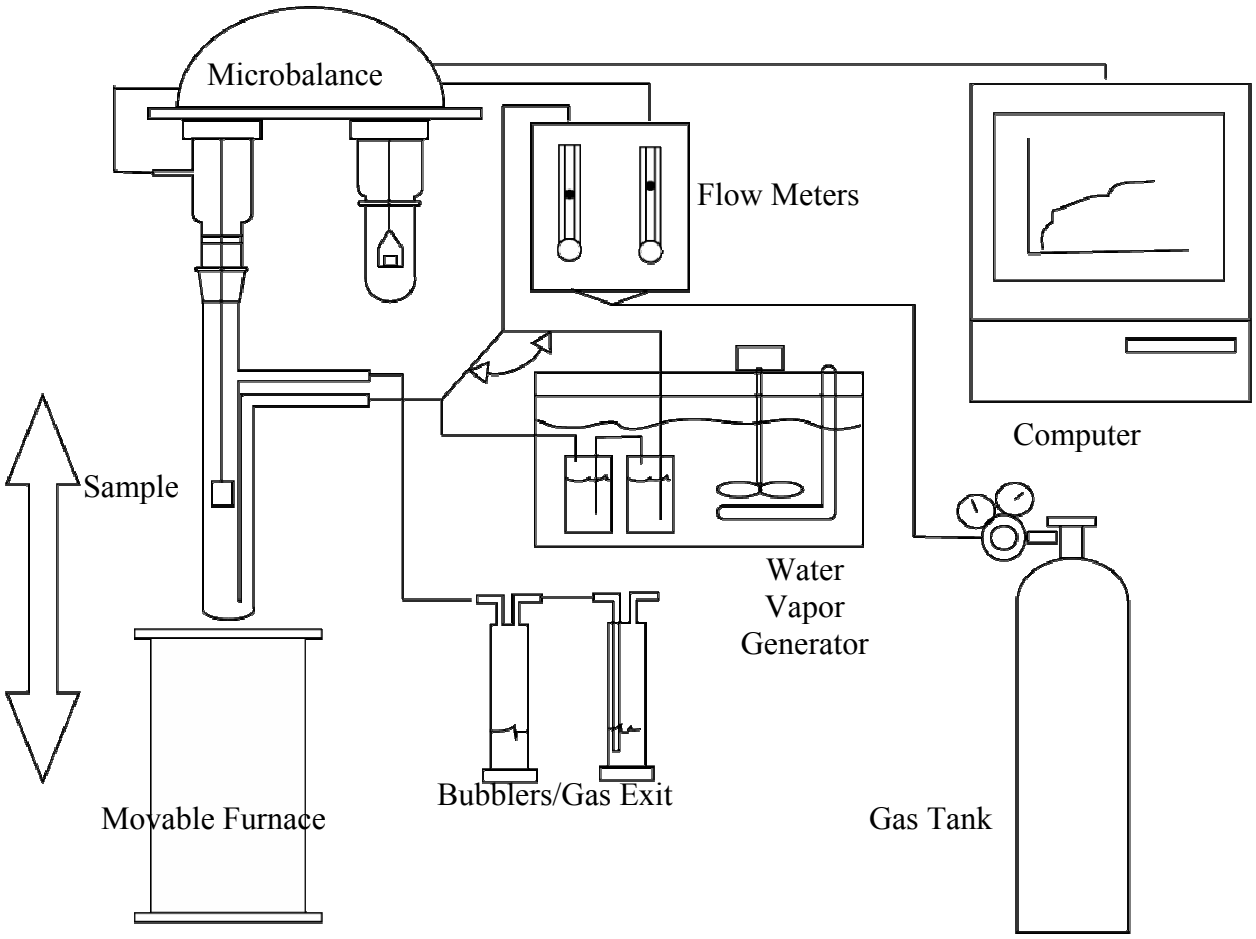

Figure 4-2 Schematic diagram of the TGA apparatus used in this work

4.1.2 Cyclic Oxidation

This type of exposure simulates the heating and cooling that would occur if the fuel cell is shut down. The cycles used are 45 minutes in the furnace at temperature, followed by 15 minutes of cold time outside the furnace. The furnace setup for this exposure is identical to that used for the isothermal exposures (Figure 4-1). The difference is that a drive mechanism is added to automatically move the sample in to and out of the furnace. The drive consists of a magnet that is attached to a long threaded shaft. A reversible motor turns the shaft to move the magnet. The motor is turned on, off, and reversed by mechanical switches set at the ends of the shaft (used to set the magnet travel distance) and mechanical timers. Since the furnace is the same, the samples are prepared the same was as described above, i.e. cut to correct size, drilled and polished.

4.2 FUEL CELL SPECIFIC TESTING

Simple oxidation testing is very useful in most cases for evaluating the performance of materials at high temperatures. Unfortunately, for solid oxide fuel cell applications, normal testing does not represent the complex environment that an interconnect will see in service. Therefore, more simulative testing must be developed and performed as a way to better evaluate a material. Apparatuses for two of these more simulative tests have been built and will be discussed below.

4.2.1 Dual Atmosphere

As explained previously, one of the functions of the fuel cell interconnect is to act as a bipolar gas separator, meaning it is the barrier between the fuel and oxidizing gases. Also mentioned previously, this situation has been shown to alter the oxidation mechanisms of some materials, and therefore is an important test to develop. Difficulties arise due to the fact that many of the

candidate materials are available in sheet form. Two designs have been developed and built to accommodate coupon samples and tubes, but the tube apparatus will not be discussed as none of the materials of interest are available in tube form.

The more frequently used apparatus is for the more common, yet complicated situation where the material is only available as a coupon sample. A cup shape was machined from a 1" diameter rod of Rene N5 superalloy to act as the sample holder (Figure 4-3). The cup has two holes in the outside bottom that run about half the thickness of the base of the cup. These holes merge in the last half to form one larger hole on the inside bottom. The two bottom holes have tubes of IN600 brazed into them that run out of the furnace environment. These two tubes attach to the fuel gas entrance and exit the system. When a sample large enough to cover the hole in the bottom is placed in the cup, it effectively closes the fuel gas system. When a different gas is introduced to the reaction chamber, a dual atmosphere condition is set up with the sample, cup, and brazed tubes acting as the separators. Maintaining this condition depends on quality brazing of the tubes and a good seal between the sample and the cup bottom. Mica washers are used to create the sample/cup seal. Because they are compression seals, they work best when pressure is applied to push the sample into the cup bottom. This is achieved by first arranging the furnace in a vertical configuration, bending the brazed tubes once they exit the furnace and placing a jack underneath, and finally adding a tube to the top that fits snugly into the top of the cup. A second jack is applied to this tube opposing the first jack and allows a seal to be made.

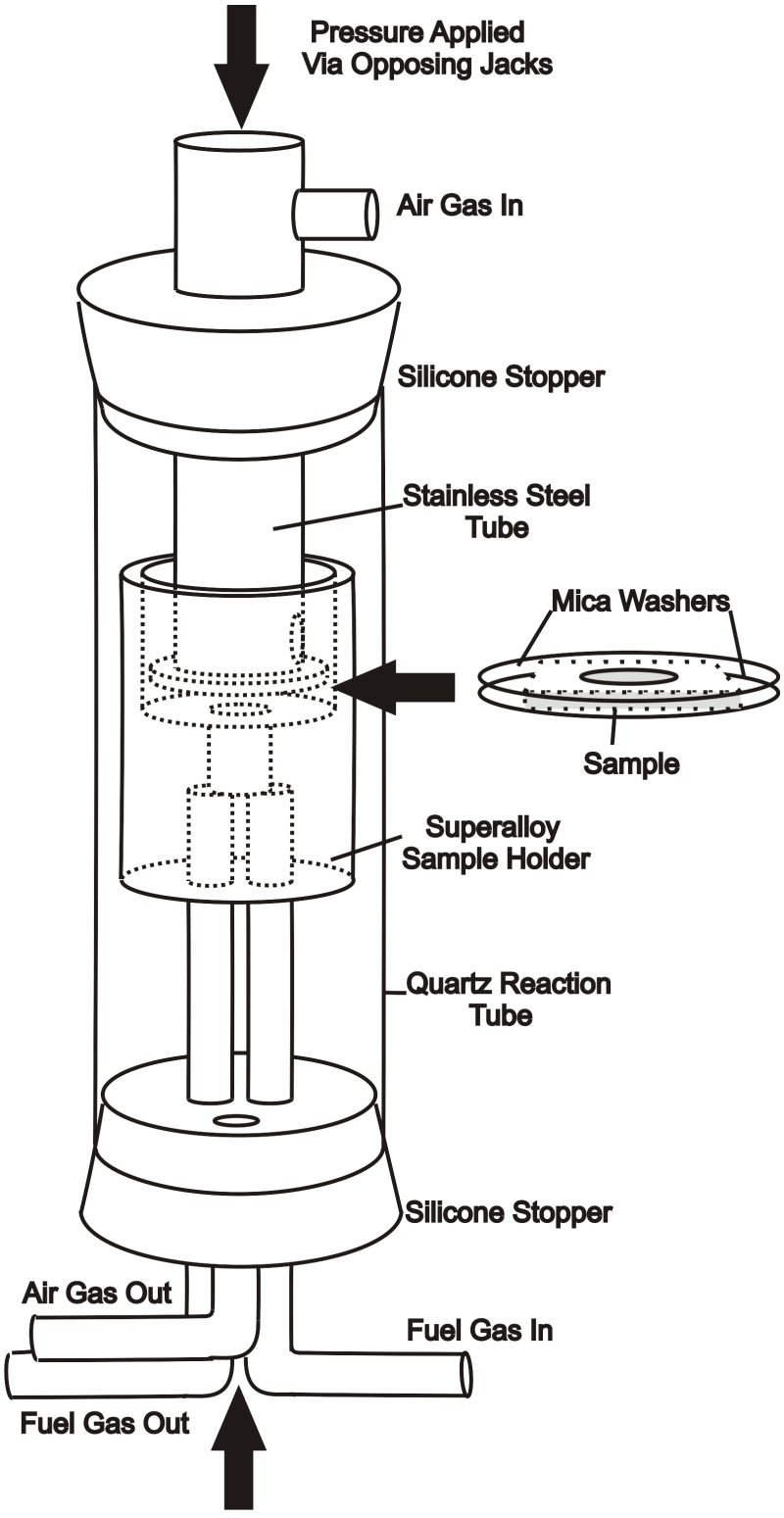

Figure 4-3 Schematic of the dual atmosphere apparatus for coupon samples.

4.2.2 Area Specific Resistance Measurements

Along with the oxidation behavior of the material, the electrical properties of the oxide scale are of vital importance in fuel cell applications. The measurements are done using the four point probe technique. A four probe test uses 4 leads, 2 voltage and 2 current. One of each is placed on opposing sides of the sample and a current is applied. The voltage drop is measured. With the voltage drop (V) and current (I) known, the resistance (R) can be calculated using Ohms law, Equation 30. The resistance can then be used to calculate the two values usually quoted in the literature, the area specific resistance (ASR) and the electrical conductivity ($\sigma = 1/\rho$) by setting Equations 29 and 31 equal to each other. This is a very common measurement for the semiconductor industry, but the measurement is further complicated for SOFC applications by the fact that the measurement must be done at temperature. The apparatus used to perform the measurements, as well as some other details pertaining to methods for electrode attachment are described below.

4.2.2.1 System Design: The main components of the system are the furnace and the electronics. Figure 4-4 shows the horizontal furnace with a programmable controller and the accompanying parts of the heating component of the system. The reaction tube in the furnace is made of quartz and features a thermocouple well for monitoring the furnace temperature externally. The reaction tube end cap also contains a hole for the electrical leads to exit the system. Gases introduced during the test are controlled by a flow meter and exit via an oil bubbler. There is also an attachment to a vacuum to allow for the use of low PO_2 gases such as Ar – 4%H_2. The end cap of the reaction tube has a ground joint inside that connects to a mullite tube that is used to support the Macor sample holder (shown in inset of Figure 4-4) and leads. This minimizes the stress on the leads while moving the sample to and from the furnace. The

four Pt wire leads run through two pieces of four hole alumina thermocouple shielding. Each end has an ample amount of wire left over to make the necessary contacts. The thermocouple shielding runs out of the system through a hole in the end cap.

Two pieces of equipment are used to measure the electrical properties. The primary unit is a current source/voltmeter made by Jandel (Figure 4-5). The unit is attached to the leads using a single breakout cable that was custom made for this application. The cable breaks into four wires, red, yellow, blue, and green. Alligator clips were attached to the end of each wire and are the clipped on to the appropriate lead wire during the test. The red and yellow wires must be paired on the same side of the sample, with the blue and green wires paired on the other side. The unit is turned on by a switch on the back left side. Other controls are forward, reverse, and off that control the current, push buttons to control the current output, a decade (x10) button for the current output, two buttons for the voltage measurement range (200mV and 2000mV), and a knob for the maximum voltage the unit can use to generate the desired current. The final feature is the ability to connect a second multimeter for the occasions when the voltage measured is below 0.01mV. On those occasions, a Keithley multimeter is attached and the voltage is read from it.

4.2.2.2 Platinum Paint Method: This is the method for attaching the electrodes that the system was designed to use. This method is used by Dr. Johnson at NETL. Samples are first oxidized to create the oxide scale. Scotch tape is used to mask off identical areas on both sides of the sample, making sure the tape is firmly attached. Platinum paint is then applied to the oxide scale using a paint brush in a dabbing motion. Once the area is covered, the paint is allowed to dry. The paint appears to have good adherence to chromia, but some oxides (ex. NiO) may require several thin layers of paint followed by a sintering step to build up a continuous

layer. The tape is then slowly removed from the sample, leaving a neat, measureable painted area. Once the tape is removed and the area recorded, the sample is placed in the sample holder. Pt foil electrodes, that have been permanently spot welded to the lead wires (two leads per sheet), are placed on either side of the sample. Inert ceramic plates are placed outside of the electrodes and the entire sandwich is compressed using the screws in the holder. The sample is then put into the furnace. The paint should be given some time at temperature prior to beginning measurements so it has sufficient time to sinter. Figure 4-6 shows a cartoon of the final appearance of the sample with the electrodes attached.

4.2.2.3 Test Procedure: The test is fairly simple, but time consuming to perform. The sample is oxidized for the desired time at the desired temperature. The electrodes are painted on, dried, and the sample is inserted into the sample holder, which in turn is placed on the mullite tube. This fixture is placed in the furnace and heated to the desired sintering temperature. The leads are attached to the Jandel unit using the alligator clips on the breakout cable. When the sample is sufficiently sintered, the furnace is taken to the first test temperature, typically 900^{o}C. The current is set to 1mA output by setting the unit to 1000 and pushing the decade (x10) button. The forward button is pushed and the voltage measurement is recorded. The current is changed to 5mA and then 9.9999 mA, and the voltage is recored at each step. Then the reverse button is pushed and the same currents are used again. After the six voltage measurements are made, the temperature can be changed and the measuring procedure repeated. When the testing is complete, the data are used to calculate a resistance, which in turn is multiplied by the electrode area to give the area specific resistance. Typically, plots are made of Log ASR/T vs 1/T to represent the data in order to calculate the activation energy for electrical conduction.

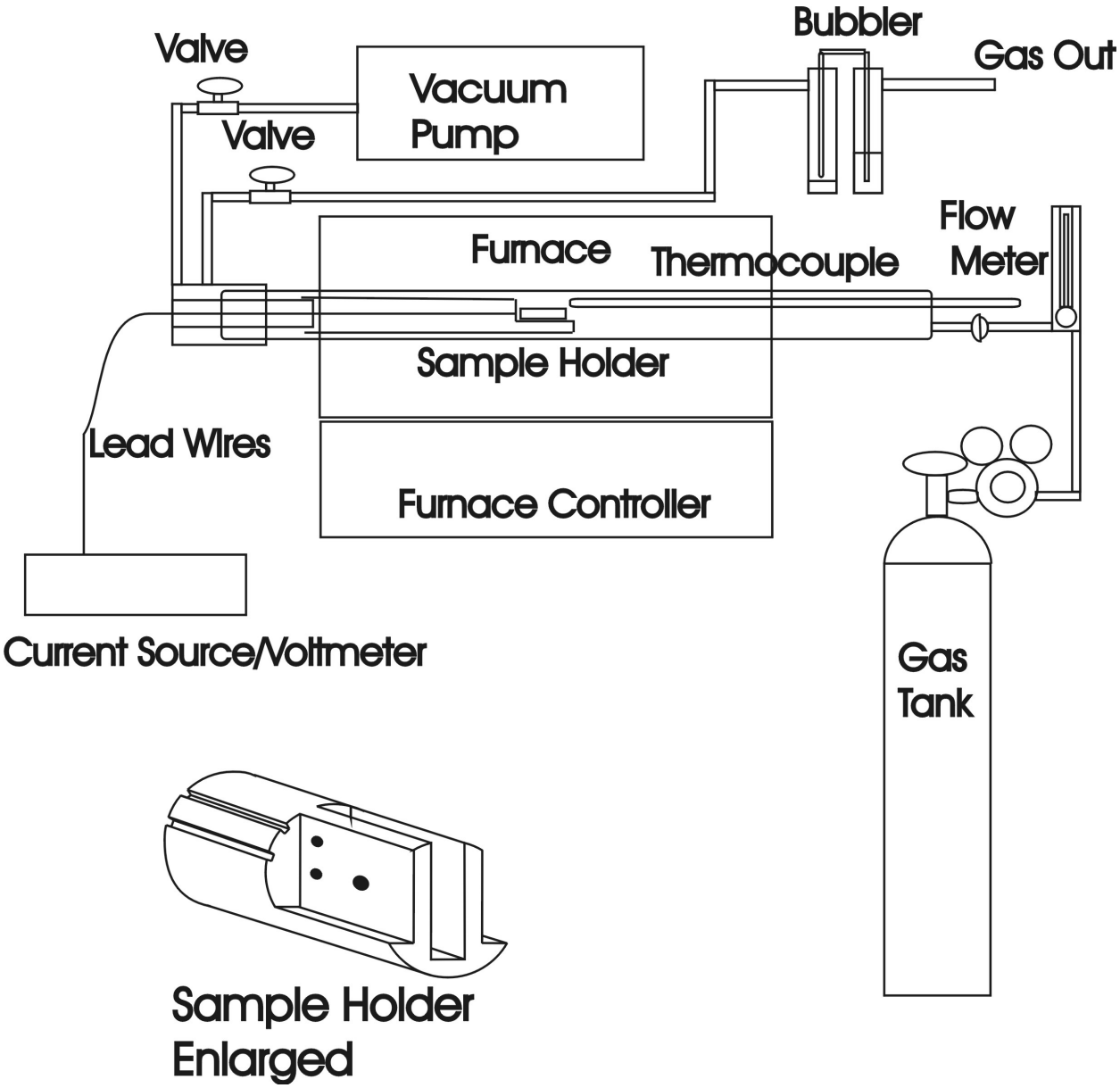

Figure 4-4 Schematic of the furnace used for the ASR measurements

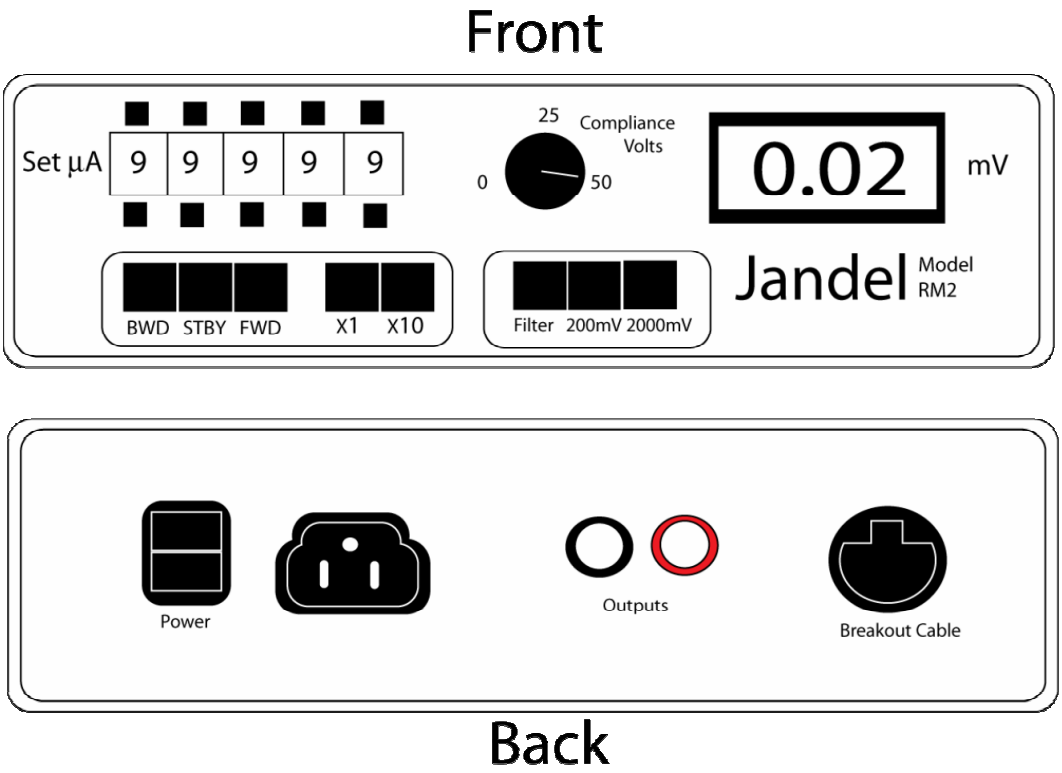

Figure 4-5 Schematic of the electronic equipment used for ASR measurement

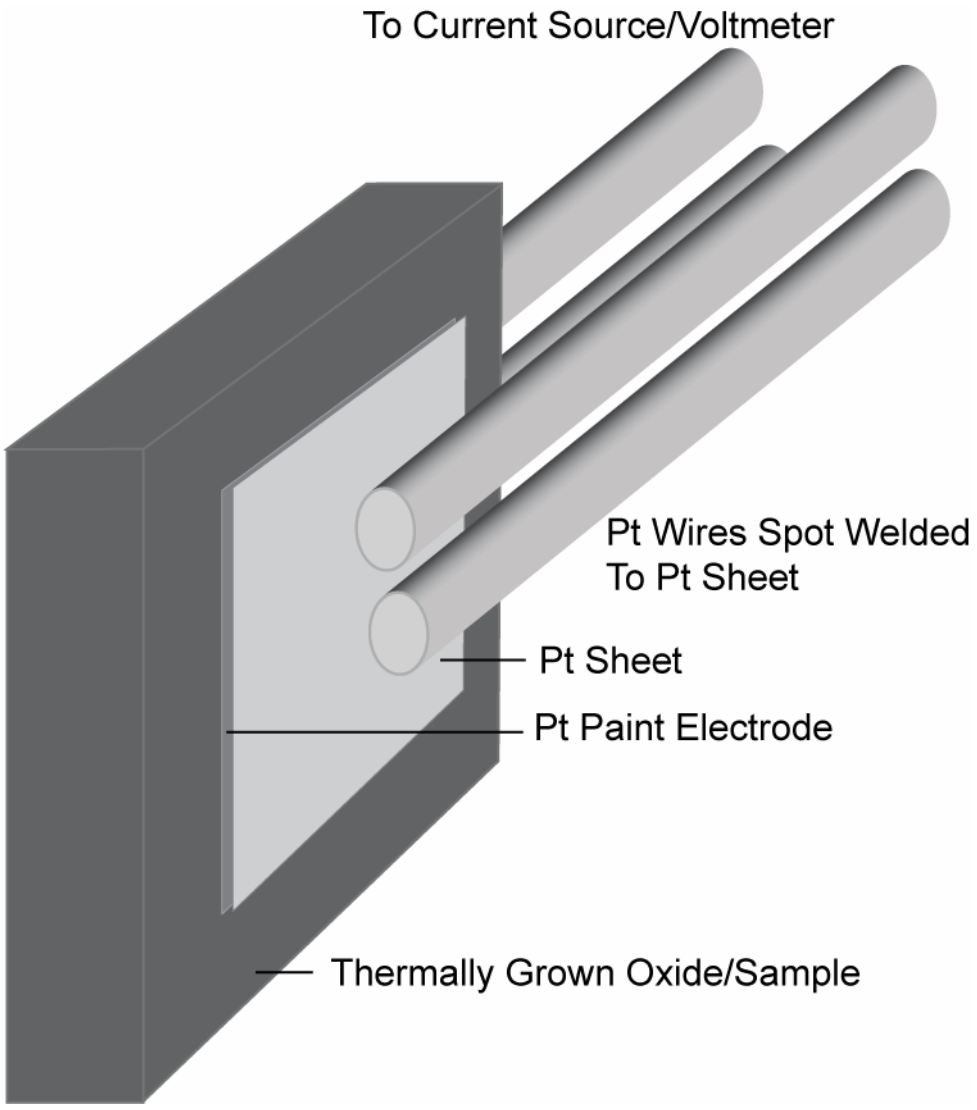

Figure 4-6 Cartoon showing a sample with the electrodes and leads attached using the Pt paint method

4.2.3 In Cell Testing

The results of the TGA test in both dry and wet environments are only useful as a self comparison, and does not give any insight into possible vaporization of the specimen in the dry environment. The initial idea for quantifying the vaporization was that if there is vaporization from the interconnect material, it will poison the cell and result in a measurable decrease in performance. Results that include only the vaporization would require the samples to be placed in the gas stream near the interconnect and not actually in use. After some preliminary results of the oxidation behavior of the Fe-Cr-Ti alloys indicated much more rapid growth of the oxide, it was deemed more valuable to actually use the sample as the interconnect itself on the cathode side to combine the effects of vaporization and oxidation. Intricacies in the data can give an idea of which is the main culprit for the degradation and will give the direction to focus future work on these types of alloys.

These experiments were carried out at NETL Morgantown with the help of Dr. Johnson. In the current test (Figure 4-7), the cell was loaded in a similar manner as the typical button cell testing. The apparatus that was used, shown in Figure 4-8, is a test rig that was built for testing button cells. A mica washer was placed on a ceramic flange, followed by a strip of Pt mesh and another washer. The strip was allowed to bow upwards. Tape was used to hold the washers and mesh in place. Pt paint was applied to the mesh and the cell was placed on the washer with the anode side contacting the mesh. After another mica washer was placed in the stack, the cathode was painted with Pt paint and a small square of Pt mesh was applied. More paint was put on the mesh, followed by the sample. Another strip of mesh was placed on top of the sample perpendicular to the first one. A final washer was added and taped. The top flange was then put

into place and the whole stack was taped. Silver wire was welded to each piece of mesh. The wire and mesh were then used to wrap around a thicker "rope" of silver wires. At this point, the flange set up is ready to be put into the testing apparatus.

The assembly, shown in Figure 4-7, was placed into a tube furnace and heated from room temperature to 800^{o}C at a rate of 6.5 degrees per minute. The cells were then exposed to a 10% hydrogen in N_2 mixture on the anode side, with a total flow rate of 400 CC/min. Gases on both the anode and cathode side were fed to the cell through an coaxial center ¼ inch diameter feed tube, and the exhaust was removed through the outer 1 inch diameter support tube. The cathode had 1000 CC/min. air flow at all times. After two hours under these conditions the anode gas was changed to 3% H_2O in 97% H_2 at 400 cc/min. The cell was then set to 0.7 volts using an Agilent N3303A load box. The voltage and current signals were then collected as a function of time using a LabVIEW program on a PC

The cells were all identical, anode supported cells supplied by Anil Virkar at the University of Utah. The anode was a Ni/YSZ composite approximately 1 mm thick and also containing a Ni/YSZ interlayer approximately 50μm thick. The electrolyte was YSZ approximately 20μm thick. The cathode was 50μm thick LSM with a 50 μm thick YSZ/LSM interlayer. Both interlayers were finer grained material than either the cathode or anode. See Figure 4-8 for furnace and tube assembly.

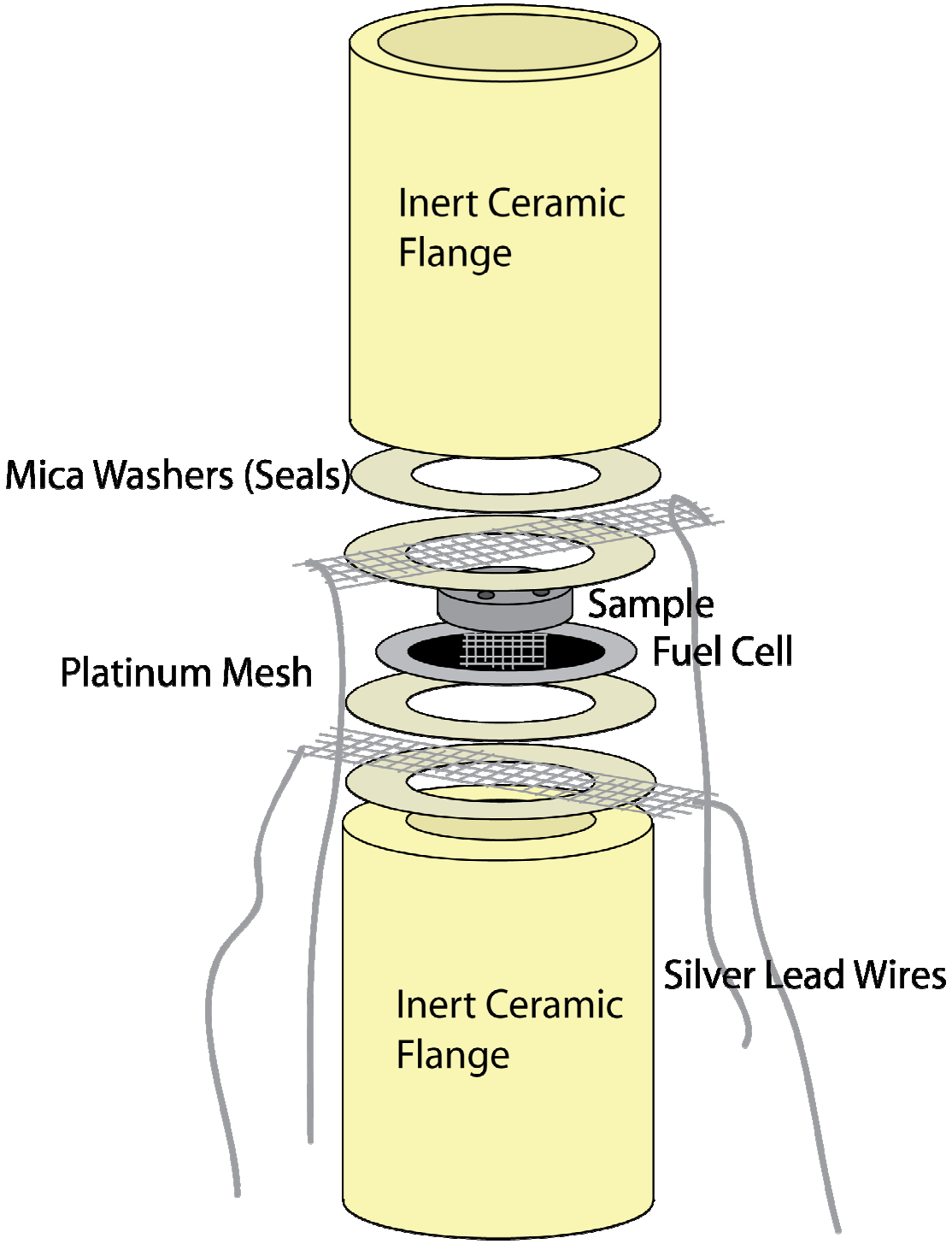

Figure 4-7 Cartoon of a close up view of the in cell testing set up

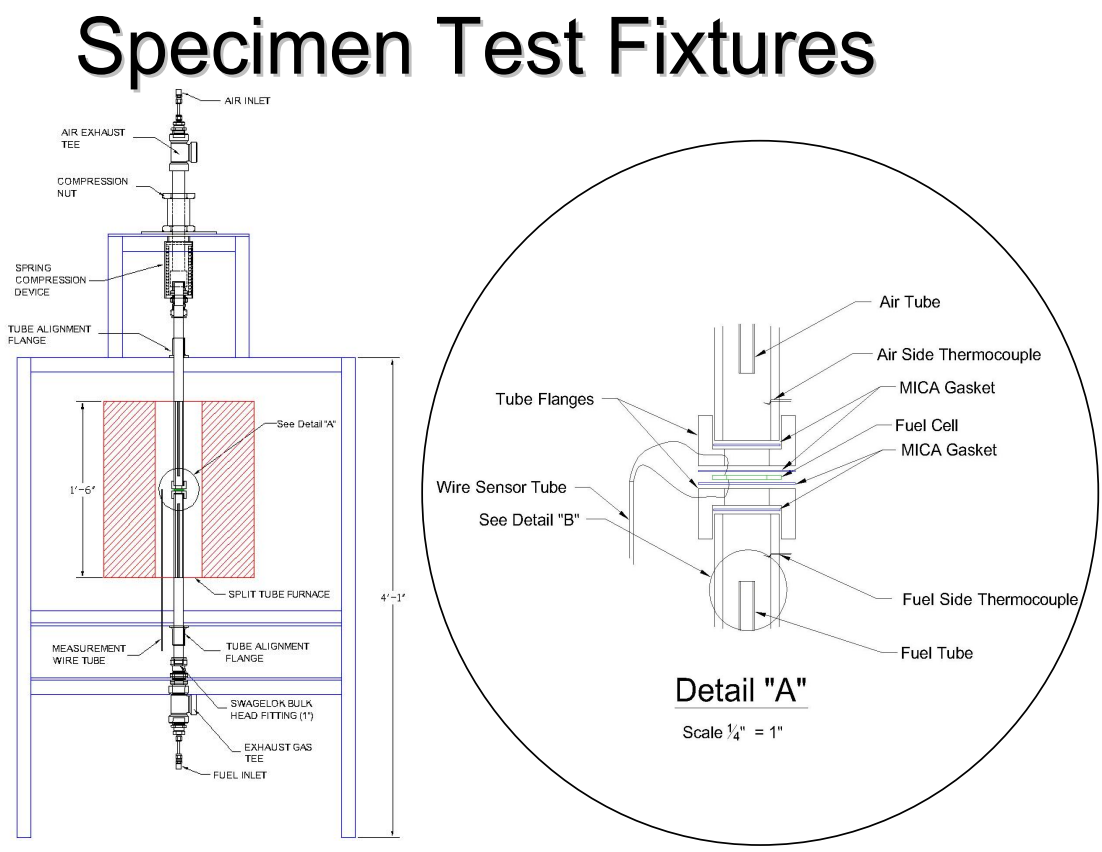

Figure 4-8 Schematic diagram of the button cell testing apparatus at NETL.

4.3 APPICATION OF OVERLAYERS/DOPANTS

Several of the methods that were attempted to improve performance involved application of materials on top of the substrate prior to oxidation. There are two methods that were used, namely sputtering and pulsed laser deposition.

4.3.1 Sputtering

Sputtering is a popular physical vapor deposition technique. A gas, frequently Ar, is introduced into a low pressure environment. A high voltage is applied to create a plasma. The Ar ions are accelerated towards the target material and impact it, knocking off material. The freed target material then falls to the substrate. Very little information has been given as to the type of sputtering used for the relevant samples in this work, as the samples were received in the as coated state from both PNNL and NETL. Sputtering does give films of the same composition as the target and is rather fast compared to techniques such as molecular beam epitaxy. Unfortunately, it requires a vacuum and is slower than the technique discussed below.

4.3.2 Pulsed Laser Deposition

Pulsed laser deposition (PLD) is another physical vapor deposition method. A high powered laser is focused and aimed at the target (which is in a vacuum). The rapid heating ejects material in a highly directional plume. The plume created is then directed at the substrate where it is deposited. The advantages of this method are that it is relatively fast and the target stoichiometry is maintained. The disadvantages include the need for a vacuum, which would hinder the up scale up of this method, and if care is not taken during the coating process, the film quality can be poor.

The PLD coatings in this work were done using the equipment and assistance of Dr. J. Leonard (Pitt). The procedures for deposition will not be discussed here as it is frequently amended, but there is an up to date written procedure available in the laboratory. Any important settings will be discussed in the appropriate results sections.

5.0 RESULTS AND DISCUSSION

5.1 COMMERCIAL ALLOYS E-BRITE AND CROFER 22APU

One way to dramatically decrease the materials costs in a system is to build it from materials that have well established manufacturing techniques and are widely available. In terms of materials for SOFC interconnects, the two commercially available alloys that are frequently used in experiment are E-Brite and Crofer 22APU. The oxidation behavior of these alloys has been discussed in the work of Hammer[10] in regards to the cyclic oxidation behavior and Yang in regards to ASR and behavior in a dual atmosphere. Due to this, the results for these alloys will only be discussed in detail for the dual atmosphere and ASR tests, both of which involve different types of apparatuses than those used in the literature. The TGA and cyclic test results will be discussed mainly to compare with the results of the Fe-Cr-Ti alloys.

5.1.1 Dual Atmosphere

The apparatus described in the procedure section was built and was used for testing. Due to the interesting dual atmosphere effect seen on stainless steel alloys (Fe nodule formation), experiments were conducted at 800^{o}C using dry air/Ar – 4%H_2 + H_2O over various times.

E-Brite has been tested for times of 2, 4, 24, and ~90 hours. Figure 5-1 shows micrographs from the longest of these experiments. All of the scales consisted of essentially chromia. No Fe was present as nodules or crystals. The air side oxide was thicker and more uniform when compared to the fuel side at all exposure times (Figures 5-1a&b). The surface

morphology appears to consist of faceted particles of varying sizes. The fuel side (Figures 5-1c&d) oxide was extremely thin in most locations, with thin, wide plates or blades of chromia growing from the surface. These are most likely growing in crystallographically favorable directions, as can be ascertained from the hexagonal appearance. This is a one common occurrence with chromia formers exposed in wet environments. Based on the results here, there does not appear to be a dual atmosphere effect on E-Brite under these exposure conditions. This agrees with Yang, but contradicts Birch's work using the same apparatus.

Several attempts were made to perform a dual atmosphere test on Crofer, but each time problems arose that prevented the results from being dependable. Birch shows no dual atmosphere effect on Crofer after 100 hours at 800^{o}C using the same apparatus used in this work and with a similar atmosphere.

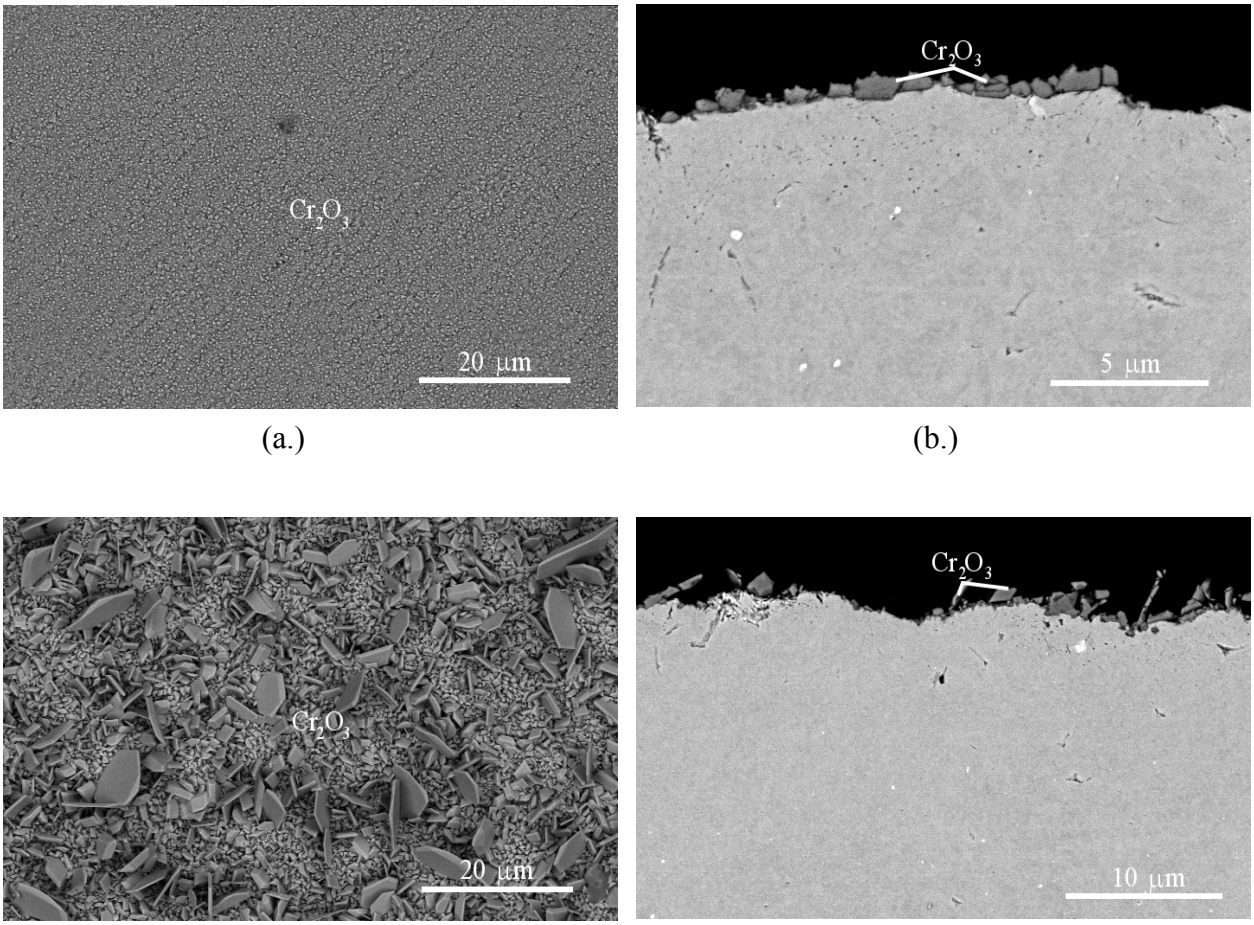

Figure 5-1 SEM micrographs showing the surface and cross-section of the air side (a&b) and fuel side (c&d) of an E-Brite sample exposed to a dual environment at 800°C for 90 hours showing only chromia on the surface.

5.1.2 ASR

To validate the newly built apparatus for ASR measurements, two samples of Crofer 22APU were exposed for 100 hours at 800^{o}C in dry air. The ASR measurement was done on the first sample using the Pt paint method, which is slightly different than the set up described in the experimental procedure (a removable Pt mesh was used instead of the permanent Pt foil). The test was unsuccessful due to problems with electrode and lead connections. The second sample was taken to NETL and the ASR measurement was performed by Dr. Johnson. The results are shown on the graph in Figure 5-2. The electrode was carefully removed from this sample and then reapplied using the Pt paint and mesh on hand. The measurement was then redone using the new apparatus. This time the connections were sufficient for successful results. These are also plotted in Figure 5-2 along with the results of a third sample oxidized for 200 hrs under the same conditions. The results of the tests on the same sample measured at Pitt and NETL are relatively close after the mesh correction is made. The 200 hr sample shows an order of magnitude higher ASR at each temperature. It is also interesting to note the change in slope in the data for the measurements at Pitt around 750^{o}C. This appears to be a product of the system, as it has appeared in other tests run by colleagues when using the Pt paint method and remains unexplained. E-Brite samples were also prepared with the same exposure conditions and intentions. but unfortunately, they had visible spallations in the oxide. If the bare metal in the spalled regions contacted the Pt paste, a short circuit would occur, resulting in artificially low values.

In order to circumvent the difficulties in using the Pt paint method with the Pt mesh, a different technique using a contact paste was developed. A sandwich consisting of two silver plates with the LSCo paste between was made. Assuming the silver has negligible resistance,

any resistance measured is due to the paste. By calculating an ASR value from this test, the results from an oxidized sample can be corrected for more accurate results. The test was run for about 210 minutes at 800^{o}C with measurements taken every 5-15 minutes. The results are shown in Figure 5-3. The ASR (area corrected curve in Figure 5-3) of the paste seems to stabilize around 0.09 Ωcm^2. A Crofer 22APU (unoxidized) sandwich was then made and tested for 100 hrs. The results (Figure 5-4) show the ASR increasing rapidly for the first 2 hrs to a value of 1.3 Ωcm^2 and then displaying a more parabolic behavior to reach a value of approximately 1.6 Ωcm^2 after 100 hrs. This value is an order of magnitude larger than the seemingly high value for the test done on the 200 hr sample using the Pt paint method. In fact, the oxide on this sample should be even thinner than that on any of the samples discussed above due to the lack of preoxidation and contact with the LSCo paste. The high values could be attributed to several things. The spot welded Pt leads could have been undercut by oxide. The contact paste could have failed to cover the entire area, had poor contact with the metal, or have not been totally continuous. There may have been a short in the silver test resulting in a low correction term.

These tests yielded mixed results. On one hand, the 100 hr Pt paint test did adequately reproduce the results from an established apparatus. On the other, the first attempt failed after several attempts to attach the electrodes. The subsequent test for the 200 hr exposure seemed to give high results. The attempt to use a simpler and possibly consistent method yielded extremely high results. The final design that was used in subsequent experiments is that described above in section 4.2.

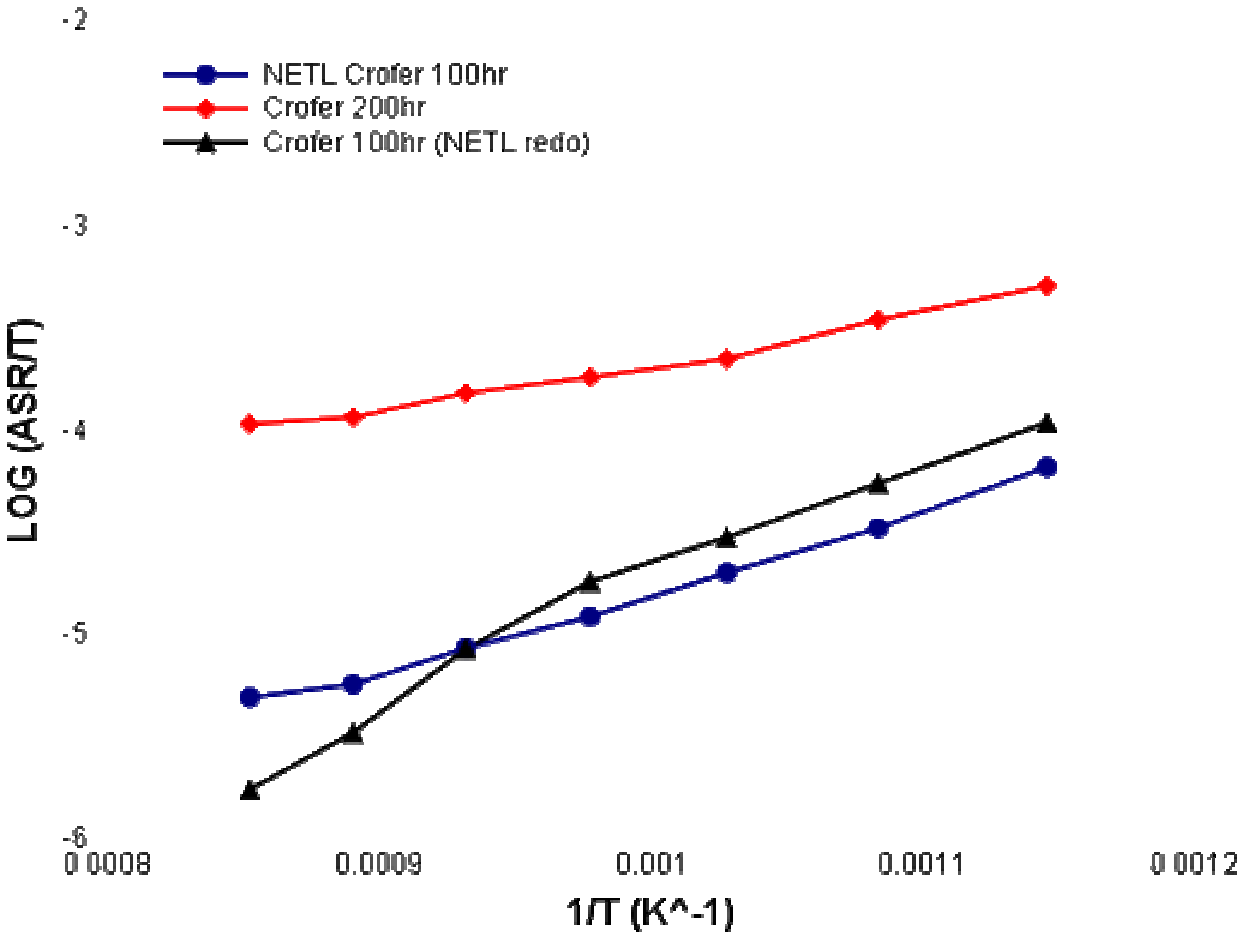

Figure 5-2 Plot of Log (ASR/T) vs. 1/T for Crofer exposed at 800°C in dry air

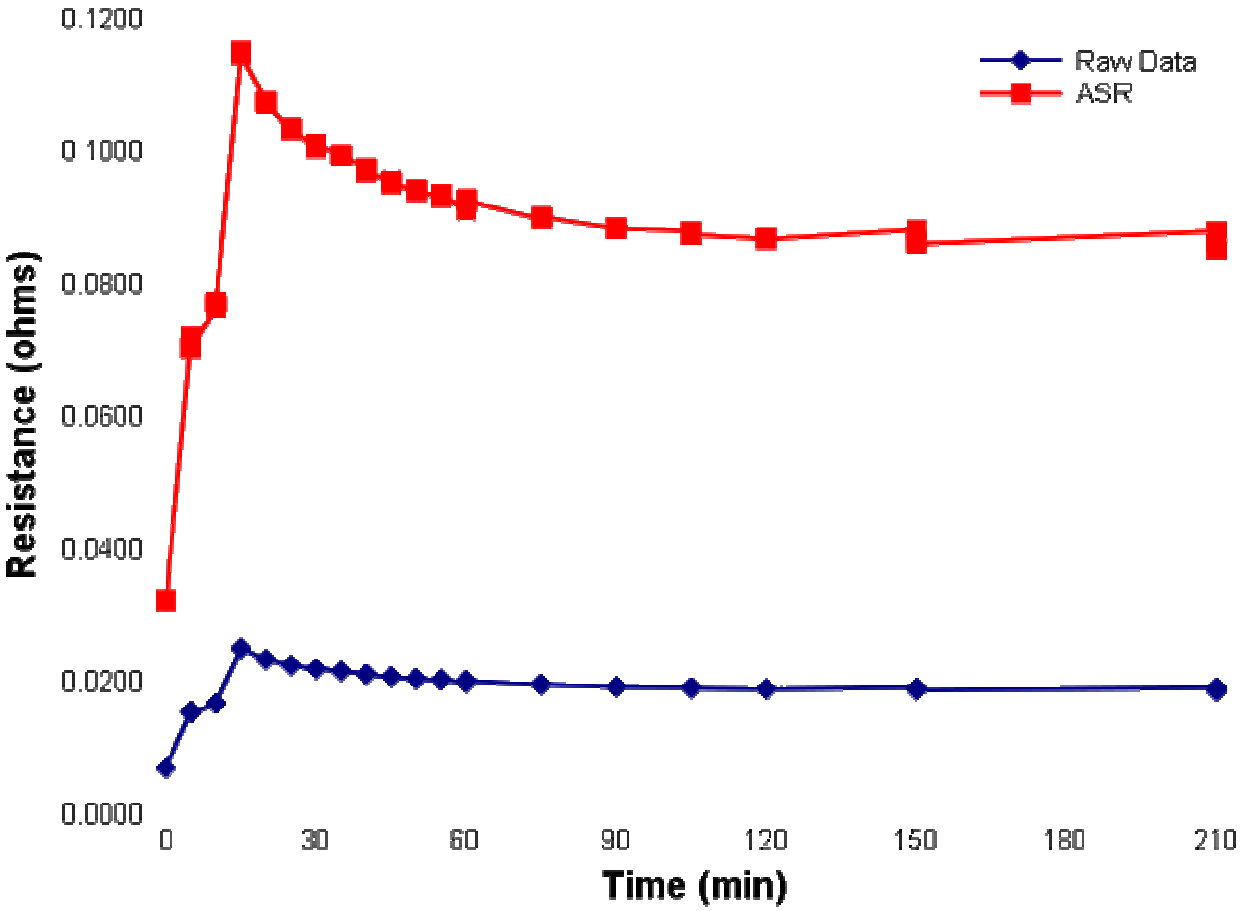

Figure 5-3 Plot of resistance vs. time for pure Ag at 800°C using the contact paste method

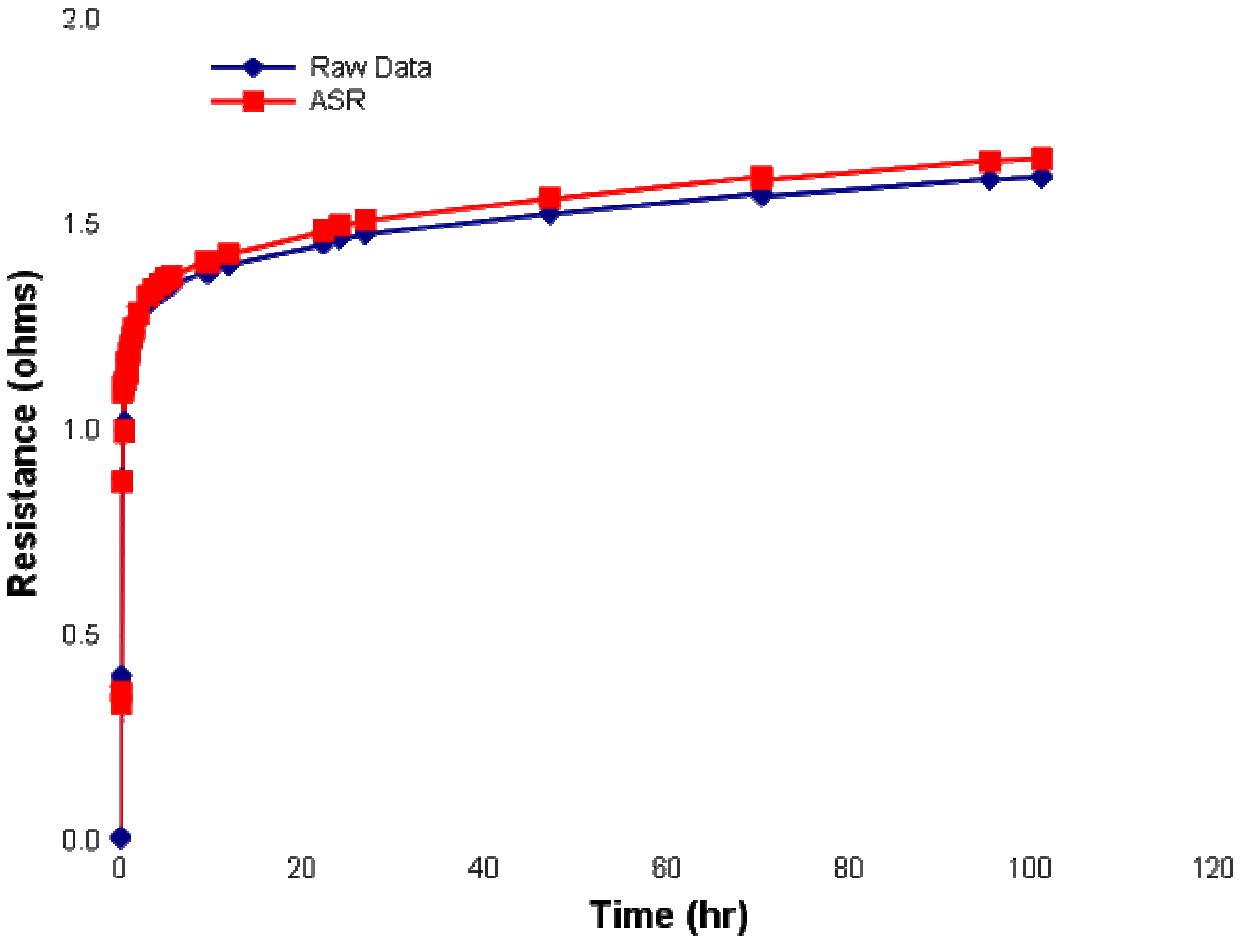

Figure 5-4 Plot of resistance vs. time for Crofer exposed at 800°C using the contact paste method

5.1.3 Short Time Testing - Crofer 22APU

As mentioned in the background section, short time experiments must be run on Crofer 22APU to gain insight regarding the mechanism and kinetics of manganese chromate formation. Samples were exposed for 24 hours, 1 hour, and 30 minutes in dry air at 800°C. X-Ray diffraction indicates that $MnCr_2O_4$ is present on the surface of the sample after 30 minutes (Figure 5-5). Observations of the surfaces using the SEM show Mn rich particles decorating what appear to be the alloy grain boundaries in the cases of the two shortest time samples, as shown in Figure 5-6a&b. Kurokowa et al[37] observed this behavior in dual atmosphere tests on T430 stainless steel. EDS results also show an increased concentration of Mn everywhere on the surface. Figure 5-6c shows a cross sectional image of the 1 hour sample. The image shows a continuous chromia scale with the same particles of $MnCr_2O_4$ that were seen on the surface and by XRD. It is important to note that the there is no visible continuous layer of $MnCr_2O_4$ at this point. After 16 hours (Figure 5-6d.), The manganese chromate particles are everywhere on the surface, with those decorating the alloy grain boundaries still visible. Figure 5-6e shows the surface of the sample exposed for 24 hours. The bulk of this surface appears to be rather uniform. The particles seen on the surface of the two previous samples are not present here. EDS analysis shows a consistent amount of Mn across the entire surface. Given all of these results, it appears that there are significant contributions from both bulk and grain boundary diffusion in the alloy to supply Mn to the oxide, with the grain boundary diffusion being only slightly more prevalent. The alloy grain boundary/oxide interface therefore should have a larger local Mn content. Given that there would be a larger Mn concentration gradient between the oxide interfaces at those locations, Mn will diffuse more rapidly there and appear on the surface above those locations first.

Experiments to fully understand this behavior would require a significant amount of work, and as such, will not be examined in detail. From the data that was generated here, Figure 5-7 has been drawn to illustrate a possible scenario for the formation of the outer layer. The illustration is not drawn to scale, as the oxide thickness and Mn concentration profile are greatly exaggerated. The process begins with the sample forming a continuous chromia scale as seen in Figure 5-7a. Mn from the alloy diffuses simultaneously via slow bulk diffusion in the alloy grain centers and rapidly at alloy grain boundaries. Due to the fact that the grain boundary diffusion is occurring at a faster rate, the local concentration of Mn around the alloy grain boundary/oxide interface is larger than in the bulk. The higher concentration of Mn leads to an larger concentration (or chemical potential) gradient, which also leads to more rapid diffusion through the oxide. A Mn diffusion front is shown in Figures 5-7b-i as a white line progressing through the oxide. In Figure 5-7f, the front above the alloy grain boundaries has reached the surface and there Mn reacts with the oxygen and chromium. This yields a particle of $MnCr_2O_4$ directly above the alloy grain boundary. If the 3-D nature of the grain boundary is considered, the resultant surface morphology is identical to that which is observed. Figures 5-7g-i then show a lateral growth of the chromate layer as the rest of the front reaches the outer surface. The formation is then complete in Figure 5-7j, where the layer has become continuous.

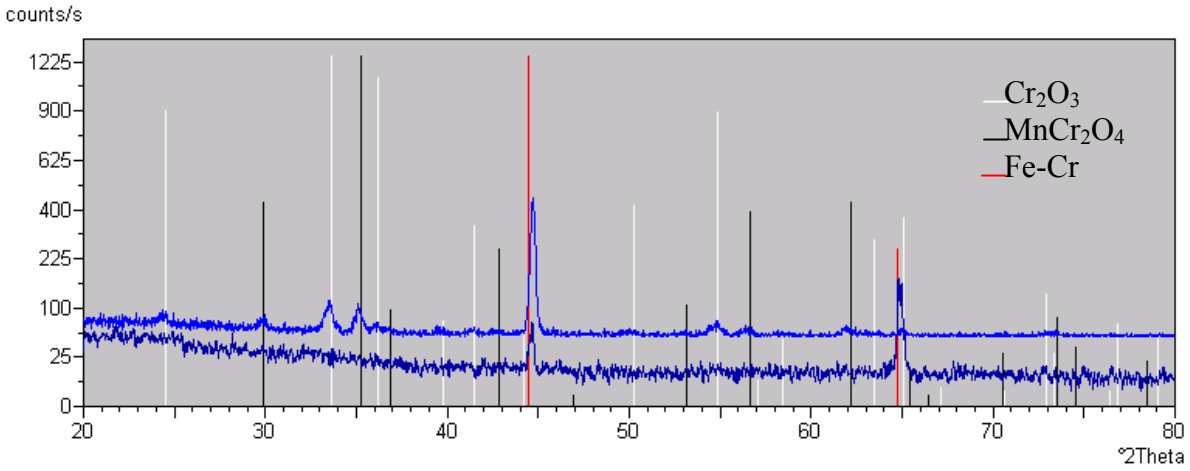

Figure 5-5 XRD patterns (dark blue = θ – 2θ scan, light blue = 1° fixed incident scan) from Crofer 22 APU exposed for 30 minutes at 800°C in dry air

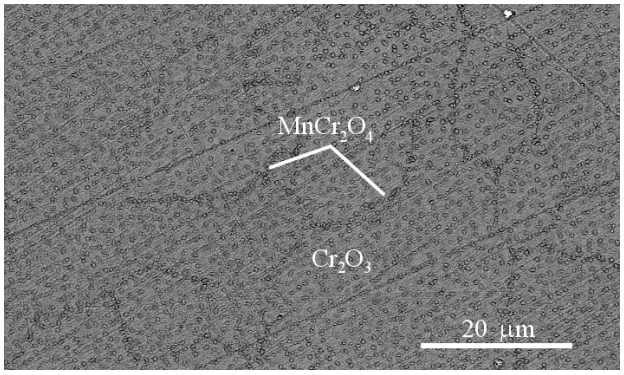

(a.)

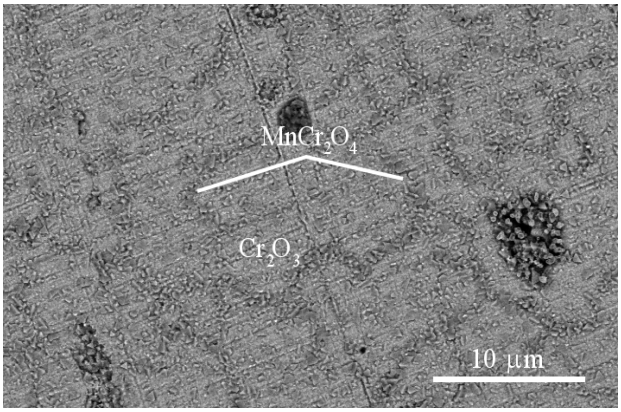

(b.)

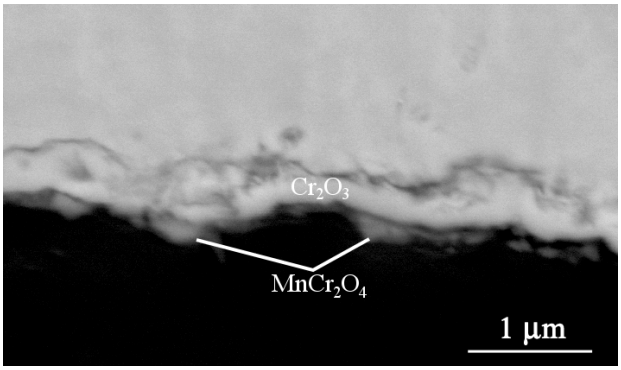

(c.)

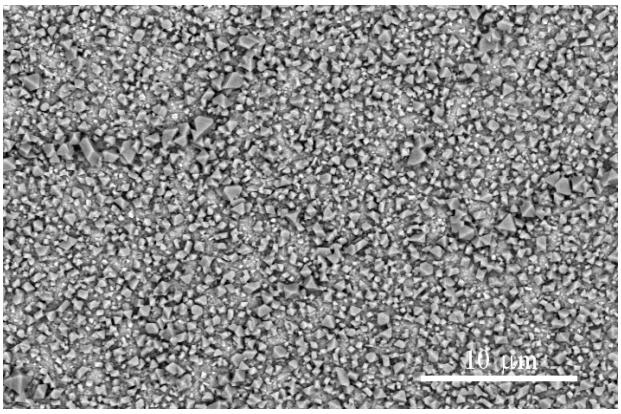

(d.)

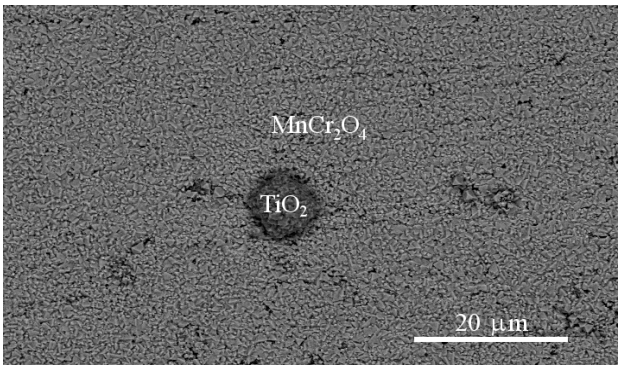

(e.)

Figure 5-6 SEM images of the surface of Crofer22APU exposed at 800°C in dry air for 30 min (a.), 1 hr (b.) (sample cross section also shown in c.), 16 hr (d.) and 24 hr (e.).

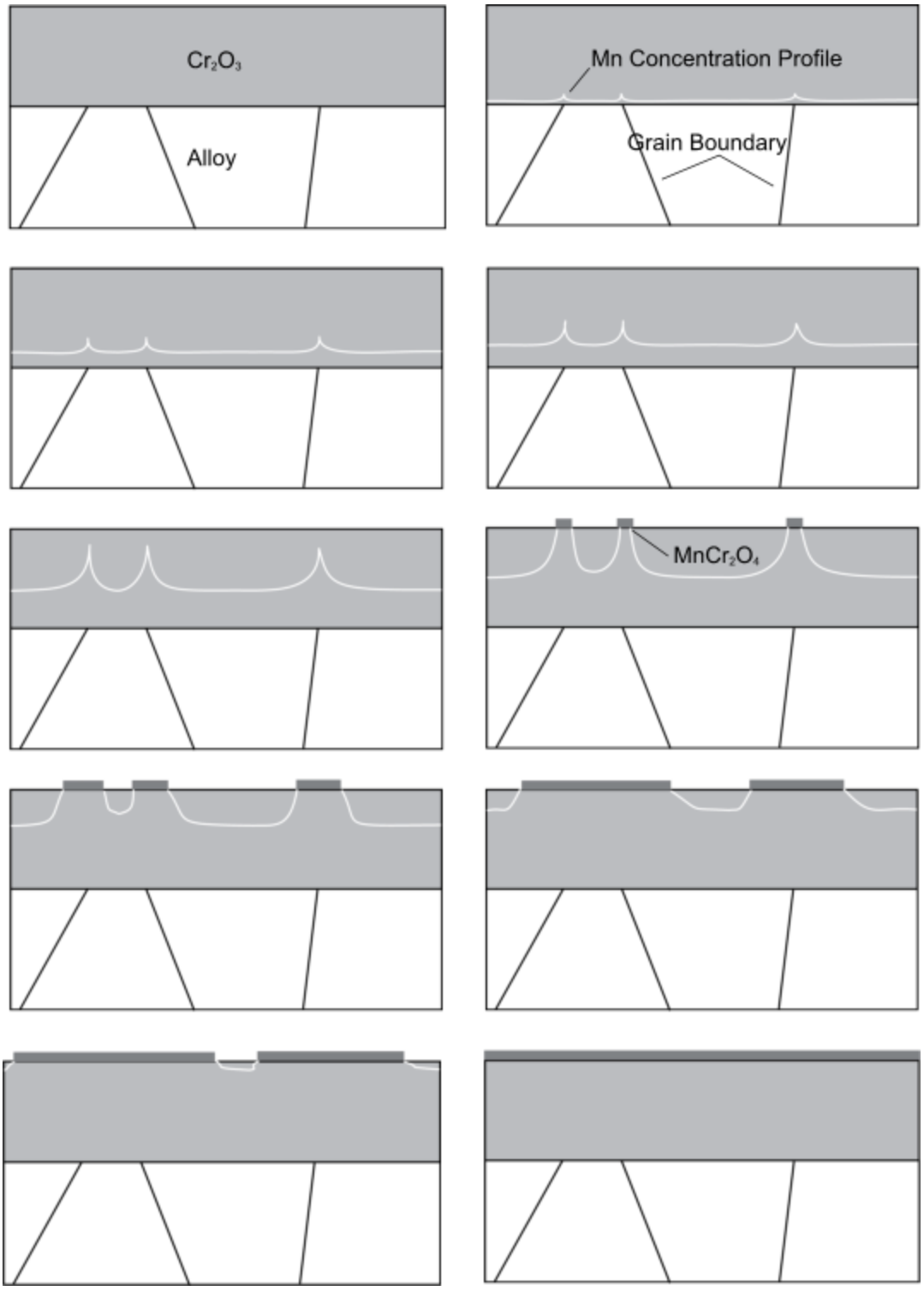

Figure 5-7 Diagram showing a possible mechanism for the development of the $MnCr_2O_4$ overlayer on Crofer.

5.2 Fe-Cr-Ti ALLOYS

The purpose of the high Ti ferritic alloys is to reduce the vaporization in a manner similar to that which occurs in the case Crofer 22APU. Unlike Crofer, these alloys are experimental and therefore their effectiveness at reducing vaporization is not well established. While the literature suggests that TiO_2 will form on the surface, those alloys did not contain nearly as much Ti as the alloys tested here. It was not previously known if the the system would form an overlayer or if all the oxidation of Ti would occur internally under the chromia scale.

5.2.1 Testing 900°C

The exposure under which IN738 was observed to form the titania layer was at 900°C. As a preliminary test of the ability of the new ferritic alloys to form the overlayer, they were exposed at 900°C for 96 hrs in dry air, although for fuel cell purposes, this is an accelerated test. The intention of this test was to show that TiO_2 does form on the surface of the Cr_2O_3 scale. XRD confirmed that Cr_2O_3 was present in all samples and rutile was present in all of the Ti containing alloys (Figure 5-8). These were the only oxides present. Observations of the surfaces using SEM show that there is an increasing amount of TiO_2 on the surface as the Ti content increases in the alloy up to the 2.78 wt% Ti alloy. Given the results of Issartel[42], this is the expected behavior. This can also be seen in Figure 5-9. Accompanying this increase of TiO_2 is a decrease of chromia "blades" and mounds protruding from the scale. The 2.78 wt% alloy has a uniform and continuous titania layer on the surface (Figure 5-9d) with a single spall induced during handling. The 3.98 wt% alloy displayed areas of continuous TiO_2 (Figure 5-9j), but also more Cr_2O_3 than the 2.78 % Ti alloy. There were

0%

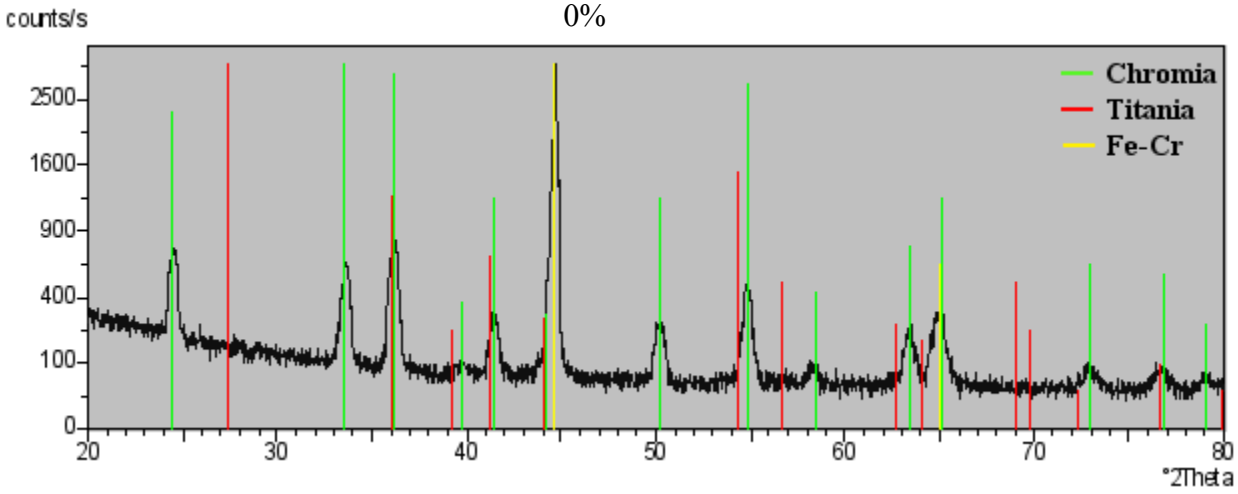
counts/s
2500
1600
900
400
100
0
20
30
40
50
60
70
80
°2Theta
Chromia
Titania
Fe-Cr

1%

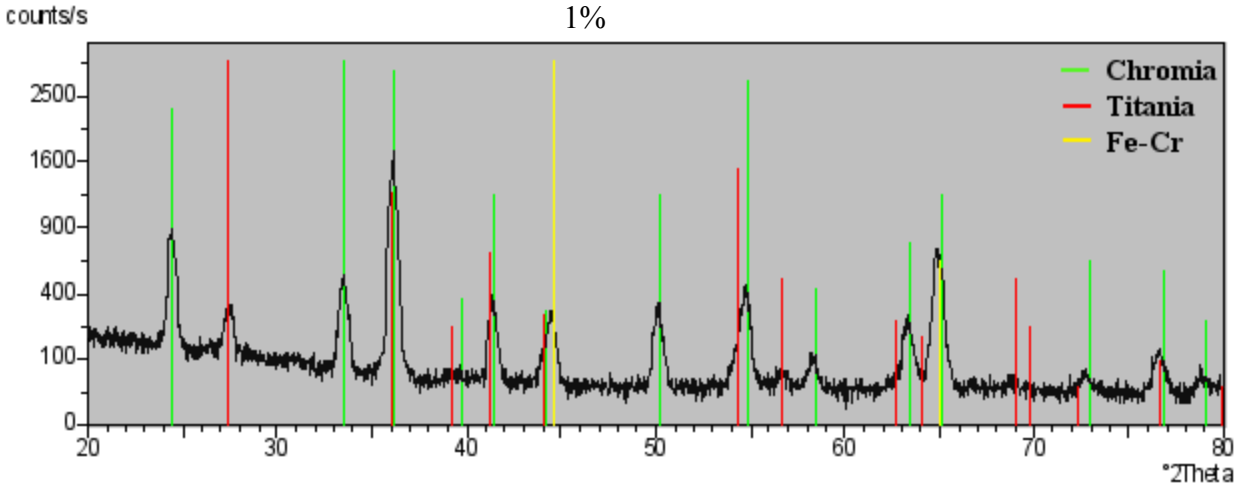
counts/s
2500
1600
900
400
100
0
20
30
40
50
60
70
80
°2Theta
Chromia
Titania
Fe-Cr

2%

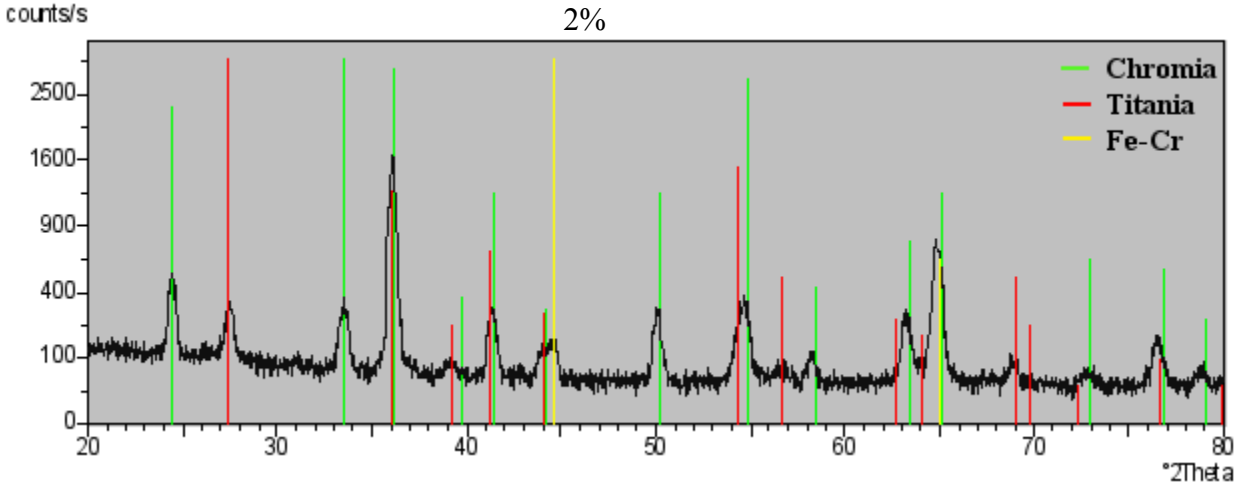
counts/s
2500
1600
900
400
100
0
20
30
40
50
60
70
80
°2Theta
Chromia
Titania
Fe-Cr

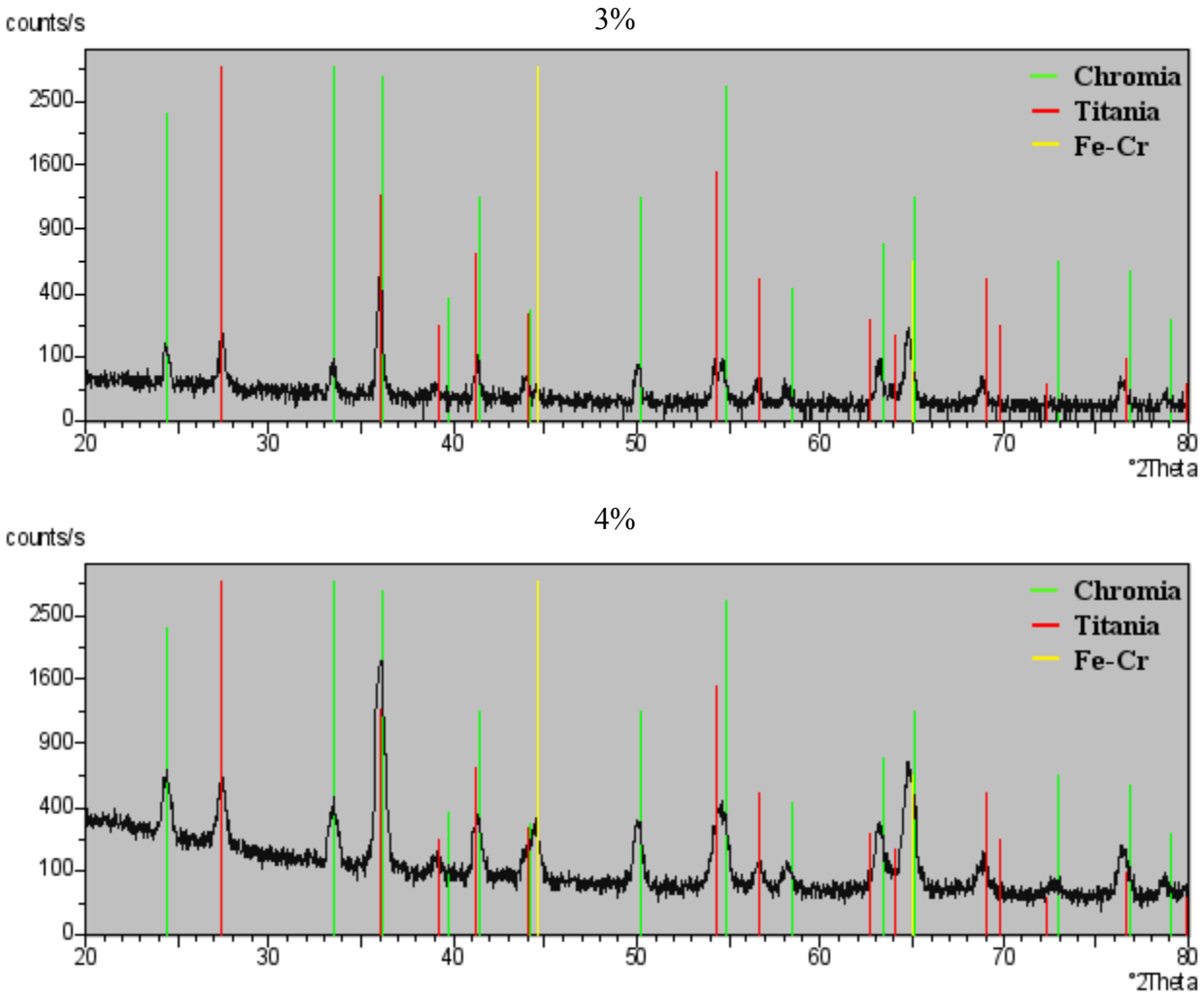

Figure 5-8 XRD patterns of Fe-Cr-Ti alloys exposed at 900°C for 100 hours in dry air

also several areas where the oxide appears to have spalled (Figure 5-10b). Internal oxidation of Ti can be seen in the spalled areas of this alloy and a spall induced during handling of the 2.78 wt% alloy (Figure 5-9h).

In cross section, the baseline alloy (Figure 5-9a) shows only chromia that ranges from 2 to 5 μm in thickness and no internal oxidation. Three trends can be seen in Figures 5-9c, e, g & i as the amount of Ti in the alloy is increased. First, there is increasingly more continuous TiO_2 layer on the surface of the protective Cr_2O_3. It is obvious that if the Ti content is increased, the chance for transient oxidation of Ti is increased and if the Ti does in fact continuously diffuse through the chromia, the rate at which a layer can form is dependent on Ti content as well. Second, there is also more extensive internal oxidation of Ti. XRD shows the internal oxides consist of Ti_2O_3 and Ti_3O_5, but there is a large series of Ti_xO_y oxides that may form. This internal oxidation is nearly continuous in the alloys with the two highest Ti contents (Figure 5-9g & i) and has left a metal layer above it. The morphology of this internal zone is virtually identical to that observed by Hammer[10] for the alloy AL453, which forms internal alumina. The metal layer in the case of AL453 is proposed to be formed by an extrusion process. The formation of the internal oxide involves a volume increase. Since this occurs at temperature, the metal is able to flow around the oxides to relieve the stresses generated. This may lead to some problems if the internal oxide becomes continuous. The main substrate could be cut off by the internal oxide, thus preventing Cr and Ti from being supplied to maintain the outer oxide. Eventually the extruded metal layer will be depleted of those elements and extremely detrimental iron oxides may form. On a positive note, the internal Ti oxides will act as a n type conductor,

as the P_{O2} is extremely low. Finally, the Cr_2O_3 layer is also increasing in thickness with increasing Ti content. This could be the result of Ti doping and/or a vast reduction in chromia vaporization.

There were also defects in some of the material and can be seen in Figure 5-10. Figure 5-10a shows an extensive network of TiN that is detrimental to the mechanical and oxidation behavior of this alloy. If the oxide thickness and morphology of Figure 5-9i and Figure 5-10a are compared, a few discrepancies are noticed. First, the oxide is much thinner that forms above a region with large amount of nitrides. Second, the oxide over that region has no noticeable rutile overlayer. Finally, the amount of internal oxidation of Ti is greatly reduced. Apparently, Ti in the these localized regions is being tied up in the TiN. This prevents most of the Ti from migrating into the oxide, which slows the growth rate and retards the formation of the outer protective layer. This means that vaporization could readily occur here. It is not clear where the nitrides originate. It is possible that nitrogen is rapidly diffusing through the oxides. This has been shown to occur in the works of Grabke, et al[55], Giggins and Pettit[56], and Pettit, et al[57]. The latter of these describes a very interesting experiment where samples of pure Cr were exposed in pure oxygen and air. The sample exposed in pure oxygen was then exposed to air. The cross sections show that the microstructures of both samples were nearly identical with nitrides forming below the oxide. This is due to the fact that there are both oxygen and nitrogen gradients present. Typically, the more stable oxide forms over the nitride. Eventually the dissociation pressure of the oxide is reached at the oxide metal interface. With the reduced levels of oxygen in the metal and a large amount of nitrogen with respect to oxygen, nitrides can then form. An alternative to this is that the localized nature of the TiN regions lends to the idea that TiN particle, which readily form in Ti bearing steels due to processing, could have been

crushed and redistributed during rolling. The stability and density of the oxides should prevent the nitrogen from escaping and will actually push the nitridation zone deeper into the alloy as the nitrides are oxidized, leaving both an oxide and nitride front. A nitride front is very clearly observed in Figure 5-10a. The dark particles deep in the alloy in Figure 5-11 are also TiN that are present in the starting alloy.

These alloys in the as processed condition also consist of two phases, one being Ti rich. This second phase could be related to the "dark areas" in the substrate noted by Issartel[42]. There appears to be a depletion zone where the alloy is single phase after exposure (Figure 5-11). A sample was oxidized for a similar time, the oxide was polished off, and the surface was analyzed using XRD. Peaks matching bcc Fe (or ferrite) had very high intensity and are most likely the dark phase in Figure 5-11. Two small peaks were also observed and they match two of the three peaks for FeTi. While it is likely possible that the FeTi phase forms for kinetic reasons, the Fe-Ti-Cr phase diagram (Figure 5-12) indicates that the phase should consist of a complex Fe-Cr-Ti compound that was not labeled on the diagram. The presence of the second phase does have some major consequences. The most prevalent of these is the effect of Ti content on the mechanical properties that was mentioned previously. Higher Ti concentrations should lead to more of the second phase forming, which most likely is the reason why the 4% Ti alloy has shown virtually zero elongation and high yield strength and UTS. Any design based on the mechanical properties could be compromised as the alloy is depleted and the second phase is dissolved. Another possible result of the second phase could be a relationship between the location of the Ti rich phase and the tendency of the internal oxide to form fingers. Morphologies similar to that allow for rapid transport of oxygen deep into the alloy and it is typically considered detrimental.

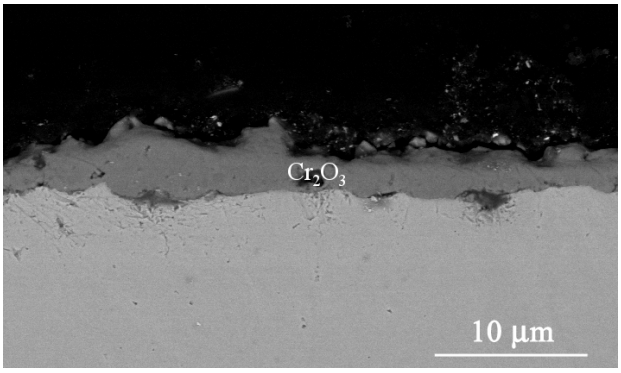
Cr_2O_3
10 µm

(a.)

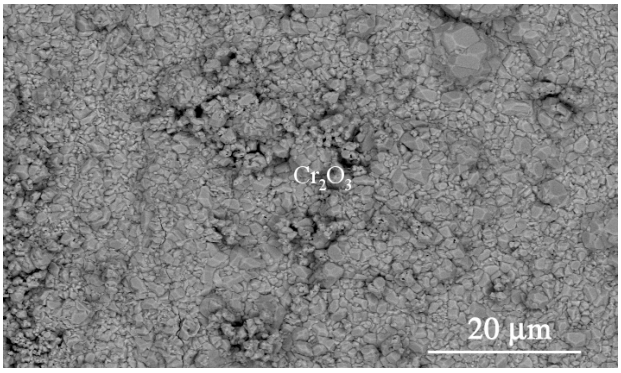
Cr_2O_3
20 µm

(b.)

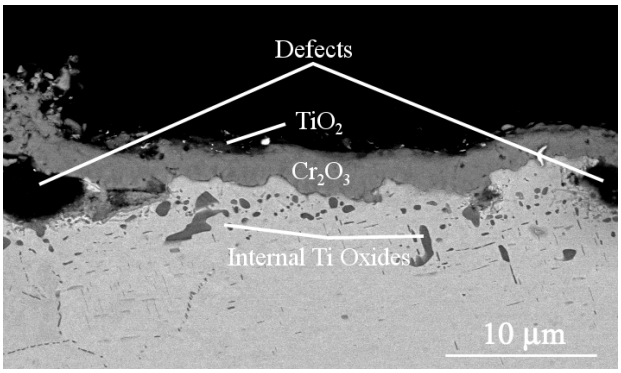
Defects
TiO_2
Cr_2O_3
Internal Ti Oxides
10 µm

(c.)

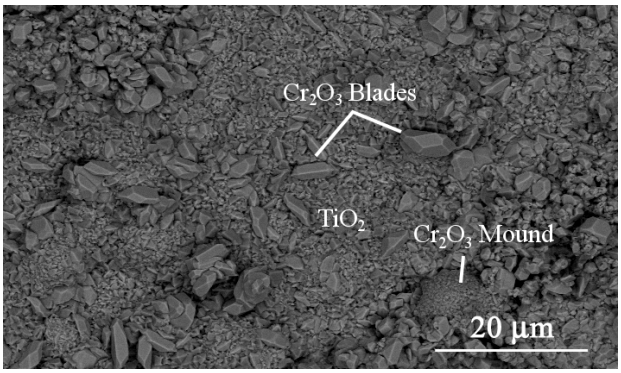
Cr_2O_3 Blades
TiO_2
Cr_2O_3 Mound
20 µm

(d.)

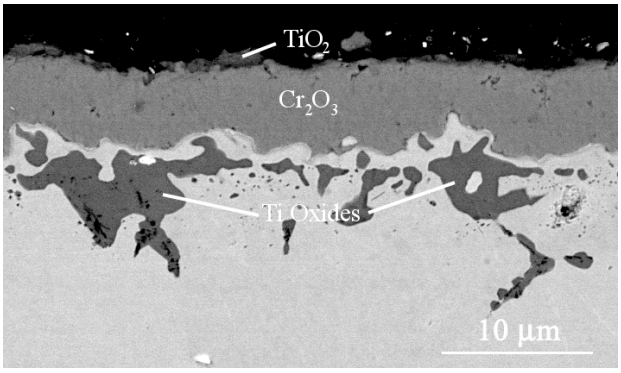
TiO_2
Cr_2O_3
Ti Oxides
10 µm

(e.)

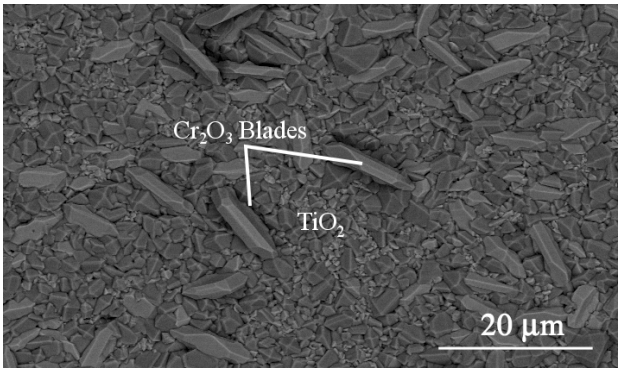
Cr_2O_3 Blades
TiO_2
20 µm

(f.)

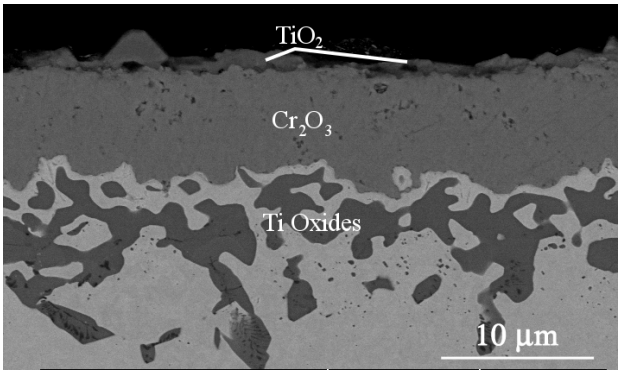

(g.)

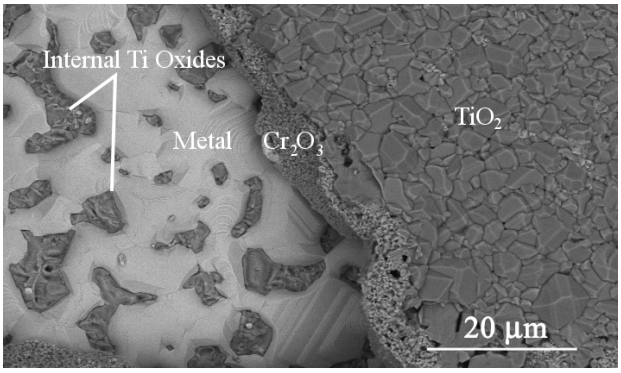

(h.)

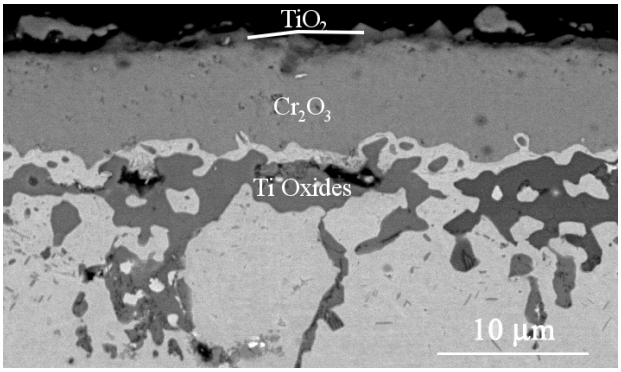

(i.)

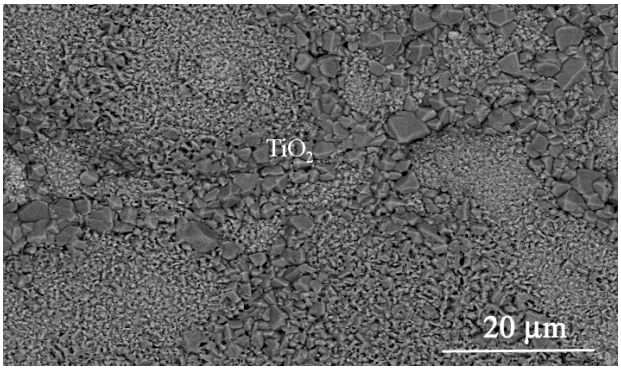

(j.)

Figure 5-9 Surface and cross – sectional SEM micrographs of alloys exposed for 96 hrs at 900°C in dry air containing 0.004% (a&b), 0.84% (c&d), 1.65% (e&f), 2.78% (g&h), and 3.98% (i&j) titanium

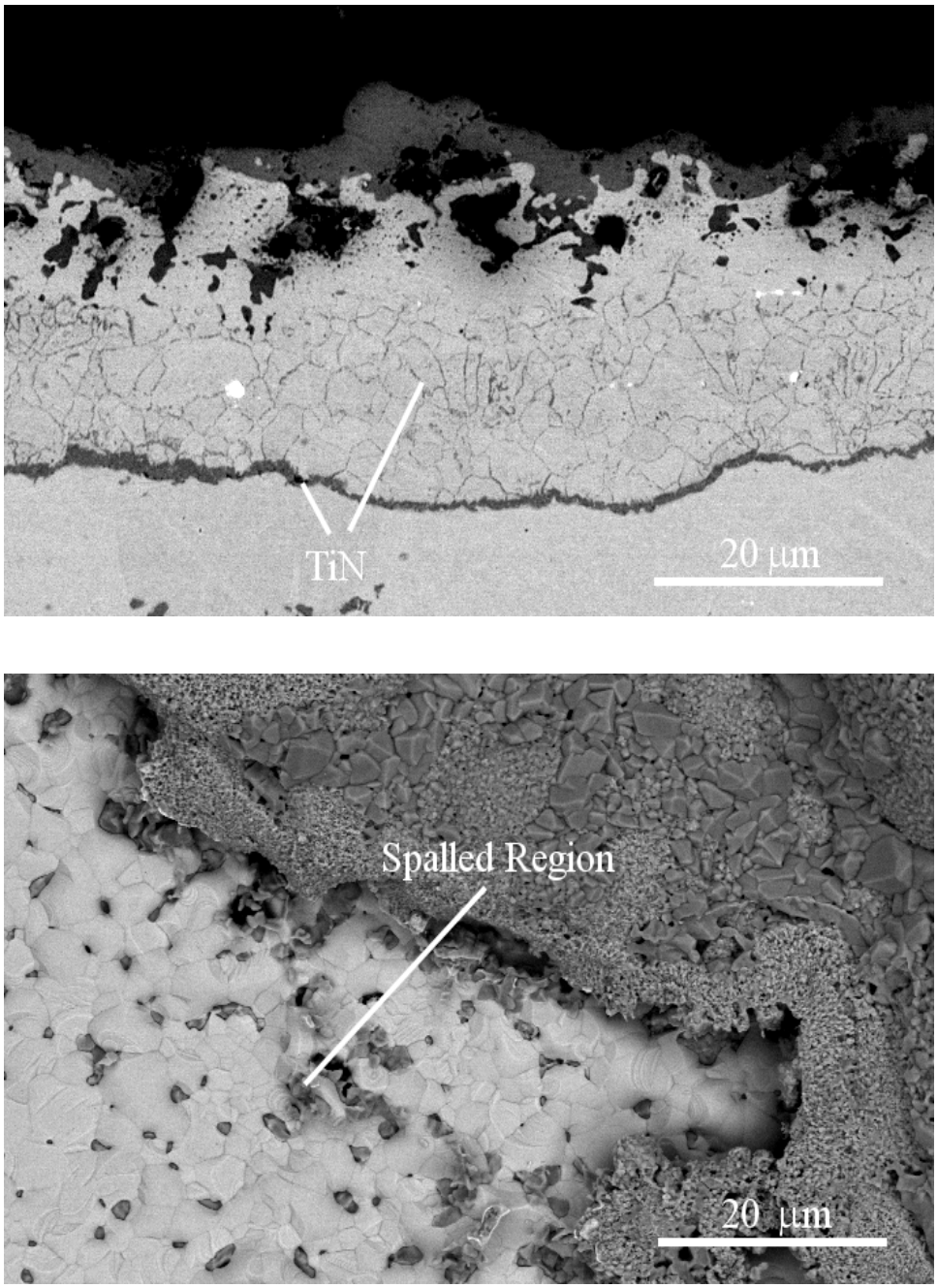

Figure 5-10 SEM cross-sectional micrograph of Fe-22Cr-3.98Ti exposed for 96 hrs at 900^{o}C in dry air showing internal TiN (a.) and surface micrograph showing spalling (b.).

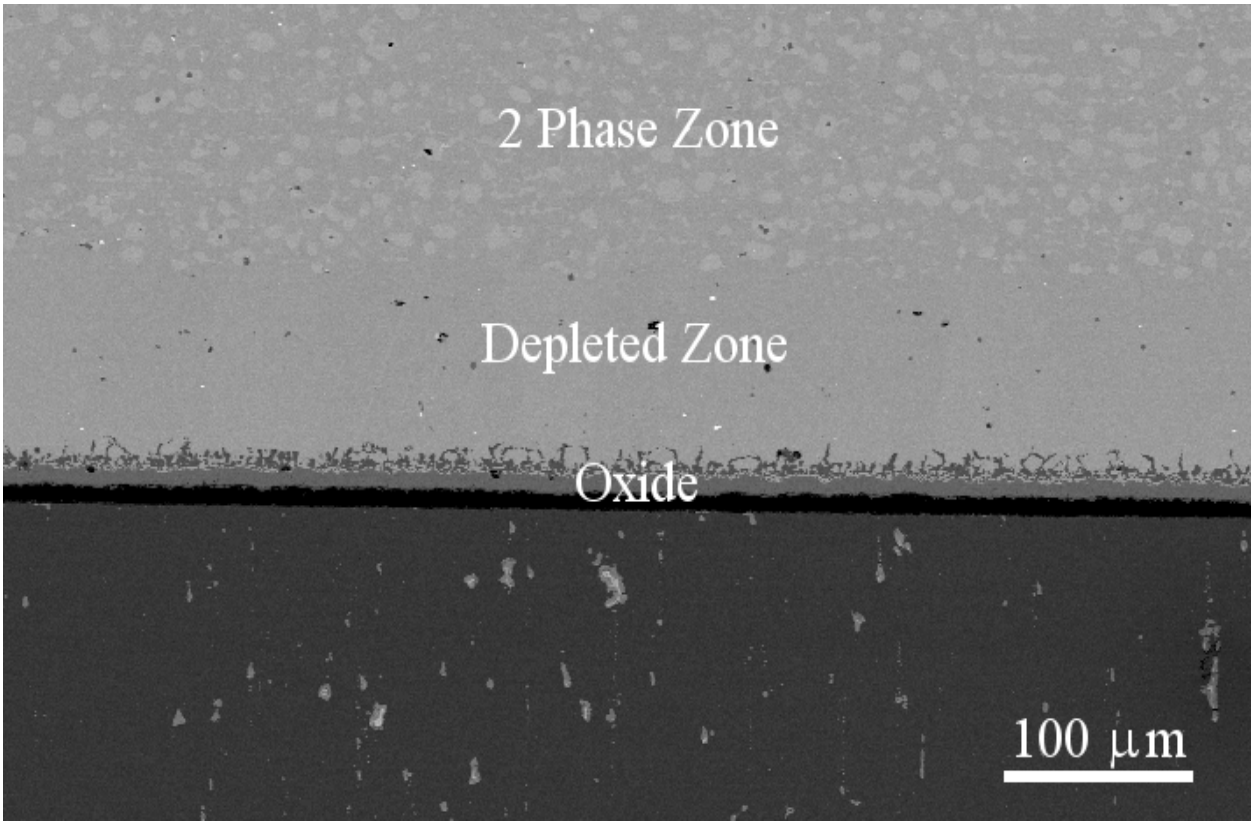

Figure 5-11 SEM micrograph of a sample containing 2.78% Ti and exposed for 96 hrs at 900^{o}C in dry air showing a two phase structure in the substrate with an apparent depletion zone.

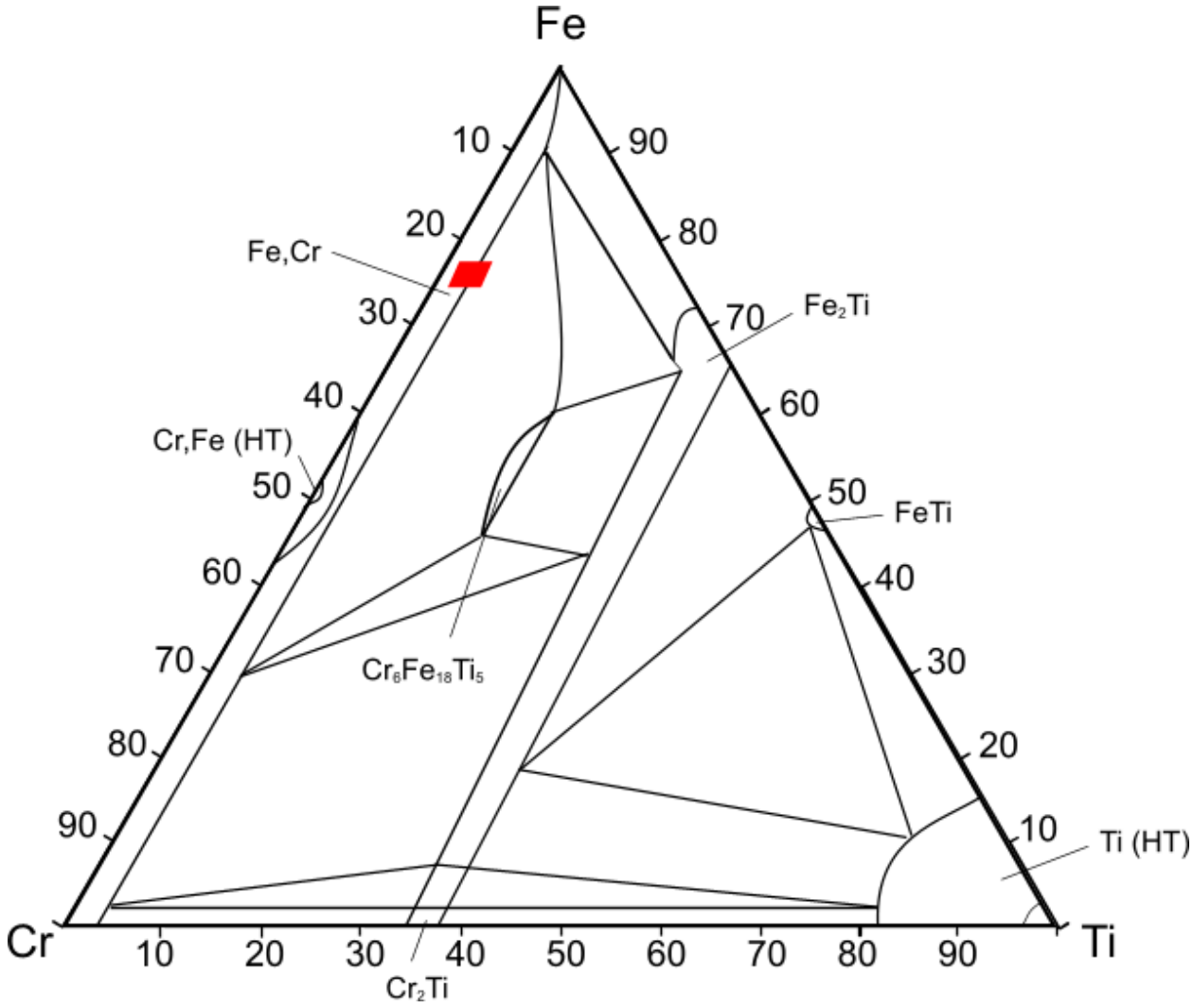

Figure 5-12 Fe-Cr-Ti phase diagram at 800°C[60]. The red area represents the compositions of the Fe-Cr-Ti alloys in this study.

5.2.1.1 TGA Testing – 900°C: To show that the formation of the TiO_2 overlayer does in fact reduce the rate at which the volatile chromia species forms, TGA tests have been performed at 900°C. Tests were performed in dry and wet air for each alloy in the series as well as E-Brite and Crofer 22APU. Table 5-1 shows the parabolic rate constant measured for each alloy for comparisons to the values mentioned in the background. E-Brite, Crofer, and the baseline alloy are on par with the literature values. The same trend of increasing k_p value with increasing Ti concentration reported by Issartel[42] is observed here. The value reported for the highest Ti content alloy is virtually identical to that of the 1% Ti alloy here. Considering the increases in growth rate with Ti content and temperature, the values calculated here are similar to those measured in this work. The alloys and exposure temperatures in Sigler's experiments[43] are more closely related to those measured in this work. The k_p values are extremely close for the 0.46%Ti alloy used in that work and the 0.84% Ti alloy here.

Figure 5-13 shows the mass change vs. time plots for the results. As with the 100 hour tests at 900°C, the chromia appears to grow faster with increasing Ti content (higher mass gains in Figure 5-13) in dry air. A significant portion of this large mass gain is due to the internal oxidation. This is clearly illustrated in Figure 5-17, where the internal oxide is nearly as thick as the external oxide. A difference between the dry and wet exposures is also observed. The data shows lower weight gains in the wet air exposures. This would imply that some amount of vaporization is occurring since the vaporization occurs more rapidly in wet atmospheres.

Table 5-1 Parabolic growth rate constant, $k_p(g^2/cm^4s)$for alloys tested at 900°C

Alloys	Dry	Wet
E-Brite	3.70E−13	1.31E-013
Crofer	5.71E−13	2.92E−13
Fe-22Cr	1.93E−12	1.53E−13
Fe-22Cr-1Ti	3.39E−12	1.86E−12
Fe-22Cr-2Ti	9.72E−12	4.41E−12
Fe-22Cr-3Ti	1.51E−11	1.18E−11
Fe-22Cr-4Ti	1.64E−11	1.12E−11

Figures 5-14 – 19 shows surface SEM micrographs of the samples after exposure in the TGA apparatus. The baseline alloy (Figure 5-14) formed a pure chromia scale in both atmospheres. Comparing the scale thicknesses, the scale in the dry condition is thicker than that for the wet exposure. The is due to the enhanced vaporization when the hydrated chromia vapor is able to form. All samples that have Ti additions (Figures 5-15 – 18) show large grains of TiO_2 on the surface along with some smaller Cr_2O_3 particles (Note: The voids in some cross-sections are due to loss of internal oxides during metallographic preparation). Given this, it is not entirely surprising that the wet exposures show signs of vaporization, since there is still chromia on the surface. If this is, in fact ,the case, then the wet air samples should show less chromia on the surface than the dry air samples. It appears that this is correct when the surfaces are compared. The cross-sections show that the TiO_2 overlayer does not undercut any protruding chromia to form a fully continuous layer. The chromia that is left on the surface is then free to vaporize until the TiO_2 is able to overgrow the the area in question to seal it. Strangely, it appears that the oxides are thicker on the wet air samples. The only explanations for this are either spallation occurred, the amount of vaporization is enough to counter the increased growth, or the oxide in the wet exposures is much lower in density. Being that there are very few signs of spallation and it is unlikely the density would vary as drastically as required to be plausible, there must be large amounts of vaporization occurring. It is important to note that 900^oC is on the high end of the range where chromia forming alloys are effective in any application, not just those sensitive to the oxide vaporization. The testing at 900^oC are accelerated tests. The 3.98% Ti alloy (Figure 5-18) once again shows regions of TiN formation above which there is no TiO_2 overlayer.

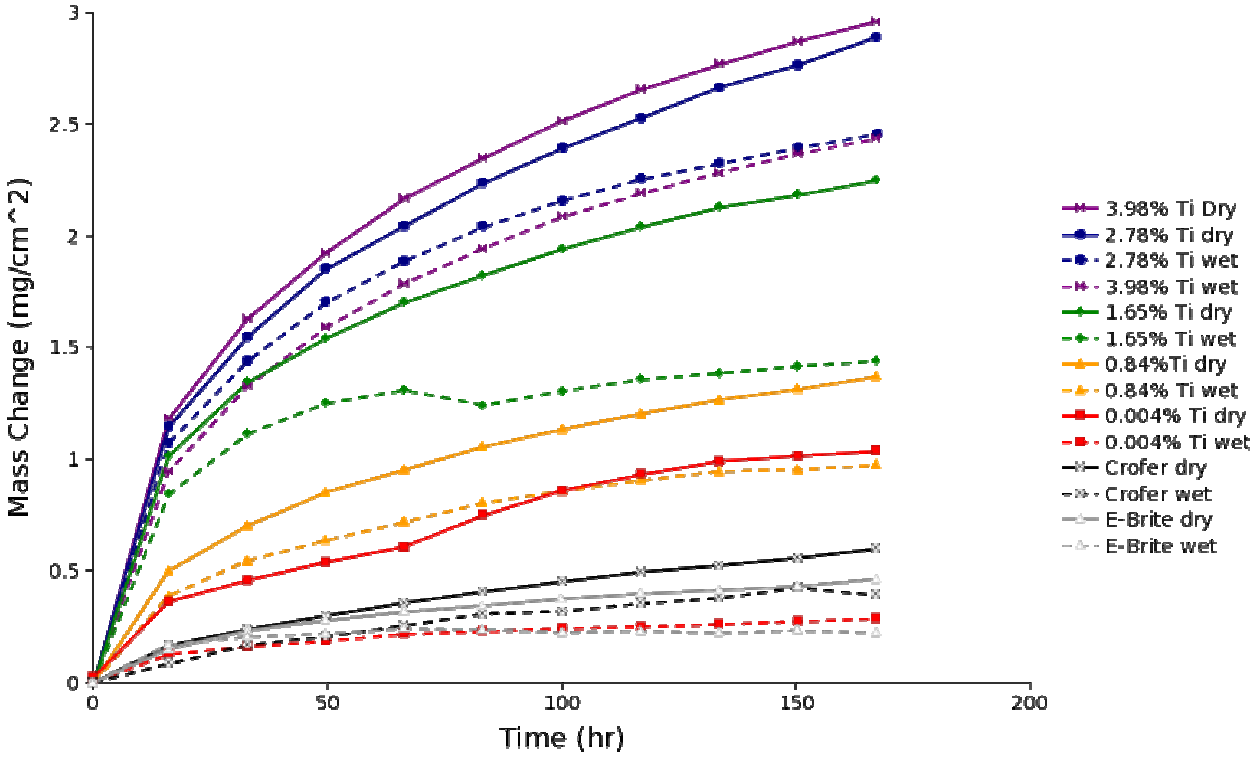

Figure 5-13 Mass change vs. time plots for TGA tests at 900°C

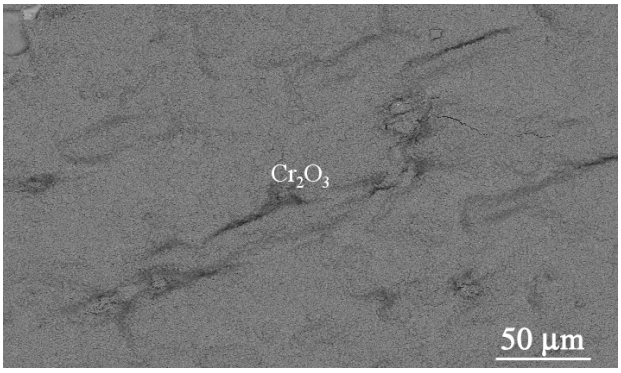

(a.)

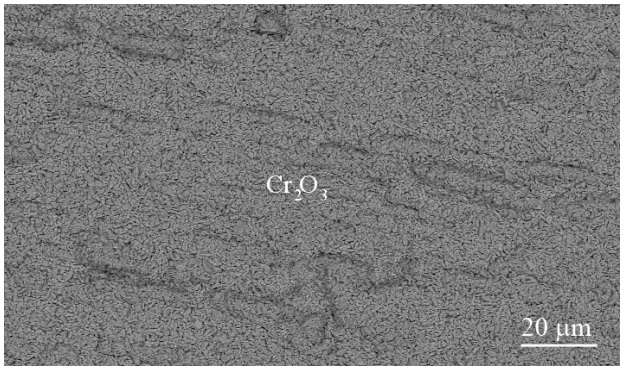

(b.)

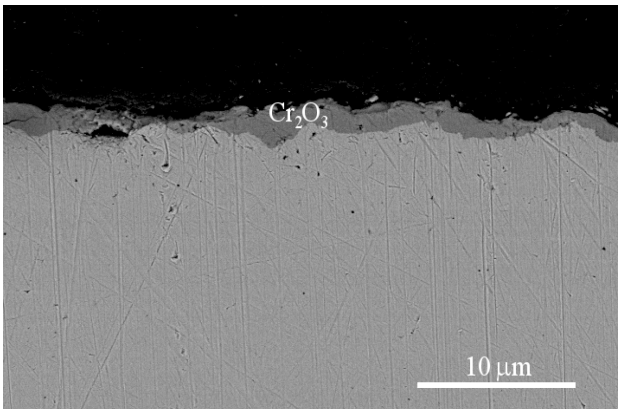

(c.).

Figure 5-14 Surface and cross-sectional micrographs of the baseline alloy after exposure at 900^{o}C in dry (a) and wet (b&c) TGA experiments.

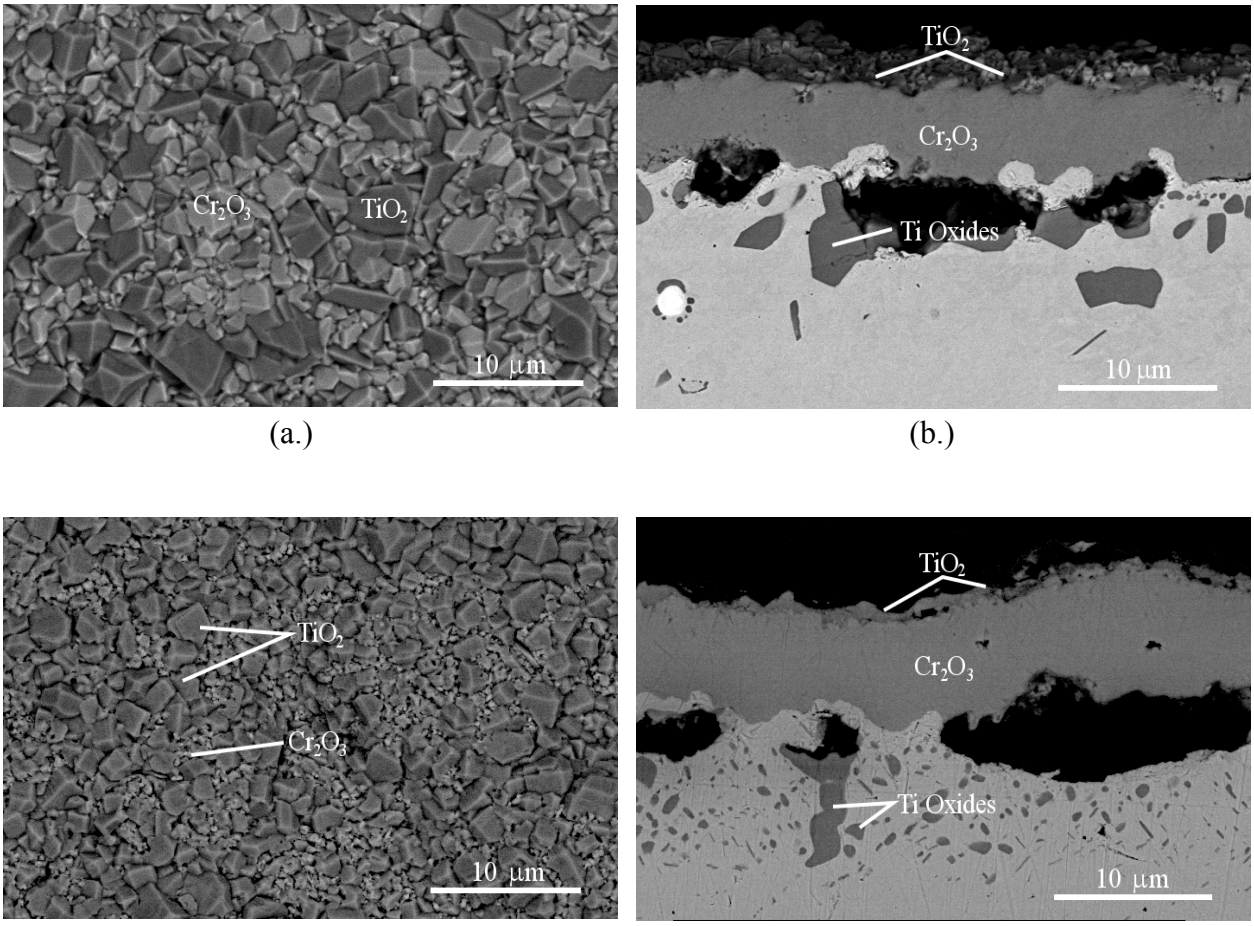

Figure 5-15 Surface and cross-sectional micrographs of the Fe-22Cr-0.84Ti alloy after exposure at 900^{o}C in dry (a&b) and wet (c&d) TGA experiments.

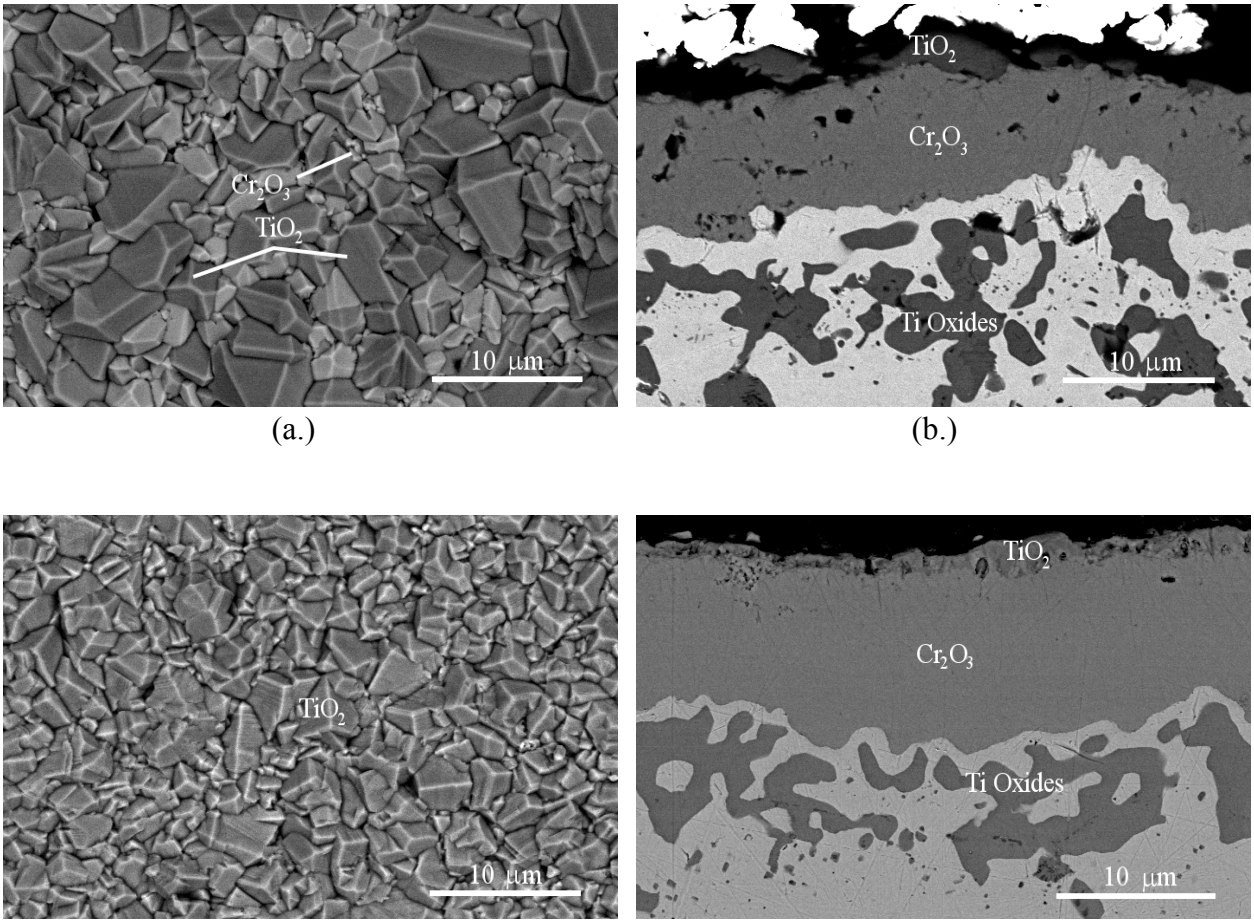

Figure 5-16 Surface and cross-sectional micrographs of the Fe-22Cr-1.65Ti alloy after exposure at 900^{o}C in dry (a&b) and wet (c&d) TGA experiments.

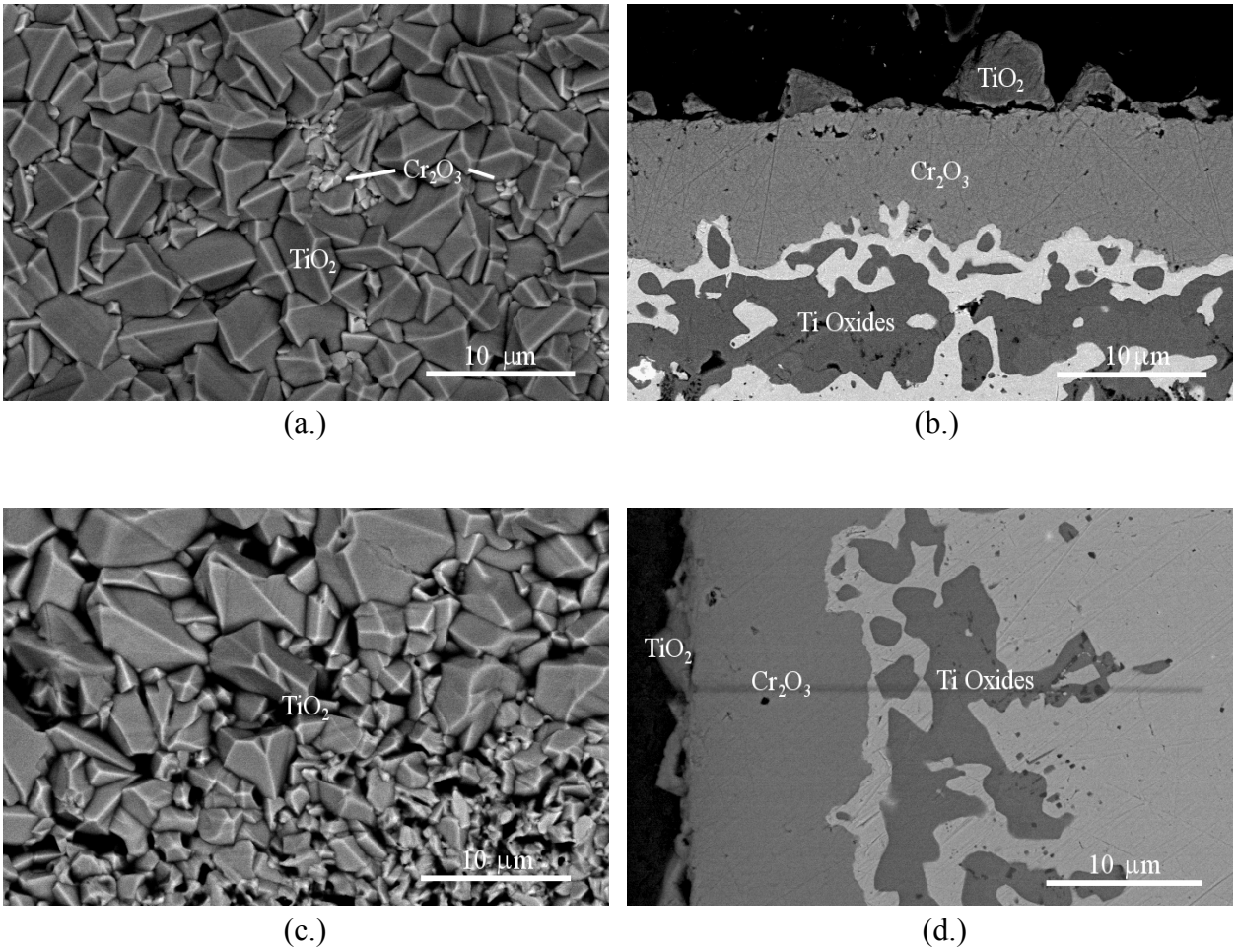

Figure 5-17 Surface and cross-sectional micrographs of the Fe-22Cr-2.78Ti alloy after exposure at 900^{o}C in dry (a&b) and wet (c&d) TGA experiments.

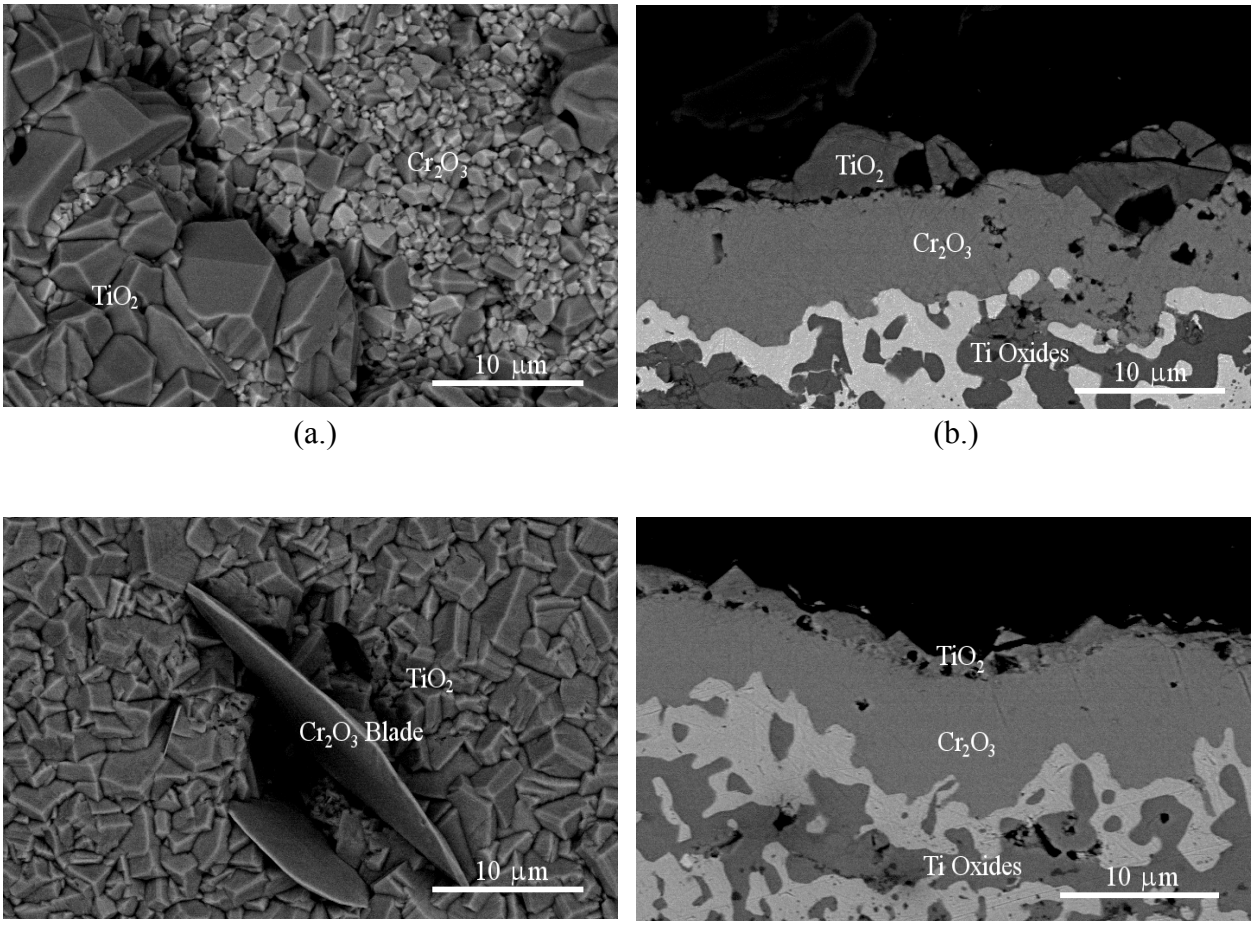

Figure 5-18 Surface and cross-sectional micrographs of the Fe-22Cr-3.98Ti alloy after exposure at 900^{o}C in dry (a&b) and wet (c&d) TGA experiments.

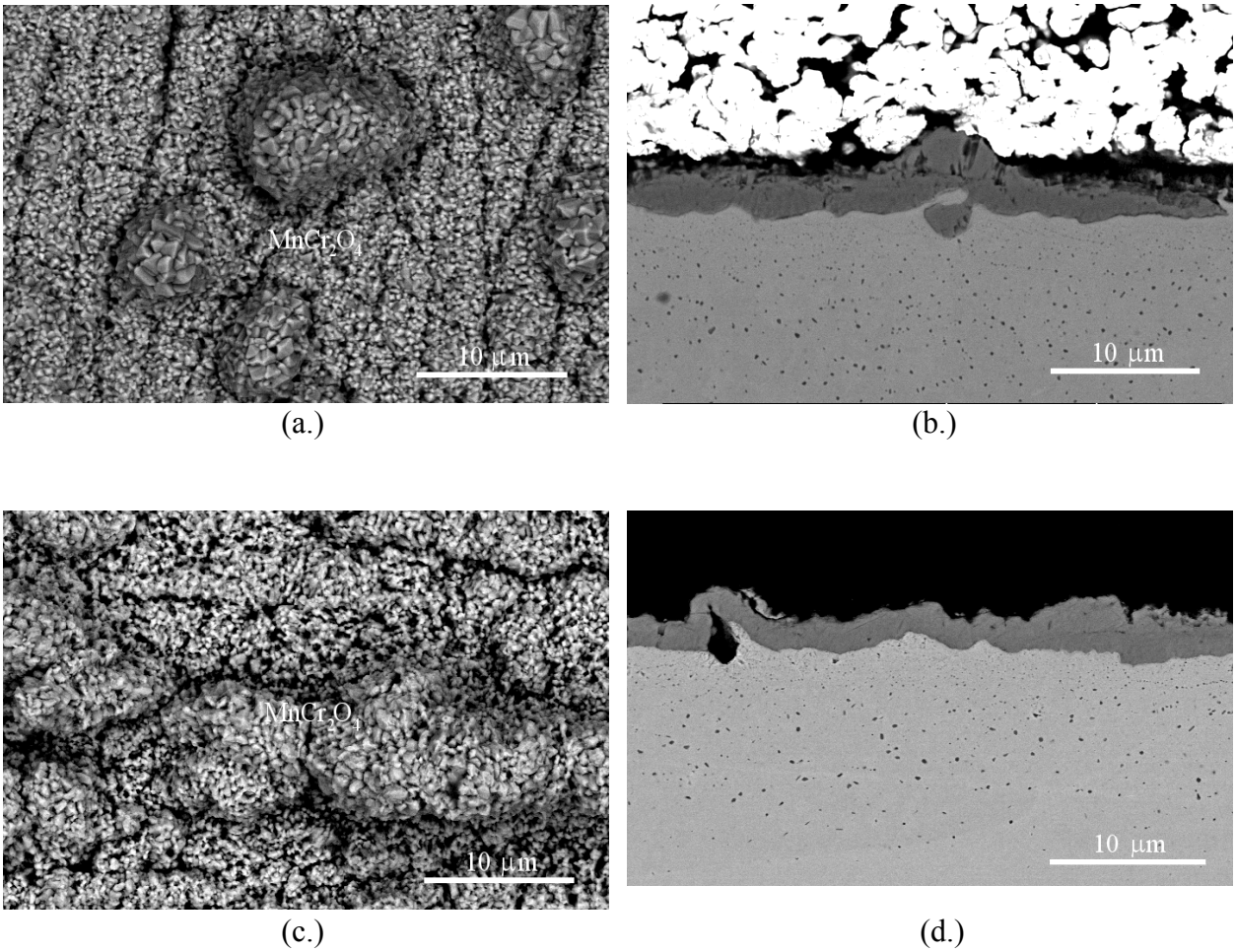

(a.) (b.)

(c.) (d.)

Figure 5-19 Surface and cross-sectional micrographs of Crofer after exposure at 900^{o}C in dry (a&b) and wet (c&d) TGA experiments.

Crofer is shown in Figure 5-19. The surface morphologies appear to be similar in dry and wet air, with the oxide formed in wet air appearing to be less dense or compact. This could be due to some vaporization. In cross-section, the oxides are of similar thickness. This agrees with the relatively small difference between the dry and wet curves in Figure 5-13.

5.2.2 Testing at 800°C

The tests run at 900°C are in reality accelerated tests, as the actual SOFC target temperature is frequently quoted to be 800°C. It is at this lower temperature that the bulk of the work has been done to characterize these alloys. The results presented here are from cyclic, TGA, dual atmosphere, isothermal, ASR, and in cell testing and should provide an adequate understanding of how suitable the Fe-Cr-Ti alloys are for SOFC applications.

5.2.2.1 TGA: The TGA testing results are shown in Figure 5-20 for dry and wet exposures. The data was not drastically different than that at 900°C, although the alloys that were more susceptible to chromia vaporization show larger differences in behavior. Alloys that fit this would be the 0, 1, and 4% Ti alloys. The baseline (0% Ti) alloy actually showed weight loss in less than 25 hours. The reason the 0 and 0.84% Ti alloys show a larger difference can be attributed to the lack or slow growth of the protective overlayer. The initial indication for the reason the 3.98% Ti alloy fits into this group was spallation, as the surface appeared mottled to the naked eye. This was not the case, and will be explained later. In all cases, the wet exposure did show a weight loss compared to dry. In terms of mass change and growth rate, the same trends applied. The amount of oxidation increased with increasing Ti content, and Crofer gained less weight than all of the Ti bearing alloys. Table 5-2 contains the calculated kp values from the TGA data. The values for E-Brite, Crofer, and, to a lesser extent, the 0%Ti alloy are comparable

to those in the literature for similar alloys. The kp value of the 0.84% Ti alloy is once again very close to the value that Sigler[43] reports for Fe-20Cr-0.46Ti. The rest of the values for the Fe-Cr-Ti alloys are larger as is expected.

Table 5-2 Parabolic growth rate constant, k_p(g^2/cm^4s)for alloys tested at 800°C

Alloys	Dry	Wet
E-Brite	5.84E−14	x
Crofer	4.44E−14	2.66E−14
Fe-22Cr	1.58E−13	5.16E−14
Fe-22Cr-1Ti	4.66E−13	1.58E−13
Fe-22Cr-2Ti	8.95E−13	5.97E−13
Fe-22Cr-3Ti	1.46E−12	7.36E−13
Fe-22Cr-4Ti	1.26E−12	4.22E−13

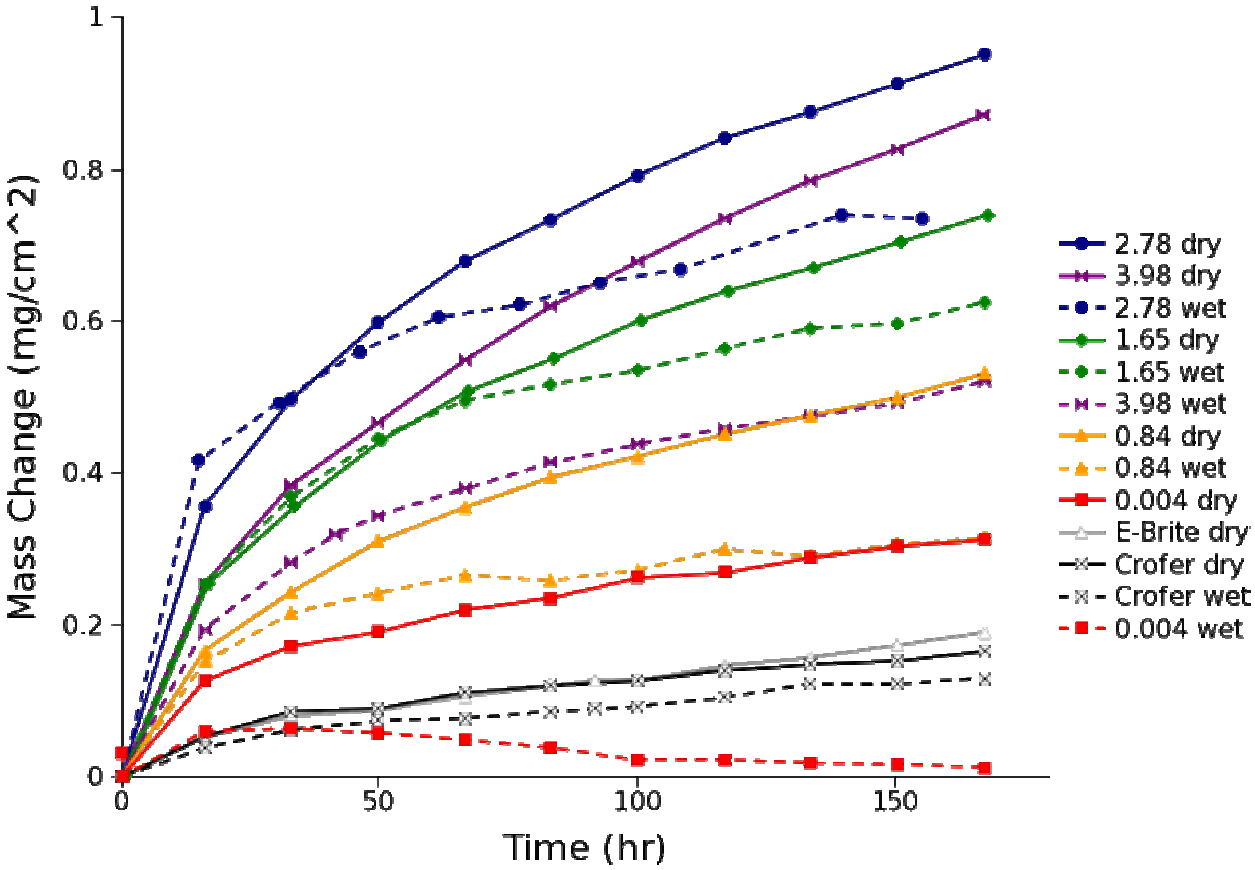

Figure 5-20 Mass change vs. time plots for TGA tests at 800°C

The baseline alloy (Figure 5-21) formed a pure chromia scale in both dry and wet atmospheres. There is a small amount of bare metal visible in the dry air sample, meaning that the interfacial toughness is relatively low for this alloy. This can be explained by the lower Ce and La content in this heat. Comparison of the cross-sections of the dry and wet exposures shows a decrease in the oxide thickness from about 3 μm to less than 1 μm. This is expected, since the data shows that the samples began losing weight during the test. A final feature, which is also seen on many of the other samples exposed in the same exposure conditions, is the presence of very large, faceted chromia plates with very high aspect ratios forming on the surface of the wet air sample.

Figures 5-22 - 25 are samples that contain Ti. Comparison of the surfaces of the dry samples (labeled a in each Figures 5-22 - 25) shows a decrease of the thick chromia blades as they give way to rutile with a blocky morphology with increasing Ti content. The trend reverses itself at the 3.98% alloy (Figure 5-25) where the blades are once again visible. All of the alloys have some TiO_2 on the surface, with the 1.65% (Figure 5-23) and 2.78% (Figure 5-24) having a continuous or nearly continuous layer. The outer oxide thickness and amount of internal oxidation in both wet and dry air (labeled b and d in the Figures 5-22- 25) roughly follow the same trend. With the exception of the 1% Ti alloy, there is a significant decrease in the oxide thickness moving from the dry atmosphere to the humidified air. This is different from the observations at 900^{o}C. This still implies that there is some vaporization occurring, as expected from the data in Figure 5-20.

Crofer (Figure 5-26), as a comparison, behaved as expected. The outer surfaces in both dry and wet conditions were rich in Mn and Cr (Figure 5-26a & c). From these surfaces, the polishing lines are still visible, implying that the oxides are very thin. Observations of the cross sections (Figures 5-26b & d) confirm this, as the resultant oxides are the thinnest of all those grown in this

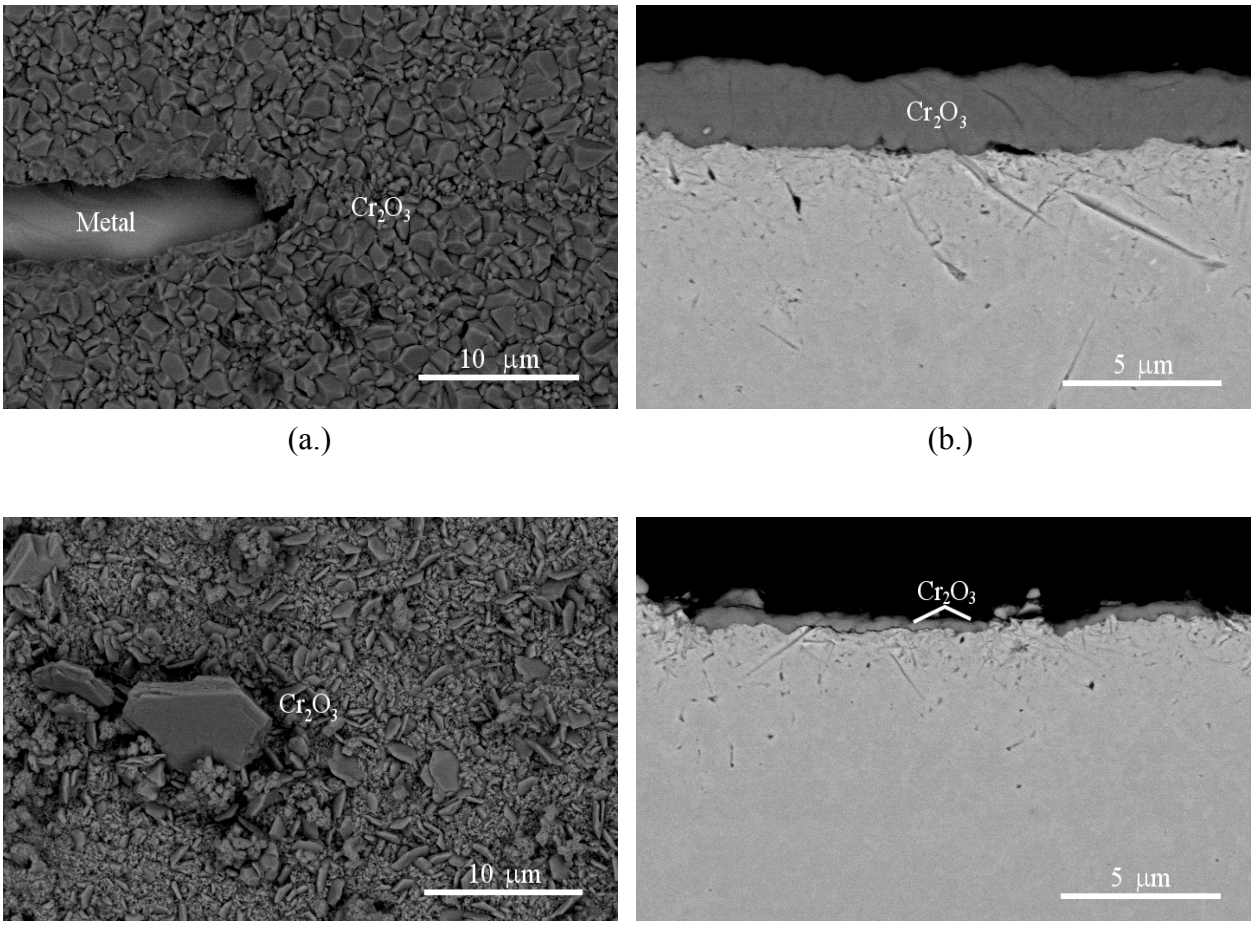

Figure 5-21 Surface and cross-sectional micrographs of the Fe-22Cr-0Ti alloy after exposure at 800^{o}C in dry (a&b) and wet (c&d) TGA experiments.

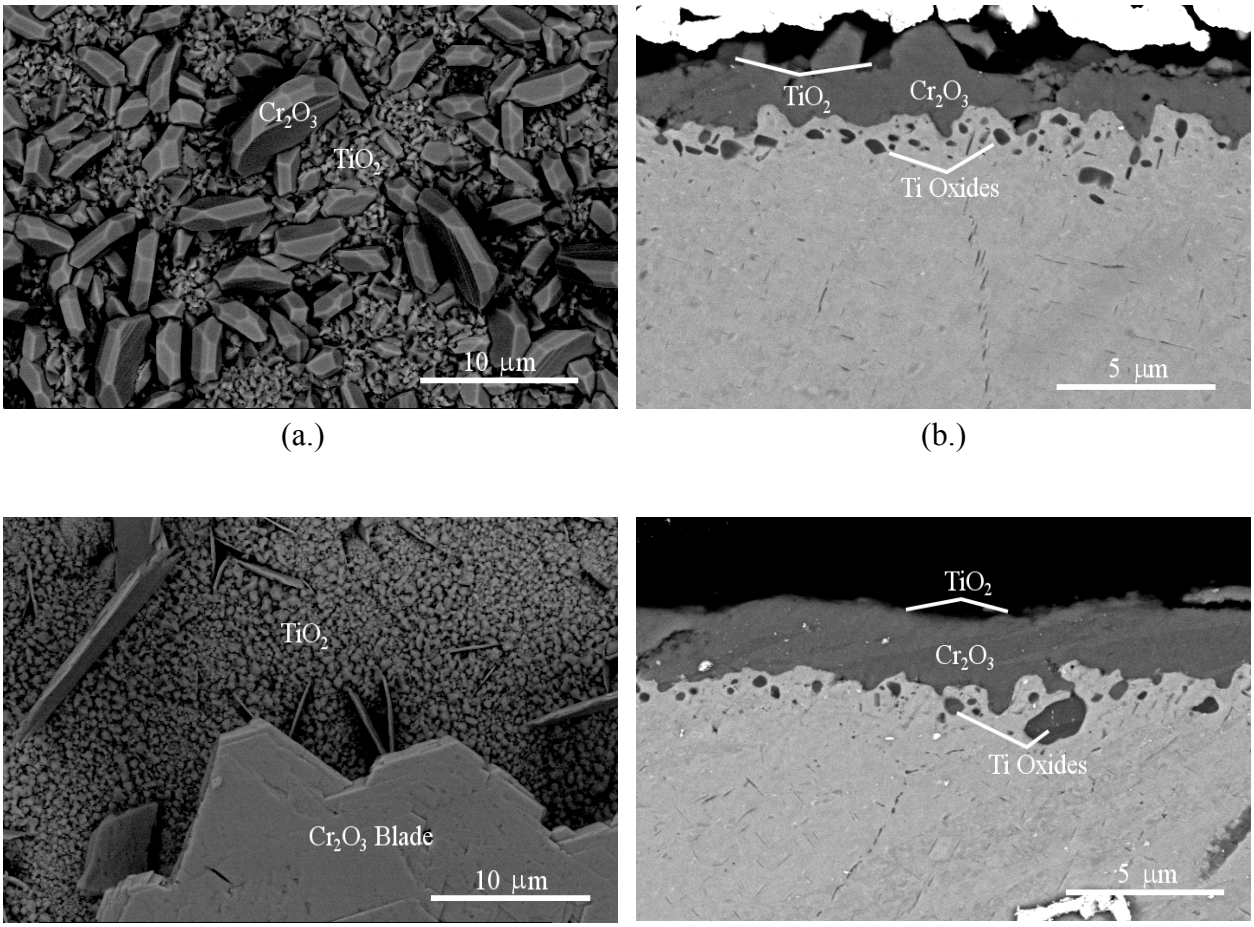

Figure 5-22 Surface and cross-sectional micrographs of the Fe-22Cr-0.84Ti alloy after exposure at 800^{o}C in dry (a&b) and wet (c&d) TGA experiments.

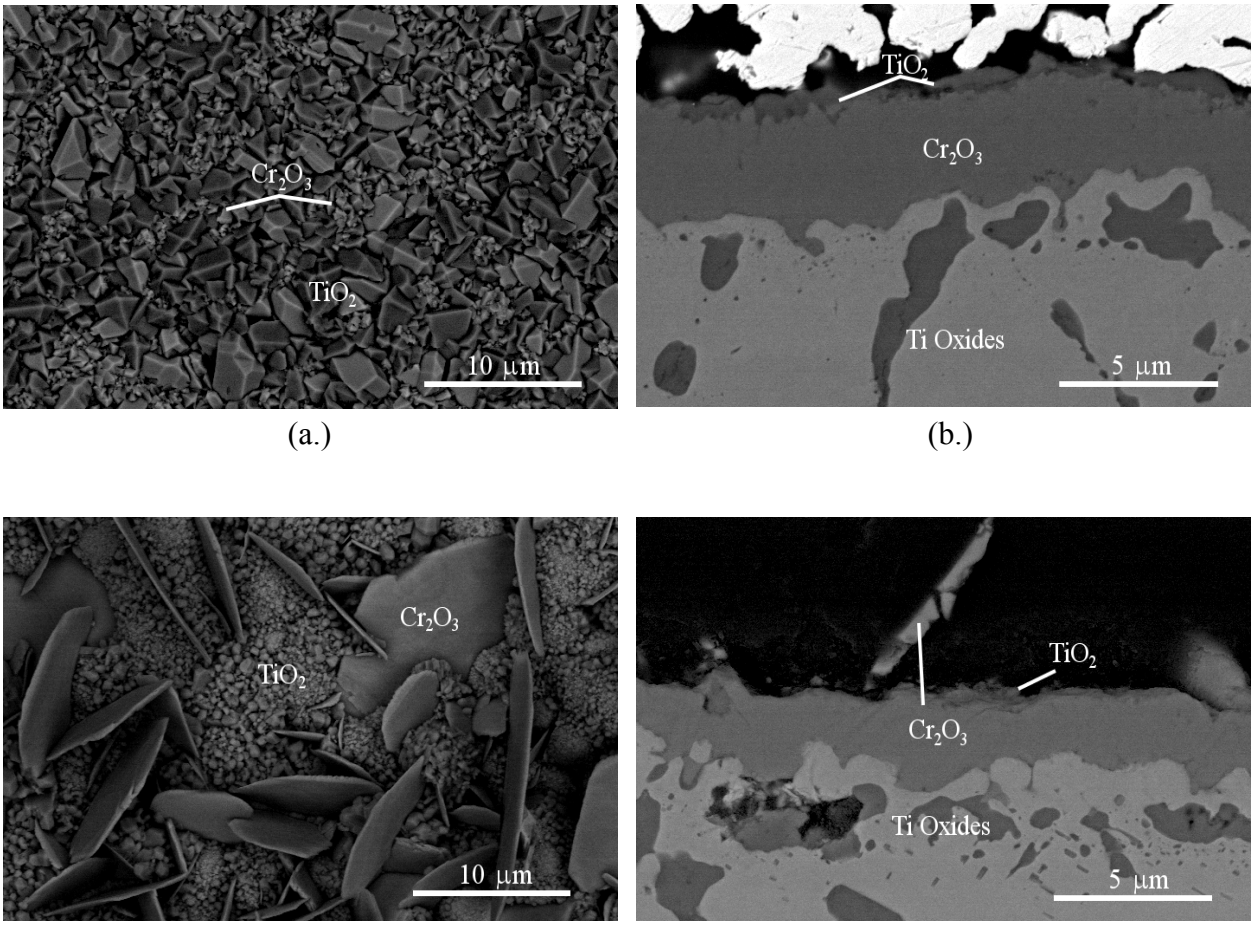

Figure 5-23 Surface and cross-sectional micrographs of the Fe-22Cr-1.65Ti alloy after exposure at 800^{o}C in dry (a&b) and wet (c&d) TGA experiments.

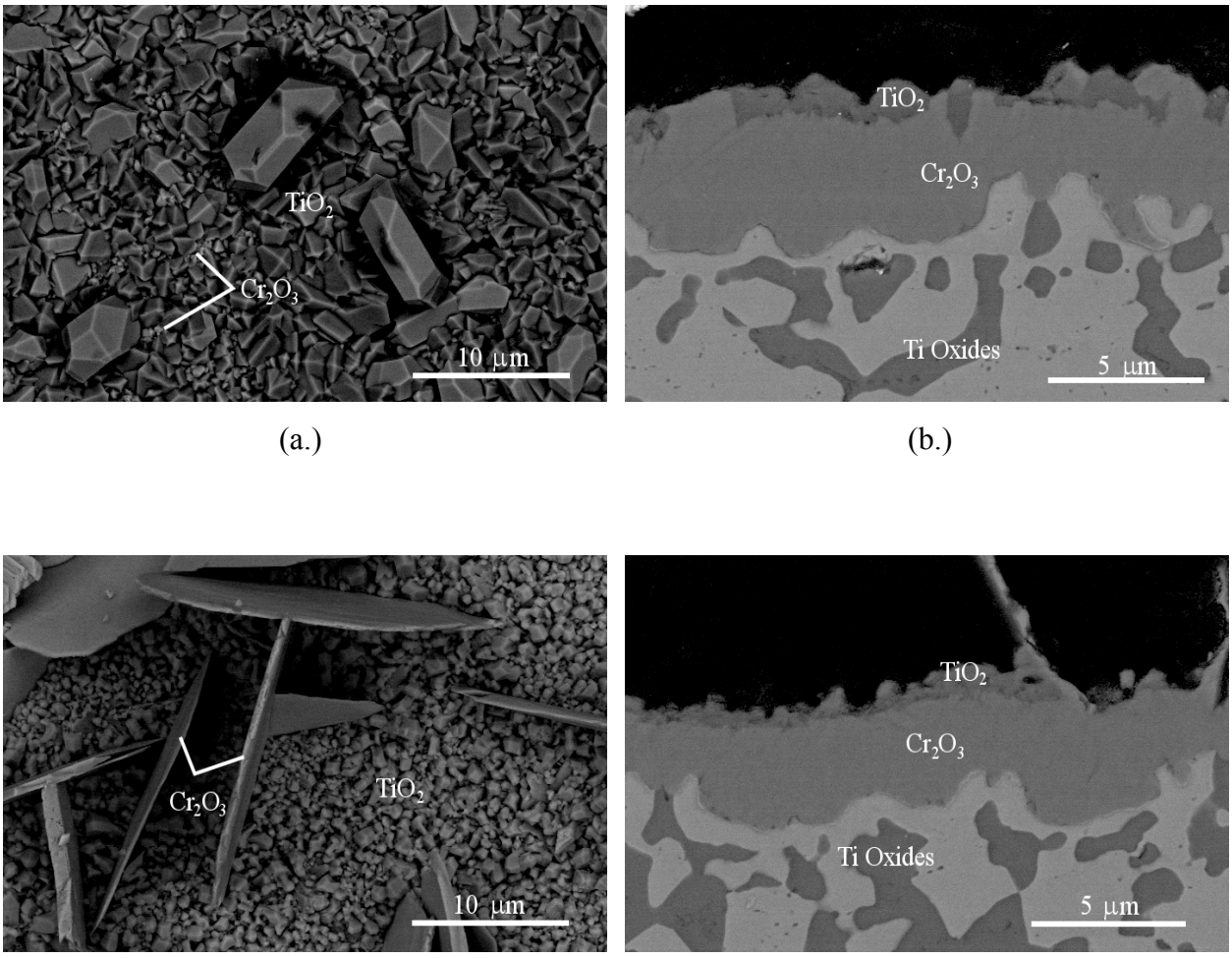

Figure 5-24 Surface and cross-sectional micrographs of the Fe-22Cr-2.78Ti alloy after exposure at 800^{o}C in dry (a&b) and wet (c&d) TGA experiments.

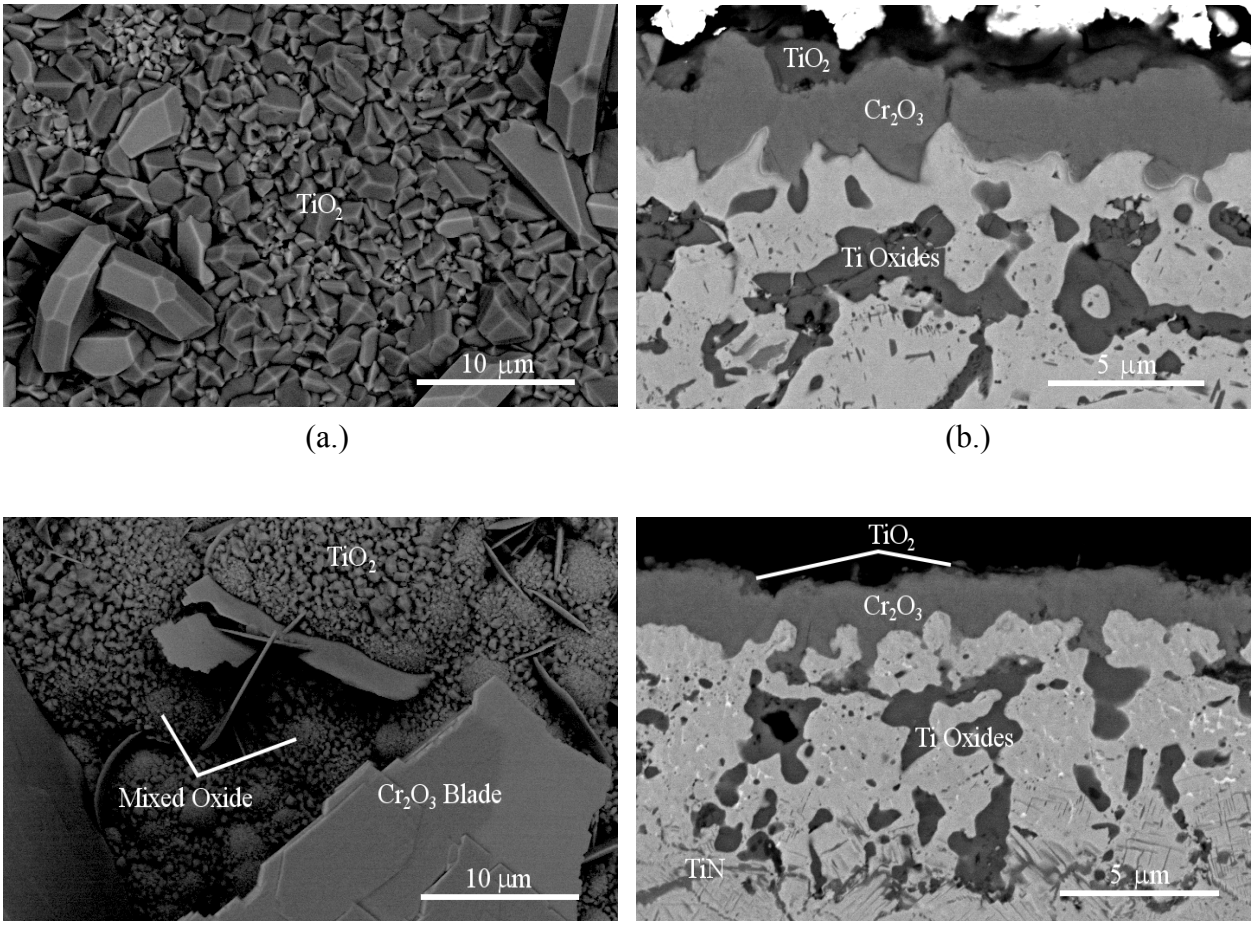

Figure 5-25 Surface and cross-sectional micrographs of the Fe-22Cr-3.98Ti alloy after exposure at 800^{o}C in dry (a&b) and wet (c&d) TGA experiments.

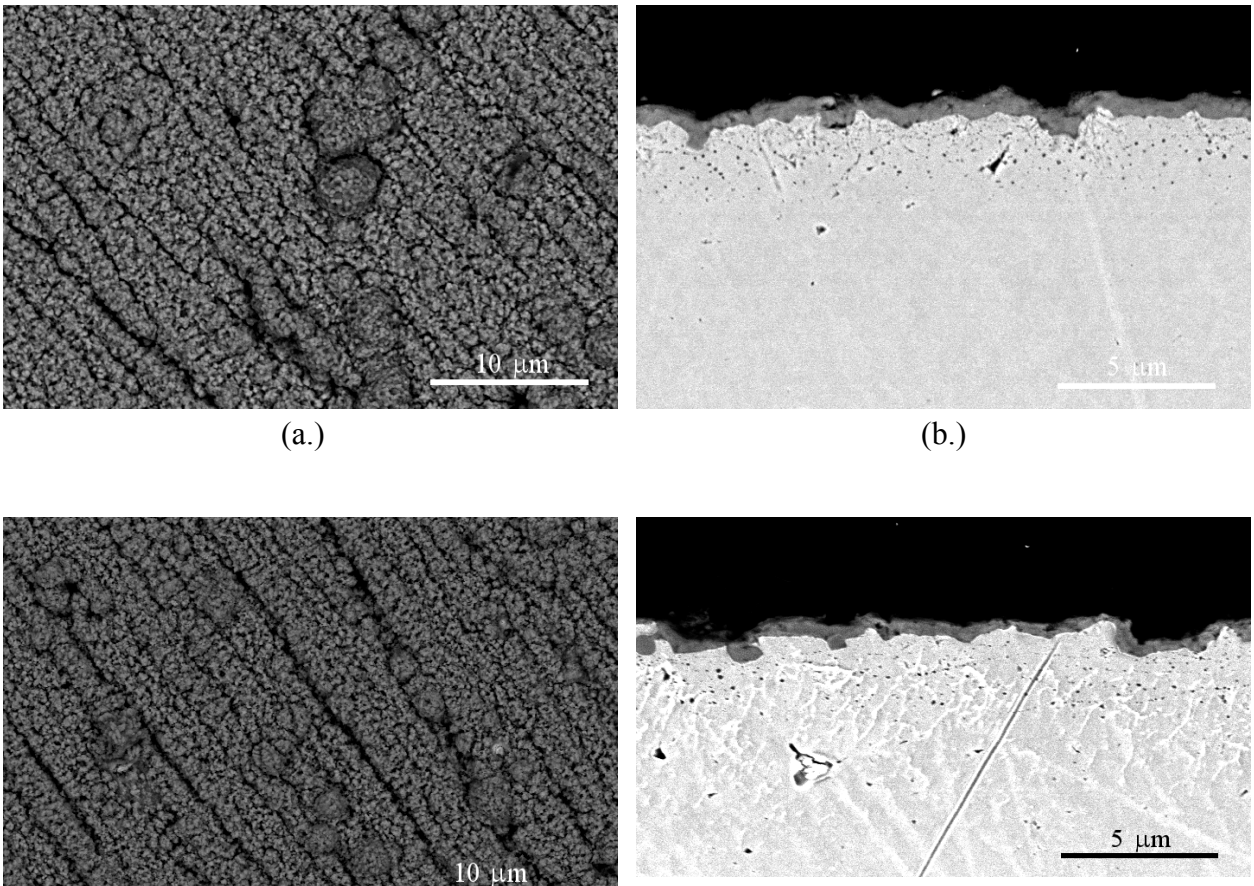

(a.) (b.)

(c.) (d.)

Figure 5-26 Surface and cross-sectional micrographs of Crofer after exposure at 800^{o}C in dry (a&b) and wet (c&d) TGA experiments.

experiment with the exception of the baseline alloy exposed in wet air. The oxide grown in wet air is thinner than that for the dry air case, once again, implying vaporization. In neither case was the manganese chromate layer clearly visible.

5.2.2.2 Progression of Oxide Growth with Time (Isothermal testing): To follow the growth of the microstructure of these materials, a sample of each material was exposed for 24, 100, 360, and 500 hrs isothermally at 800^{o}C in dry air. Figures 5-27 - 30 are the resulting cross-sectional and surface micrographs. For the most part, the oxide thicknesses increase with exposure time. There are some cases where the thickness does not appear to have changed much or appears to be thinner at the longer exposure time. The most likely reason is something temperature related such as the furnace not maintaining the correct temperature or the location of the sample in the furnace changing. As expected, the amount of internal oxidation and the depth of the depletion zone also increase with time. The most important thing to note about this experiment is that the amount of TiO_2 on the surface is increasing. This is illustrated best in Figure 5-28 which are the micrographs for the 2.78% Ti alloy. As time progresses, the outer layer in the cross-sections is gaining thickness. From the surface, the TiO_2 particles are also coarsening. For both the growth and coarsening to occur, Ti must continue to be supplied to the surface from the oxide and in turn, from the substrate. This is proof that the TiO_2 is not a transient phenomenon. Further implications are that the oxide should be able to reform its two layer structure when and if spalling occurs, assuming the local Ti concentration is sufficient to do so. This may be hindered by the internal oxidation. Once again, the 3.98% Ti alloy formed the nitride structure leaving areas of unprotected chromia (Figure 5-30).

This experiment makes it very clear that Ti does, in fact, diffuse continuously through the oxide and forms a layer on the surface. This is not entirely surprising, given the fact that several elements are known to diffuse through chromia. Cox, et al.[39] predict that Ti^{3+} should have a mobility that is only slightly slower than Mn^{2+}. TiO_2 is the stable Ti oxide at these temperatures and pressures, and the oxidation state of titanium should be Ti^{4+}. The ionic radius of Ti^{4+} is smaller than Ti^{3+} (56 angstroms and 81 angstroms, respectively) and should therefore move much more easily through the chromia. It is not hard to imagine that studies similar to those by Lohnig[40] would show that lattic diffusion is extremely fast for Ti. What is unexpected is that the Ti has the opportunity to be incorporated into the chromia in the first place. Considering the thermodynamic calculation discussed for MnO incorporation into chromia, it seems odd that Ti does not remain totally below the chromia as a continuous oxide layer or as internal oxides. The concentration of Ti is much larger than that of Mn in an alloy like Crofer, which increases the Ti activity in the alloy compared to the case of Crofer. The stability of its oxides lead to a dissociation pressure of titanium oxide that is much lower than the p_{O2} at the alloy/chromia interface. All of these factors are favorable for the oxidation reaction to occur below the oxide. This does occur, as the observations here show. It is not clear why Ti is still present in the chromia in amounts that lead to continuous overlayers. This is particularly interesting when alumina and silica (similar stability) are not seen to behave the same way.

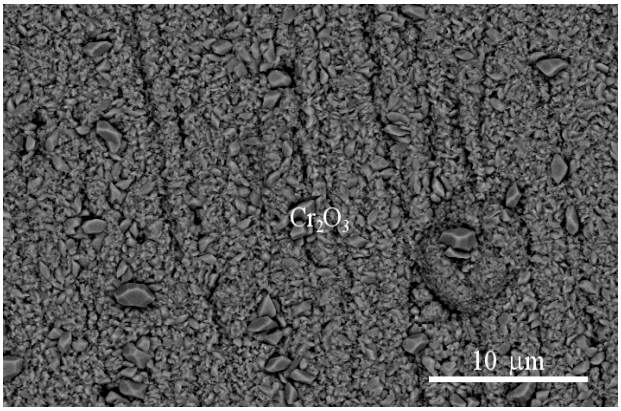
Cr_2O_3
10 μm

(a.)

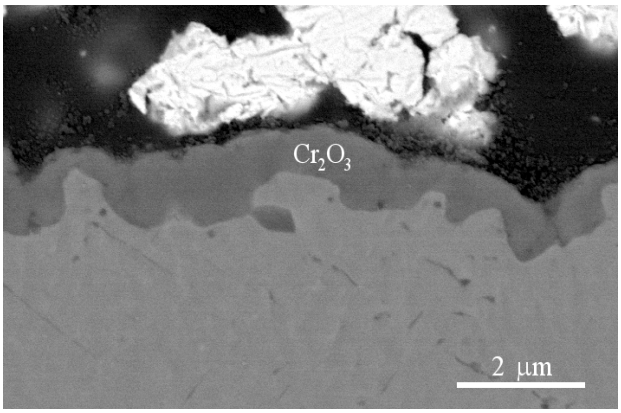
Cr_2O_3
2 μm

(b.)

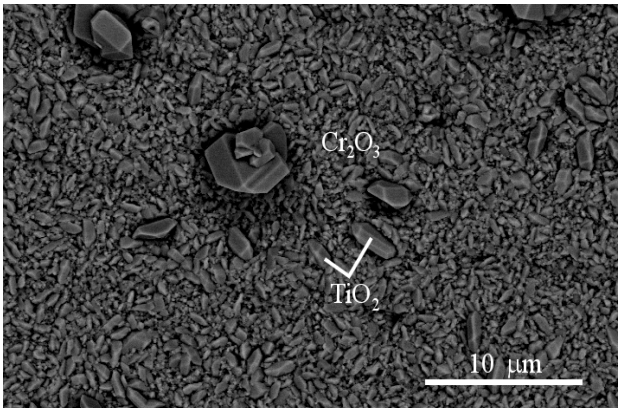
Cr_2O_3
TiO_2
10 μm

(c.)

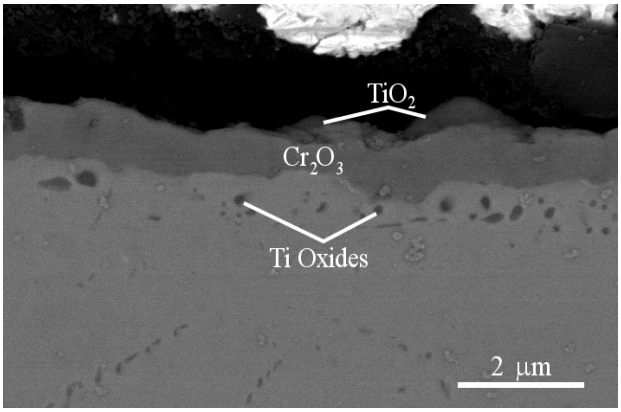
TiO_2
Cr_2O_3
Ti Oxides
2 μm

(d.)

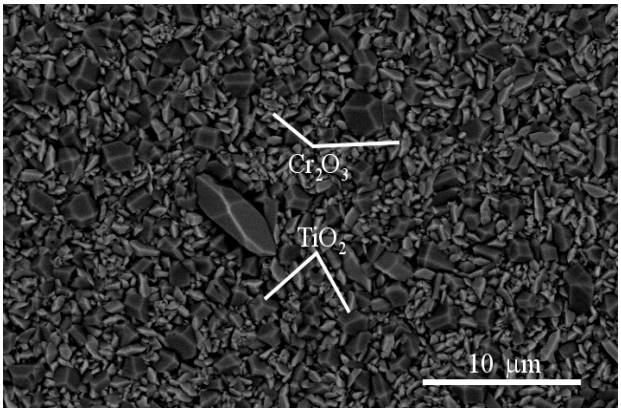
Cr_2O_3
TiO_2
10 μm

(e.)

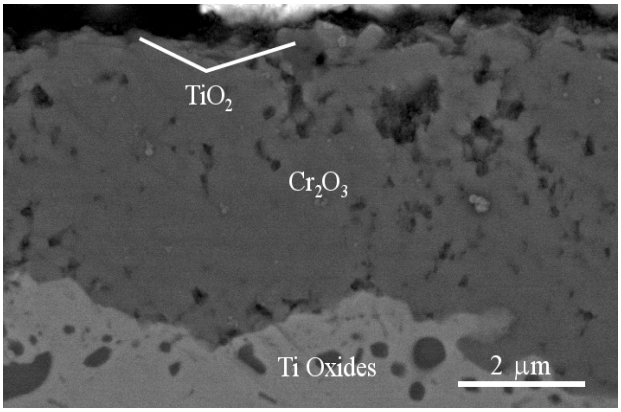
TiO_2
Cr_2O_3
Ti Oxides
2 μm

(f.)

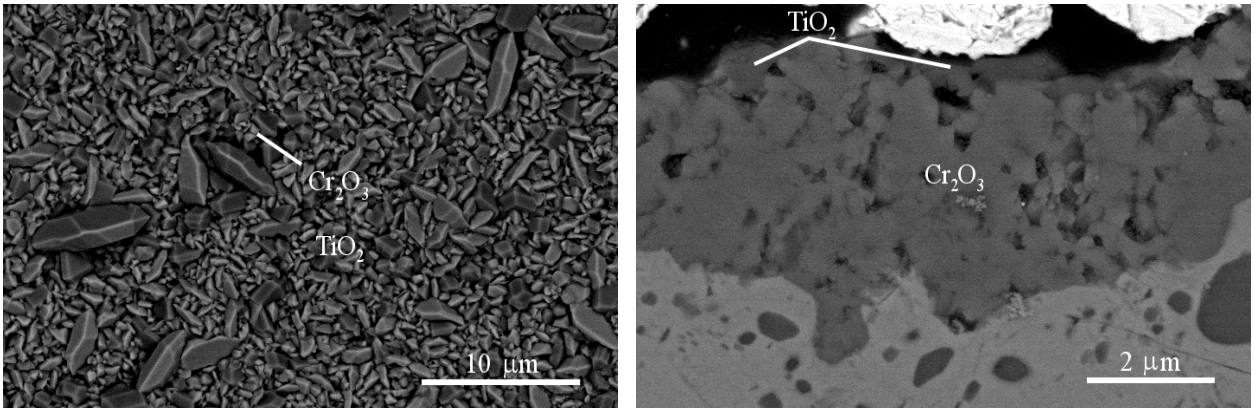

(g.) (h.)

Figure 5-27 SEM micrographs of the Fe-22Cr-0.84Ti alloy exposed in dry air at 800°C for 24 hours (a&b), 100 hours (c&d), 360 hours (e&f) and 500 hours (g&h)

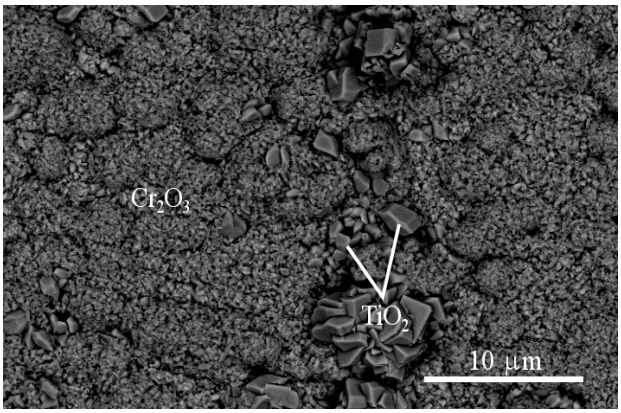
Cr_2O_3
TiO_2
10 μm

(a.)

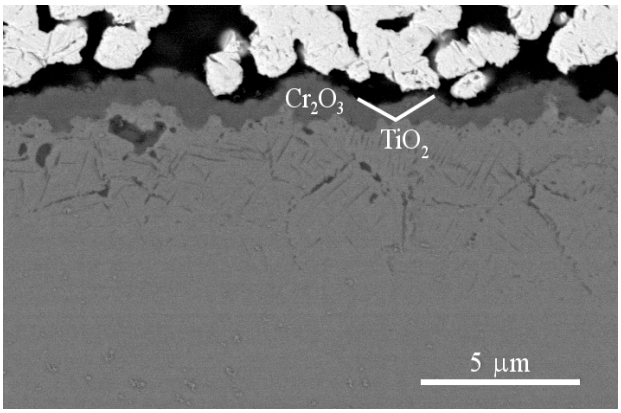
Cr_2O_3
TiO_2
5 μm

(b.)

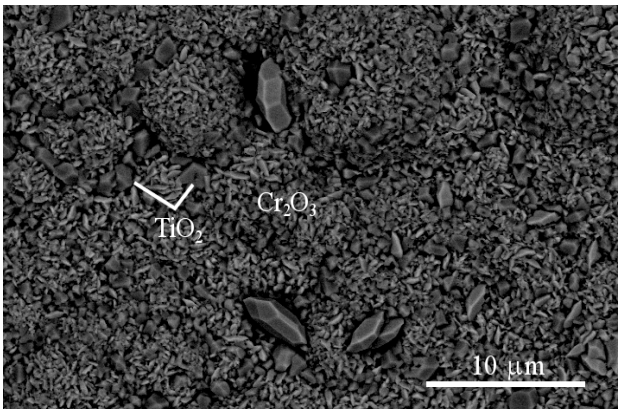
TiO_2
Cr_2O_3
10 μm

(c.)

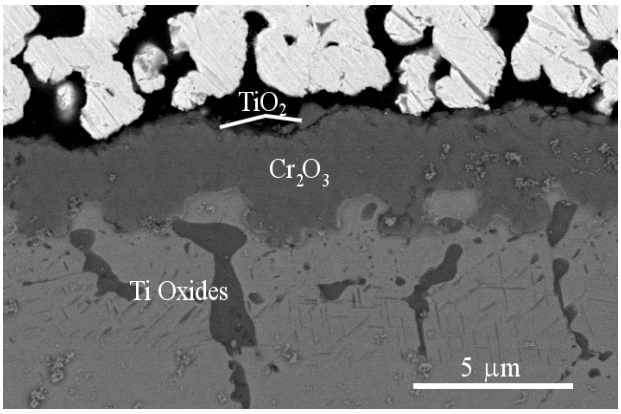
TiO_2
Cr_2O_3
Ti Oxides
5 μm

(d.)

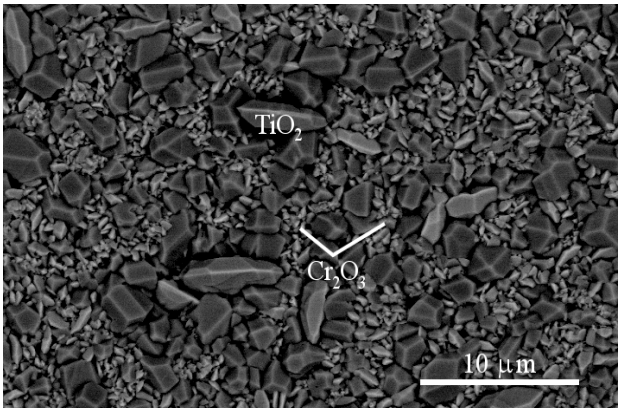
TiO_2
Cr_2O_3
10 μm

(e.)

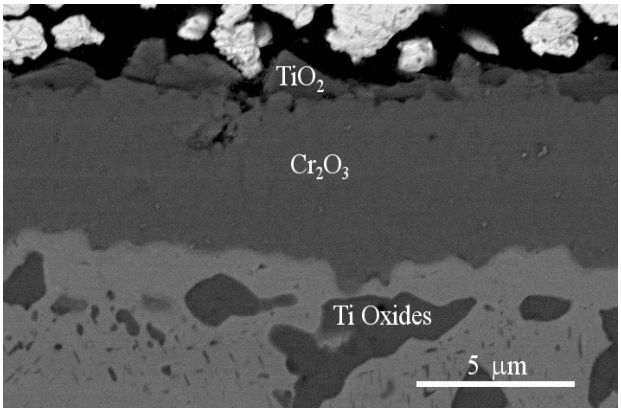
TiO_2
Cr_2O_3
Ti Oxides
5 μm

(f.)

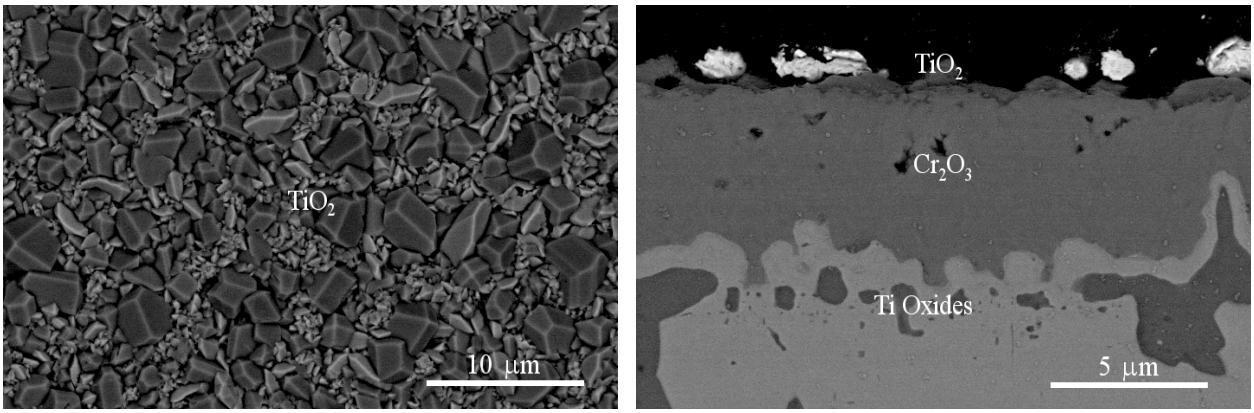

(g.) (h.)

Figure 5-28 SEM micrographs of the Fe-22Cr-1.65Ti alloy exposed in dry air at 800°C for 24 hours (a&b), 100 hours (c&d), 360 hours (e&f) and 500 hours (g&h)

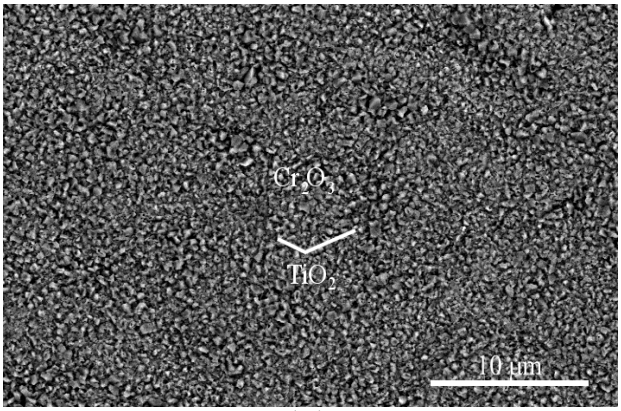
Cr_2O_3
TiO_2
10 µm

(a.)

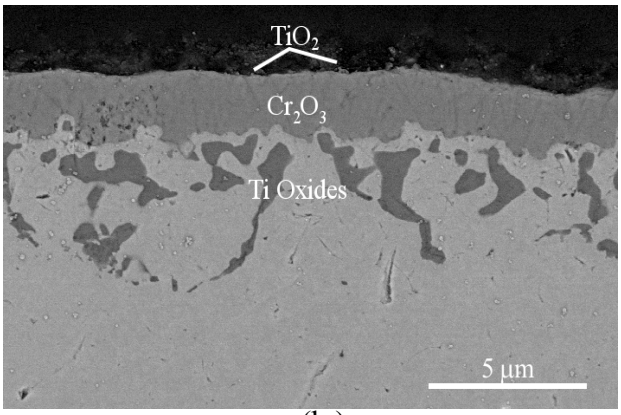
TiO_2
Cr_2O_3
Ti Oxides
5 µm

(b.)

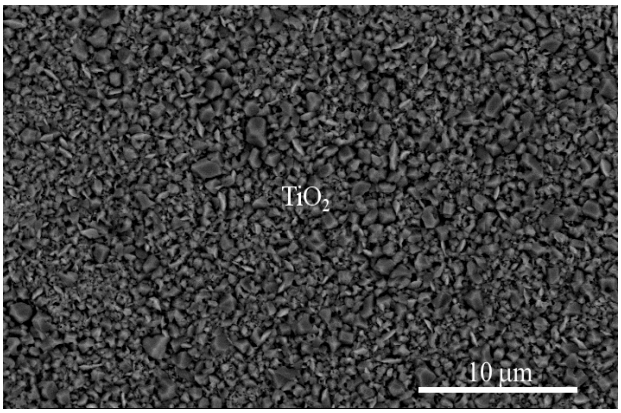
TiO_2
10 µm

(c.)

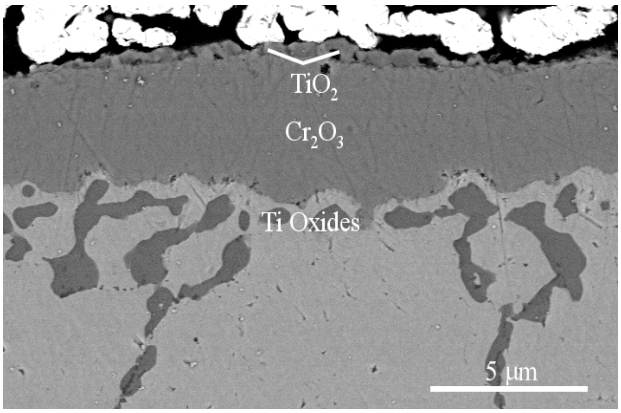
TiO_2
Cr_2O_3
Ti Oxides
5 µm

(d.)

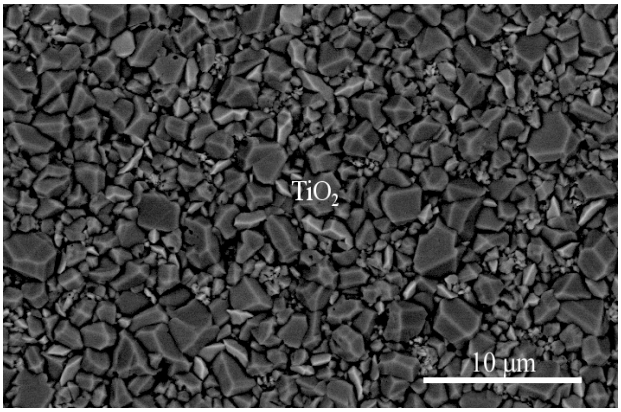
TiO_2
10 µm

(e.)

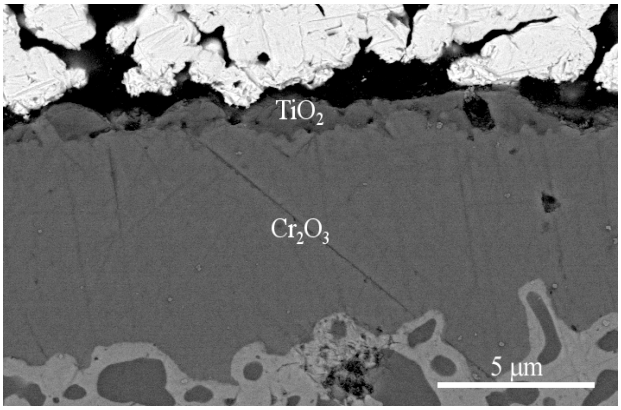
TiO_2
Cr_2O_3
5 µm

(f.)

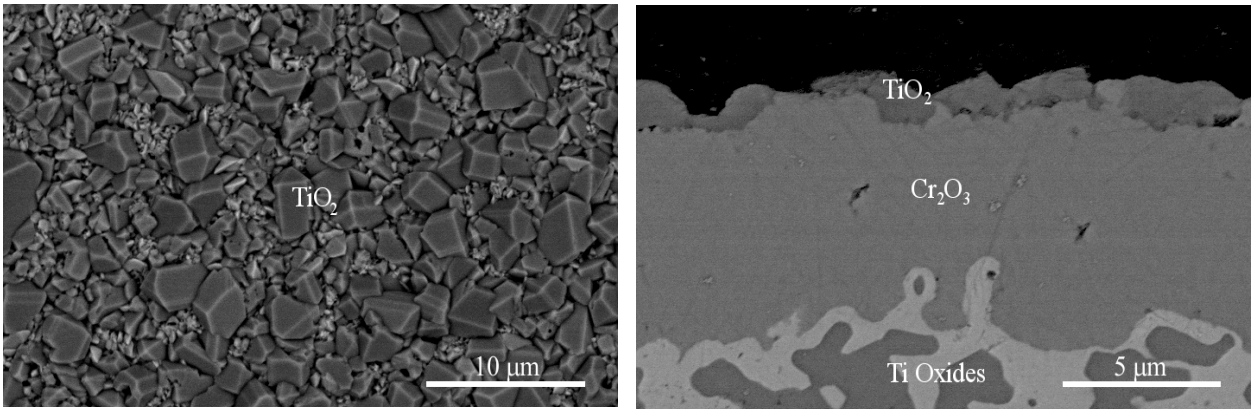

(g.) (h.)

Figure 5-29 SEM micrographs of the Fe-22Cr-2.78Ti alloy exposed in dry air at 800°C for 24 hours (a&b), 100 hours (c&d), 360 hours (e&f) and 500 hours (g&h)

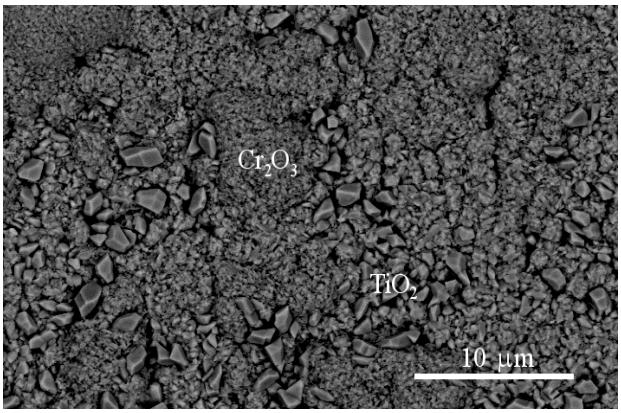
Cr_2O_3
TiO_2
10 μm

(a.)

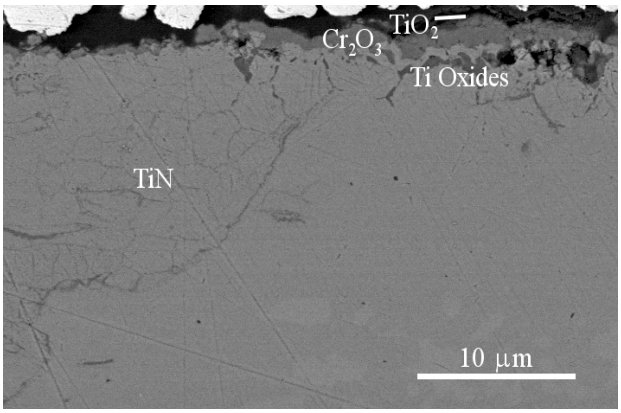
TiO_2
Cr_2O_3
Ti Oxides
TiN
10 μm

(b.)

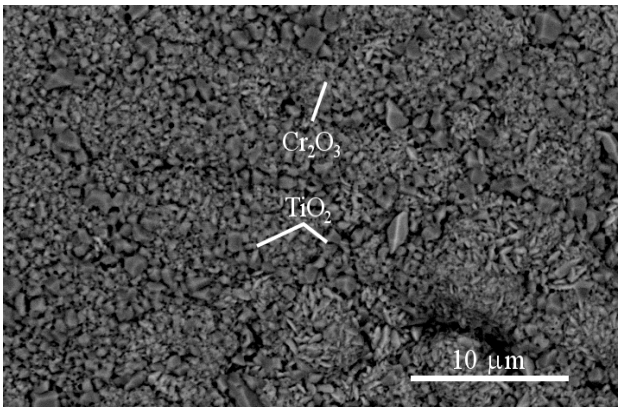
Cr_2O_3
TiO_2
10 μm

(c.)

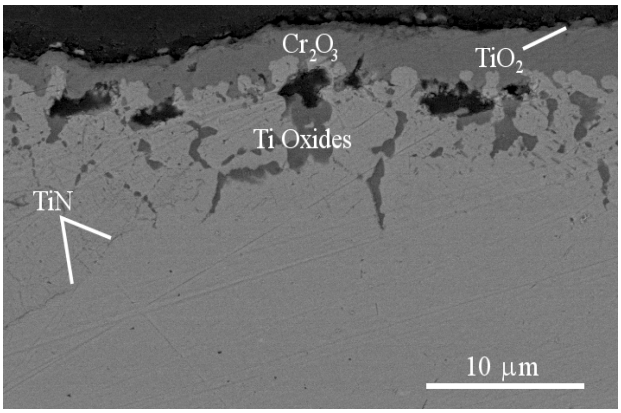
Cr_2O_3
TiO_2
Ti Oxides
TiN
10 μm

(d.)

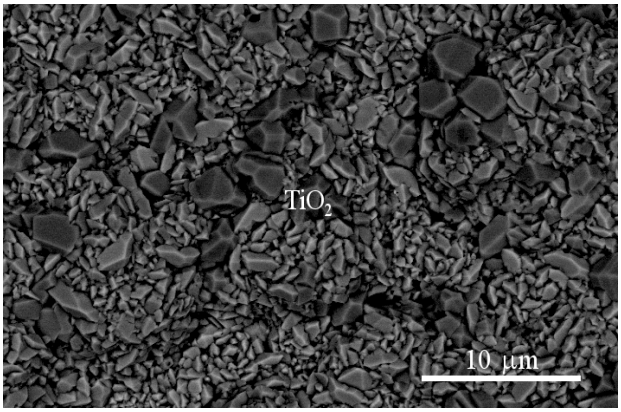
TiO_2
10 μm

(e.)

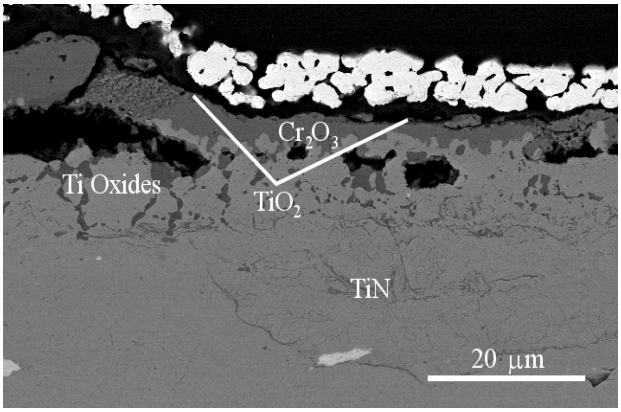
Cr_2O_3
Ti Oxides
TiO_2
TiN
20 μm

(f.)

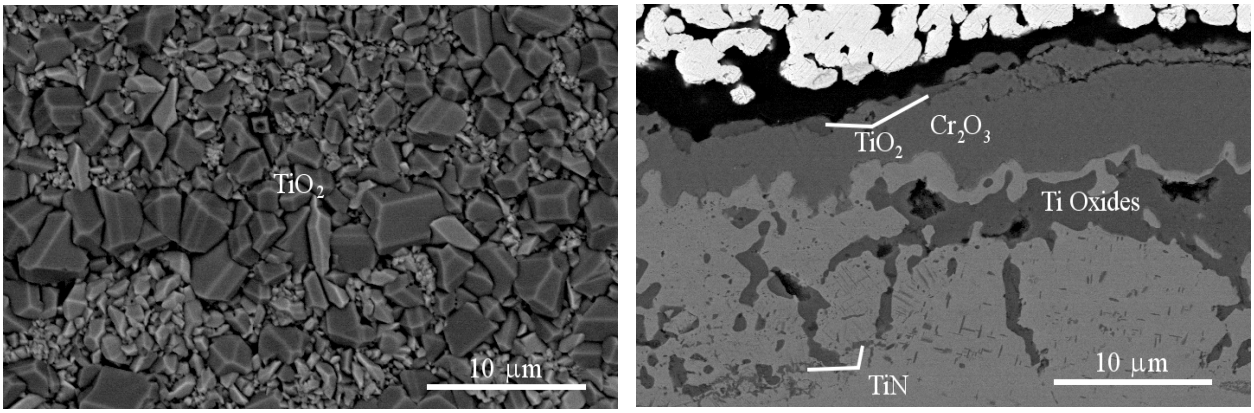

(g.) (h.)

Figure 5-30 SEM micrographs of the Fe-22Cr-3.98Ti alloy exposed in dry air at 800°C for 24 hours (a&b), 100 hours (c&d), 360 hours (e&f) and 500 hours (g&h)

5.2.2.3 ASR Measurements: To characterize the effect of the oxide growth in terms of the electrical properties, ASR measurements were performed on the samples from the previous section. During the measurement, the samples were heated to 700^{o}C for a short time to sinter the Pt paint electrode. When the voltage drop stabilized, the temperature was then raised to 800^{o}C for the actual measurement. Measurements were taken periodically during a one hour period as the samples stabilized. In most cases the voltage drop was still decreasing after one hour, but in order to complete the measurements in a timely manner and to affect the least amount of change in the oxide due to extended exposure, the measurement was terminated at that time. No sample was measured beyond 1 hour to determine the length of time to fully equilibrate. This was not performed, because bulk chromia is known to require long periods of time to equilibrate and the oxide being tested is part of a dynamic system, i.e. the oxide is continuously growing. Figure 5-31 is a plot of ASR vs $t^{1/2}$. Similar to the ASR measurements done at 900^{o}C, Crofer has the lowest ASR value, while the Fe-Cr-Ti alloys all have curves in the same vicinity of each other. There is no apparent trend in terms of the Ti content from this plot. With the exception of the 1.65% Ti alloy, there is a systematic increase in ASR after 500 hours. Several factors could explain this increase, ranging from the samples finally forming a continuous overlayer to slightly higher exposure temperatures. All of the samples were exposed in the same furnace and all samples exposed for the same amount of time were done simultaneously. The sharp drop for the 1.65% Ti sample is not readily explainable. A final point to note relative to this plot is that ASR can be related to the k_p value as shown in Eqn 31.

The ASR values do not seem to tell the entire story of the electronic behavior of the different alloys, particularly since the Fe-Cr-Ti alloys are experimental. Figure 5-32 is a plot of resistivity vs time, where the resistivity is calculated from the ASR values and the approximate

oxide thickness from the cross sections of the samples shown in Figures 5-27 - 30. On this plot, Crofer is near the top of the plot and its resistivity appears to drop rapidly and then becomes rather flat (even considering the increased ASR values at 500 hours). The curves for the Fe-Cr-Ti alloys are low and with the exception of the 2.78% Ti alloy, they have a downward trend. The implications of this plot are that the Ti doped oxide may be more conductive than the Mn doped case, and therefore if optimization steps can produce the same conditions while reducing the growth rate, Ti doping is the better strategy. One negative conclusion that can be drawn stems from the fact that most of the results clearly show that the 2.78% Ti alloy most readily forms the outer rutile layer and most likely has the highest Ti concentration in the chromia. Combining that with the upwards trend in the plot may mean that there is a limit to the amount of Ti in the chromia scale that is beneficial. The question then becomes what is that amount and could the other alloys reach that point with longer exposure times?

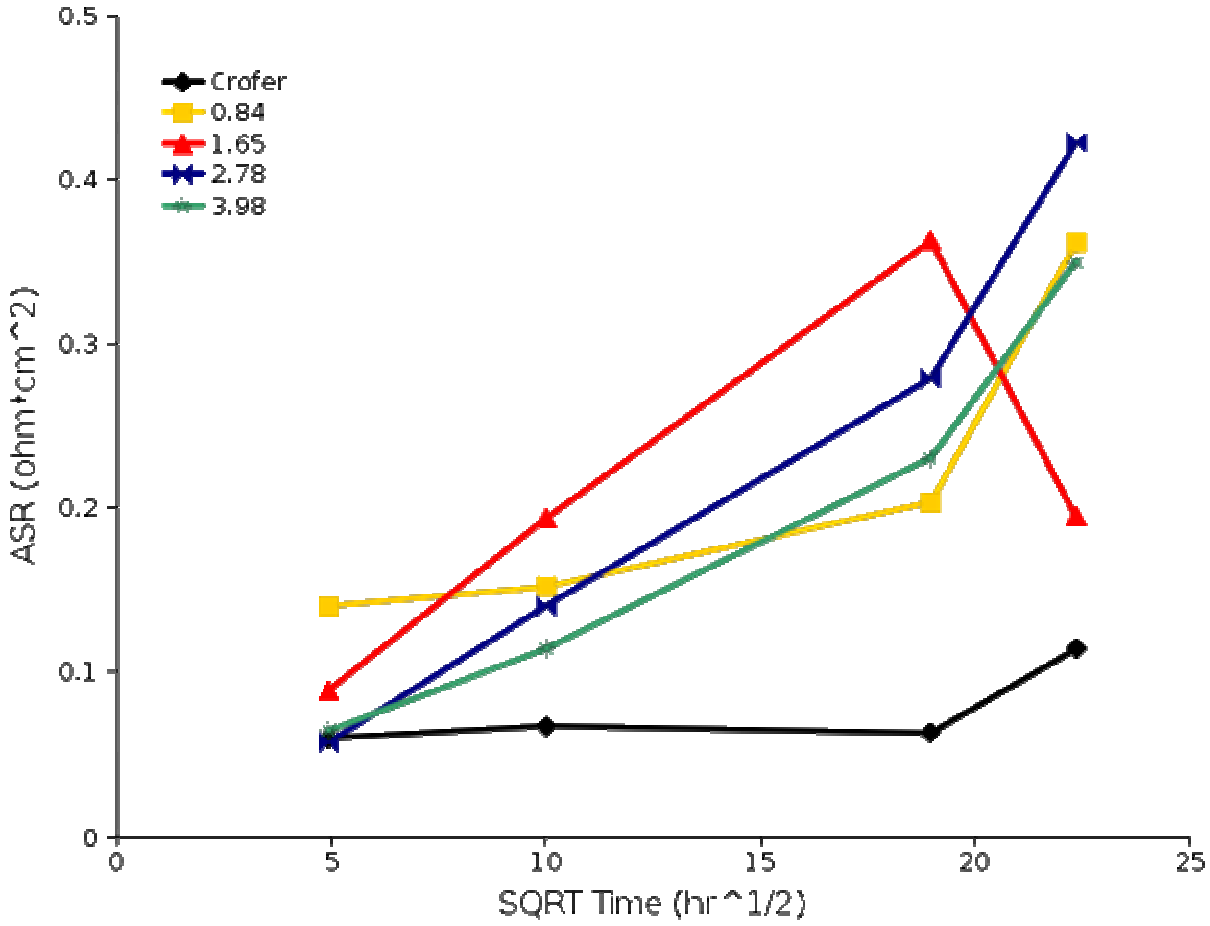

Figure 5-31 Plot of ASR vs. $t^{1/2}$ for Fe-Cr-Ti alloys and Crofer.

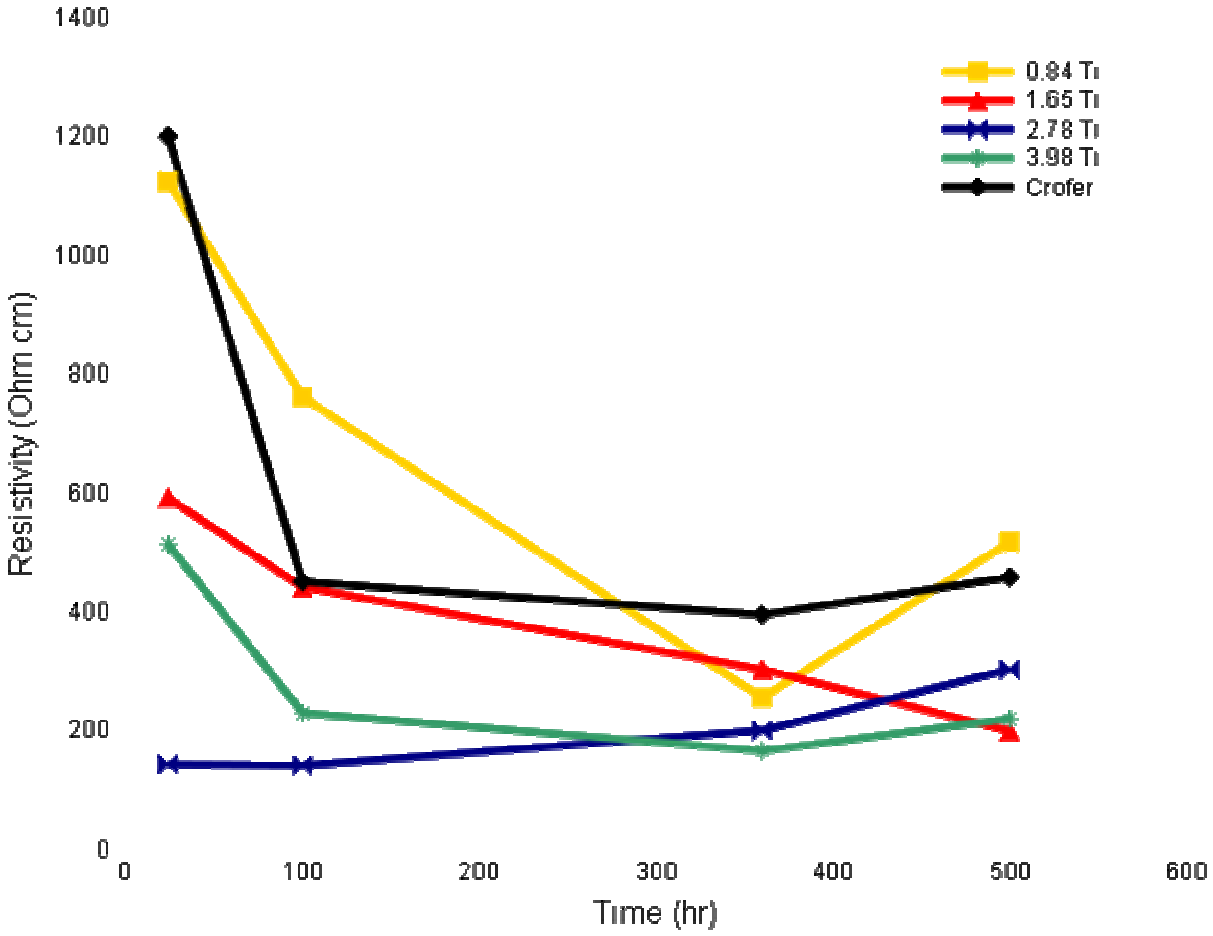

Figure 5-32 Plot of resistivity vs. time for Fe-Cr-Ti alloys and Crofer.

5.2.2.4 Cyclic Testing: Cyclic oxidation testing of the Fe-Cr-Ti alloys and Crofer was performed at 800°C for a total of 1000 cycles. Duplicate samples were tested and in all cases the two samples for each alloy behaved similarly. Figure 5-33 is a plot of the average mass of the duplicate specimens vs number of cycles. The trends are similar to those for all of the tests in which the kinetics were measured. The samples display an increase in the weight gained as the Ti content increases, but only up to 2.78% Ti. The 3.98% Ti sample shows a lower weight gain, due to the extensive formation of nitrides that tie up the Ti. As mentioned above, this leaves regions of lower Ti content in the oxide that are undoped and, therefore, grow more slowly. Another interesting thing to note is that comparing the left hand portion of Figure 5-33 with Figure 5-20 shows that there is not a large difference in the two sets of data. This would indicate that the oxide either grows so rapidly that the differences are masked, the doping increases scale plasticity (making the scale more strain tolerant), and/or the interfacial toughness is high.

Figure 5-34 shows the surface and cross-sectional micrographs of the baseline alloy after about 500 hours and 1000 hours in both dry and wet air. The oxide is purely chromia in all cases. In the dry exposures, the surface shows some of the typical chromia morphologies. There were no obvious signs of spallation. In cross-section, the oxide appears to have been pulled from the substrate during mounting, which indicates that the interface is rather weak. In the wet environment, long thin blades of chromia formed in some locations, but otherwise the surface is similar to that for the dry exposures. The cross-sections show that the oxide is thinner than for the dry samples, but also appears to be more adherent in some locations.

The Ti bearing alloys are shown in Figures 5-35 - 38. Essentially the same trends that are seen in the TGA or isothermal tests are observed for the cyclic tests as well. Increased Ti content in the alloy leads to more TiO_2 on the surface, more internal oxidation, and a thicker

oxide. The thickness also increases with time in the dry exposures and does not change or is decreased with time in wet exposures. The oxides are all rather adherent, with no signs of spallation. The same morphologies persist that were previously observed, with the chromia forming thick blades in dry conditions and long, thin blades in wet conditions. One thing to note is that at the longer times, it appears that the TiO_2 is beginning to overgrow the blades in the wet environments. This is illustrated best in Figures 5-37e – h. At 500 cycles, Figures 5-37e & f, the titania layer is thin and the chromia blades appear to terminate high above the TiO_2 covered areas. In Figures 5-37g&h, the blades no longer appear to be as tall and in cross section, the TiO_2 is thicker around the blades than in the regions between. Loss of material from the blades due to vaporization could also add to the effect of the blades appearing shorter. It is possible that with time the surface will be entirely sealed by the TiO_2 as it thickens and the blade vaporizes. The only features that are different from the isothermal tests are the appearance of what may be voids in the cross-sections. They appear at the TiO_2/Cr_2O_3 interface and at the metal/internal oxide interfaces. Both of these can be clearly seen in Figure 5-36h. It is not clear whether the void space is due to a Kirkendall effect or to sample preparation. While there is no spalling in these experiments, there could be problems at longer exposures if the voids are diffusion related.

Part of the design strategy for Crofer involved Ti additions to improve the scale adhesion. Sigler[43] mentions that if Ti is added to steels for catalytic converters to take advantage of the sulphur and other impurity getting capabilities, which would effectively aid in the scale adhesion. This may also be the case here, where no major spalling was observed despite rather thick oxides. A second effect may be related to the oxidation mechanism at work. Ti incorporated into the chromia scale increases the number of cation vacancies. This should promote the outward diffusion of cations and, therefore, the outward growth component should

be larger. In the absence of dopants, chromia is believed to grow both inwardly and outwardly, with new oxide being formed at boundaries within the oxide. The strain energy created by this type of growth leads to spalling. If Ti additions allow the outward growth to dominate, then new oxide should be formed at the gas/oxide interface and should result in less spalling. The data and micrographs for the cyclic testing show no spalling. Closer inspection of the micrographs for the oxide progression study also show that the thickness of the metal layer between the internal and external oxide remains approximately the same thickness. This is further support for the idea that the oxide is growing outward.

Crofer (Figure 5-39) shows some different behavior than the Fe-Cr-Ti alloys. In the dry experiments, oxide thickness varied widely, from 2 – 5 μm at both exposure times. The oxide is slightly thicker and more uniform at the longer time (Figure 5-39c). The surface examination shows that the surface is covered with $MnCr_2O_4$. The morphologies are the same as the isothermal experiments. The oxides in the wet experiments are thinner and much more uniform (Figures 5-39f&h). Both of these could be the result of increased vaporization in the moist air. The microstructure is very similar to that observed by Hammer[10] in a nearly identical experiment. The surface morphology is slightly different, in that there is a network of what look like mounds of oxide (similar to a that observed for a chromia only oxide).

Considering the above discussion related to a possible effect of Ti additions, Mn should behave in the opposite manner. Mn acts as an acceptor dopant and, therefore, should increase the anion vacancy concentration. This in turn should promote inward growth and new growth occurs at the metal/scale interface, more similar to alumina. This idea is supported by the observation of the continuous chromia undercutting the metal in some areas. The undercutting is either the oxide and metal deforming to relieve the strain energy or localized inward growth.

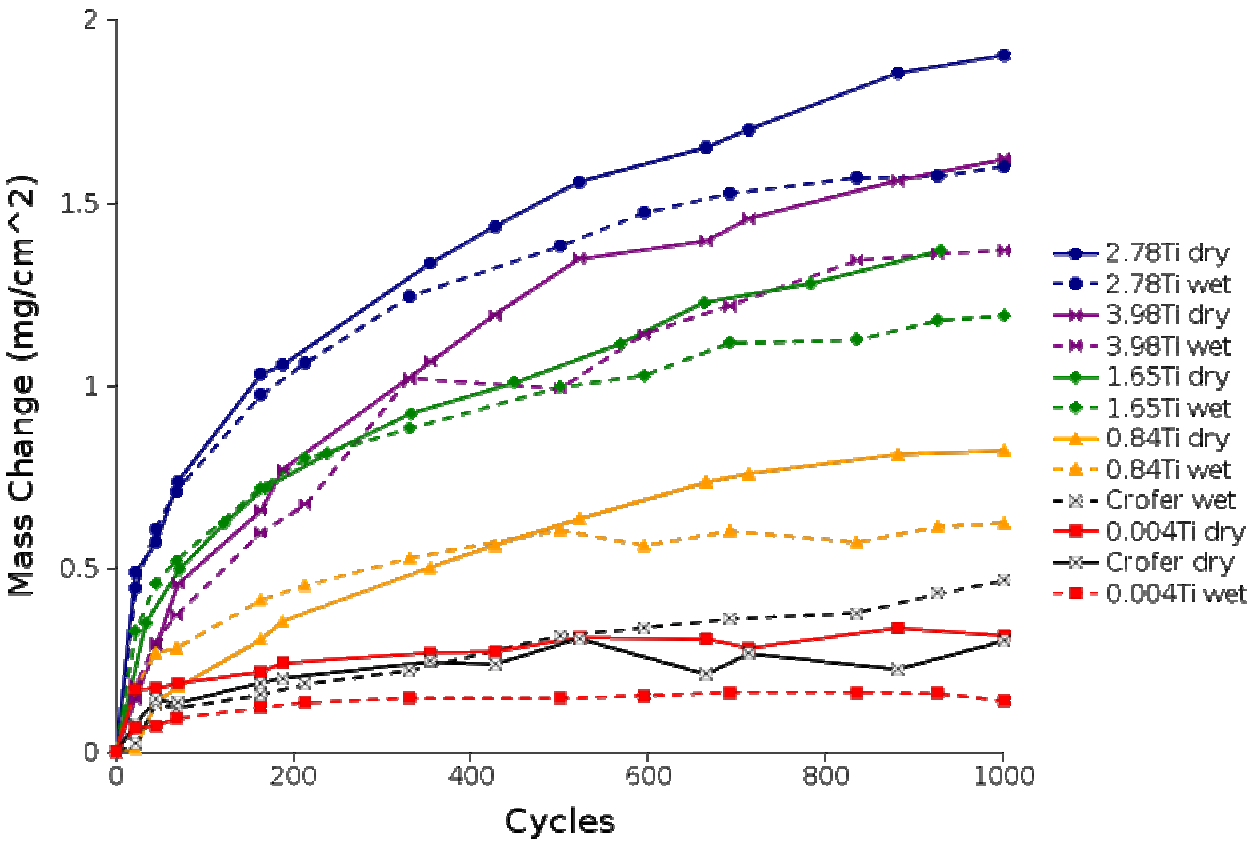

Figure 5-33 Plot of mass change vs. number of cycles for Fe-Cr-Ti alloys and Crofer at 800°C in dry and wet air.

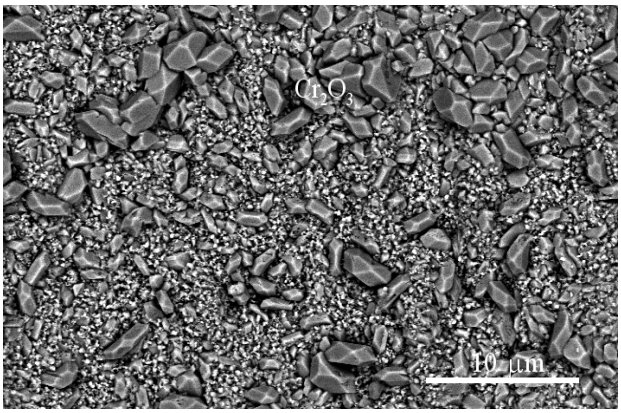
Cr_2O_3
10 μm

(a.)

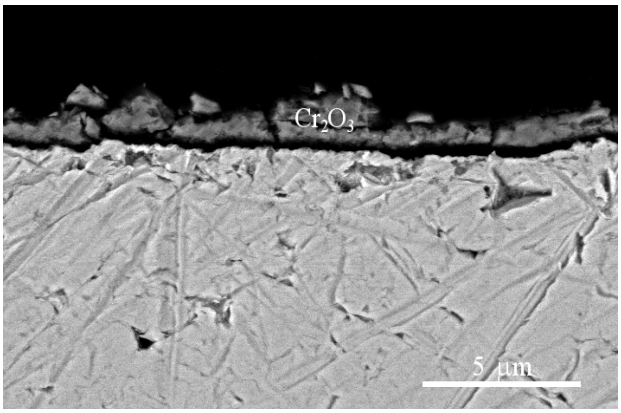
Cr_2O_3
5 μm

(b.)

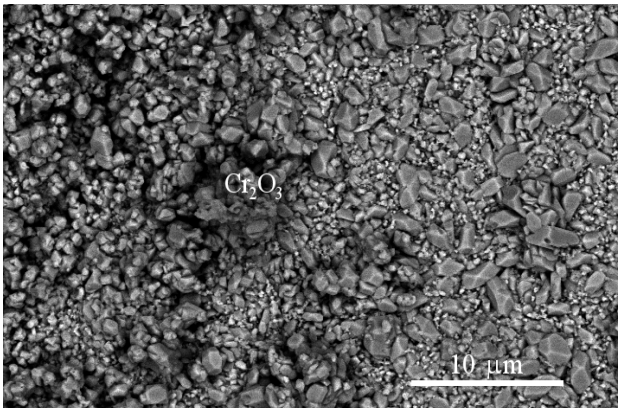
Cr_2O_3
10 μm

(c.)

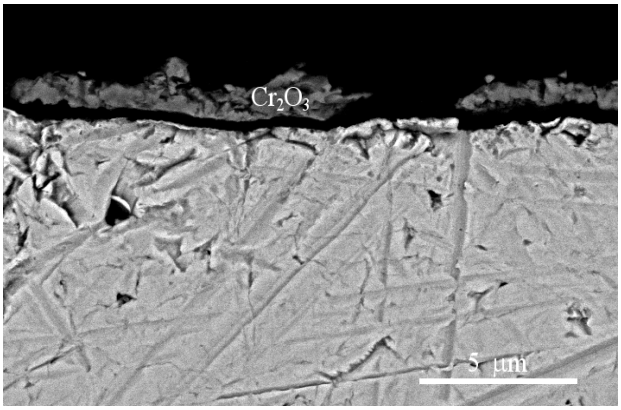
Cr_2O_3
5 μm

(d.)

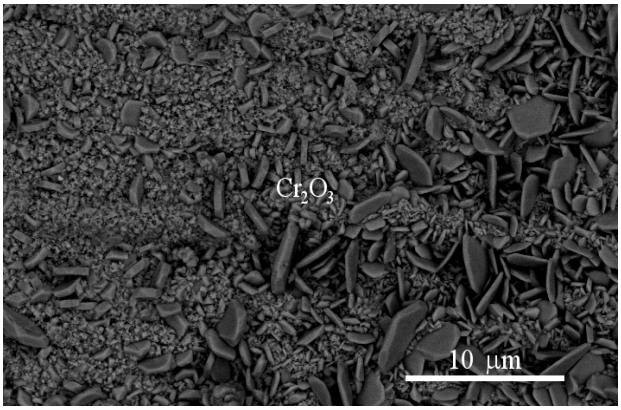
Cr_2O_3
10 μm

(e.)

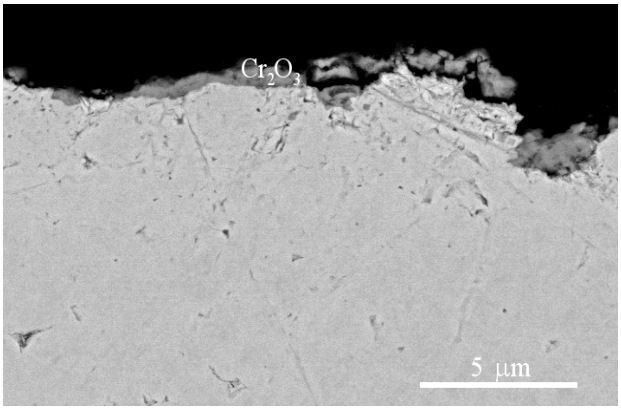
Cr_2O_3
5 μm

(f.)

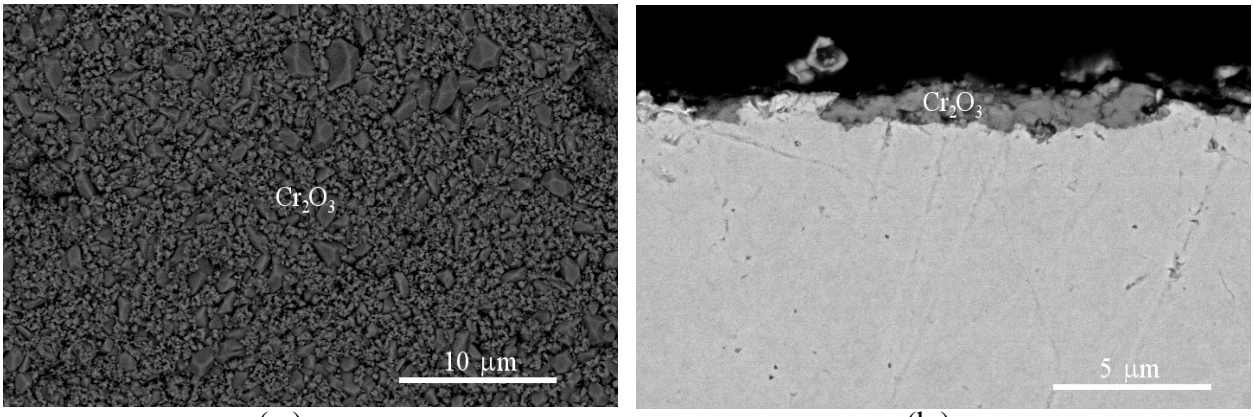

(g.) (h.)

Figure 5-34 SEM micrographs from the surface and cross-section of Fe-22Cr-0Ti exposed at 800°C for 521 cycles in dry air (a&b), 1000 cycles in dry air (c&d), 500 cycles in wet air (e&f), and 1000 cycles in wet air (g&h).

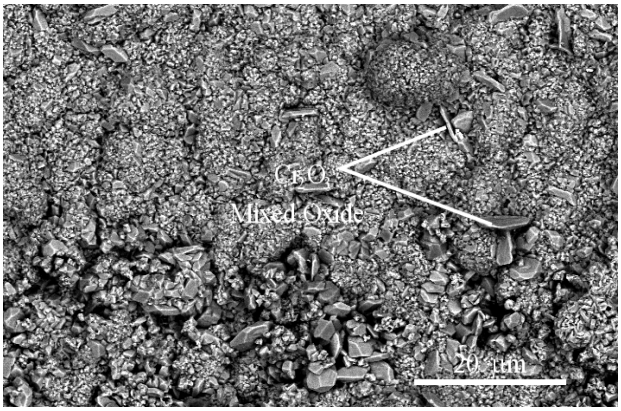
Cr_2O_3
Mixed Oxide
20 μm

(a.)

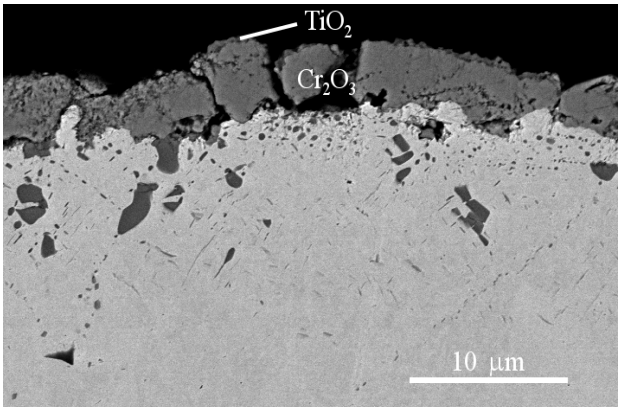
TiO_2
Cr_2O_3
10 μm

(b.)

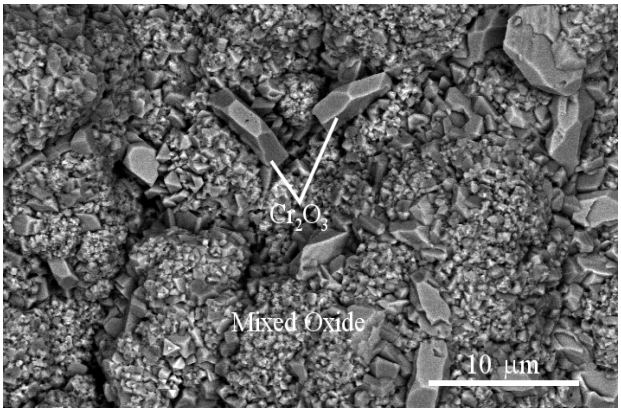
Cr_2O_3
Mixed Oxide
10 μm

(c.)

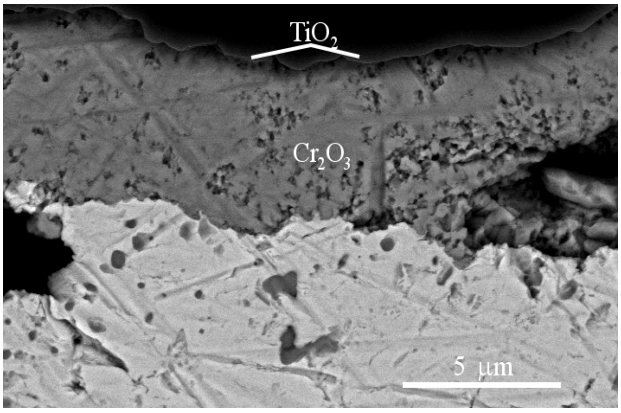
TiO_2
Cr_2O_3
5 μm

(d.)

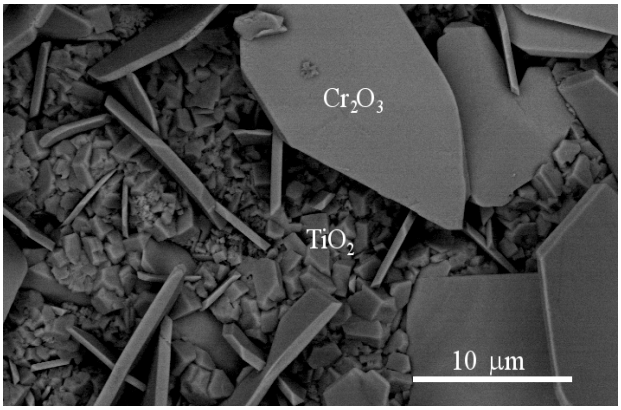
Cr_2O_3
TiO_2
10 μm

(e.)

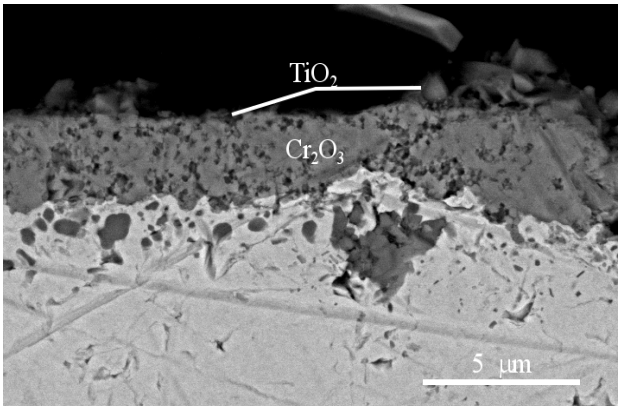
TiO_2
Cr_2O_3
5 μm

(f.)

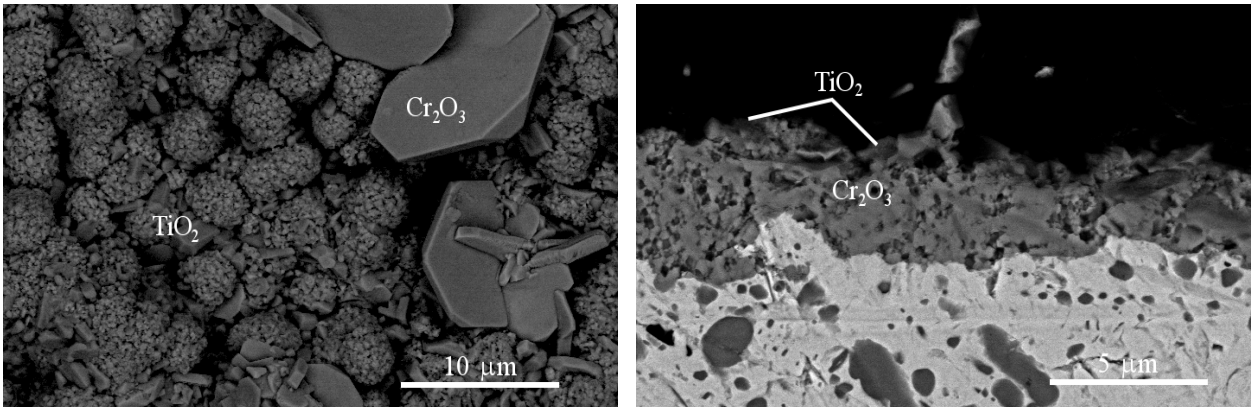

(g.) (h.)

Figure 5-35 SEM micrographs from the surface and cross-section of Fe-22Cr-0.84Ti exposed at 800°C for 521 cycles in dry air (a&b), 1000 cycles in dry air (c&d), 500 cycles in wet air (e&f), and 1000 cycles in wet air (g&h).

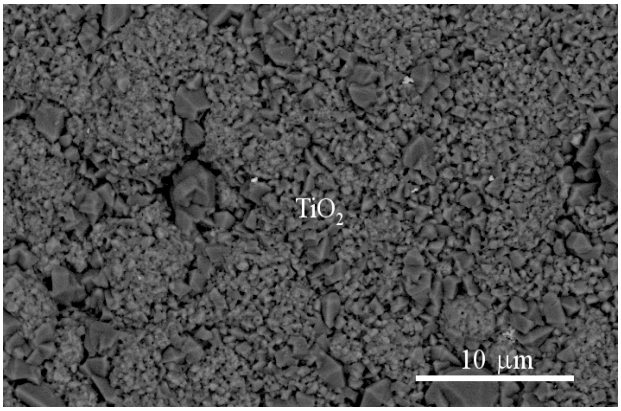
TiO2
10 μm

(a.)

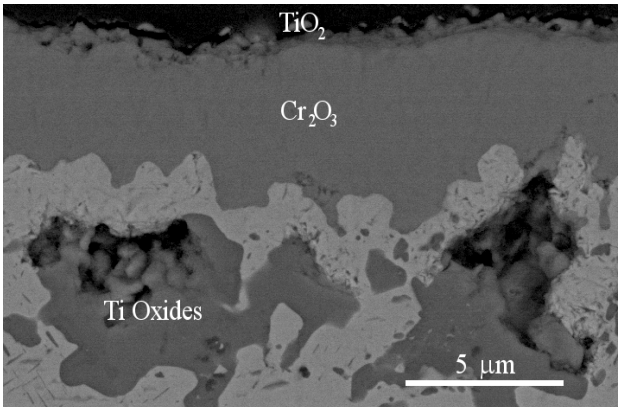
TiO2
Cr2O3
Ti Oxides
5 μm

(b.)

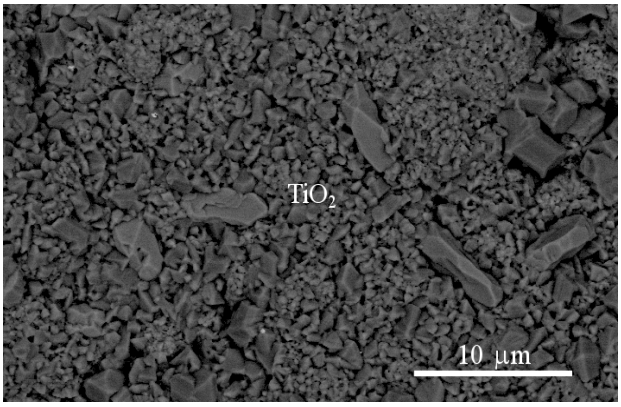
TiO2
10 μm

(c.)

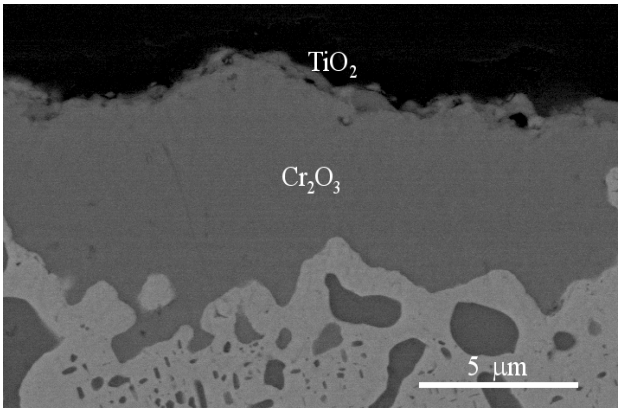
TiO2
Cr2O3
5 μm

(d.)

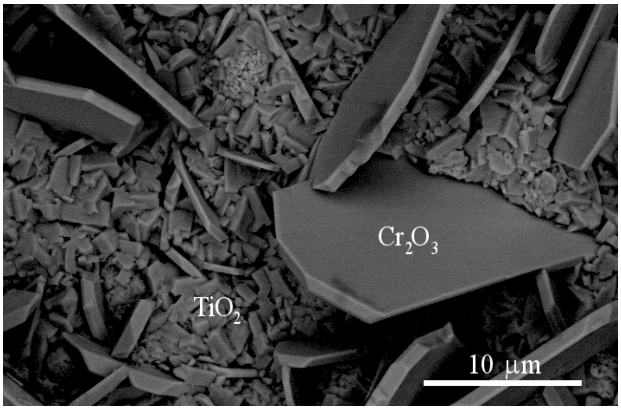
Cr2O3
TiO2
10 μm

(e.)

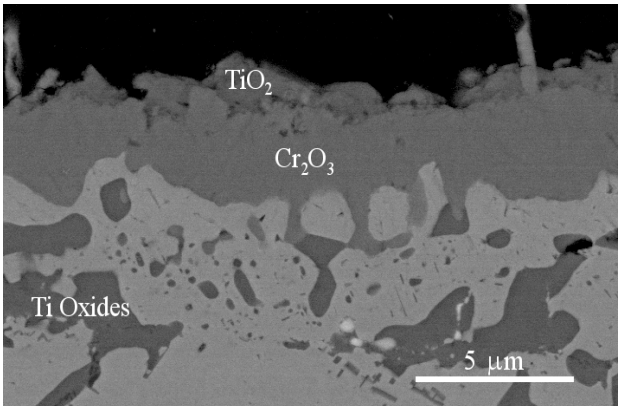
TiO2
Cr2O3
Ti Oxides
5 μm

(f.)

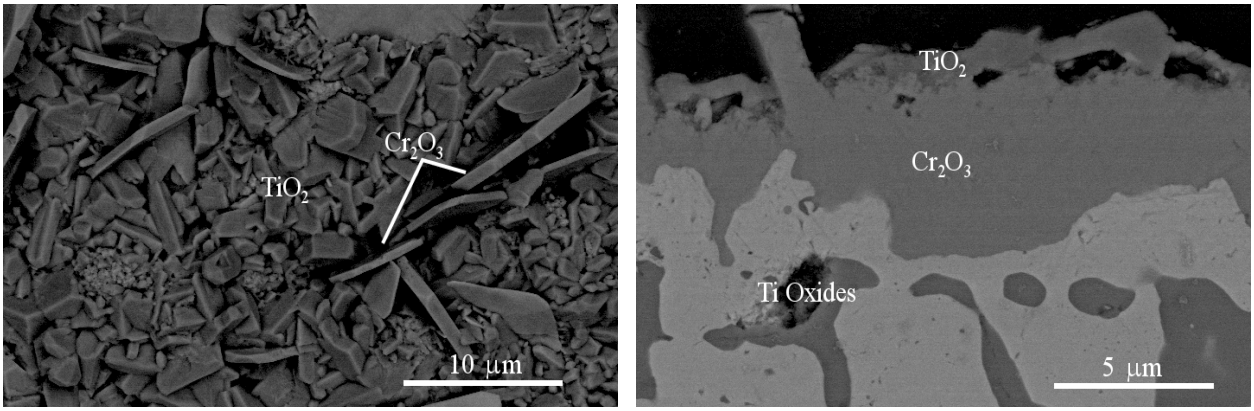

(g.) (h.)

Figure 5-36 SEM micrographs from the surface and cross-section of Fe-22Cr-1.65Ti exposed at 800°C for 568 cycles in dry air (a&b), 1000 cycles in dry air (c&d), 500 cycles in wet air (e&f), and 1000 cycles in wet air (g&h).

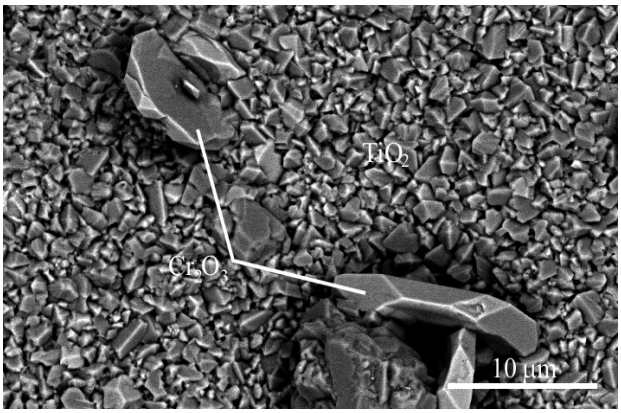
TiO_2
Cr_2O_3
10 μm

(a.)

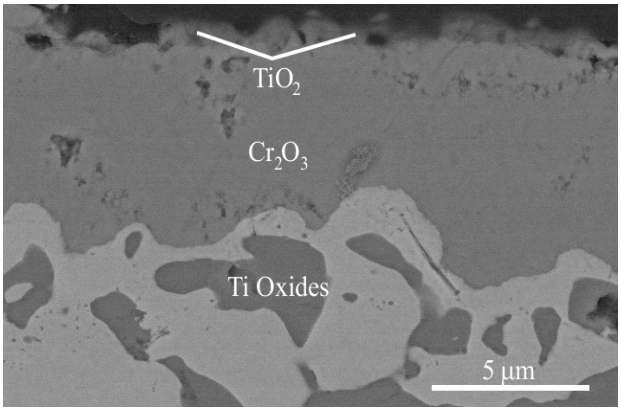
TiO_2
Cr_2O_3
Ti Oxides
5 μm

(b.)

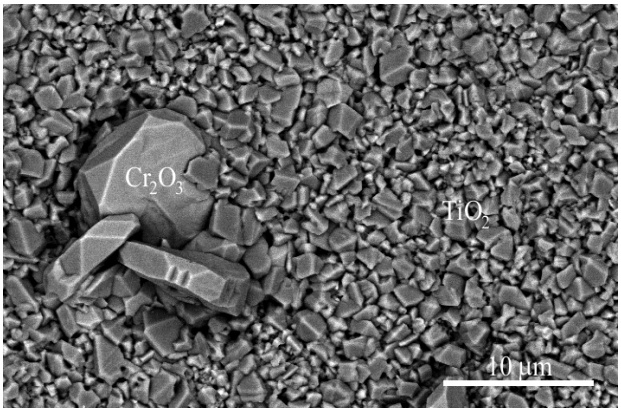
Cr_2O_3
TiO_2
10 μm

(c.)

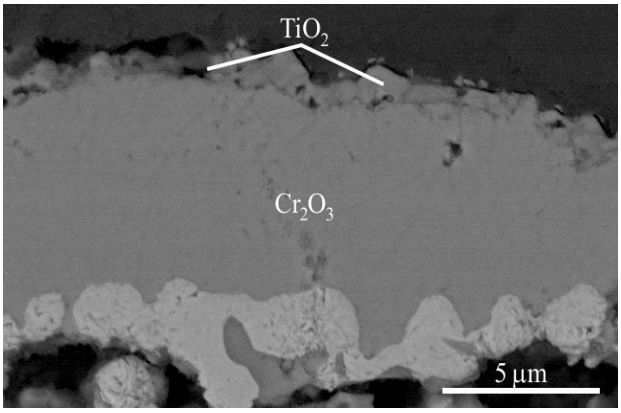
TiO_2
Cr_2O_3
5 μm

(d.)

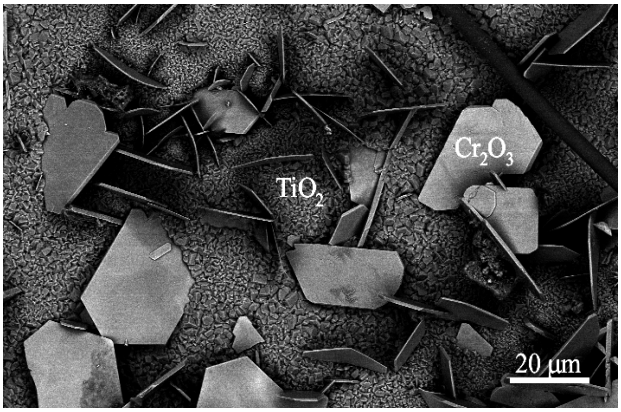
Cr_2O_3
TiO_2
20 μm

(e.)

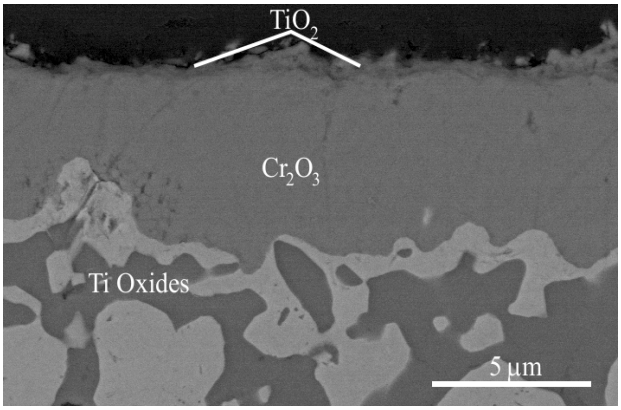
TiO_2
Cr_2O_3
Ti Oxides
5 μm

(f.)

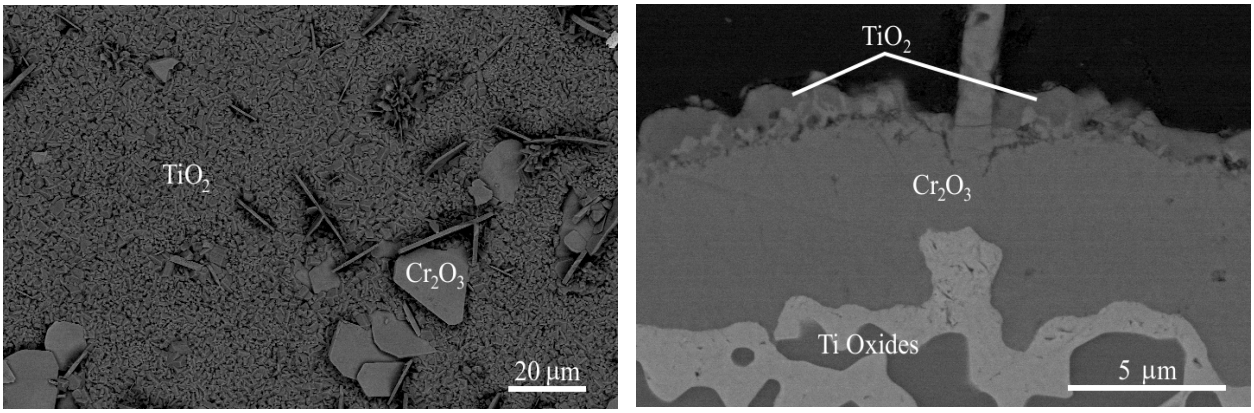

(g.) (h.)

Figure 5-37 SEM micrographs from the surface and cross-section of Fe-22Cr-2.78Ti exposed at 800°C for 521 cycles in dry air (a&b), 1000 cycles in dry air (c&d), 500 cycles in wet air (e&f), and 1000 cycles in wet air (g&h).

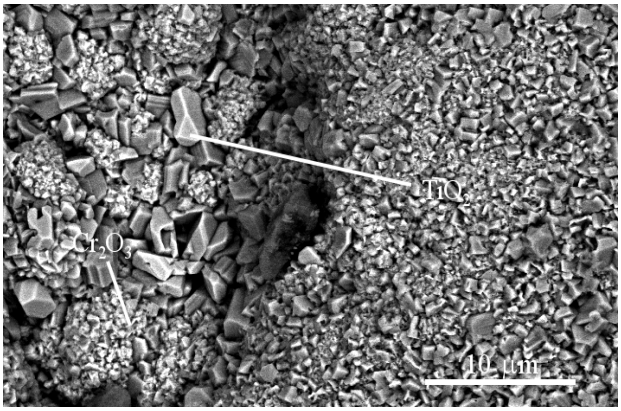
TiO2
Cr2O3
10 μm

(a.)

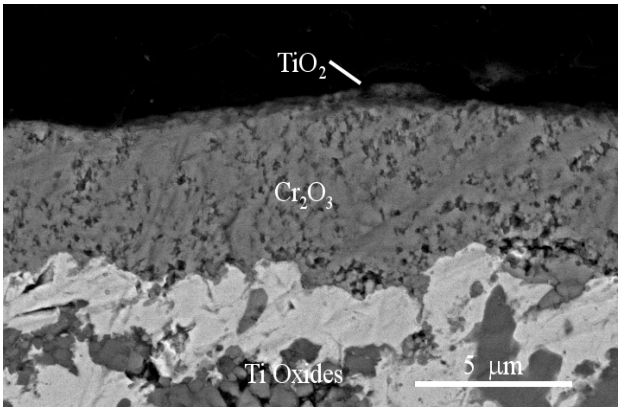
TiO2
Cr2O3
Ti Oxides
5 μm

(b.)

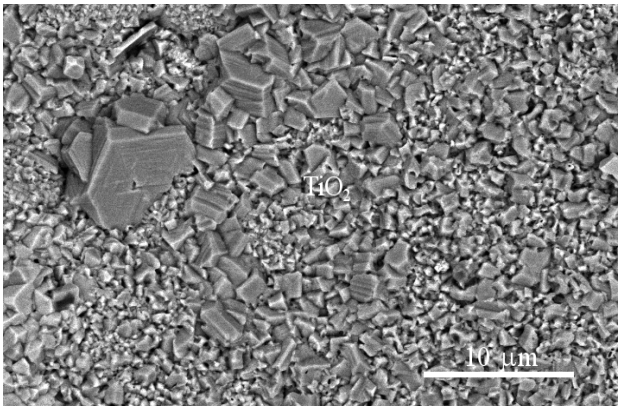
TiO2
10 μm

(c.)

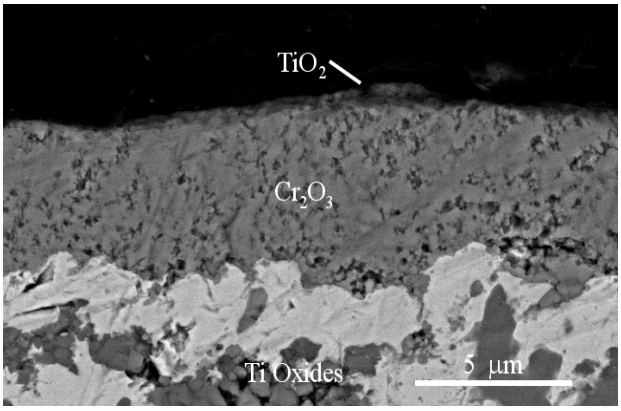
TiO2
Cr2O3
Ti Oxides
5 μm

(d.)

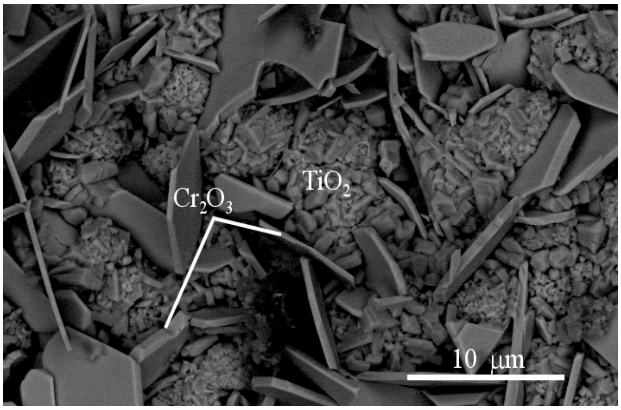
Cr2O3
TiO2
10 μm

(e.)

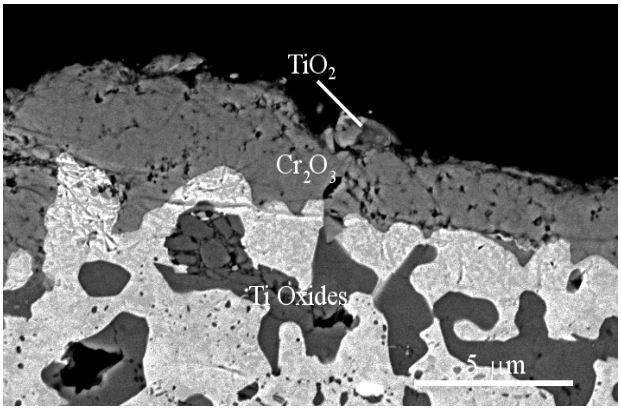
TiO2
Cr2O3
Ti Oxides
5 μm

(f.)

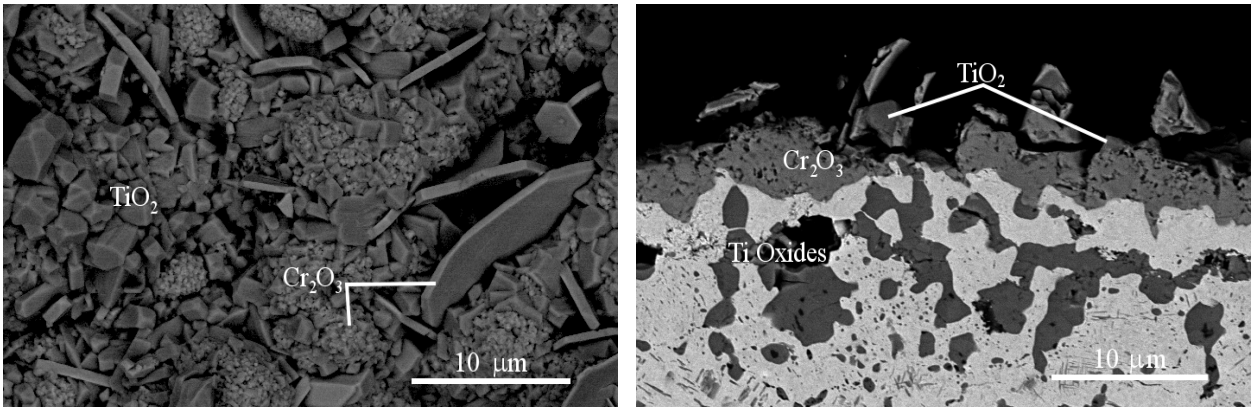

(g.) (h.)

Figure 5-38 SEM micrographs from the surface and cross-section of Fe-22Cr-3.98Ti exposed at 800°C for 521 cycles in dry air (a&b), 1000 cycles in dry air (c&d), 500 cycles in wet air (e&f), and 1000 cycles in wet air (g&h).

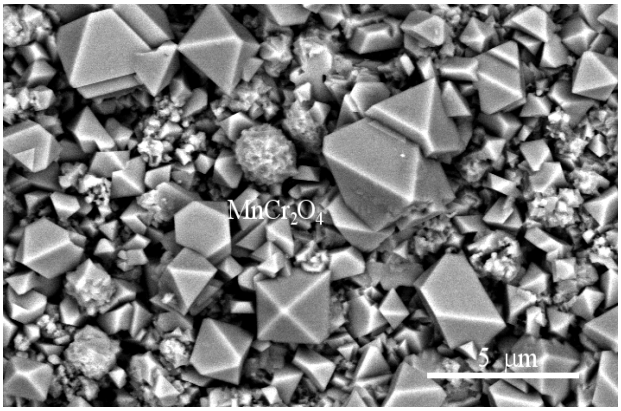
$MnCr_2O_4$
5 μm

(a.)

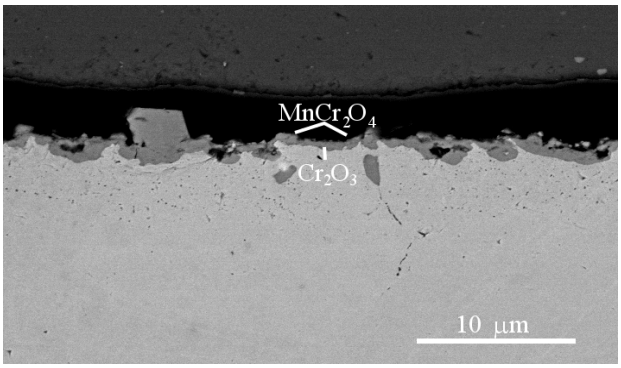
$MnCr_2O_4$
Cr_2O_3
10 μm

(b.)

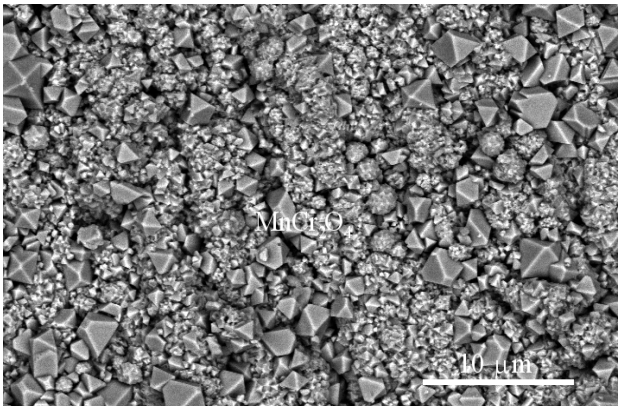
$MnCr_2O_4$
10 μm

(c.)

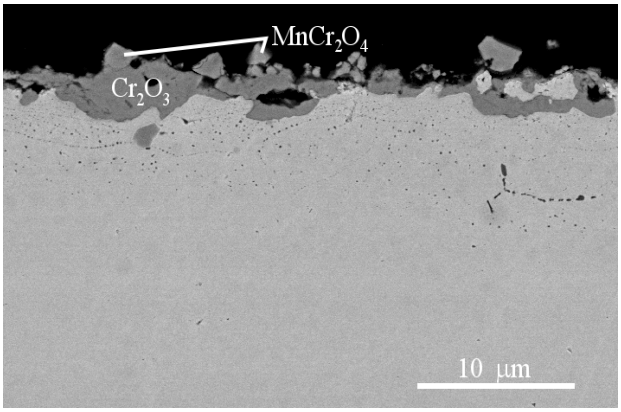
$MnCr_2O_4$
Cr_2O_3
10 μm

(d.)

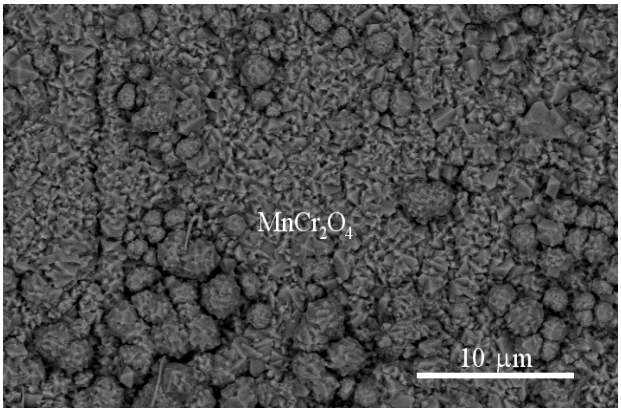
$MnCr_2O_4$
10 μm

(e.)

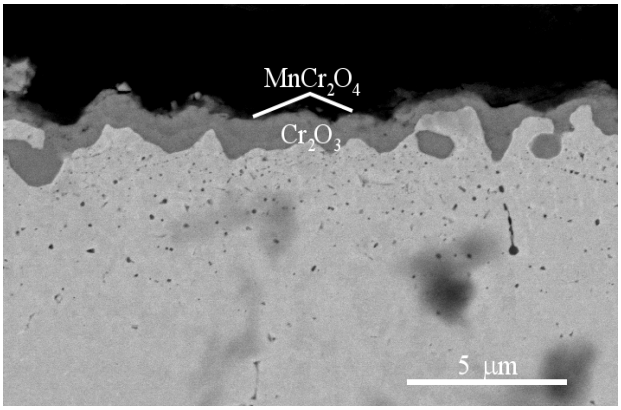
$MnCr_2O_4$
Cr_2O_3
5 μm

(f.)

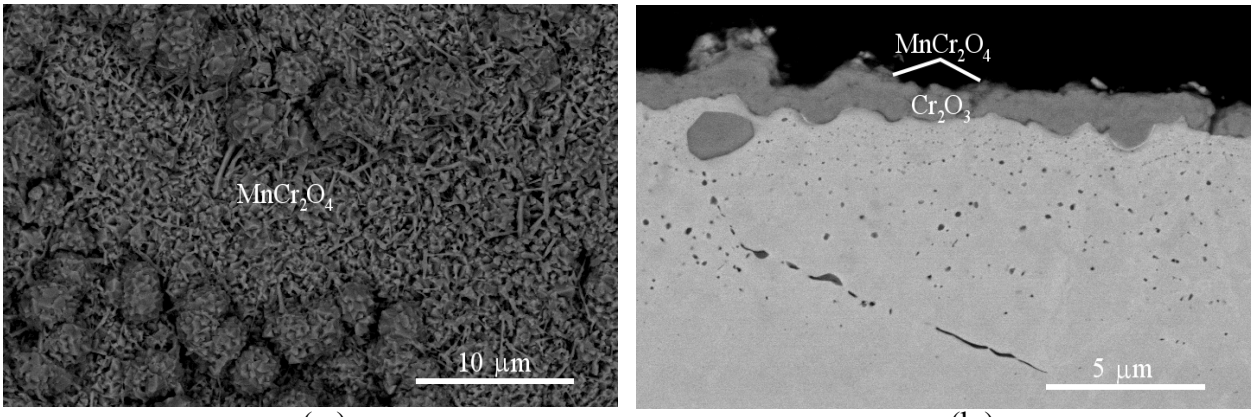

(g.) (h.)

Figure 5-39 SEM micrographs from the surface and cross-section of Crofer exposed at 800°C for 521 cycles in dry air (a&b), 1000 cycles in dry air (c&d), 500 cycles in wet air (e&f), and 1000 cycles in wet air (g&h).

5.2.2.5 Dual Atmosphere: Dual atmosphere experiments were performed at 800°C for 96 hours in order to simulate the real conditions to which an interconnect would be exposed in a SOFC. The micrographs in Figures 5-40 - 44 are representative of the cross-sections and surfaces (in some cases) of the air and fuel sides of each material. The examination will focus on determining if there are any nodules formed, if any voids formed, and/or if the oxide on the air side is much thicker than that for a dry air only exposure. The majority of the work focuses on the air side behavior, because that is where the oxidation related dual atmosphere effects have been reported.

Figure 5-40a&b shows the cross-section and surface of the cathode side of the baseline alloy. The surface morphology is very faceted, much more so than any of the other samples in this work. There are no signs of nodules on the surface, or iron for that matter. No exposure was done in dry air for the same time to directly compare the oxide thicknesses, but the TGA results, at 168 hours, can be used. Comparing to Figure 5-21b, the dual atmosphere air side oxide is, as expected, thinner. This could indicate more rapid growth of the oxide in the dual atmosphere sample, among other things. Of course only a directly comparable sample could determine for certain that more growth has or has not occurred. Voids are also not present. On the fuel side, the surface morphology (Figure 5-40c) is more fibrous, which is typical of oxides grown in wet conditions. Due to poor edge retention during the mounting of the sample, a cross-section of the fuel side was not obtained, despite several attempts. A possible increase in the oxide thickness is the only dual atmosphere effect observed in this sample for this exposure time.

Figures 5-41 - 44 are the dual atmosphere results for the Ti bearing alloys. The surface micrographs of the 0.84% (Figure 5-41) and 1.65% Ti (Figure 5-42) alloys on the cathode side are very similar, with a several thick blades. There are no signs of nodule formation. The fuel

side surface for the 0.84% Ti alloy (Figure 5-41c) has some blades, but has mostly a mound type morphology. The comparable surface for the 1.65% Ti alloy (Figure 5-42c) has a very small scale fibrous morphology with some raised sections. The surface micrographs for the 2.78% and 3.98% Ti alloys were not taken.

In cross-section, voids and nodules are also not present on the air side. Table 5-3 lists the oxide thicknesses of the air side and the 100 hour exposures from the progression of oxide growth experiment. The results of the comparison show that the alloys with no Ti or very little Ti have an increased oxide thickness in the dual atmosphere conditions compared with that for the air only conditions. The claim that Ti doping in chromia reduces the effects of hydrogen by Holt and Kofstad is in effect here and that the 0.84% an 1.65% Ti alloys do not have enough Ti to prevent hydrogen from affecting change in the oxide growth. On the fuel side, the oxides are typically thinner and more irregular. There are large particles of titania on the surface and more extensive internal oxidation than on the air side. Both of these are likely due to the low oxygen pressure environment and the material trying to preferentially form the more stable oxide.

A sample of the 1.65% Ti alloy was also exposed for 373 hours (Figure 5-45). The morphological features on both sides of the sample (Figures 5-45a&c) are identical to those for the shorter time (Figures 5-42a&c), with the addition of large TiO_2 particles now visible on the surface of the fuel side. The cross-sections (Figures 5-45b&d) are also very similar to the shorter time. Comparing the oxide thickness to the 360 hour isothermal exposure in dry air from the growth progression experiments (Figure 5-28f) shows that the oxides are similar. Assuming there is no difference in the this sample and the shorter time, then time seems to reduce any visible dual atmosphere effect. This could be due to the rutile layers gaining continuity and retarding the solution of hydrogen into the sample.

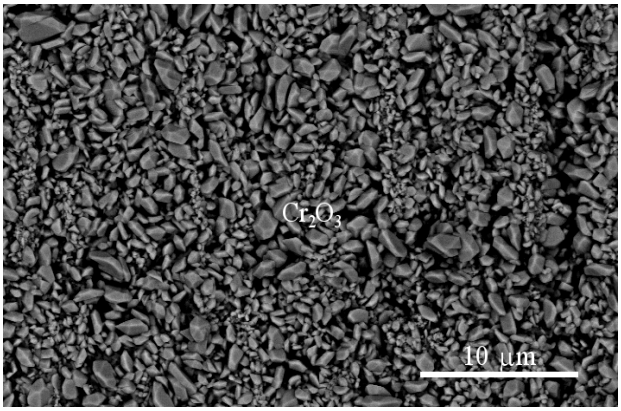

(a.)

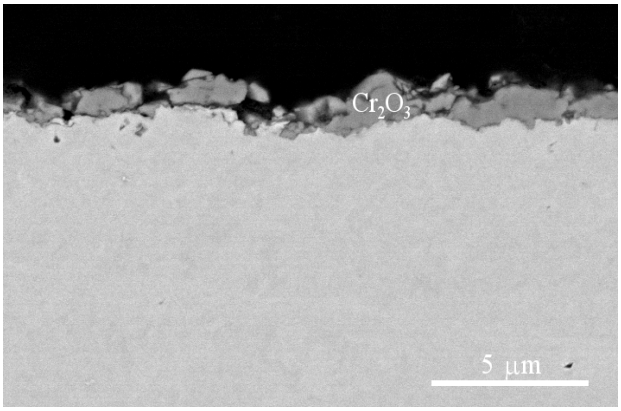

(b.)

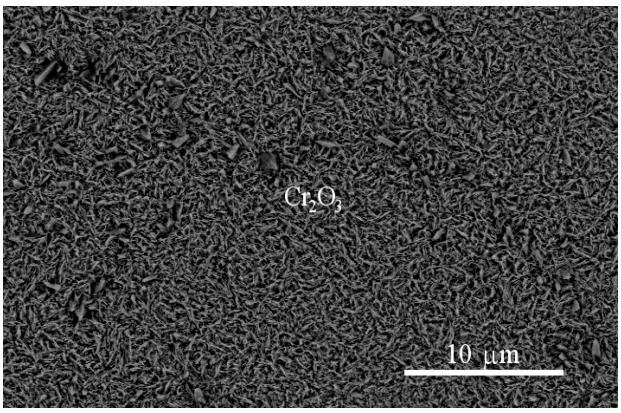

(c.)

Figure 5-40 SEM micrographs of the surface and cross-section of the air (a&b) and fuel (c) sides of Fe-22Cr-0Ti exposed 96 hours at 800^{o}C in a dual atmosphere.

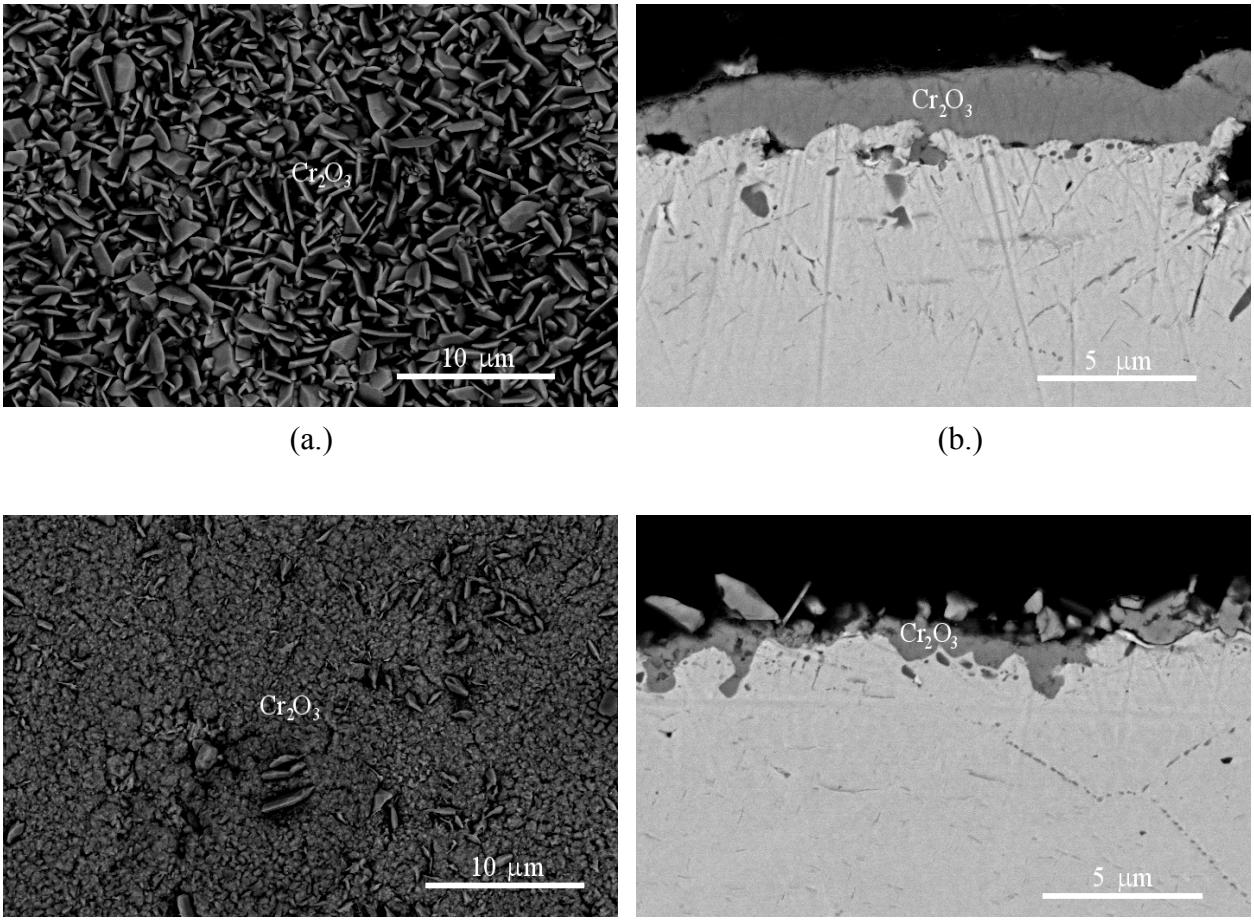

Figure 5-41 SEM micrographs of the surface and cross-section of the air (a&b) and fuel (c&d) sides of Fe-22Cr-0.84Ti exposed 96 hours at 800^{o}C in a dual atmosphere.

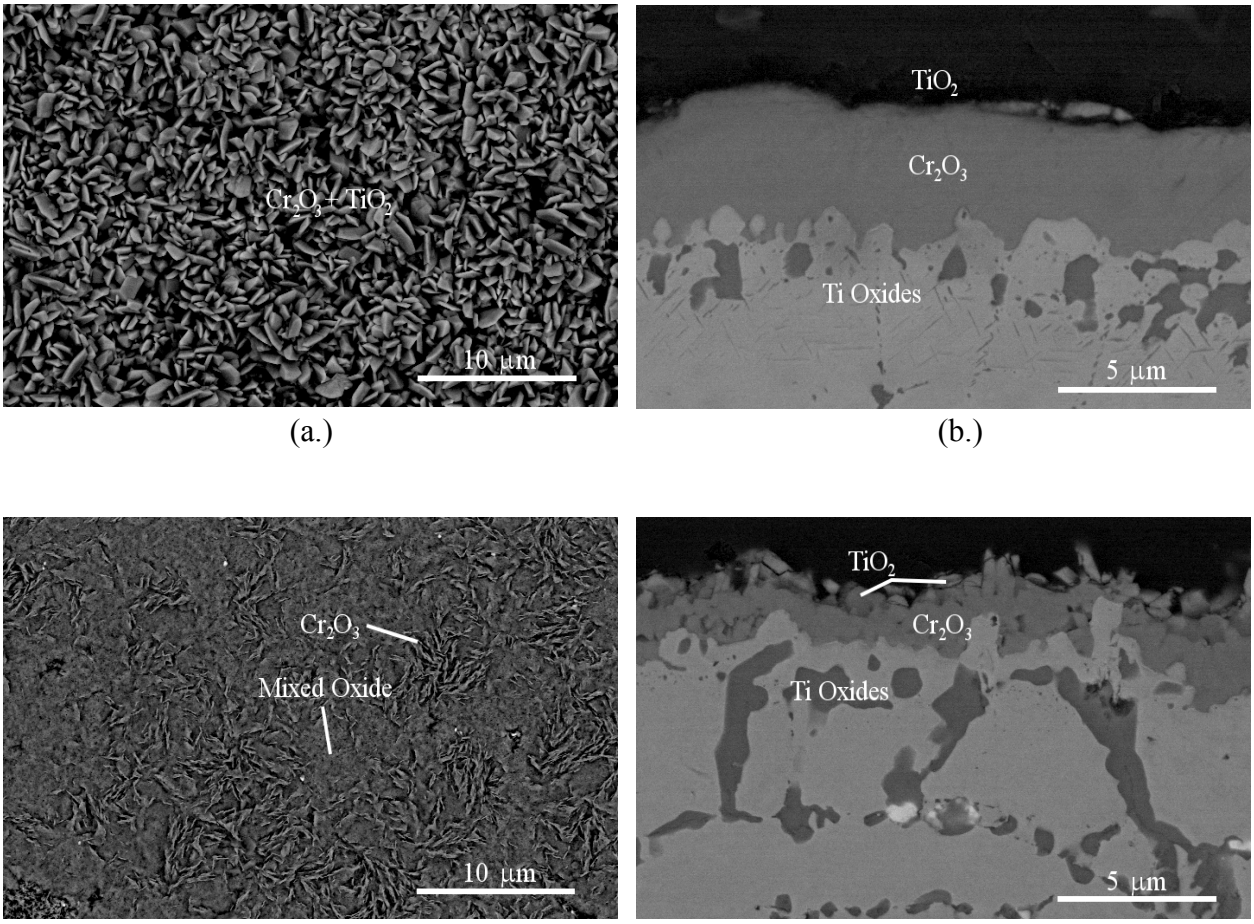

(a.) (b.)

(c.) (d.)

Figure 5-42 SEM micrographs of the surface and cross-section of the air (a&b) and fuel (c&d) sides of Fe-22Cr-1.65 Ti exposed 96 hours at 800^{o}C in a dual atmosphere.

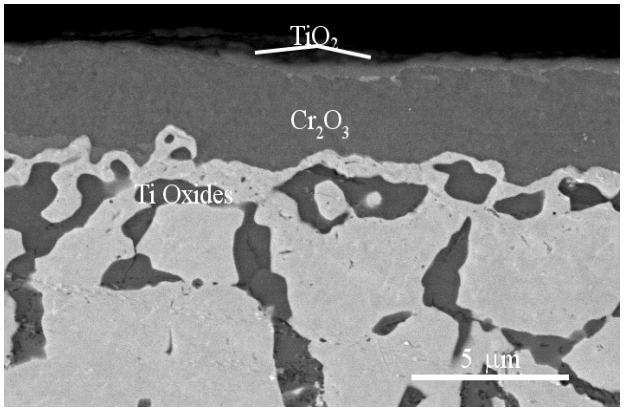

(a.)

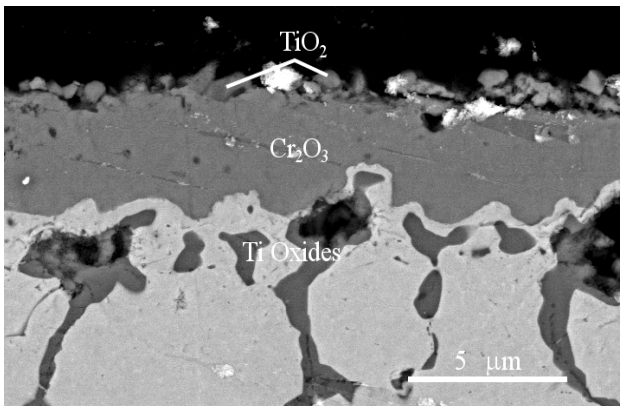

(b.)

Figure 5-43 SEM micrographs of cross-sections of the air (a.) and fuel (b.) sides of Fe-22Cr-2.78 Ti exposed 96 hours at 800°C in a dual atmosphere.

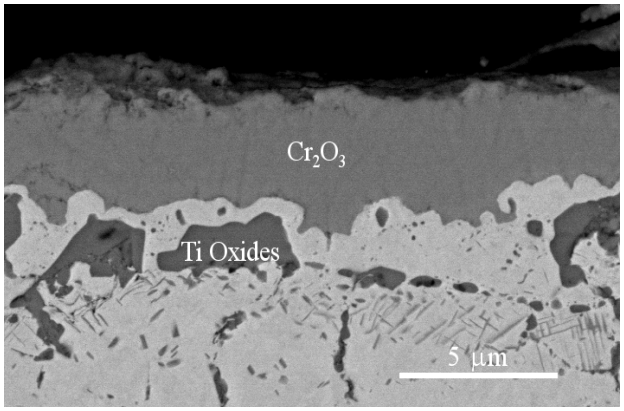

(a.)

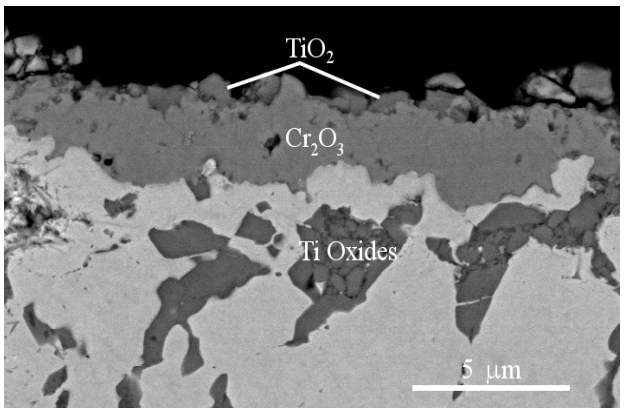

(b.)

Figure 5-44 SEM micrographs of the cross-section of the air (a.) and fuel (b.) sides of Fe-22Cr-3.98Ti exposed 96 hours at 800^{o}C in a dual atmosphere.

Table 5-3 Comparison of the oxide thickness for specimens exposed in dry only and the air side of a dual atmosphere exposure for 96 hours (unless otherwise noted).

	Oxide Thickness (μm)	
Alloy	Dry Air	Dual Atmoshere
0	2.25 (168 hrs)	2
1	0.75	2.5
2	2	3-4
3	4	4
4	2.25	2.5
2 (360hrs)	5	4-5

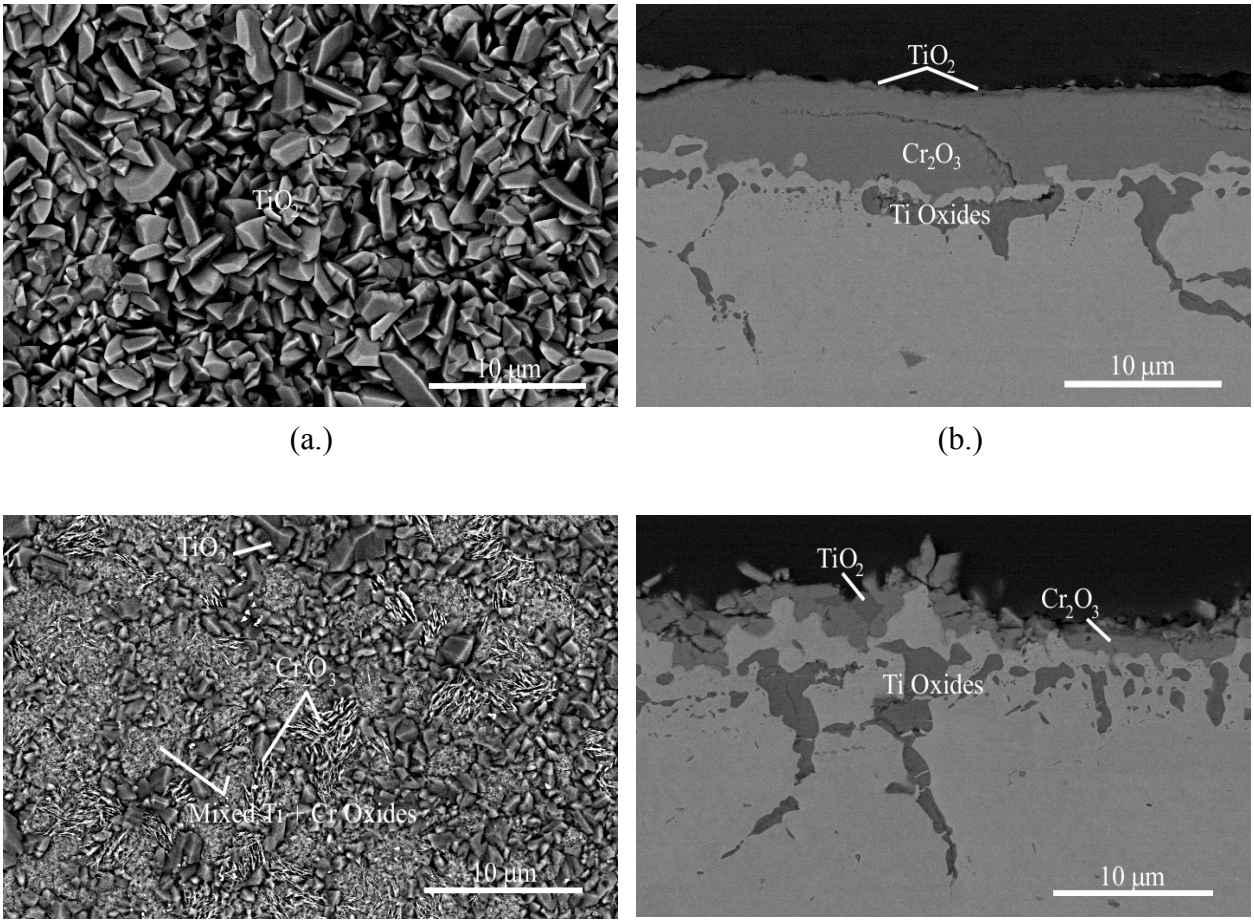

Figure 5-45 SEM micrographs of the surface and cross-section of the air (a&b) and fuel (c&d) sides of Fe-22Cr-1.65 Ti exposed 373 hours at 800°C in a dual atmosphere.

5.2.2.6 In Cell Testing: While all of the previously mentioned testing done on these alloys is meant to simulate the conditions of an SOFC, this in cell testing is to actually use the materials as an interconnect in a single cell on the cathode side. Due to the fact that this is a single cell test, it is a test for the effects of growth rate and vaporization, rather than the behavior in the dual atmosphere. Samples of E-Brite, Crofer 22APU, and Fe-22Cr-3Ti were prepared and tested. The Crofer and Fe-Cr-Ti samples were preoxidized for 24 hours at 900^{o}C in dry air in an attempt to preform their protective overlayers. The surface of Crofer was mostly manganese chromate, with ring shaped regions that were slightly higher in chromium. The Fe-22-3Ti alloy surface had large areas that were covered with rutile, but there were also large patches with the mound morphology, which typically are much higher in chromium. The sample geometry required for the test made it difficult to achieve a uniform surface finish and the higher chromium regions appear to correspond to areas that appeared higher in roughness. E-Brite does not form a protective overlayer, and was therefore not preoxidized. The results for the test are plotted in Figure 5-46 as current vs. time.

After an intermediate level of initial performance (as determined by the current at t=0 on the plot), the degradation of performance was the most rapid with E-Brite and the test was stopped after about 16 hours. Returning the cell to open circuit voltage shows recovery (identified by the jump in the data), but the current drop off is extremely rapid afterwards (rapid decrease after the jump) and returns to the same level of current after only a few hours (Figure 5-46). Experience dictates that this is usually due to cathode poisoning, which is expected with the chromia only scale that E-Brite forms[58]. Figure 5-47 is a X-ray map of the fracture surface of the used cell. The bright red region corresponds to the electrolyte material, which consists largely of Zr. The blue regions are cathode material, and in this case are determined by Mn. Mn was

chosen as the marker in order to determine if large concentrations of Mn and Cr corresponded, which would imply that manganese chromate has formed there. Cr is shown as green on the map. The map is focused on the intermixed zone between the cathode and electrolyte. In this region, it is possible to see what appears to be a continuous network of green (Cr) between the red (Zr) and blue (Mn), lending to the conclusion that this cell was poisoned.

Crofer degraded the slowest of the three after the worst initial performance, with the test stopped after about 46 hours. The slow decrease is due to the slow growth rate of the oxide and the decrease in the vaporization rate due to the thermally grown overlayer. The fact that it does show a noticeable increase does indicate that there is likely some poisoning occurring, but at a much reduced rate relative to E-Brite. This test did not include a return to open circuit voltage. The X-ray map in Figure 5-48 shows some poisoning.

The results for the Fe-22Cr-3Ti alloy are more difficult to analyze. The initial performance was by far the best. The rate of degradation was rapid, but partitioning the amount due to poisoning from that due to the rapid oxidation rate is difficult. To further complicate the issue, one of the leads came loose during the test, resulting in a 10 hour period with no data recorded. Reattaching the lead was effectively a return to open circuit voltage and a small recovery is seen. This was followed by a very short period of rapid decrease and then slow degradation until the test was stopped at 40 hours. The rapid decrease period could be due to a small amount of poisoning, as seen in Figure 5-49, because the TiO_2 layer was not continuous. Once again, experience says that the slower decrease period is then due to oxidation with a small amount of poisoning[58]. An identical sample with better surface preparation has been prepared

and is in queue for retesting. Samples of the 3% and 2% alloys are also set to be tested that have been preoxidized in wet air at 800^{o}C for 2 hours in order to perform a thin TiO_2 layer while vaporizing any Cr_2O_3 that might form during the treatment.

It is difficult to determine which of the two samples that form protective overlayers performed better in this test. Both alloys did show signs of poisoning the cathode, but it is not directly measureable. It is important to note that the preoxidation treatment chosen does in fact favor Crofer, as the conditions where chosen based on the short time experiments described above. No detailed work was done to determine the optimum conditions to preform either overlayer, so the conditions were chosen when the manganese chromate layer was known to be continuous. The initial performance of the Ti bearing alloy was nearly twice that of Crofer, but dropped rapidly. This reinforces the need to develop a technique for reducing the growth rate and vaporization rate, as 50 hours to failure is entirely too short for SOFC applications. It is possible that the situation could have improved had the tests been run for a longer period of time. Ni was tested and showed a curve that was similar to that for Crofer, with the exception that the current started to increase with time. Given the fact that chromia is very slow to equilibrate, the current may have also began to rise for the Crofer and Fe-Cr-Ti alloys, assuming poisoning was not a major factor. The in situ type ASR tests that are performed by Yang[38] show that the ASR of Crofer can actually decrease for 200-250 hours before beginning to slowly increase. Once again, if poisoning is held in check, it should be possible for at least Crofer, if not both alloys to recover some of the performance that was lost.

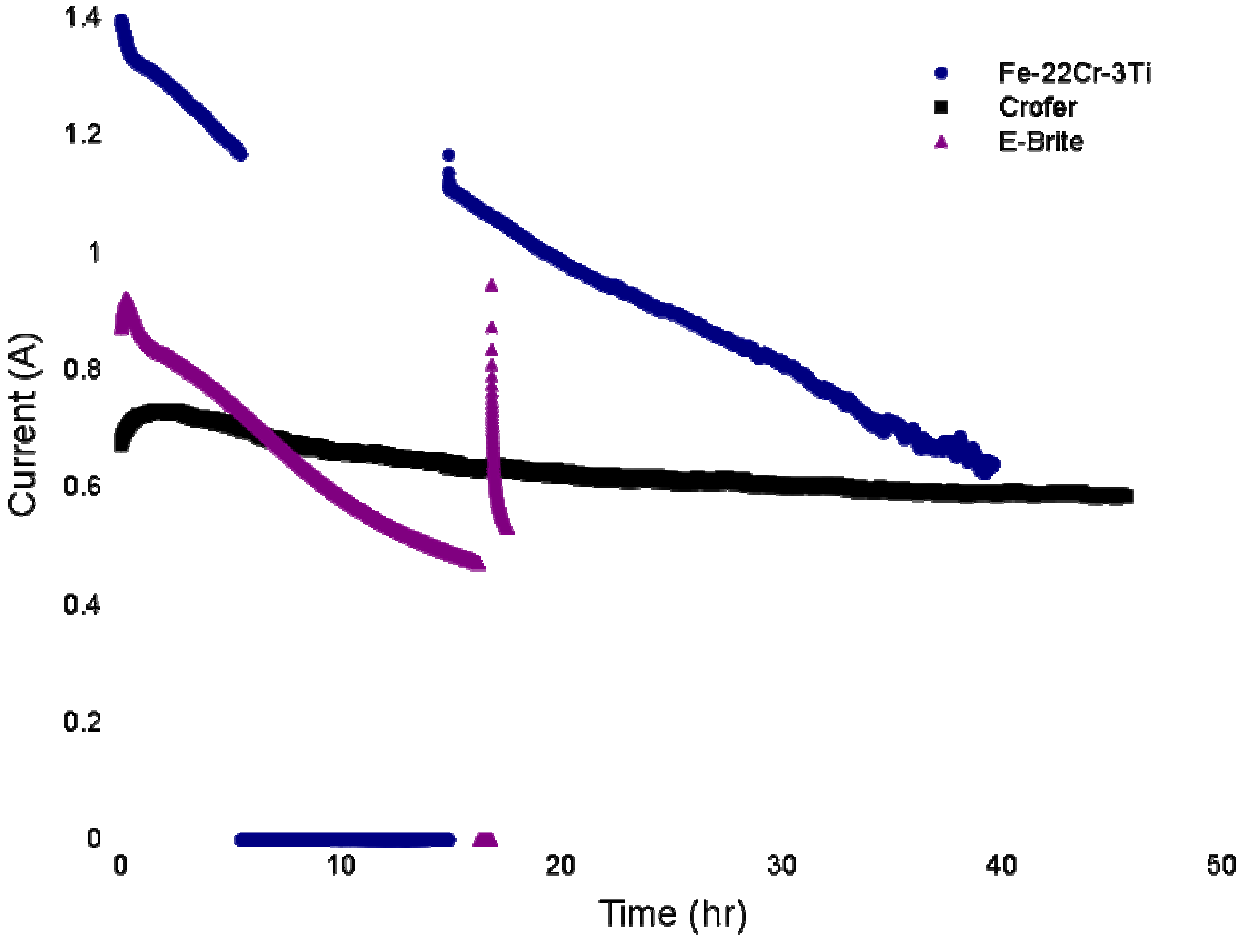

Figure 5-46 Current vs. Time plot for the button cell tests with E-Brite, Crofer, and the Fe-22Cr-2.78Ti alloy used as the cathode side inteconnect.

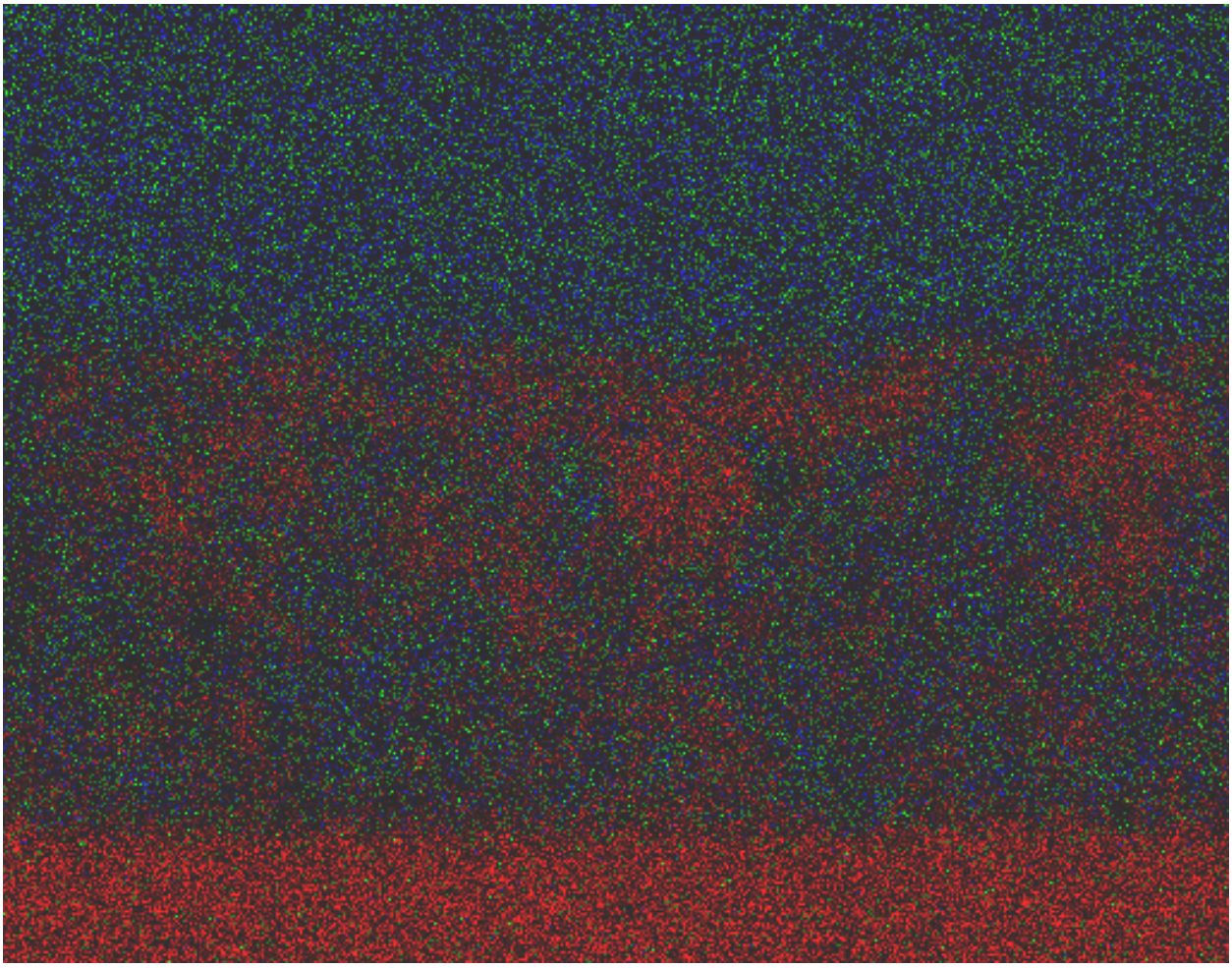

Figure 5-47 X-ray map taken from the cross-section of the button cell used in a cell test with E-Brite as the cathode side interconnect (Red = Zr, Blue = Mn, and Green = Cr)

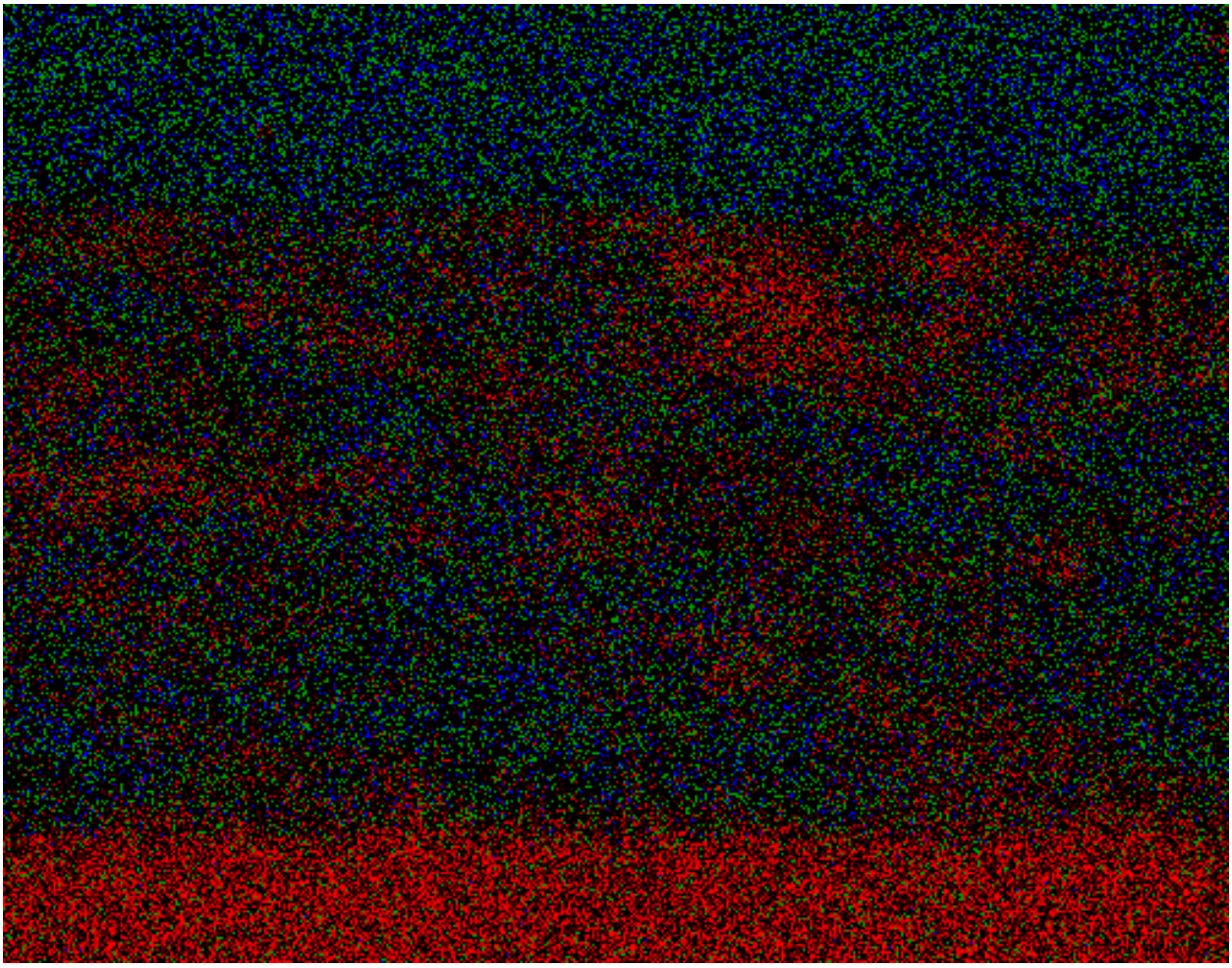

Figure 5-48 X-ray map taken from the cross-section of the button cell used in a cell test with Crofer as the cathode side interconnect (Red = Zr, Blue = Mn, and Green = Cr)

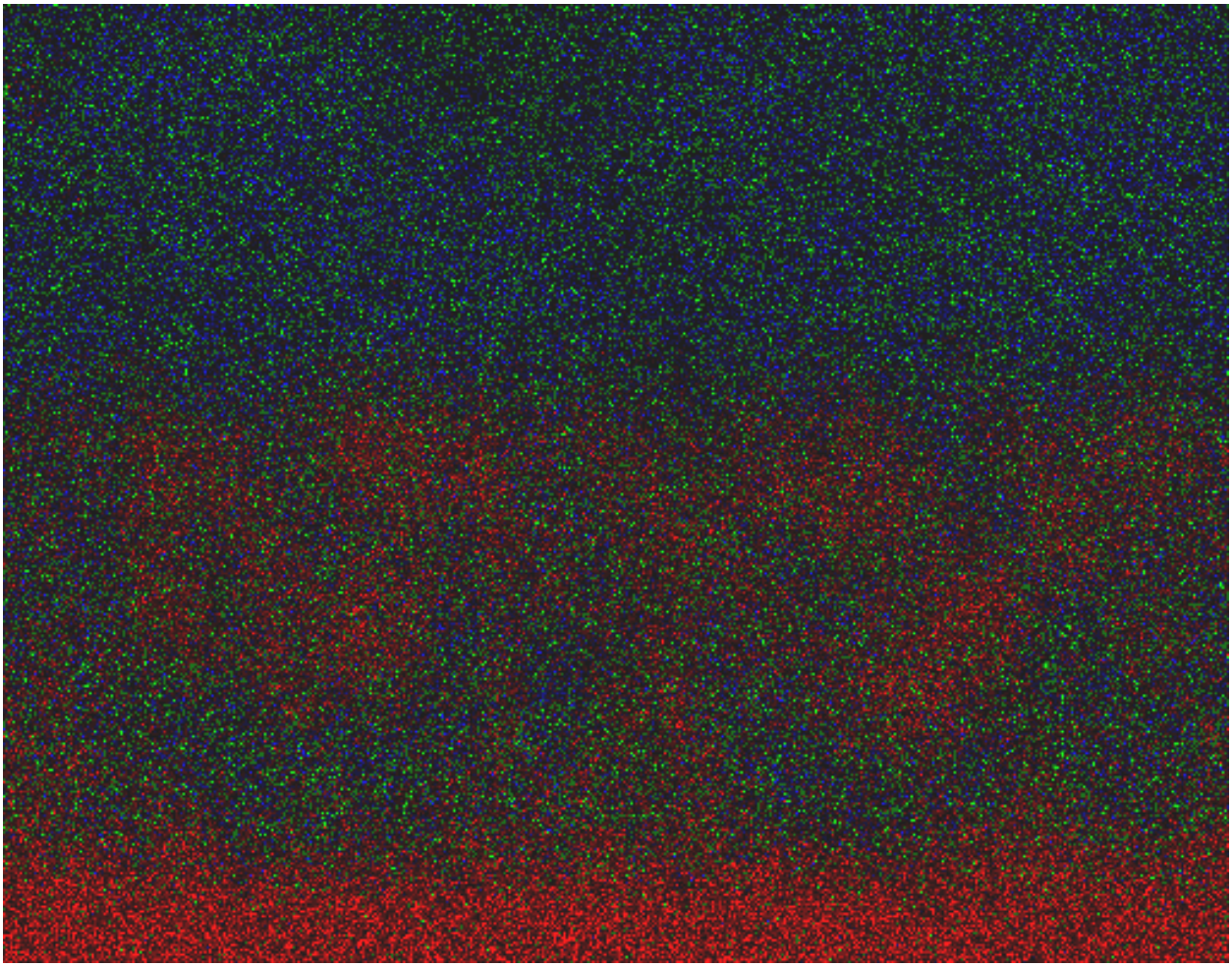

Figure 5-49 X-ray map taken from the cross-section of the button cell used in a cell test with the Fe-22Cr-2.78Ti alloy as the cathode side interconnect (Red = Zr, Blue = Mn, and Green = Cr)

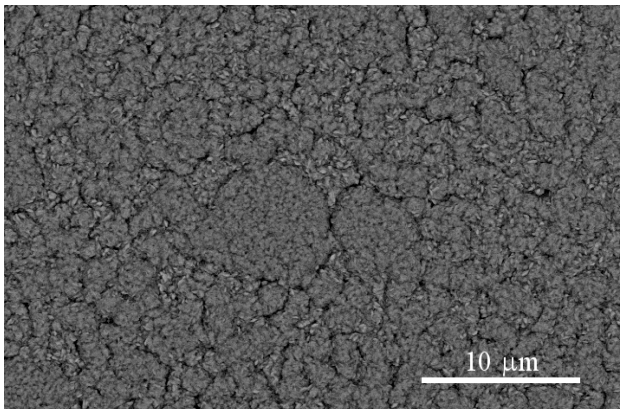

(a.)

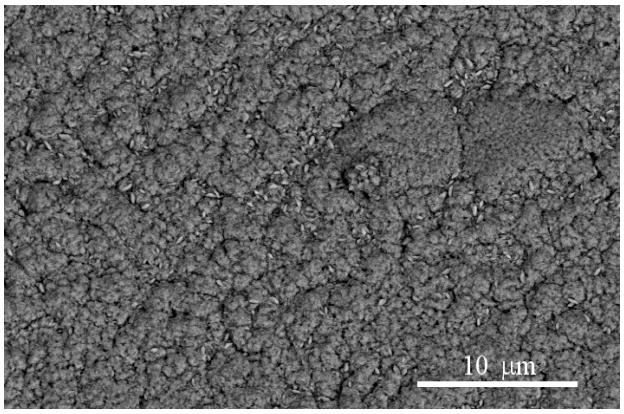

(b.)

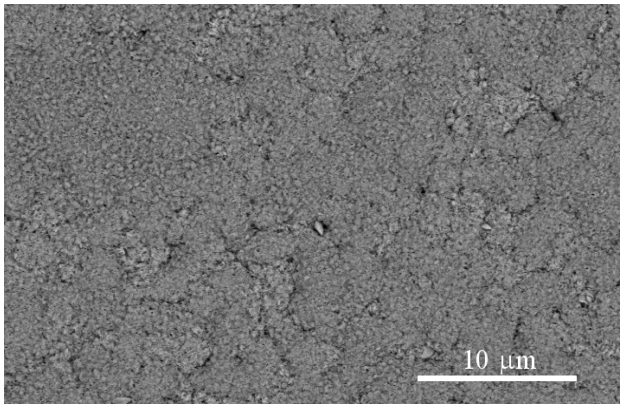

(c.)

Figure 5-50 SEM micrographs of 2.78 %Ti alloy exposed at 800^{o}C for 1 hr (a.), 2 hr (b.), and 16 hr (c.)

5.2.2.7 Short Time Tests: Samples of the 2.78% Ti alloy were exposed for short times, similarly to the exposures for Crofer to determine the mechanism for rutile formation on top of the chromia scale. Figure 5-50a shows the surface after 1 hour of exposure. The oxide is a mixture of both chromia and titania with no clear separation of each phase. This trend continues in Figures 5-50b&c, which are after 2 and 16 hours. It is not clear if the the titania layer forms the same way as manganese chromate from these tests. There is nearly three times as much Ti in the alloy as there is Mn in Crofer, which means that Ti does not need to depend on alloy grain boundary diffusion as strongly as Mn in Crofer to diffuse to the oxide surface. The more bulk nature allows Ti to be incorporated everywhere simultaneously. Much more detailed work needs to done at shorter times to determine more specifics about how this phenomenon occurs.

5.2.3 Testing at 700^{o}C

Due to the fact that there will always be a push to lower the SOFC operating temperature, exposures were also performed at 700^{o}C for 96 hours in dry air. SEM observations of the surface show that there is mostly chromia on the surface of the samples (Figure 5-51a, c, e, g &i). There are some titania particles on the surface, but they are not easily discernible from some of the chromia particles. As expected, the baseline alloy forms chromia only. There does appear to be a significant increase in the amount of titania particles on the samples as the Ti content increases. Once again, the particles are still few in number and a continuous layer has not formed in any case. Observing the cross sections of these samples was very difficult, as the oxides were very thin. All of the alloys had scales of one micron or less (Figures 5-51b, d, f, .h,&j) With the higher temperature exposures, the thickness of the chromia and amount of internal oxidation increased with Ti content up to the 2.78% Ti alloy then was thinner for the

3.98% Ti alloy. Some sort of preoxidation (higher temperature or longer time at 700^{o}C) must be done in order to quickly form the TiO_2 layer if this material is to suppress vaporization from the beginning of its lifetime in a fuel cell at lower temperatures.

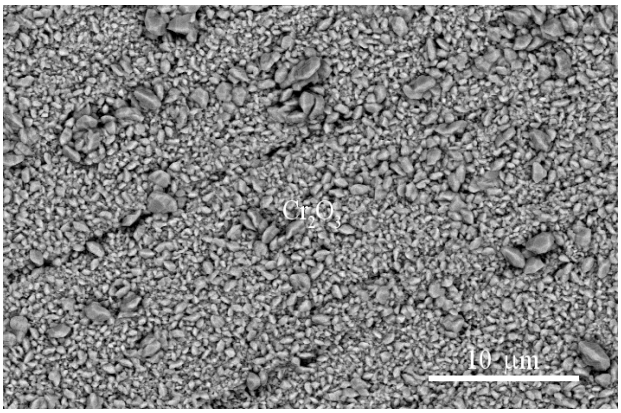
Cr_2O_3
10 μm

(a.)

(b.)

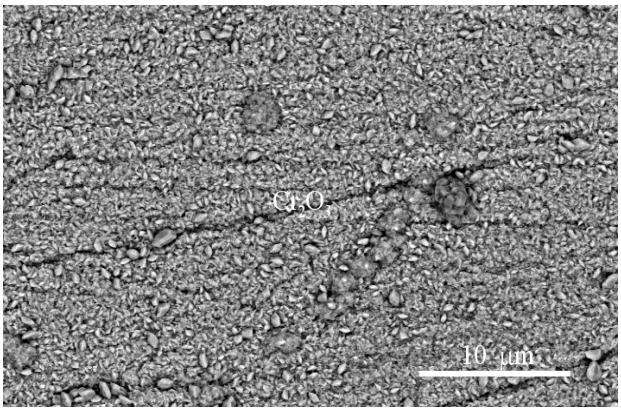
Cr_2O_3
10 μm

(c.)

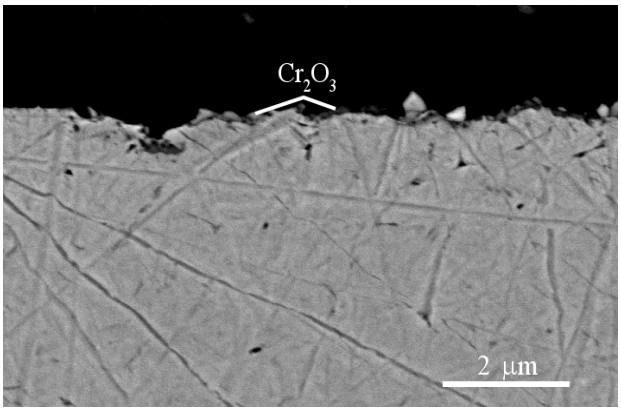
Cr_2O_3
2 μm

(d.)

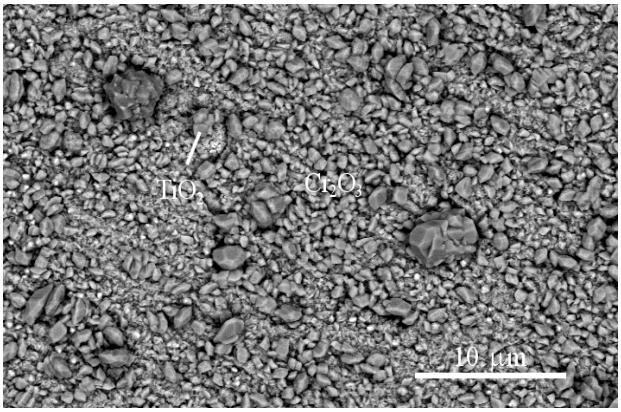
TiO_2
Cr_2O_3
10 μm

(e.)

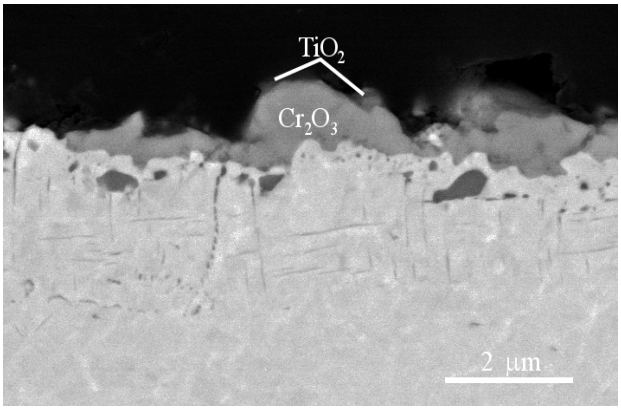
TiO_2
Cr_2O_3
2 μm

(f.)

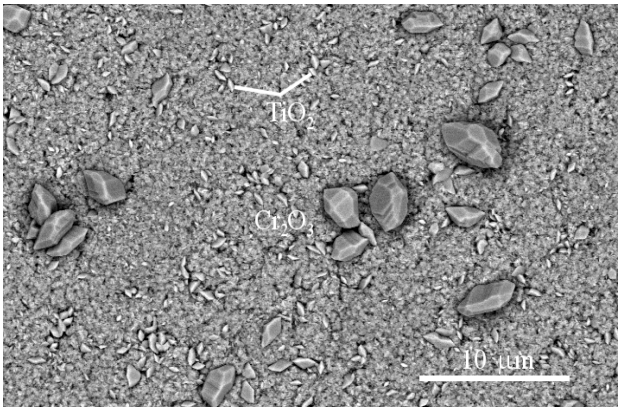

(g.)

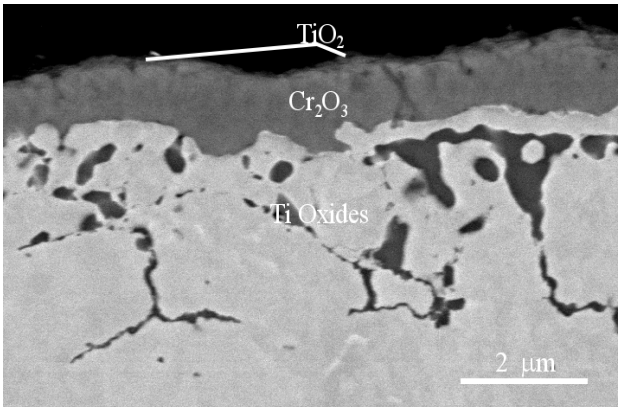

(h.)

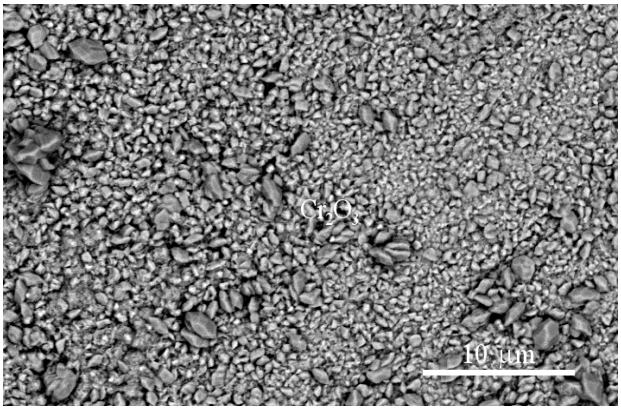

(i.)

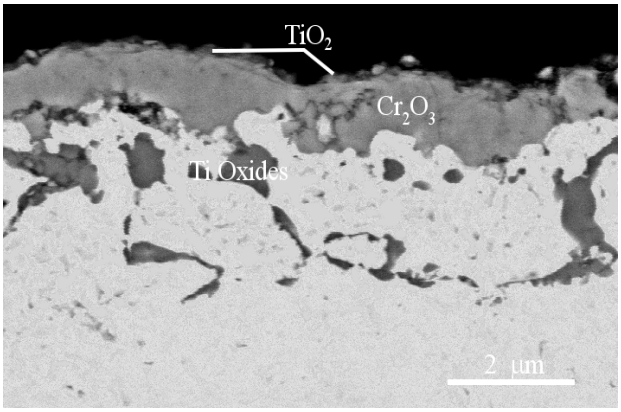

(j.)

Figure 5-51 SEM micrographs of the surfaces and cross-sections of samples containing 0.004% (a&b), 0.84% (c&d), 1.65% (e&f), 2.78% (g&h), and 3.98% (i&j) titanium exposed at 700°C for 96 hrs in dry air.

5.3 COATINGS

5.3.1 Initial Tests

Coatings, Sr doped $LaCrO_3$ and $LaFeO_3$, were applied to several different substrate materials by sputtering. X-Ray diffraction of the as coated samples show the deposited coating is amorphous (Figure 5-52a). Figure 5-53a shows the specimen in the as coated condition. Exposure of the samples at 800°C in dry air for 100 hours yields a porous (Figure 5-53b), crystalline coating of the correct phase, as shown by the XRD patterns in Figure 5-52b. The chromia formed under the coating (Figure 5-53b) is noticeably thinner than that on the uncoated side of the sample (Figure 5-53c), which occurs due to the coating acting as a diffusion barrier. Unfortunately, the porous nature of the coating will not hinder the vaporization to its full potential. It is believed that during the crystallization of the coating, the coating undergoes phase changes from amorphous to a less dense chromate prior to forming the final, denser chromite phase, leaving the coating porous.

5.3.2 Annealing/Crystallization

The intermediate chromite phase may be avoided if a pretreatment is done in a low P_{O2} environment, leaving the coating a dense chromite phase[59]. Samples exposed in an Ar-4%H_2 mixture (P_{O2}~10^{-8}) do indeed appear denser than those exposed in dry air only (Figure 5-54a). Unfortunately, the lack of pores to compensate for the large volume changed associated with the crystallization causes cracks (Figure 5-54b) that run the entire thickness of the coating (Figure 5-54a). Once again, the effectiveness of the coating to hinder vaporization is compromised. A previously cracked sample has been reexposed for 96 hours at 800°C to determine if the cracks continue to propagate. Figure 5-55 shows the surface of this sample at low and high magnification, as well as a cross sectional image. When comparing Figure 5-55a to Figure 5-

55b, it appears the coating has not cracked further. It even appears that the cracks may be healing themselves as shown by apparent termination of the crack in Figure 5-55b. It is important to notice that the coating appears to be porous at the termination sites, which in fact is confirmed by Figure 5-55c.

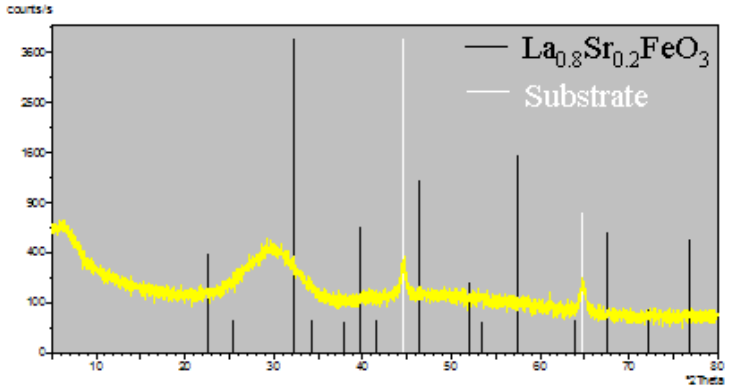

(a.)

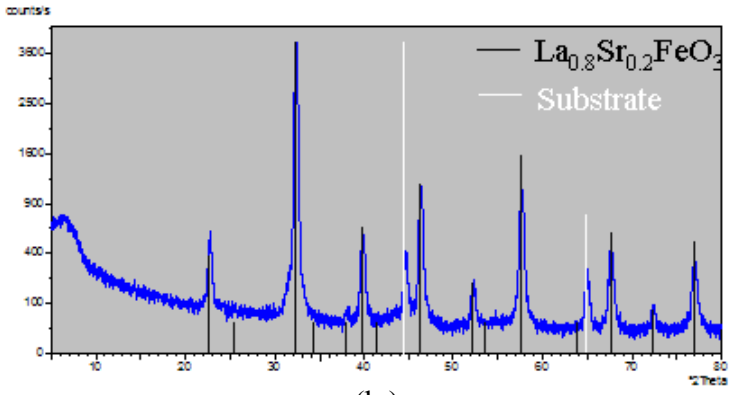

(b.)

Figure 5-52 XRD patterns of a Sr doped Lanthanum Ferrite before (a.) and after exposure (b.)

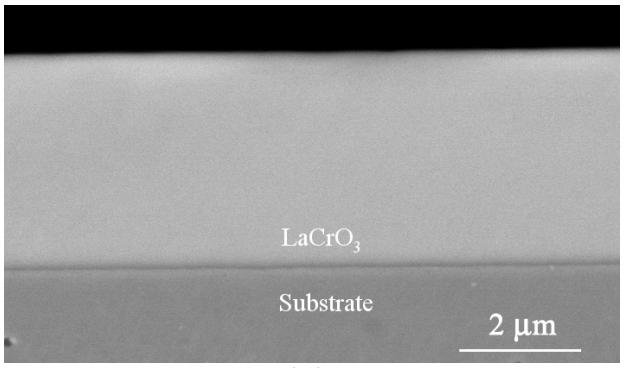

(a.)

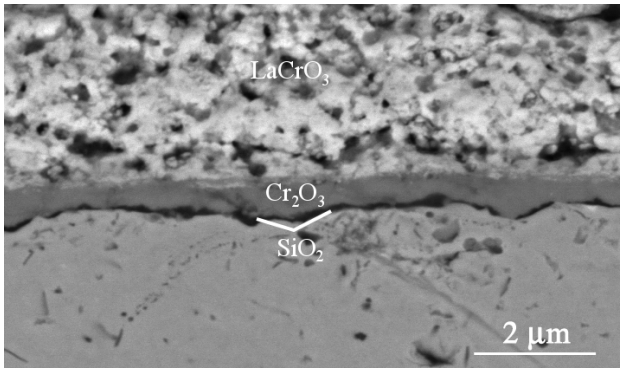

(b.)

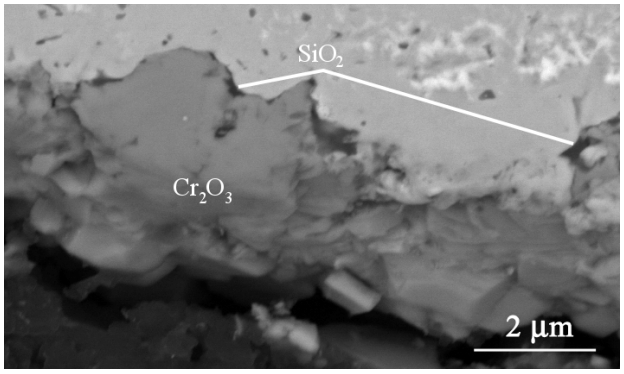

(c.)

Figure 5-53 Cross-sectional SEM images of a coated E-Brite sample as coated (a), as well as the coated (b.) and uncoated (c.) sides after 100 hrs exposure at 900^{o}C in air.

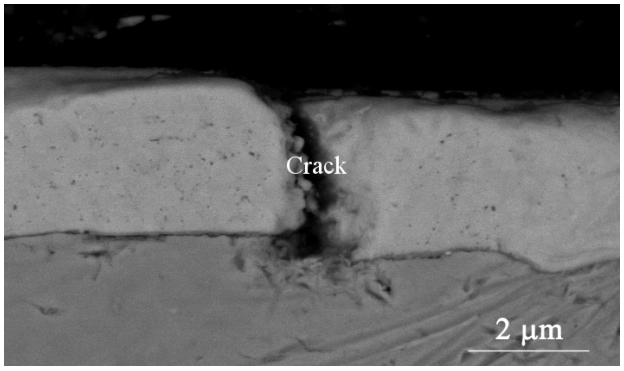

(a.)

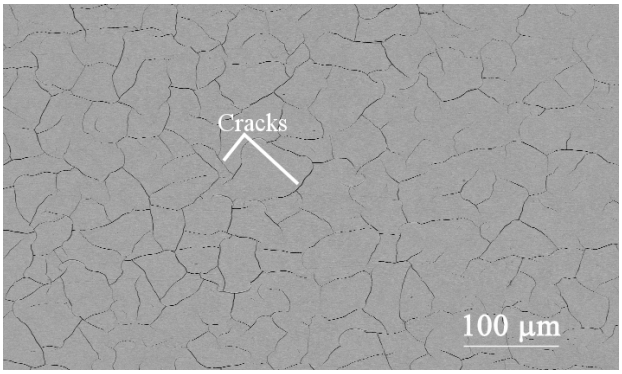

(b.)

Figure 5-54 Backscatter SEM images of the cross section (a.) and surface (b.) of a pretreated $La_{0.8}Sr_{0.2}FeO_3$ coating showing profuse vertical cracking.

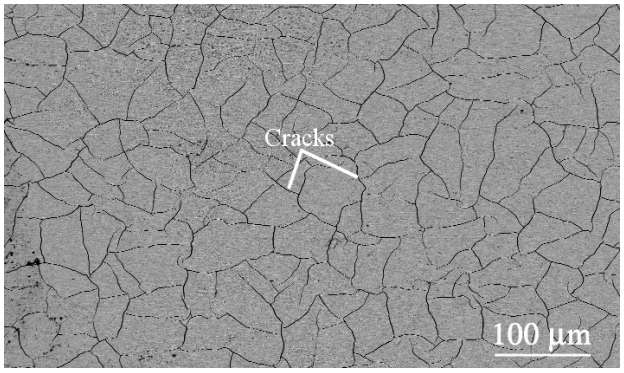

(a.)

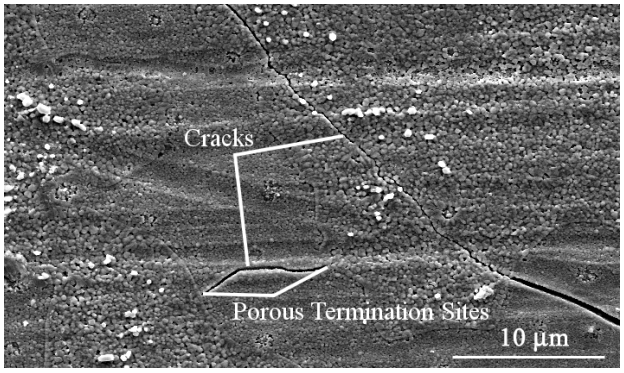

(b.)

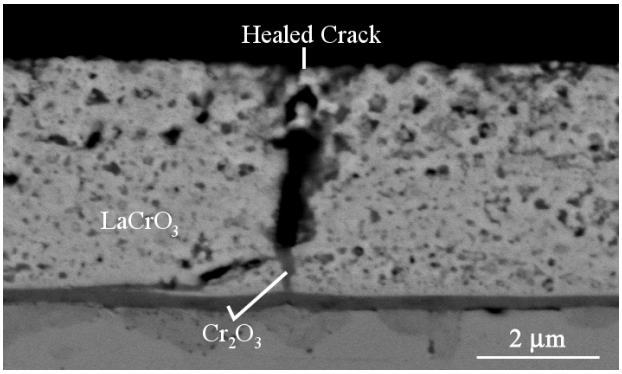

(c.)

Figure 5-55 SEM micrograph of a $LaSrCrO_3$ coating surface after reexposure at low (a.) and high (b.) magnification, as well as the corresponding cross – sectional image (c.).

5.3.3 Thickness Effect

A second possible reason for the annealed coatings to crack, is that there is an effect of coating thickness. It is common for oxide scales to begin to build up strain energy. Once this stored strain energy reaches a critical value, the system will react to release the energy. The oxide can deform or crack or the metal can deform. In this case, the strain energy release occurred by tensile cracking. Samples with 0.2 and 0.8 μm thick undoped $LaCrO_3$ coatings and samples with 5.5 and 10 μm thick Ca doped $LaCrO_3$ coatings were given the same pretreatment exposure to determine if the cracking does also have a thickness dependence. Figure 5-56 shows the surfaces and cross sections of the samples.

There appears to be no surface cracking in the two thinnest coatings (Figure 5-56a&c). No cracks were visible in the cross – section of the 0.2 mm coating (Figure 5-56b). There did appear to be a delamination in the center of the 0.8 μm coating (Figure 5-56d). This is most likely due to an interruption during the deposition process.

The 5.5 μm coating showed the most profuse cracking from the surface view(Figure 5-56e), similar to those shown above. The cracks are rather vertical and run to the substrate (Figure 5-56f). The fact that the "dirt" in the image appears to go behind the coating on the left side, means that it is not an artifact of the metallographic preparation per se, but was present prior to mounting. This leads to the idea that this particular crack was rather severe (wide) to be so deeply and compactly filled that the "dirt" was able to remain during metallographic preparation.

The thickest coating, at 10 μm, shows similar cracking on the surface (Figure 5-56g) as the above samples, but it also appears less severe. Several of the cracks are wedge type as shown in Figure 5-56h. A clear line can be seen in the coating, separating a porous inner layer from a

dense outer layer. All of the cracks began at the surface and terminated at this line. The porous inner layer must add some strain tolerance to the inner layer. While the grading of coatings is frequently desired and useful, it was not intentional in this case, as its porous nature combined with the pathways to the surface from the cracks reduce the ability of the coating to prevent vaporization. While there does appear to be a thickness effect, it must be noted that the thicker, cracked coatings contain the dopants Ca and Sr. The thinner coatings are undoped. The role that the dopants may play in the cracking has not been explored in this work, although these elements can act as sintering aids.

5.3.4 Crack Sealing

Given the popularity and benefits of using a coating, efforts were made to seal the cracks. The cracks appear to be wide enough to allow for some material to fill the crack and thereby seal off the path to the chromia scale. Two strategies were taken. The first was to simply aluminize the surface using chemical vapor deposition. The second is a sol gel process that results in the cracks being filled with La_2O_3. It is important to note that both of these processes add significant cost to the already expensive coating.

The theory behind the aluminizing strategy is that the cracks make up only a small amount of the surface area that little is lost in terms of the electrical properties when the aluminum oxidizes, assuming it deposits only in the cracks. Given the stability of the oxide coating, the aluminizing reaction would consist of the Al bearing gas reacting preferentially with "metal" (assuming the substrate did not oxidize) to form Fe and/or Cr aluminides. If the substrate had

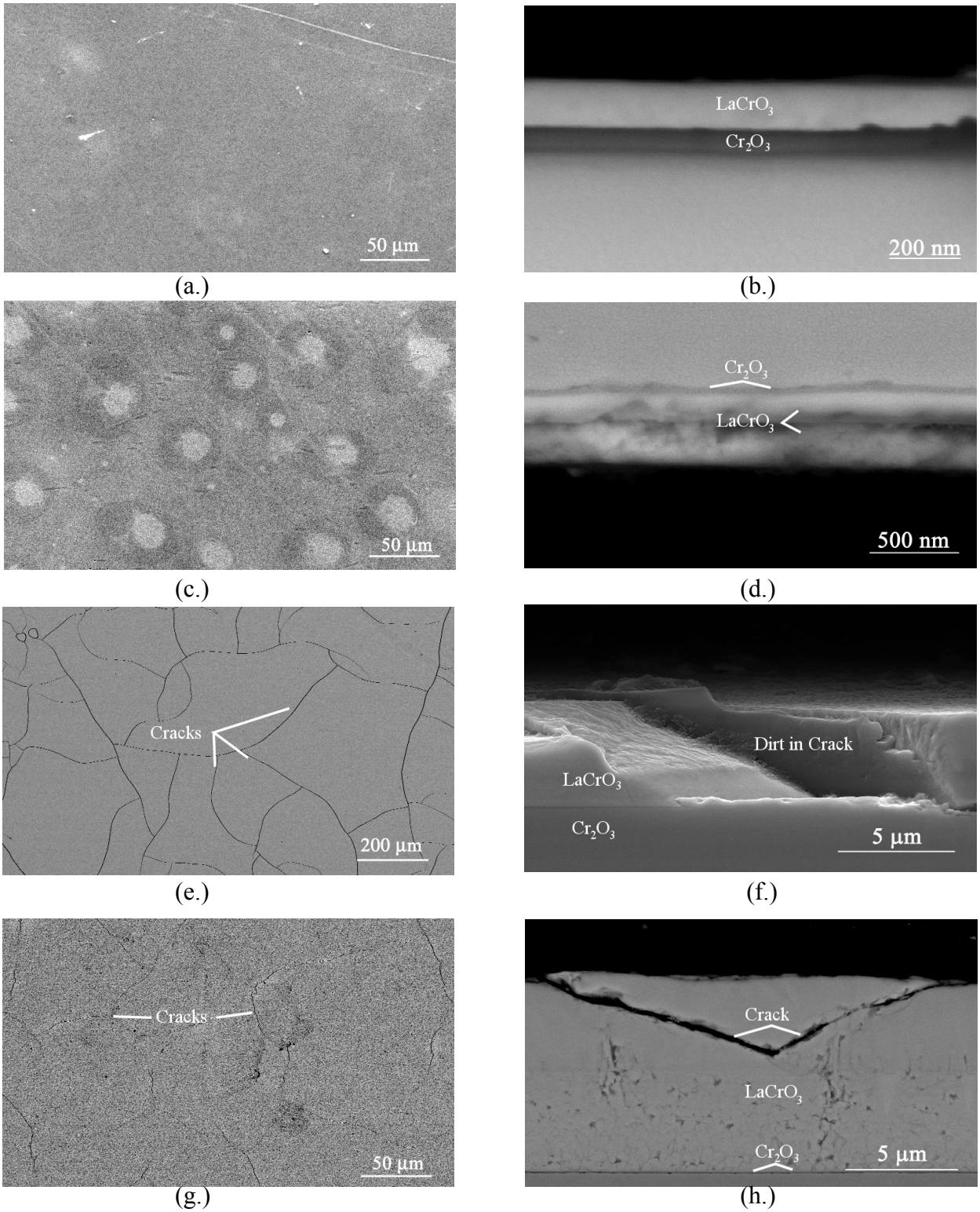

Figure 5-56 Surface and Cross – sectional SEM micrographs of 0.2 µm (a & b), 0.8 µm (c & d), 5.5 µm (e & f.), and 10 µm (g & h) thick coatings annealed for 2 hrs at 800°C in Ar-4%H_2.

oxidized, the Al would have to displace the Cr in the oxide formed on the substrate to form there, leaving alumina. It was not certain if this would occur, if the coating would be subject to a similar reaction, and finally, if the coating would be deposited after all of the oxides had been converted to alumina.

Samples with cracked (2hrs 800^{o}C Ar-4%H_2) $La_{0.8}Sr_{0.2}FeO_3$ and $La_{0.8}Sr_{0.2}CrO_3$ coatings were sent out to Howmet for aluminizing. Figure 5-57a shows the initial cracked surface and Figure 5-57b shows the surface after aluminizing for the ferrite coating. To the naked eye, the surface of the aluminized sample was shiny metallic as opposed to the gunmetal color of the coating, leading to the conclusion that aluminum did in fact wet the coating and covered the surface. EDS proved that the surface was covered by Al. Visible on the surface of the sample are the beginnings of grain boundary ridges, as are typical with aluminde coatings. The aluminum overlayer also showed cracking of its own. Figure 5-57c is a cross-sectional micrograph with the results of a line scan across the thickness of the sample. The Al has penetrated 50 μm on both sides of the sample, which is much more than desired. There is no sign of the coating and very few oxides. It appears that the chromia and coating were reduced and the both went into solution. The result of the coating is essentially a high Al content FeCrAl coating on a now Al containing ferritic stainless steel doped with La. While this may have some interesting properties and applications, this system is not well suited for use as an SOFC interconnect. With the plethora of problems that are noted here, this strategy must be considered a failure.

The theory behind the second strategy is to use lanthanum oxide to fill the cracks, as it is already a component of the system. Any chromium that interacts with the seal would result in the formation of $LaCrO_3$. The precursor Lanthanum III nitrate-hexahydrate was dissolved into

deionized water. Samples identical to those used in the aluminizing experiments were then placed into the beaker. The entire beaker was placed in a Struers Epovac and a vacuum was pulled in order to remove any air trapped in the cracks that may prevent full penetration of the solution. After 5 minutes, the samples were removed from the solution and placed under a heat lamp to dry. Figure 5-57d shows the results of this experiment. From the surface, the cracks appear to be partially filled (~75%). These results are promising, but would likely worsen after any exposure that would decompose the precursor and sinter the La_2O_3. If the cost is determined to be acceptable, further work should be done to develop this strategy.

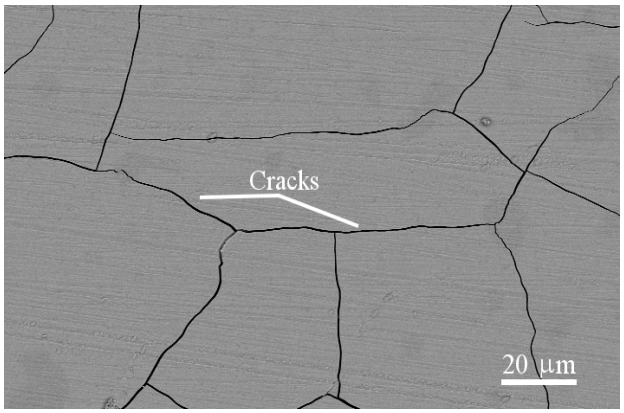

(a.)

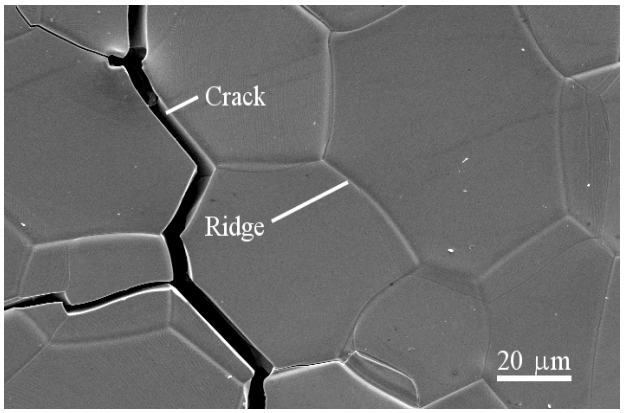

(b.)

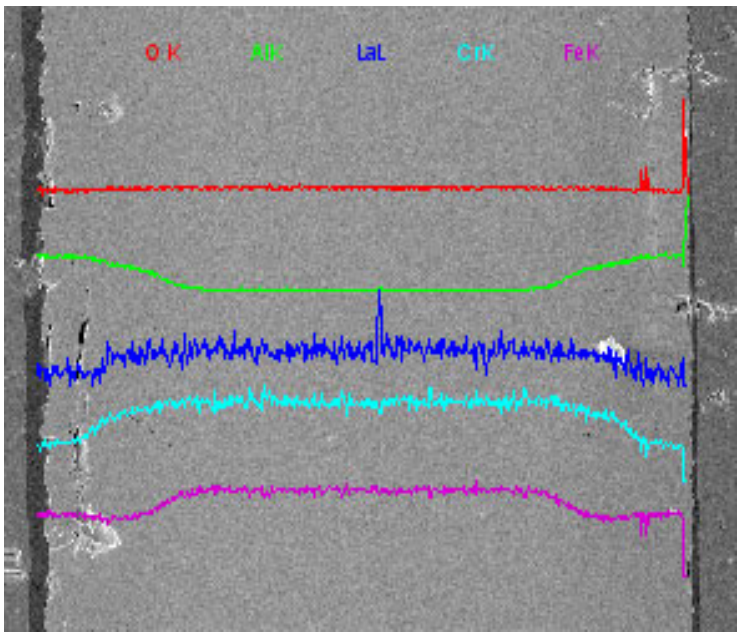

(c.)

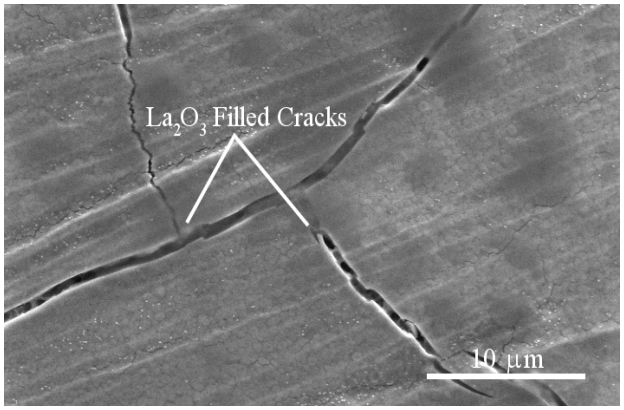

(d.)

Figure 5-57 SEM micrographs showing the intial cracked coating surface (a.), the surface after aluminizing (b.), the cross-section with line scan results after aluminizing (c.), and the surface after La_2O_3 treatment (d.)

5.4 DOPING

Pulsed laser deposition has been used to apply dopant layers of CeO_2 on one side of E-Brite substrates polished to 0.05 μm SiO_2. The deposition times were 15 and 5 minutes and a pressure of 0.02 torr. To the naked eye, the coated surfaces displayed interference colors and appeared to vary in thickness (color changes) and coating adherence (some areas appeared flaky). The coated surfaces were also observed using the SEM. While the thickness variations were not discernable, the coating did range from regions that were extremely uniform to regions that were very mottled with debris on the surface. The samples were then oxidized for 100 hours at 800^{o}C in dry air. Figure 5-58 shows the comparison of the two dopant layer thicknesses and the corresponding uncoated sides. The ceria layer in Figure 5-58a, at ~0.75 μm, is too thick for use as a practical dopant layer and was very porous. The oxide under the thick ceria is on the order of 0.25 μm, which when compared to the ~0.75 μm scale for the undoped side (Figure 5-58b), it is apparent there was some effect due to the presence of the ceria. The subsequent coating attempt yielded similar results with a nanoscale ceria layer, as illustrated in Figure 5-58c & d. The doped oxide appears to be a factor of two thinner than the undoped oxide. These reductions in the growth rate are in accordance with the literature. The vast amount of ceria on the first sample did not allow for comment on the growth direction of the oxide. Observations of the sample with the shorter deposition time show that while the ceria coating was not clearly visible, it was detected near the outer surface of the extremely thin oxide. This implies that the doping was affective. As this effect has been well established in the literature and these tests are in agreement about the effectiveness of ceria, no further tests were done on E-Brite.

Upgrades to the PLD equipment and more experience using it has resulted in further optimization of the dopant layer. A sample of the 2.78% Ti ferritic alloy was coated using the new technique. The sample was polished to 600 grit, so as to not gain any advantages due to surface finish. It was then exposed to a four minute deposition, during two of which an adjustable shield was placed in front of the sample in order to protect the sample while the surface of the target was cleaned. The shield was then removed for the last two minutes to deposit ceria on the sample. At this point the sample was rotated 180^{o} and the process was repeated. The sample was then flipped and other side was coated in the sample manner.

The sample was tested cyclically at 800^{o}C (Identical to the previously described cyclic testing). To the naked eye, the sample still retained the light grey appearance that the author has come to associate with the Fe-Cr-Ti alloys. Figure 5-60 shows the kinetic data for the doped samples and the undoped sample previously exposed. There appears to be no effect of the dopant on the mass change, as would be expected from the large decrease reported by Ecer. The micrographs in Figures 5-59a & b show the cross sections of the doped and undoped samples after 1000 cycles. The dopant resulted in only a small decrease in the chromia thickness. The doped oxide is also much more irregular. The amount and depth of the internal oxidation is the same for both cases. The white line running through the oxide is the ceria. If the dopant layer is considered to be an inert marker, it appears that the chromia is growing almost entirely inward, which is expected from the work of Ecer[49]. The titania layer is thicker than that for the undoped case and grows outwardly through the ceria layer. In fact the thickness of the TiO_2 layer appears to compensate for the reduced Cr_2O_3 thickness and could be the reason that the mass changes are the same as the undoped sample.

This is a baffling situation. On one hand, the Ti doping is creating cation vacancies that are expected to increase the outward diffusion of chromia and on the other, the ceria doping is expected to prevent outward diffusion. Being that the ceria is found at the chromia/titania interface, it would appear that the chromia growth was inward, though the thickness of the chromia is not substanially reduced. This would imply that either oxygen transport is enhanced or that the oxide growth without ceria is also largely inward. This does not appear to be supported by the previous experiments where the titania layer is shown to thicken with time and chromia frequently has a highly crystallographic blade morphology, both of which seem to be results of outward diffusion. The outward diffusion of the Ti might be due to the fact that the ionic radius of Ti is smaller than that of Cr, and therefore is not as affected by the reactive element doping. This could be the reason the ceria layer is located at the chromia/titania interface, but still does not account for the oxide thickness. More detailed work needs to be performed to understand this phenomenon.

Due to the availability of the precursor used for the crack filling by La_2O_3, it was also attempted to dope a sample with La_2O_3. La doping has been discussed in the literature and is typically not as effective as CeO_2. It was deterimined to be worth trying though due to some possible beneficial effects, such as forming lanthanum chromite with any chromia that remains of the surface. The dopant was applied in a similar fashion as described above for crack filling. It differed in that a vacuum was not required (relatively flat surface) and that a syringe was used to place the solution on the samples. A sample of the 2.78% Ti ferritic alloy was doped to to ~1-2 mg/cm^2 (after drying). The sample was then cyclically tested at 800^{o}C. Unfortunately, the samples were not fully dried or decomposed prior to testing and immediately showed large weight losses. The kinetic data is shown in Figure 5-60. The dopant layer was also able to spall

off during testing and handling, further distorting the weight change data. Therefore the only method of comparing the effectiveness of lanthanum oxide doping is to compare the oxide thicknesses to the undoped and ceria doped samples (Figure 5-59a, b, &c). At first glance, the La_2O_3 appears to be more effective than the CeO_2 doping, but when the amount of dopant is considered (there is signifcantly more La_2O_3 applied to the surface), it is not possible to determine this to be true. Disregarding the oxide thicknesses, the dopant differed from the CeO_2 doping only in that the dopant mostly remained on the outer surface of the oxide.

From these initial tests, it does not appear that slowing the oxide growth rate for the Fe-Cr-Ti alloys is likely to occur using CeO_2 or La_2O_3 as dopants. The oxidation does not decrease to an extent that would justify the added expense of the dopant. The oxide layers grown are irregular, which will cause contact problems in application. It is very likely that the presence of the Ti in the oxide increases the growth rate to such an extent that it would require a much larger amount of dopant to decrease the growth rate. Care must be taken also that the dopant does not interfere with the formation of the TiO_2/Cr_2O_3 microstructure and is not detrimental when placed into the SOFC system. Much more work must be done in this area.

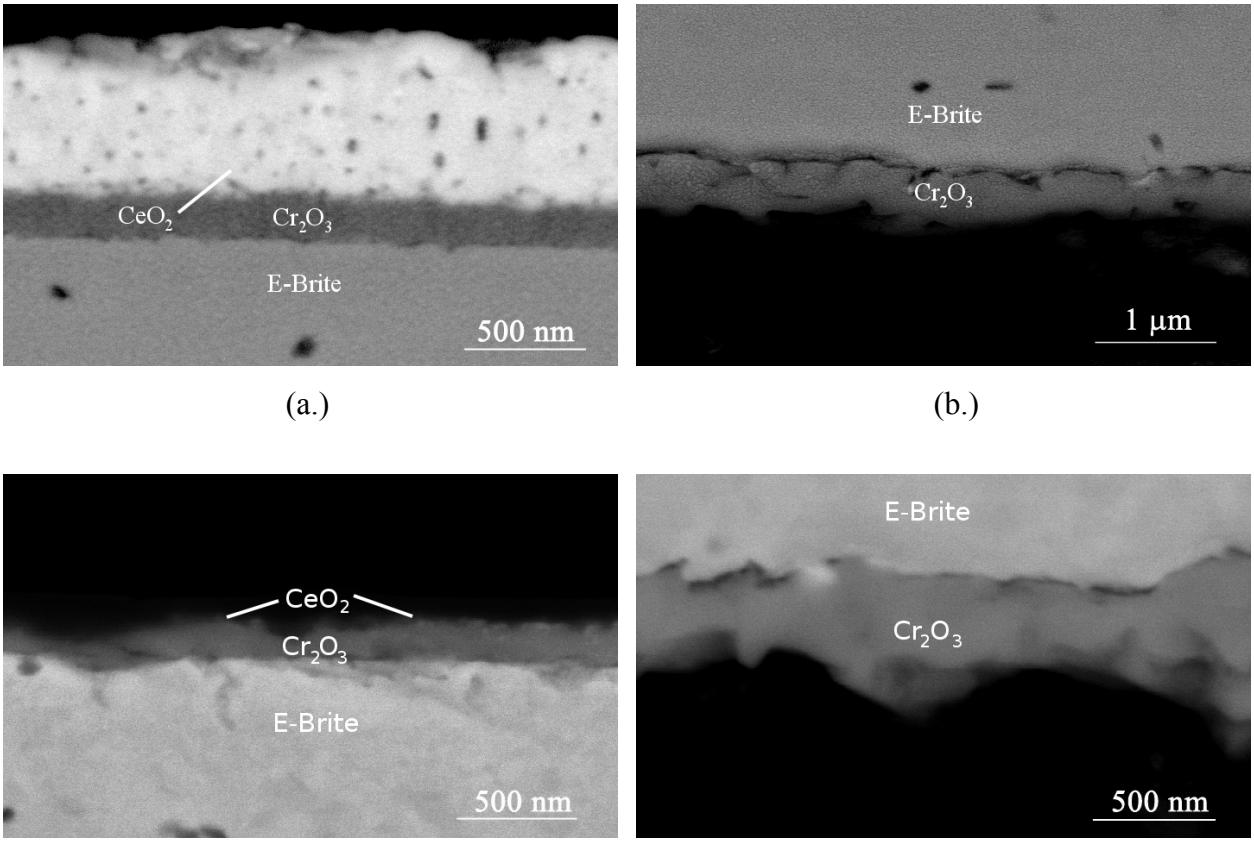

(a.) (b.)

(c.) (d.)

Figure 5-58 Micrographs of samples coated with CeO_2 using pulsed laser deposition for 15 min (a.) and 5 min (c.) and the corresponding uncoated sides (b.&c.) exposed for 100 hrs in dry air at 800^{o}C

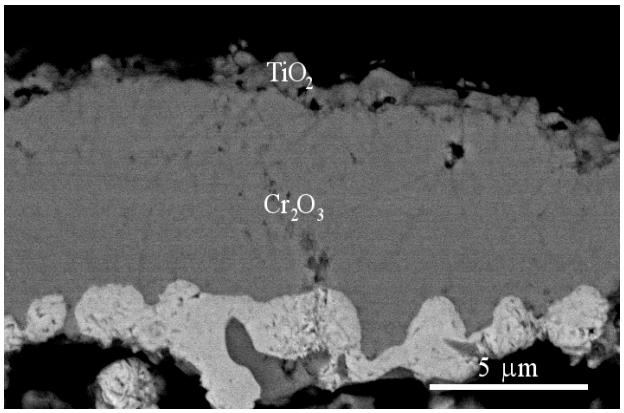

(a.)

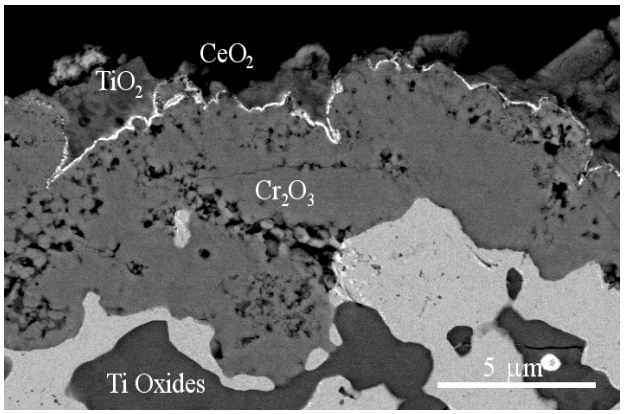

(b.)

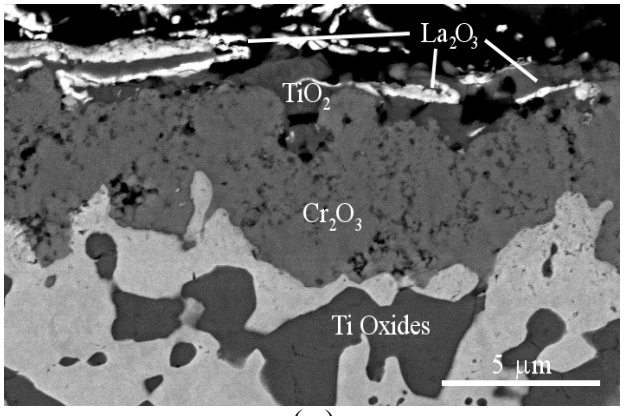

(c.)

Figure 5-59 SEM micrographs of undoped (a.), CeO_2 doped (b.), and La_2O_3 doped Fe-22Cr-2.78Ti exposed for 1000 cycles in dry air at 800°C.

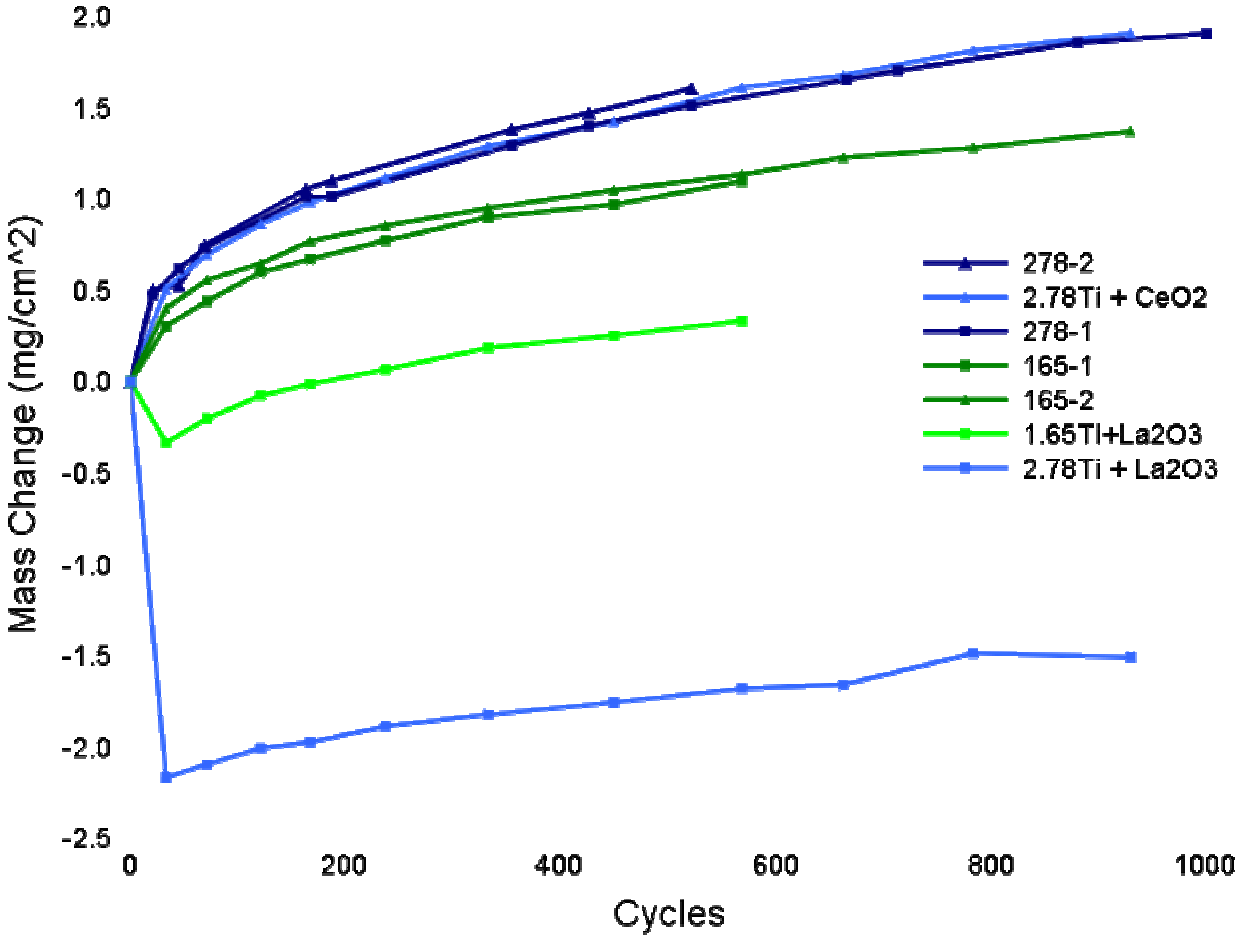

Figure 5-60 Plot of mass change vs. number of cycles for doped and undoped the Fe-22Cr-1.65Ti and Fe-22Cr-2.78Ti alloys.

6.0 SUMMARY AND CONCLUSIONS

- E-Brite and Crofer have been shown to behave similar to the behavior reported in the literature for the experiments performed in this work
- Short time experiments on Crofer show that Mn diffuses rapidly through the oxide in areas above alloy grain boundaries, forming a network of $MnCr_2O_4$ at those locations prior to forming a continuous layer
- Ti does diffuse through chromia to form an outer layer of titania as well as forming internal oxides of various other Ti oxides. The propensity to form both of these increases with increasing Ti content in the alloy. The outer layer is not due to transient oxidation. This overlayer does increase the resistance to vaporization.
- Ti doping greatly increases the growth rate of the chromia scale, with increasing oxide growth rate with increasing Ti. The oxide growth direction also changes from more inward growth to outward growth.
- Experiments in wet exposures did tend to result in some weight loss, which is indicative of vaporization, but the TiO_2 layer was penetrated in several locations by very high aspect ratio blades of chromia. These blades contribute to the weight loss.
- While the ASR values for the Fe-Cr-Ti alloys are higher than that measured for Crofer, when the increased oxide thickness is considered, it has been shown that the resistivity is actually lower than that for Crofer. The resistivity decreases with increasing Ti. This can

be interpreted to mean that if the oxide growth can be reduced, most likely by doping, and the oxidation mechanism remains the same, these alloys could have a much lower ASR than Crofer.

- The weight change data for the cyclic testing of the Fe-Cr-TI alloys is very close to the results of the TGA testing over similar time periods. Very little spalling was observed. This indicates that the oxide formed is very tough and adherent.
- There is not a major dual atmosphere effect observed in these alloys. Lower Ti containing alloys tended to have thicker oxides on the air side than that for an air only exposure. The difference between the dual atmosphere and air only oxides decreases with increasing Ti content. This is likely due to Ti reducing the amount of hydrogen that can be incorporated into the oxide on the fuel side.
- In cell testing shows that the initial performance of the 3% Ti alloy was higher than that of E-Brite and Crofer. Crofer displayed the least amount of performance drop (which implies the degradation is mostly due to oxidation), followed by the Fe-Cr-Ti alloy, and E-Brite. The rapid drop of E-Brite is due to poisoning. The Fe-Cr-Ti alloy likely has a combination of both oxidation and poisoning due to the fact that the chromia was still present on the surface. Preoxidation will be needed for the Fe-Cr-Ti alloys to be used.
- $LaCrO_3$ coatings were shown to be porous unless pretreated and crack depending on coating thickness. Both porosity and cracking prevent the coating from being effective in supressing vaporization. Steps to counteract the cracking were unsuccessful. These coatings are not favorable for use in SOFCs/
- Doping of E-Brite with CeO_2 produced results similar to those seen in the literature. The effect of CeO_2 and La_2O_3 were very small on the growth of the Fe-Cr-Ti alloys. The

dopants remain near the surface with rutile growing through. Any decrease in the growth of chromia appears to be compensated by increased TiO_2 growth, leaving the mass change nearly identical to the undoped sample with a similar exposure.

- The Fe-Cr-Ti alloys do show some potential in some of the areas important for use as an SOFC interconnect (interfactial toughness, low resistivity, ability to reduce vaporization, etc.). Unfortunately, the reason for these enhancements (Ti doping) are also the cause of its greatest downfall, i.e. its rapid growth rate.

7.0 FUTURE WORK

There is still much work to be done on all the topics discussed above. There are also some new directions that the work must take due to some of the results. The recommended future work to be done is discussed below.

- The most obvious recommendations for future work is to continue the testing and development of the Fe-Cr-Ti alloys. Possible experiments could involve longer isothermal exposure times or cyclic tests with cycles more characteristic of the SOFC operating conditions. Studies determining the conditions to effectively preform the rutile layer and the subsequent behavior of the alloy are of importance. Further work could even determine the most effective amount of Ti in the alloy to balance the mechanical properties, electrical properties, and the oxidation resistance.
- A large portion of this work was predicated on the phenomenon of certain minor alloying elements, such as Mn and Ti, can diffuse through a dense, protective oxide, such as chromia. This is known to also happen in several other systems. Work must be done to understand this effect in order to better utilize it when necessary and to also prevent it when it may be detrimental.
- While it would be difficult to develop, a standardized method for determining the ASR of a sample should be in place. Currently, ASR values are realistically only comparable to measurements from the same apparatus. This effectively means that an investigator must

take literature results with much caution or take the time to perform the experiment themselves.

- Much more work needs to be performed in order to fully understand the dual atmosphere effect. A large portion of the work performed on interconnect candidate materials is still only performed in single atmospheres. In fact, a vast majority of the literature involving dual atmosphere experiments is work performed at a single research facility, that being PNNL. While the apparatus used in this work has replicated results from PNNL using pure metals such as silver and nickel, it has yet to do so with ferritic stainless steels.
- Coatings that are more effective at reducing vaporization, stable in most conditions, and more durable need to be developed. It appears investigators have already abandoned the $LaXO_3$ type coatings in favor of Mn – Co spinels.
- The reduction of the growth rate of chromia when reactive element dopants are present is very well documented in the literature. Despite the fact that decreasing the oxide thickness would result in better ASR properties, there does not appear to be a large amount of work involving externally doping metals for interconnects and how they would affect the SOFC.

REFERENCES

1. Solid State Energy Conversion Alliance (SECA), www.netl.doe.gov/technology/coalpower/fuelcells/, accessed 3/19/2006

2. Perry, T. and Fuller, M., A Historical Perspective of Fuel Cell Technology in the 20th Century, Journal of the Electrochemical Society, 2002, 149(7), p.S59-S67.

3. Ford Focus FCV - Hybrid Ford Motor Compay, http://www.ford.com/en/vehicles/specialtyVehicles/, accessed 11/10/2006

4. D. Hakim, Taking the Future for a Drive, New York Times, November 2, 2005

5. Fuel Cell Handbook 6th edition, Department of Energy, 2002

6. fc_comparison_chart, http://www.eere.energy.gov/hydrogenandfuelcells/, accessed 3/16/2006

7. Zhu, W.Z. and Deevi, S.C., Development of Interconnect Materials for Solid Oxide Fuel Cells, Materials Science and Engineering A, 2003, A00, p.1-17.

8. Z. Yang, J. Stevenson, and P. Singh, Solid Oxide Fuel Cells, Advanced Materials & Processes, 2003, 161(6), p.34-37.

9. J. Thijssen, The Impact of Scale-Up and Production Volume on SOFC Stack Cost, 7th Annual SECA Workshop and Peer Review, September 12, 2006.

10. J. Hammer, K. Coyne, S. Laney, R. Jackson, F. Pettit, & G. Meier, Oxidation of Ferritic Stainless Steels in Simulated Solid Oxide Fuel Cell.., Oxidation of Metals, 2007, 67(1/2), p.1-38.

11. M. Birch, Oxidation of Metallic Interconnects in Solid Oxide Fuel Cells, Senior Research Project, Department of Materials Science and Engineering, University of Pittsburgh, 2004

12. P. Kofstad, High Temperature Oxidation, Elsevier Applied Science, London, 1988

13. N. Birks, G. Meier, & F. Pettit, Introduction to High Temperature Oxidation of Metals, Cambridge University Press, Cambridge, 2006

14. C. Wagner, Theorectical Analysis of the Diffusion Processes Determining the Oxidation, Journal of the Electrochemical Society, 1952, 99(10), p.369-380.

15. D. Smyth, The Defect Chemistry of Metal Oxides, Oxford University Press, New York, 2000

16. A. Holt and P. Kofstad, Solid State Ionics, 1994, 69, p.137-143.

17. A. Holt, P. Kofstad, Electronic conductivity and defect structure of Mg-doped Cr_2O_3, Solid State Ionics, 1997, 100, p.201-209.

18. A. Holt, P. Kofstad, Electrical conductivity of Cr_2O_3 doped with TiO_2, Solid State Ionics, 1999, 117, p.21-25.

19. C. Tedmon, Journal of the Electrochemical Society, 1966, 133, p.766.

20. K. Hilpert, D. Das, M. Miller, D.H. Peck, R. Weiss, Chromium Vapor Species over Solid Oxide Fuel Cell Interconnect Materials.., Journal of the Electrochemical Society, 1996, 143, p.3642.

21. S. Jiang, Journal of the European Ceramic Society, 2002, 22, p.361-373.

22. K. Fujita, T. Hashimoto, K. Ogasawara, H. Kameda, Y. Matsuzaki, T. Sakurai, Journal of Power Sources, 2004, 131, p.270-277.

23. S. Badwal, R. Deller, K. Foger, Y. Ramprakash, J. Zhang, Solid State Ionics, 1997, 99, p.297-310.

24. D. England and A. Virkar, Journal of the Electrochemical Society, 1999, 146(9), p.3196-3202.

25: K. Hance, Effects of Water Vapor on the Oxidation Behavior of Alumina and Chromia Forming Superalloys at Temperatures Between 700^{o}C and 1000^{o}C, PhD Dissertation, Materials Science and Engineering Department, University of Pittsburgh, 2005

26. A. Sabioni, A Huntz, E. Luz, M. Mantel, and C. Haut, Comparative Study of High Temperature Oxidation Behavior of AISI 304, Materials Research, 2003, 6(2), p.179-185.

27. T. Brylewski, M. Nanko, T. Maruyama, K. Przbylski, Solid State Ionics, 2001, 143, p.131-150.

28. T. Brylewski, J. Dabek, K. Prsybylski, Journal of Thermal Analysis and Calorimetry, 2004, 77, p.207-216.

29. K. Huang, P. Hou, J. Goodenough, Solid State Ionics, 2000, 129, p.237-250.

30. R. Peraldi, B. Pint, Oxidation of Metals, 2002, 61(5-6), p. 463-483.

31. H. Grabke, Corrosion, 1995, 51(711)

32. D. England, A. Virkar, Journal of the Electrochemical Society, 2001, 148, p.A330.

33. W.J. Quadakkers, T. Malkow, P.Abellion, U.Flesch, V. Shemet, L. Singhauser, Proc. 4th European Solid Oxide Fuel Cell Forum, 2000.

34. P. Singh, Personal Correspondence, 2003

35. Z. Yang, M. Walker, P. Singh, J. Stevenson, Journal of the Electrochemical Society, 2003, 6(10), p.B35-37.

36. R.W. Jackson, Unpublished research, 2005

37. H. Kurokowa, K. Kawamura, T. Maruyama, Solid State Ionics, 2004, 168(1-2), p.13-21.

38. Z. Yang, J. H, M. Walker, G. Xia, S. Simner, J. Stevenson, Journal of the Electrochemical Society, 2004, 151(1), p.A1825-1831.

39. M. Cox, B. McEnaney, V. Scott, Nature-Physical Science, 1972, 237, p.839.

40. R. Lobnig, H. Schmidt, K. Hennesen, H. Grabke, Oxidation of Metals, 1992, 37(1/2), p.81-83.

41. J. Pron-Abellan, V. Shement, F. Tietz, L. Singheiser, W. Quadakkers, A. Gil, Proc. Solid Oxide Fuel Cells VII, 2001

42. C. Issartel, et. al., Effects of titanium on a ferritic steel oxidation at 950^{o}C, Materials Science Forum, 2004, 461-464, p.69-76.

43. D. Sigler, Oxidation of Metals, 1996, 46(1/2), p.335-364.

44. C. Johnson, Personal Communication, 2005

45. Z. Yang, G. Xia, S. Simner, J. Stevenson, Journal of the Electrochemical Society, 2005, 152(9), p.A1896-A1901.

46. R. Smith, et al., Presentation at MS&T conference - Cincinnatti, 2006

47. Y. Yang, T. Wen, H. Tu, D. Wang, J. Yang, Characteristics of lanthanum strontium chromite prepared by glycine nitrate, Solid State Ionics, 2000, 135, p.475-479.

48. G. Ecer and G. Meier, The Effect of Ceria on the Oxidation of Ni-50Cr Alloys, Oxidation of Metals, 1979, 13(2), p.159.

49. G. Ecer, R. Singh, G. Meier, Oxidations of Metals, 1982, 18(1/2), p.55.

50. H. Qi, D. Lees, Oxidation of Metals, 2000, 53(5/6), p.507-527.

51. M. Bennet, A.Tuson, D. Moon, J. Titchmarsh, Influence of cerium ion implanation on chromium oxidation, Surface and Coatings Technology, 1992, 51, p.65-72.

52. L. Ramanathan, Corrosion Science, 1993, 35(5-8), p.871-878.

53. S. Patil, S. Kuiry, S. Seal, R Vanfleet, Sythesis of nanocrystalline ceria particles for high temperature oxidation., Journal of Nanoparticle Research, 2002, 4, p.433-438.

54. J. Shen, L. Zhou, T. Li, Journal of Materials Science, 1998, 33, p.5815-5819.

55. H. Grabke, Materials and Corrosion, 2005, 56(6), p.384.

56. Giggins and Pettit, , Oxidation of Metals, 1980, 14(5).

57. F. Pettit, J. Goebel, G. Goward, Thermodynamic analysis of the simultaneous attack of some metals by two oxidants, Corrsion Science, 1969, 9, p.903.

58. C. Johnson, Personal Communication, 2006

59. C. Johnson, Personal Communication, 2004

60. N. Boriskina and I. Kornilov, Russian Journal of Inorganic Chemistry, 1964, 9(5), p. 636-639